

Sharp Interface Level Set Method on a Co-located Grid for Nucleate Boiling with Power Transients

*Submitted in partial fulfillment of
the requirements for the degree of
Doctor of Philosophy
by*

SANJID C S
(174100008)

Supervisors:
PROF. JANANI SRREE MURALLIDHARAN
and
PROF. ATUL SHARMA



Department of Mechanical Engineering
Indian Institute of Technology Bombay
Mumbai 400076 (India)

January 2023

Dedicated to Parents and Wife

Declaration

I declare that this written submission represents my ideas in my own words and where others' ideas or words have been included, I have adequately cited and referenced the original sources. I also declare that I have adhered to all principles of academic honesty and integrity and have not misrepresented or fabricated or falsified any idea/data/fact/source in my submission. I understand that any violation of the above will be a cause for disciplinary action by the Institute and can also evoke penal action from the sources which have thus not been properly cited or from whom proper permission has not been taken when needed.

SANJID C S

Date: January 2023

(174100008)

Abstract

In the present work, contributions are made in two major aspects, one is Level Set Method (LSM)-based Computational multi-Fluid Dynamics (CmFD) *development* on co-located grid for problems *with* and *without* phase change; and second is CmFD *application and analysis* of developed in-house code for studying the effect of power transients on single bubble nucleate boiling; presented in two parts for this thesis. *Part I* on CmFD development presents the numerical methodologies—discretization, solution method, and solution algorithm—and validation/verfication of the present in-house codes, whereas *Part II* presents the effect of power transients-based periodic heat flux on single bubble nucleate boiling. The Part I of the thesis presents a series of CmFD development on co-located grid—presented as three chapters. The first chapter is on Ghost Fluid Method (GFM)-based Sharp Interface (SI) and Balanced Force Method (BFM)-based, Diffuse Interface (DI) level set methods on co-located grid, for CmFD without phase change. The second chapter is on comparison of numerical methodology and computational performance between the present LSMs (DI and SI) on co-located grid and published LSMs (DI and SI) on staggered grid. The third chapter presents numerical methodology and validation study for the extension of the novel SI-LSM_{col} for heat transfer-induced phase change problems. The present in-house codes are developed on various coordinates systems—2D Cartesian and axisymmetric—whereas, for nucleate boiling simulation the present SI-LSM_{col} is also parallelized using Message Passing Interface (MPI). The Part II of the thesis presents an application of present SI-LSM_{col} for analysis of single bubble nucleate boiling under the effect of power transients; presented as two chapters. The first chapter presents the effect of periodic exponential heat flux on single bubble nucleate boiling, utilizing a novel simulation methodology. Following the discussion on problem formulation—designing of input heat flux (periodic exponential heat flux) and simulation methodology—the effect of various input parameters associated with periodic exponential heat flux on bubble dynamic parameters: bubble departure diameter D_d , bubble growth period t_g , and bubble departure frequency f ; and vertical coalescence are presented in detail. This study is extended and presented in second chapter of the Part II to various

other periodic heating patterns—step and linear heating—and compared with the results of periodic exponential heat flux.

The first chapter on Part I, on Computational multi-Fluid Dynamics (CmFD) development, presents an extension of the Ghost Fluid Method (GFM)-based Sharp Interface Level Set Method (SI-LSM) (originally proposed on a staggered grid) for a co-located grid system. Further, this chapter presents a comparative study for the GFM-based SI-LSM and a balanced force method (BFM)-based Diffuse Interface Level Set Method (DI-LSM). The BFM-based DI-LSM avoids a pressure-interfacial force decoupling, during the implementation of the MIM, by a proper-discretization of the surface tension term; not needed for the single-phase flow. Whereas, the GFM-based SI-LSM implicitly couples two immiscible, incompressible fluids via interface jump condition, which makes the Momentum Interpolation Method (MIM) for the two-fluid flow *same* as that for a single-fluid flow. A *unified*, for both SI-LSM and DI-LSM, mathematical and numerical formulations are presented. Order of accuracy study is performed (in-between first-order and second-order) similar to that reported earlier for the various CmFD methods. Finally, validation and relative-performance study are presented for four test cases: static droplet, dam break, drop coalescence, and Rayleigh-Taylor instability. For the static droplet, the relative-performance of the present SI-LSM as compared to the DI-LSM is found similar to that in the literature for SI-VOF (Volume of Fluid) method as compared to DI-VOF method. For the various test cases, superior performance is demonstrated for the SI-LSM as compared to DI-LSM. This chapter presents a broader *perspective* to the MIM for a single-versus-two fluid-flow and diffuse-versus-sharp approaches; and a *novel* GFM-based SI-LSM on a co-located grid.

The second chapter on part I presents a comparative analysis of numerical methodology for Level Set Method (LSM) of various types—DI-LSM on Staggered grid (DI-LSM_{stag}), SI-LSM on Staggered grid (SI-LSM_{stag}), DI-LSM on Co-located grid (DI-LSM_{col}), and SI-LSM on Co-located grid (SI-LSM_{col}). Specifically, for the various LSMs, a unified numerical methodology is presented that shows *similar* methodology for the Ghost Fluid Method (GFM)-based SI-LSM on both the grid systems. Whereas, for the DI-LSM, the present study highlights that a balanced force method (BFM) is required to avoid the pressure-interfacial force-decoupling on the co-located grid which is not needed on the staggered grid. For the present LSM, order of accuracy is demonstrated in-between first-order and second-order; similar to that in the published literature for various multi-phase flow solvers. Finally, validation and relative accuracy studies are presented for static droplet, dam break, and Rayleigh-Taylor instability. For the various test cases, maximum accuracy is found for the SI-LSM_{col} as compared to the other three LSMs on

same grid size. This chapter presents a broader perspective to the numerical formulation for a CmFD development on sharp-versus-diffuse interface models on a staggered-versus-co-located grid system.

The third chapter and last in part I, presents an interfacial jump condition-based formulation on co-located grid to avoid *pressure-velocity decoupling* and *pressure-interfacial force imbalance* for phase change CmFD problems with high density ratio, implemented into in-house SI-LSM_{col} code. This numerical formulation enables high density ratio CmFD simulations without conventional balanced force method. For validation/verification several benchmark CmFD test cases for phase change are simulated—Solidification, one-dimensional moving interface, one-dimensional sucking interface, growth of suspended bubble in superheated liquid, film boiling, and single bubble dynamics in nucleate boiling—and shows good agreement between present SI-LSM_{textcol} and published results, showing the robustness of present numerical methodology on co-located grid.

The first chapter in the part II, proposes a numerical methodology to perform single bubble nucleate boiling with power transients. Periodic exponential variation in transient heat flux is utilized which enables proper characterization of the power transient parameters, parametric investigation of power transients on single bubble dynamics, and comparison between steady and transient heating condition. For constant time averaged heat flux q_{avg} in power cycle it was observed that heating parameters are not having any influence on bubble departure diameter D_d and bubble growth period t_g whereas the bubble departure frequency f is enhanced until vertical coalescence is observed. Parametric investigations, based on time period of periodic heating t_p and q_{avg} , reveals the existence of a range in excursion time τ which causes an increase in bubble release frequency f , with applicability for controlling bubble dynamics with power transients and improving efficiency of thermal management devices using nucleate boiling.

The second chapter on part II presents the effect of various periodic heating patterns—exponential, step, and linear heat fluxes on various bubble dynamic parameters—bubble departure diameter D_d , bubble growth time t_g , and bubble departure frequency f —and its comparison utilizing the novel simulation methodology. In the previous chapter, main focus was on problem formulation, proposition of novel simulation methodology, and effect of periodic exponential heat flux on single bubble nucleate boiling. Whereas, in this chapter, utilizing the proposed simulation methodology the effect of periodic step and linear heat flux on single bubble nucleate boiling are investigated. The present problem formulation also enables us to compare the effect of various periodic heat flux. As observed for periodic exponential heat flux, the periodic step heat flux shows in-

significant effect of bubble departure diameter D_d and bubble growth time t_g . The bubble departure frequency f increases by reducing the time associated with maximum heat flux in a step heating cycle and similar phenomenon is observed with exponential periodic heat flux with reducing excursion time τ . For vertical coalescence under similar heating conditions, periodic step heating resulted in early coalescence of bubble as compared to periodic exponential heat flux. Whereas, periodic linear heat flux is exactly similar to the steady heating condition without any vertical coalescence due to the time scale associated with time period of heating cycle. Overall, for similar steady heat flux and time averaged heat flux in a heating cycle no significant difference is obtained for bubble departure diameter D_d and bubble growth time t_g . Whereas, periodic exponential and step heat flux increases the bubble departure frequency f with early vertical coalescence occurring in periodic step heat flux.

Overall, within level set method, the present work demonstrates a physically accurate alternate numerical formulation for conventional balanced force method on co-located grid using ghost fluid method by comparing its computational performance with various other published multiphase solvers. The present work also presents a new perspective to the BFM for the DI-LSM, and a broader perspective to the momentum interpolation for the single-versus-two fluid flow and sharp-versus-diffuse interface approaches on co-located and staggered grid. The robustness of present SI-LSM on co-located grid is further shown on various coordinate systems—Cartesian and axi-symmetric—along with MPI-based parallel computing capability for heat transfer induced phase change problems. The novel numerical investigation on nucleate boiling under the effect of power transients shows the capability of present SI-LSM_{col} for complex multi-physics problems. Further, the proposition of simulation methodology for nucleate boiling with power transients and various problems studied will be useful for future researchers; and may lead to better design of cooling equipments using nucleate boiling with power transients.

Keywords: *Computational multi-Fluid Dynamics, Level Set Method, Sharp Interface, Diffuse Interface, Co-located grid, Staggered Grid, Phase Change, Single Bubble Nucleate Boiling, Power Transients.*

Contents

Abstract	vii
List of Figures	xvii
List of Tables	xxix
List of Symbols	xxxi
1 Introduction	1
1.1 Methods for Computational multi-Fluid Dynamics (CmFD) Development	2
1.1.1 Marker and Cell method	3
1.1.2 Volume of Fluid	4
1.1.3 Level Set Method	5
1.2 Grid Systems for CmFD: Staggered and Co-located	9
1.3 Nucleate Boiling	10
1.3.1 Modeling of Representation and Advection of Interface	12
1.3.2 Surface Tension and Phase Change Modelling	12
1.4 Literature Survey	15
1.4.1 Diffuse and sharp Interfaces-based LSM	15
1.4.2 CmFD development on Staggered and Co-located Grid System . .	18
1.4.3 CmFD development on co-located grid for heat transfer-induced phase change	21
1.4.4 Nucleate Boiling with Power Transients	24
1.5 Scope and Objective of Present Work	27
1.5.1 On Ghost Fluid Method-based Sharp Interface Level Set Method on a Co-located Grid and its comparison with Balanced Force- based Diffuse Interface Method	27
1.5.2 On Comparison of Staggered and Co-located Grid-based Diffuse and Sharp Interface Level Set Method	29

1.5.3	Sharp Interface Level Set Method on a Co-located Grid for CmFD with Heat Transfer-induced Phase Change	30
1.5.4	Single bubble nucleate boiling over a base plate, subjected to Power Transients	30
1.5.5	Effect of Heating Patterns on Single bubble nucleate boiling over a base plate	31
1.6	Organization of report	31
2	On Ghost Fluid Method-based Sharp Interface Level Set Method on a Co-located Grid and its comparison with Balanced Force-based Diffuse Interface Method	35
2.1	Unified mathematical formulation for SI-LSM and DI-LSM	35
2.1.1	Conservation Equations	38
2.1.2	Subsidiary Equation	40
2.2	Unified numerical methodology for DI-LSM and SI-LSM on a co-located grid	40
2.2.1	Discretization method: Physical law-based FVM	41
2.2.2	Solution method: Semi-explicit pressure projection method	42
2.2.3	Solution algorithm	48
2.3	Validation and Performance Study for the BFM-based DI-LSM and GFM-based SI-LSM on a Co-located Grid	49
2.3.1	Capillary wave	50
2.3.2	Static Droplet	51
2.3.3	Dam break simulation	64
2.3.4	Droplet coalescence over a horizontal pool	65
2.3.5	Rayleigh-Taylor instability	67
2.4	Closure	68
3	On Comparison of Staggered and Co-located Grid-based Diffuse and Sharp Interface Level Set Method	69
3.1	Introduction	69
3.2	Mathematical formulation	70
3.2.1	Conservation equations	71
3.2.2	Subsidiary Equation	73
3.2.3	Thermo-physical properties	73
3.3	Numerical methodology	74
3.3.1	Discretization of Computational Domain and Governing Equations	75

3.3.2	Solution method for the Flow properties: Semi-Explicit Pressure Projection Method	77
3.3.3	Solution algorithm	81
3.4	Validation and relative accuracy study	82
3.4.1	Capillary wave: Order of Accuracy Study	84
3.4.2	Static Droplet	84
3.4.3	Dam break simulation	87
3.4.4	Rayleigh-Taylor instability	88
3.4.5	Computational time	91
3.5	Closure	92
4	Sharp Interface Level Set Method on a Co-located Grid for CmFD with Heat Transfer-induced Phase Change	93
4.1	Mathematical formulation	93
4.1.1	Conservation equations	94
4.1.2	Subsidiary Equation	96
4.1.3	Interfacial boundary condition	98
4.2	Numerical methodology	99
4.2.1	Discretization of Computational Domain and Governing Equations	100
4.2.2	Solution method: Semi-Explicit Pressure Projection Method . . .	100
4.2.3	Solution algorithm	105
4.3	Validation of present SI-LSM _{col} for benchmark CmFD problems with heat transfer-induced phase change	106
4.3.1	Solidification problem	108
4.3.2	One-dimensional moving interface problem	108
4.3.3	One-dimensional sucking interface problem	110
4.3.4	Growth of suspended bubble in superheated liquid	112
4.3.5	Film boiling	113
4.3.6	Single bubble dynamics in nucleate boiling	116
4.4	Closure	119
5	Single bubble nucleate boiling over a base plate, subjected to Power Tran- sients	123
5.1	Introduction	123
5.2	Mathematical and Numerical Details	124
5.3	Validation study: Single bubble Nucleate Boiling over a plate	125

5.4	Computational Modelling: Nucleate Boiling over a base plate, subjected to a periodic Heat-Flux	127
5.4.1	Designing of input heat flux for power transients with periodic exponential heating	128
5.4.2	Parametric Details associated with input heat flux	132
5.4.3	Simulation methodology and parameters monitored	134
5.5	Effect of Periodic-versus-Steady Heat Flux BC on the Bubble Dynamics during the Nucleate Boiling	135
5.5.1	Bubble departure diameter (D_d) and bubble growth period (t_g)	136
5.5.2	Bubble departure frequency	138
5.5.3	Vertical coalescence	140
5.5.4	Effect of seed diameter (D_{seed}) and activation temperature (ΔT_{act})	148
5.6	Time-wise evolution of vertical coalescence during nucleate boiling under the effect of periodic exponential heat flux	150
5.7	Discussion	153
5.8	Closure	154

6 Effect of Heating Patterns on Single Bubble Nucleate Boiling over a Base Plate

6.1	Introduction	157
6.2	Numerical methodology	157
6.2.1	Heating patterns for power transients and associated input parameters	158
6.2.2	Parametric values associated with input heat flux	161
6.3	Effect of Periodic-versus-Steady Heat Flux BC on the Bubble Dynamics during the Nucleate Boiling: A Comparative Study on Exponential, Step, and Linear Periodic Heating	162
6.3.1	Bubble departure diameter (D_d), and bubble growth period (t_g)	162
6.3.2	Bubble departure frequency	165
6.4	Vertical coalescence	165
6.5	Effect of modified periodic heating patterns on the bubble dynamics	166
6.5.1	Power transients with exponential rise and delay (case-2 and case-3 heating pattern)	166
6.5.2	Bubble departure diameter (D_d) and Bubble growth period (t_g)	168
6.5.3	Bubble departure frequency f	170
6.5.4	Vertical coalescence	170

6.6 Closure	172
7 Conclusions of the Present Work and Scope for Future Work	173
7.1 Conclusions of the present work	173
7.1.1 On Ghost Fluid Method-based Sharp Interface Level Set Method on a Co-located Grid and its comparison with Balanced Force- based Diffuse Interface Method	173
7.1.2 On Comparison of Staggered and Co-located Grid-based Diffuse and Sharp Interface Level Set Method	175
7.1.3 Sharp Interface Level Set Method on a Co-located Grid for CmFD with Heat Transfer-induced Phase Change	175
7.1.4 Single bubble nucleate boiling over a base plate, subjected to Power Transients	176
7.1.5 Effect of Heating Patterns on Single bubble nucleate boiling over a base plate	178
7.2 Scope for Future Work	178
A Numerical implementation details of SI-LSM_{col}	181
A.1 A finite volume method-based pressure Poisson equation for SI-LSM on co-located grid	181
A.2 Velocity prediction equation for SI-LSM on co-located grid	185
References	191
List of Publications	211
Acknowledgements	213

List of Figures

1.1	Application of nucleate boiling in (a) immersion cooling (Kampl, 2014) and (b) inkjet printing technology (Ruhlamath, 2022).	2
1.2	Schematic of massless Lagrangian particle (\bullet) distributed in computational domain for marker and cell method.	3
1.3	Interface representation using VOF method, showing volume fraction field for control volumes completely filled with fluid-1, fluid-2, and partially filled (Nguyen-Thi <i>et al.</i> , 2021).	4
1.4	Interface representation using level set method showing (a) fluid sub-domains and interface based on level set function ϕ , and (b) various contour plot of ϕ	6
1.5	. (a) Co-located and (c) Staggered grid in a computational domain for a level set method based CMFD development. For the respective grid systems, same and different control volumes for velocity and pressure are shown in (b) and (d) (Sharma, 2016).	10
1.6	Schematic representation of (a) experimentally and (b) numerically captured vapor bubble during a single bubble nucleate boiling	11
1.7	Flow diagram showing the various scales-based general classification of computational methods for nucleate boiling simulation.	13
2.1	Schematic of a representative computational domain along with the various types of grid points for a two-fluid flow, with the fluids separated by a (a) diffuse interface ($-\epsilon \leq \phi \leq \epsilon$) for the DI-LSM and (d) sharp interface $\Gamma(\phi = 0)$ for the SI-LSM. For a representative partially-filled Cartesian control volume (CV), the associated interfacial grid point "P" in the (b, e) fluid-1, and (c, f) fluid-2 inside the Ω_1 and Ω_2 subdomains, respectively. .	37

2.2	Computational setup of the sufficiently different CmFD problems: (a) capillary wave, (b) static droplet, (c) dam break, (d) droplet coalescence, and (e) Rayleigh-Taylor instability; considered for the present validation and performance study.	49
2.3	(a) Computation of the present LSMs with the analytical solution (Prosperetti, 1981) for the temporal variation of non-dimensional amplitude simulated with grid size of 64×64 and (b) L_2 norm of the error-based order of accuracy study for the present LSMs along with that reported for various multiphase solvers.	50
2.4	Comparison of computed pressure field for (a, c, e) DI-LSM and (b, d, f) SI-LSM at density ratio ρ_1/ρ_2 of (a, b) 1, (c,d) 10^3 , and (e,f) 10^5 , for an inviscid static droplet of radius $r=2$ placed at the center of computational domain of size 8×8 with <i>exact curvature</i> κ_{exact} specified. The simulations are performed on a grid 40×40 ($r/h = 10$ or $h = 0.2$), time step $\Delta t = 10^{-6}$, and convergence tolerance 10^{-12} for pressure. Results are plotted after one time-step and all values are dimensional.	54
2.5	Comparison of computed pressure field (a, c, e) DI-LSM and (b, d, f) SI-LSM at density ratio ρ_1/ρ_2 of (a, b) 1, (c, d) 10^3 , and (e, f) 10^5 , for an inviscid static droplet of radius $r=2$ placed at the center of computational domain of size 8×8 with <i>exact curvature</i> κ_{exact} specified. The simulations are performed on a grid 40×40 ($r/h = 10$ or $h = 0.2$), time step $\Delta t = 10^{-6}$, and convergence tolerance 10^{-12} for pressure. Results are plotted after 1000 time-step and all values are dimensional.	55
2.6	For exact curvature κ_{exact} case, time-wise variation of the error in (a, c, e) pressure $E(\Delta P)$ and (b, d, f) maximum magnitude of spurious currents $E(\vec{U}_{max})$ at density ratio ρ_1/ρ_2 of (a, b) 1, (c, d) 10^3 , and (e,f) 10^5 . Computational set-up is similar to Fig. 2.4 and 2.5.	56
2.7	Comparison of computed pressure field for a) DI-LSM ($\chi = 1$), b) SI-LSM ($\chi = 1$), c) DI-LSM ($\chi = 10^3$), d) SI-LSM ($\chi = 10^3$), e) DI-LSM ($\chi = 10^5$), and f) SI-LSM ($\chi = 10^5$) for an inviscid static droplet with $r=2$ placed at the center of computational domain of size 8×8 with <i>computed curvature</i> κ_{comp} . The simulations are performed with $\chi = 1$ on a grid 40×40 ($r/h = 10$ or $h = 0.2$), time step $\Delta t = 10^{-6}$ and pressure convergence tolerance 10^{-12} . Results are plotted after one time-step and all values are dimensional.	58

2.8 Comparison of computed pressure field for a) DI-LSM ($\chi = 1$), b) SI-LSM ($\chi = 1$), c) DI-LSM ($\chi = 10^3$), d) SI-LSM ($\chi = 10^3$), e) DI-LSM ($\chi = 10^5$), and f) SI-LSM ($\chi = 10^5$) for an inviscid static droplet with $r=2$ placed at the center of computational domain of size 8×8 with <i>computed curvature</i> κ_{comp} . The simulations are performed with $\chi = 1$ on a grid 40×40 ($r/h = 10$ or $h = 0.2$), time step $\Delta t = 10^{-6}$ and pressure convergence tolerance 10^{-12} . Results are plotted after 1000 time-step and all values are dimensional.	59
2.9 For computed curvature κ_{comp} case, time-wise variation of the error in (a, c, e) pressure $E(\Delta P)$ and (b, d, f) maximum magnitude of spurious currents $E(\vec{U}_{max})$ at density ratio ρ_1/ρ_2 of (a, b) 1, (c, d) 10^3 , and (e,f) 10^5 . Computational set-up is similar to Fig. 2.7 and 2.8.	60
2.10 Variation in (a) error in ΔP_{tot} and (b) maximum magnitude of spurious current with grid size for the present CSF model-based DI-LSM and SSF model-based SI-LSM as compared to the CSF and SSF models-based VOF methods with various curvature estimations (Francois <i>et al.</i> , 2006). An inviscid static droplet with $r = 2$ at the center of computational domain 8×8 is simulated with κ_{comp} . The density ratio $\chi = 10^3$, time step $\Delta t = 10^{-6}$ and pressure tolerance 10^{-12} . All the values are taken after one time-step and dimensional.	61
2.11 Effect of various thermo-physical properties a) surface tension coefficient σ , b) viscosity ratio μ_1/μ_2 , c) dynamic viscosity of fluid μ_1 , d) density of fluid-1 ρ_1 , and e) time-step Δt on errors for total pressure $E(\Delta p_{total})$, maximum pressure $E(\Delta p_{max})$, and maximum velocity $E(\vec{u}_{max})$. Results are plotted after one time-step and all values are dimensional.	63
2.12 Comparison of the (a) present LSM-based results and published experimental results (Martin and Moyce, 1952), for the temporal variation of leading edge distance (of the interface at the bottom wall) for a water column and (b) instantaneous interface obtained from the present DI-LSM (dashed line) and SI-LSM (solid line) at a non-dimensional time $\tau = 1.5$, and (c) computational time taken till $\tau = 2.4$ on grid size of 144×80 . For each LSMs, the results are presented for Conjugate Gradient (CG) and BiCGSTAB solvers for the pressure Poisson equation.	64

3.7	For the present LSMs-based dam break simulations on a staggered and co-located grid systems, (a) time-wise variation of leading edge distance and column height as compared to the published experimental results (Martin and Moyce, 1952), and (b) instantaneous interface at $\tau = 2.4$	88
3.8	Verification of Rayleigh-Taylor instability showing the comparison of present LSMs with published numerical result (Huang <i>et al.</i> , 2020) for the temporal variation of non-dimensional bubble and spike distance.	89
3.9	For the present LSMs-based simulation of the Rayleigh-Taylor instability on a staggered and co-located grid systems, comparison of instantaneous interface at various time instants.	90
3.10	Computational time taken by various LSMs for droplet coalescence till non-dimensional time $\tau = 0.6$ with various grid sizes.	91
3.11	Comparison of BiCGSTAB and CG iterative methods for pressure Poisson equation simulating droplet coalescence showing (a) time-wise evolution of non-dimensional maximum height and (b) computational time till $\tau = 0.6$ on grid size of 120×240	91
4.1	Schematic of a representative computational domain along with the various types of grid points for a two-fluid flow showing (a) various grid points for flow field $\Phi (= P, \vec{U}, \theta)$ and various interfacial CV's filled with real and ghost fluid for b) main CV filled with fluid-1 in Ω_1 sub-domain and ghost fluid-1 in Ω_2 sub-domain, whereas c) shows main CV filled with fluid-2 in Ω_2 sub-domain and ghost fluid-2 in Ω_1 sub-domain.	94
4.2	Schematic for the co-located grid system, showing grid point arrangement for pressure (P), velocities (U and V), and temperature (θ) along with level set function ϕ and their respective control volumes.	99
4.3	Computational setup of different CmFD phase change problems: (a) solidification, (b) one-dimensional moving interface, (c) one-dimensional sucking interface, (d) growth of suspended bubble in superheated liquid, (e) film boiling, and (f) single bubble nucleate boiling.	107
4.4	Solidification problem simulated with present SI-LSM _{col} showing time-wise evolution of interface and compared with analytical solution (Carslaw, 1959).	109
4.5	For one-dimensional moving interface problems, (a) superheated vapor-saturated liquid and (b) saturated vapor-superheated liquid, comparison of present SI-LSM _{col} and analytical solution (Perez-Raya and Kandlikar, 2016) for the time-wise evolution of interface.	110

4.6 One-dimensional sucking interface problem simulated with present SI- LSM _{col} showing (a) time-wise evolution of interface and (b) temperature distribution at $\tau = 0.24$, and compared with analytical solution (Irfan and Muradoglu, 2017).	111
4.7 Growth of suspended bubble in superheated liquid simulated with present SI-LSM _{col} showing time-wise evolution of interface for (a) case-1 ($\rho_2/\rho_1 =$ 10) and (b) case-2 ($\rho_2/\rho_1 = 1605$), and compared with analytical solution (Scriven, 1962).	113
4.8 Bubble dynamics in film boiling simulation obtained with present SI- LSM _{col} , observed at various non-dimensional time (a) $\tau=0$, (b) $\tau=84$, (c) $\tau=88$, (d) $\tau=120$, (e) $\tau=150$ and (f) $\tau=156$. The colour contour shows the non-dimensional temperature distribution within the vapour.	114
4.9 Film boiling simulated with present SI-LSM _{col} showing time-wise evolu- tion of wall averaged Nusselt number \overline{Nu}_{wall} and compared with the cor- relations of Berenson (Berenson, 1961) and Klimenko (Klimenko, 1981).	115
4.10 Single bubble nucleate boiling simulated with present SI-LSM _{col} for wall superheat of 6.17 K and static contact angle of 38°. The figure shows the bubble shape and temperature distribution at various instances of ebulli- tion cycle, (a) seeding of a new bubble (b) maximum base area covered during growth phase and (c) at the instance prior to bubble departure.	118
4.11 Single bubble nucleate boiling simulation with present SI-LSM _{col} show- ing the time-wise evolution of apparent diameter of bubble from seed- ing to departure and compared with published experiment (Siegel and Keshock, 1964). The simulation corresponds to wall superheat value of 6.17 K and a static contact angle of 38°.	119
5.1 Schematic of computational domain and boundary conditions utilized for validation with experimental results of Siegel and Keshock (1964), and Bovard <i>et al.</i> (2017).	126
5.2 Validation of present in-house code SI-LSM _{col} for single bubble dynamics in nucleate boiling utilizing Siegel and Keshock (1964).	127
5.3 For the nucleate boiling simulation subjected to steady heating conditions, with (a) showing the computational domain with initial bubble seed, and schematic of initial temperature distribution in the near-wall liquid region for (b) constant wall temperature T_W and (c) uniform heat flux boundary condition for the base plate.	128

5.4 Evolution of ebullition cycle with time for an ethanol vapor bubble subjected to steady heat flux $q_{steady} = 5000 \text{ W/m}^2$. No appreciable difference in bubble departure diameter D_d , bubble growth period t_g and bubble waiting period t_w of the vapor bubble between 23 rd and 27 th ebullition cycle could be noticed.	129
5.5 Variation of heat flux with time during exponential mode of heating when (a) q_{min} and t_p are constant, (b) q_{min} and τ are constant, and (c) t_p and τ are constant.	130
5.6 Schematic of power transients with exponential heating pattern utilized in this study. The q_{max} and q_{min} are the minimum heat flux occurring during an exponential power cycle. While t_p is the time period of the periodic exponential power cycle and q_{avg} corresponds to the time averaged heat flux during a power cycle.	132
5.7 Schematic of heat flux variation with time for (a) various excursion time with time period of periodic heat flux to be constant and (b) various exponential time period of periodic heat flux for a constant excursion time.	133
5.8 Simulation methodology utilized for initializing the temperature and velocity field required for nucleate boiling simulation subjected to power transients.	135
5.9 Effect of heating time period (t_p) and excursion time (τ) on the bubble departure diameter and bubble growth period for, (a), (b) $q_{avg} = 5000 \text{ W/m}^2$, (c), (d) $q_{avg} = 10000 \text{ W/m}^2$, and (e), (f) $q_{avg} = 15000 \text{ W/m}^2$, compared with their corresponding bubble departure diameter at $q_{steady} = q_{avg}$. For larger t_p note that the above results are not shown for smaller τ value since the cases correspond to vertical coalescence.	137
5.10 Effect of heating time-period t_p and excursion time τ on the bubble departure frequency f for (a) $q_{avg} = 5000 \text{ W/m}^2$, (b) $q_{avg} = 10000 \text{ W/m}^2$, and (c) $q_{avg} = 15000 \text{ W/m}^2$, and compared with their corresponding bubble departure frequency f at $q_{steady} = q_{avg}$. For larger t_p note that the above results are not shown for smaller τ value since the cases correspond to vertical coalescence.	139

- 5.11 Schematic representation showing an ebullition cycle (a) without and (a) with vertical coalescence. The seed location (shown with red colour marking) is the point at which activation temperature is monitored for seeding the bubble. Here, $h_{top,seed}$ corresponds to height of the seed bubble from seed location while $h_{bottom,dep}$ corresponds to the distance from the bottom of the departed bubble to seed location. 141
- 5.12 Variation in (a) minimum excursion time with q_{avg} for various constant heating time and (b) minimum excursion time with heating time period for various q_{avg} constant values. The symbols correspond to numerical data and the solid line indicates curve fitted with a polynomial function with order n 143
- 5.13 Variation in maximum heat flux at which vertical coalescence is not observed under various operating condition with (a) q_{avg} for various constant heating time period and (b) heating time period for different constant q_{avg} values. The symbols correspond to numerical data and the solid line indicates curve fitted with polynomial function with order n 144
- 5.14 Schematic of transient heat flux supplied to the nucleate boiling system with one heating cycle consisting of an exponential rise and a delay period. During exponential rise the heat flux is varied from q_{min} to q_{max} within a time of t_1 , while during the delay period the heat flux is maintained at a constant value of q_{min} till a time of t_1 . The q_{avg} corresponds to the time averaged heat flux during one heating cycle. 145
- 5.15 Comparison of timewise evolution in bubble diameter between present simulation and Mikic model with correction factor (n) at various q_{steady} values, a) 5000 W/m^2 and $n = 1.39$ b) 10000 W/m^2 and $n = 1.36$, and c) 15000 W/m^2 and $n = 1.35$ 146
- 5.16 Schematic representation showing the various conditions resulting in the occurrence and non-occurrence of vertical coalescence if (a) $q_{max} < q_{safe,vc}$ and (b) $q_{max} > q_{safe,vc}$ 148
- 5.17 Effect of seed diameter (D_{seed}) on (a) $q_{safe,vc}$ and (b) $\tau_{safe,vc}$ for different heating times with constant $q_{avg}(= 10000 \text{ W/m}^2)$. The error bar shows a deviation of $\pm 10\%$ 149
- 5.18 Variation of $q_{max,safe}$ with heating time for different ΔT_{act} . The plot corresponds to a constant $q_{avg} (= 15000 \text{ W/m}^2)$ value. 150

5.19 Time-wise evolution of bubble count representing periodic vertical coalescence phenomenon for $\tau = 0.74 \text{ ms}$, $t_p = 4 \text{ ms}$, and $q_{avg} = 10000 \text{ W/m}^2$. The blue and red colored unfilled circles represent seeded bubbles which are uncoalesced and coalesced with previously departed bubbles, respectively.	151
5.20 Time-wise evolution of cavity temperature with time for the ebullition cycles shown in the inset of Fig. 5.19. For better representation of the time-wise evolution of cavity temperature during this complex process only the instantaneous variation in a) cavity temperature with heat flux, b) apparent diameter with heat flux, c) apparent diameter with cavity temperature, and d) apparent diameter, cavity temperature, and heat flux consolidated together is shown.	153
5.21 Variation in time averaged Nusselt number for various ebullition cycles shown in the inset of Fig. 5.19 with and without vertical coalescence.	154
6.1 Simulation methodology utilized for investigating the effect of various modes of power transients.	158
6.2 Periodic variation in heat flux with each cycle showing (a) exponential, (b) step, and (c) linear variations utilized to investigate the effect on single bubble nucleate boiling dynamics.	159
6.3 Schematic representation of a cycle in periodic step heat flux showing the variation in q_{max} with t_1 for constant q_{avg} and t_p	160
6.4 Variation in bubble departure diameter D_d and bubble growth period t_g with the input parameters —(a)-(b) τ for exponential, (c)-(d) t_2/t_1 for step, and (e)-(f) slope m for linear periodic heat fluxes for various time period t_p of periodic heating. All the simulations are performed with constant $q_{avg} = 10000 \text{ W/m}^2$ and $q_{min} = 100 \text{ W/m}^2$ for step heating. Further, the inset shows corresponding periodic heat flux utilized. For larger t_p note that the above results are not shown for smaller τ (t_2/t_1) value in the exponential (step) periodic heat flux since the cases correspond to vertical coalescence.	163
6.5 Variation in bubble departure frequency (f) with the input parameters —(a) τ for exponential, (b) t_2/t_1 for step, and (c) slope m for linear periodic heat fluxes for various time period t_p of periodic heating. All the simulations are performed with constant $q_{avg} = 10000 \text{ W/m}^2$ and $q_{min} = 100 \text{ W/m}^2$ for step heating. Further, the inset shows corresponding periodic heat flux utilized.	164

6.6 Variation of the $q_{safe,vc}$ (critical value of q_{max} above which there is an onset of vertical coalescence) with increasing time period (t_p) for periodic exponential and step heat fluxes. All simulations are performed with $q_{avg} = 10000 \text{ W/m}^2$ and $q_{min} = 100 \text{ W/m}^2$ for step heating.	166
6.7 Various heating patterns investigated to study the effect on single bubble nucleate boiling dynamics, with each periodic heat flux cycle consisting of (a) exponential rise and delay, and (b) exponential rise, delay, and exponential rise.	167
6.8 Effect of time period of periodic heating t_p and excursion time τ on (a) bubble departure diameter D_d and (b) bubble growth period t_g of the bubble for case-2 and case-3 heating patterns, compared with case-1 and steady heating condition for $q_{avg} = q_{steady} = 10000 \text{ W/m}^2$	169
6.9 Effect of time period for periodic heating t_p and excursion time τ on bubble departure frequency f of the bubble for case-2 and case-3 heating patterns, compared with case-1 and steady heating condition for $q_{avg} = q_{steady} = 10000 \text{ W/m}^2$	171
6.10 For case-1, case-2, and case-3 heating patterns variation in (a) $\tau_{safe,vc}$ with q_{avg} for various constant t_p and (b) $\tau_{safe,vc}$ with t_p for various q_{avg} constant values. The symbols correspond to numerical data and the solid line indicates curve fitted with a polynomial function with order n	171
6.11 For case-1, case-2, and case-3 heating patterns variation in (a) $q_{safe,vc}$ with q_{avg} for various constant t_p and (b) $q_{safe,vc}$ with t_p for various q_{avg} constant values. The symbols correspond to numerical data and the solid line indicates curve fitted with a polynomial function with order n	172
A.1 Various interfacial control volumes depending on the position of interface with respect to “P” grid point, showing a) “P” grid in fluid-1 and interface between “P” and “W” grid points, b) “P” grid in fluid-2 and interface between “P” and “E” grid points, c) “P” grid in fluid-1 and interface between “P” and “S” grid points, and d) “P” grid in fluid-2 and interface between “P” and “N” grid points.	183

A.2 Various interfacial control volumes for calculating U -velocity correction depending on the position of interface with respect to “ P ” grid point, showing a) “ P ” grid in fluid-1 and interface between “ P ” and “ W ” grid points, b) “ P ” grid in fluid-2 and interface between “ P ” and “ E ” grid points, c) “ P ” grid in fluid-1 and interface between “ P ” and “ W ” as well as “ P ” and “ E ” grid points, and d) “ P ” grid in fluid-2 and interface between “ P ” and “ W ” as well as “ P ” and “ E ” grid points.	187
A.3 Various interfacial control volumes for calculating V -velocity correction depending on the position of interface with respect to “ P ” grid point, showing a) “ P ” grid in fluid-1 and interface between “ P ” and “ S ” grid points, b) “ P ” grid in fluid-2 and interface between “ P ” and “ N ” grid points, c) “ P ” grid in fluid-1 and interface between “ P ” and “ S ” as well as “ P ” and “ N ” grid points, and d) “ P ” grid in fluid-2 and interface between “ P ” and “ S ” as well as “ P ” and “ N ” grid points.	188

List of Tables

1.1	Curvature calculation in various computational methodologies utilized for nucleate boiling simulation	14
1.2	Timeline associated with CmFD development on Eulerian grid.	19
1.3	Literatures contributing/improving the perspective of numerical methodology for diffused or sharp interface method utilizing level set method on staggered or co-located grid.	20
1.4	Published and present work on single bubble <i>nucleate boiling</i> simulation utilizing various interface capturing methods on staggered/co-located grid.	23
1.5	Published and present work on the effect of various modes of power transients on nucleate boiling.	28
1.6	Published and present work on a comparative study for the diffuse and sharp interface-based numerical methods for CmFD, and their relative performance study.	29
2.1	For the static droplet problem comparison of errors for the spurious current and pressure-jump across the interface for the present DI-LSM and SI-LSM. The results are obtained for an inviscid static droplet with $r=2$ placed at the center of computational domain of size 8×8 with <i>exact curvature</i> specified. The simulations are performed on a grid 40×40 ($r/h = 10$ or $h = 0.2$), time step $\Delta t = 10^{-6}$ and convergence tolerance as 10^{-12} for pressure. The values are taken after one time-step and all values are dimensional.	53

2.2	For the static droplet problem, comparison of errors for the spurious current and pressure-jump across the interface for the present DI-LSM and SI-LSM. The results are obtained for an inviscid static droplet with $r=2$ placed at the center of computational domain of size 8×8 with <i>computed</i> curvature κ_{comp} . The simulations are performed on a grid 40×40 ($r/h = 10$ or $h = 0.2$), time step $\Delta t = 10^{-6}$ and convergence tolerance as 10^{-12} for pressure. The values are taken after one step and all values are dimensional.	57
3.1	Comparison of various errors obtained after one time-step for the static droplet problem with $\chi = 10^3$ utilizing present LSMs.	86
4.1	Film boiling simulated with present SI-LSM _{col} showing minimum and maximum wall averaged Nusselt number ($\overline{Nu}_{wall,min}$ and $\overline{Nu}_{wall,max}$) , and compared with results of Gada (2012) simulated with diffuse interface level set method on staggered grid.	116
5.1	Thermo-physical properties of water and ethanol, utilized for the single bubble nucleate boiling simulation.	127
5.2	For the present parametric study, on the effect of periodic heat-flux on the nucleate boiling, range of values chosen for various exponential heating cycle parameters.	134
5.3	Input parameters associated with exponential heating cycle for $q_{avg} = 5000 \text{ W/m}^2$ and $t_p = 8 \text{ ms}$ to determine the occurrence and non-occurrence of vertical coalescence. The ✓ and ✗ symbol shows the values for which vertical coalescence is observed and not observed, respectively.	142
5.4	Input parameters of heating cycle for the heat flux pattern shown in Fig. 5.14 to evaluate the necessary and sufficient condition for vertical coalescence with $q_{avg} = 5000 \text{ W/m}^2$	144
5.5	Effect of seed diameter (D_{seed}) on D_d , t_g and f for two different heating conditions utilized.	149
6.1	For a periodic step heating, with a constant $q_{avg} = 10000 \text{ W/m}^2$, $t_p = 8 \text{ ms}$, and $q_{min} = 100 \text{ W/m}^2$ variation in t_1 or t_2 and the resulting q_{max}	161
6.2	For periodic linear heat flux, variation in q_{min} and q_{max} with the slope of the linear heating m	162

List of Symbols

Roman Symbols

A	Non-dimensional advection term	39
B	Interfacial jump boundary condition for pressure	46
c_p	Specific heat, J/kgK	98
D	Rate of deformation tensor	95
D_d	Bubble departure diameter	130
D	Non-dimensional diffusion term	39
Fr	Froude number	38
g	Acceleration due to gravity, m/s^2	8
H	Non-dimensional height of computational domain	64
Ja	Jacob number	97
k	Thermal conductivity, W/mK	95
l_c	Length scale	39
L	Non-dimensional width of computational domain	64
\dot{M}	Interfacial mass flux	98
M	Non-dimensional mass flux	41
Nu	Nusselt number	114
Pr	Prandtl number	95
P	Non-dimensional pressure	38

p	pressure, N/m^2	52
Re	Reynolds number	38
<i>t</i>	Time, s	6
<i>t_p</i>	time period of periodic heat flux	131
U	Non-dimensional velocity in horizontal direction	41
\vec{U}	Non-dimensional velocity vector	38
<i>u</i>	Velocity, m/s	6
<i>u_c</i>	velocity scale	39
V	Non-dimensional velocity in vertical direction	41
We	Weber number	38

Greek Symbols

α	Thermal diffusivity, m^2/s	116
χ	Density ratio	65
$\delta_\epsilon(\phi)$	Dirac Delta function	6
ϵ	Interface thickness	7
η	Viscosity ratio	65
Γ	Interface	46
γ	Non-dimensional specific heat	95
$H_\epsilon(\phi)$	Smoothened Heaviside function	6
κ	Curvature	8
μ	Dynamic viscosity coefficient, Ns/m^2	8
ϕ	Level set function	5
ρ	Density, kg/m^3	8
σ	Surface tension coefficient, N/m	8

τ	Excursion time	131
τ	Non-dimensional time	38
θ	Non-dimensional temperature	95
ζ	Non-dimensional thermal conductivity	95

Superscripts

*	Intermediate	42
n	Time level	42
ST	Surface tension	38

Subscripts

1	Fluid-1	39
2	Fluid-2	39
act	Activation	129
col	Co-located grid	27
e	east face-center	39
E	Cell center grid point at east control volume	39
G	Ghost	97
l	liquid	118
ml	microlayer	117
N	Cell center grid point at north control volume	39
n	north face-center	39
PC	phase change	98
P	Cell center grid point at main control volume	39
sat	saturation	95
s	south face-center	39

S	Cell center grid point at south CV	39
TBL	Thermal boundary layer	116
t_g	Bubble growth period	130
t_w	Bubble waiting period	130
wall	wall	95
w	west face-center	39
W	Cell center grid point at west control volume	39

Acronyms

<i>BFM</i>	Balanced force method	8
CAP	Capillary	47
CFL	Courant-Friedrichs-Lowy	47
CmFD	Computational multi-Fluid Dynamics	1
CSF	Continuum Surface Force	16
CV	Control volume	9
DI-LSM	Diffuse Interface Level Set Method	7
<i>GFM</i>	Ghost fluid method	8
GFN	Grid Fourier number	47
LSM	Level set method	5
MIM	Momentum Interpolation Method	18
NBPT	Nucleate Boiling with Power Transients	17
SI-LSM	Sharp Interface Level Set Method	7
SSF	Sharp Surface Force	16
TVD	Total Variation Diminishing	17
VOF	Volume of Fluid	4

Chapter 1

Introduction

Computational multi-Fluid Dynamics (CmFD) is an advanced topic in Computational Fluid Dynamics (CFD), concerned with *development* of numerical methodology and its *application* for analysis of interaction of immiscible fluids with or without phase change. Motivation for these development is for academic research and industrial applications—solidification, boiling, combustion, epitaxial growth, microfluidics etc. Figure 1.1 shows few of these applications. *Nucleate boiling* is one among these domains which progressed tremendously using CmFD, for improving fundamental understanding and for applications like immersion cooling (El-Genk, 2012; Narumanchi *et al.*, 2008), nuclear reactors (Su *et al.*, 2016), inkjet printers (Asai, 1991), MEMES (Okuyama *et al.*, 2005; Karayiannis and Mahmoud, 2017; Cornwell and Kew, 1993) etc. Even though nucleate boiling is an active area of research for past 9 decades since Nukiyama introduced boiling curve (Nukiyama, 1966), physical insight improved significantly over past 23 years since Son and Dhir utilized CmFD for investigating single bubble nucleate boiling (Son *et al.*, 1999). Interestingly till now, for single bubble CmFD studies, steady heating is utilized rather than physically relevant transient heating. Another major observation was the preference of staggered grid over co-located grid within Eulerian grid systems for these complex multiphase problems.

This realization lead to recursive occurrence of several questions: Why an easy to implement co-located grid is not so popular among CmFD development community for investigating complex multiphase multiphase problem like single bubble nucleate boiling?, Is there any limitation for co-located grid that need to be properly addressed, moreover why staggered is the preferred choice for CmFD even though difficult to implement? Is there an advantage of one grid over other? Even though nucleate boiling subjected to power transients is physically relevant than steady heating, why no CmFD studies are available?

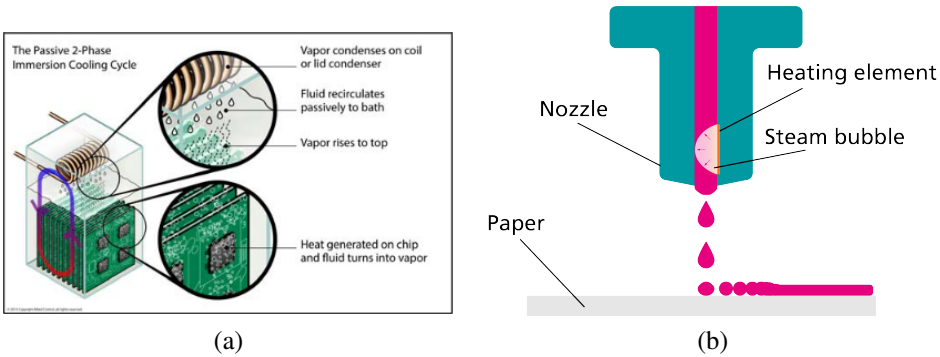


Figure 1.1: Application of nucleate boiling in (a) immersion cooling (Kampl, 2014) and (b) inkjet printing technology (Ruhlamath, 2022).

Two motivations to ponder on basis of these questions. *First*, from CmFD *development* perspective, a robust algorithm on co-located grid significantly reduces the implementation effort involved with complex multi-physics problems like nucleate boiling, and could be easily extended to complex geometries, adaptive grid, parallelization etc., in which co-located grid is the preferred. *Second*, from CmFD *application* perspective, improved understanding of nucleate boiling under the effect of power transients and its comparison with steady heating conditions. Thus, this thesis focuses on these two perspectives of CmFD; development on co-located grid and its application on *nucleate boiling with power transients* (NBPT).

1.1 Methods for Computational multi-Fluid Dynamics (CmFD) Development

Multiphase flow simulation is a challenging domain in Computational Fluid Dynamics (CFD). The existence of an interface between various fluids, sharp discontinuity of fluid properties across the interface, singular forces (like surface tension) etc., imposes numerical challenges for modelling. Thus, several computational methods are formulated for interface representation, proper inclusion of discontinuous fluid properties in the flow solver, and surface tension modelling.

Numerical methods for modelling interface in multiphase flow can be broadly classified into three types: interface fitting method, interface tracking method, and front capturing method (Salih and Ghosh Moulic, 2009). In the interface fitting method (used only for single phase flow with a free surface), the physical domain is converted into a computational domain using mapping methods in such a way that the free surface will always be located at the boundary of the computational domain. Complex motion of the free surface

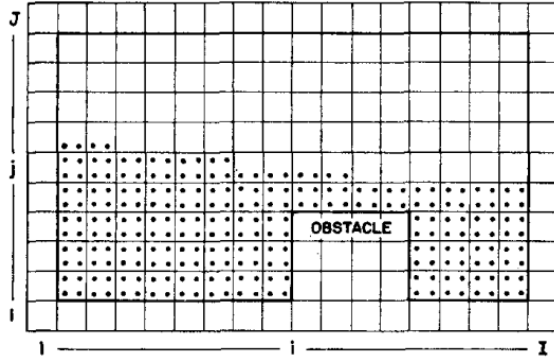


Figure 1.2: Schematic of massless Lagrangian particle (\bullet) distributed in computational domain for marker and cell method.

limits its application due to the difficulty in applying transformation functions. Another popular model is interface tracking method which can be classified into two types—front tracking method and volume tracking method. The front tracking is an Euler-Lagrangian method, where the interface is constantly tracked by certain dedicated grids while the flow domain is captured using fixed or Eulerian grids. A major advantage of this method is the ability to capture interface features much smaller than Eulerian meshes, but interfaces undergoing coalescence and breakage leads to significant challenge for numerical implementation. Other than the interface tracking methods, another popular and relatively ease to implement is interface capturing methods, which avoids complex mapping methods and Lagrangian grids and simple Eulerian framework is utilized with interface represented using several functions like volume fraction, level set function etc. The interface representation of these techniques using some popular CmFD methods are discussed below.

1.1.1 Marker and Cell method

Marker And Cell method (MAC) was introduced by Harlow and Welch (1965) [2] for visualization and simulation of incompressible flow with free surface, utilizing a set of Lagrangian massless particles throughout the cells containing fluid. This implies that a cell with marker particle contains fluid in it and cell without marker particle contains no fluid which is graphically represented in Fig. 1.2. These cells can be further classified as full cell (F), surface cell (S) and empty cell (E). The cells completely submerged inside the fluid are called as full cell (F), the cells without any fluid are called as empty cell, and if a cell contains an empty cell as its neighbor, those cells are represented as surface cell.

In this method, the domain is initialized with a velocity field and the required amount of marker particles are assigned in the cells carrying fluid. Once flow properties are solved using a suitable solution methodology, the marker particles are then advected using the



Figure 1.3: Interface representation using VOF method, showing volume fraction field for control volumes completely filled with fluid-1, fluid-2, and partially filled (Nguyen-Thi *et al.*, 2021).

actual velocity field for new time instant, enabling a numerical flow visualization. Thus, marker particles solely serves the purpose of flow visualization. Inability to handle intense interface topological changes like stretching and merging, inaccurate implementation of boundary condition on free surface, increased memory consumption etc., are the major limitations of MAC method. During interface coalescence or breakage, the marker particles need to be eliminated or extra particles need to be added to the domain for proper representation of interface so as to eliminate an unphysical sense of visualization like voids in the flow, accumulation of particles etc. Further, limitation to provide normal stress boundary condition hindered the application of MAC method to advanced multiphase flows.

1.1.2 Volume of Fluid

For multiphase simulation of complex phenomenon it was essential to consider interfacial forces even during complex interface topology. A method successful to achieve this object was initially developed Hirt and Nichols (Hirt and Nichols, 1981) using Volume Of Fluid method (VOF). Analogous to the MAC method, instead of advecting the marker particles, in the VOF method, a discrete function called volume-fraction (f) is advected. Assume, a domain is filled with fluid-1 and fluid-2. If fluid-1 is considered as the reference fluid, then volume-fraction is defined as ratio of volume of fluid-1 (reference fluid) in a Control Volume to the volume of corresponding CV. Using this definition, the cell containing fluid-1 or fluid-2 or interface CV (control volume containing interface) is identified, given as

$$f = \begin{cases} 1 & \text{CV filled with fluid-1} \\ 0 & \text{CV filled with fluid-2} \\ 0 < f < 1 & \text{Interfacial CV} \end{cases} \quad (1.1)$$

Figure 1.3 shows a graphical representation of volume-fraction field in a physical domain, consisting of fluid-1 and fluid-2. Compared to the MAC method, here only a single data in a cell is required to represent the identity of that CV, resulting in a better memory utilization than MAC. Since a way to represent the identity of a cell has been established, the next procedure is to evolve the interface in space and time. From the conservation of mass principle, a volume-fraction evolution equation can be obtained as shown in Eq. (1.2). Using any convenient flow solver algorithm, a converged velocity field can be obtained for each time step. Utilizing this velocity field, the interface is advected by solving a volume-fraction advection equation; given as

$$\frac{\partial f}{\partial t} + \frac{\partial f u_i}{\partial x_i} = 0 \quad (1.2)$$

where x , t , and u are the dimensional coordinate, time, and velocity. Further, for implementation of the interfacial forces geometric properties of the interface—normals and curvature—are required. In VOF, this is established using various methodologies like Simple Line Interface Calculation (SLIC), Piecewise Line Interface Calculation (PLIC) etc. SLIC is a geometric interface representation in which the interface in a CV is considered as a line segment aligned with either of the co-ordinate axis. The orientation of the line segment in each cell is determined by calculating the volume fraction gradient in both the coordinate direction. Since the curves cannot be accurately represented using the SLIC method due to the only availability of vertical and horizontal orientation, an alternate method called PLIC was introduced. In PLIC, an extra degree of freedom is allowed to the line segment, i.e, the ability for inclination. After determining the normal of the line segment, the interface location in the cell is determined iteratively till the condition that volume of the enclosed region generated by the interface should be equal to the volume of required fluid in that cell.

1.1.3 Level Set Method

One of the successful interface representation technique reported after VOF is the Level Set Method (LSM) introduced by Osher and Sethian (1988). Theoretically, in level set method, the interface is implicitly considered to be present in an $(N - 1)$ dimensional geometry in a ‘ N ’ dimensional fluid flow domain. For example, in a three dimensional domain, the interface is implicitly represented using a surface. Similarly, for a two dimensional domain the interface will be implicitly represented using a curve. In any multiphase simulation, a major challenge is to identify which fluid is present in each cell. In LSM, this is achieved by using a level set function (ϕ). For a two fluid domain, positive value of

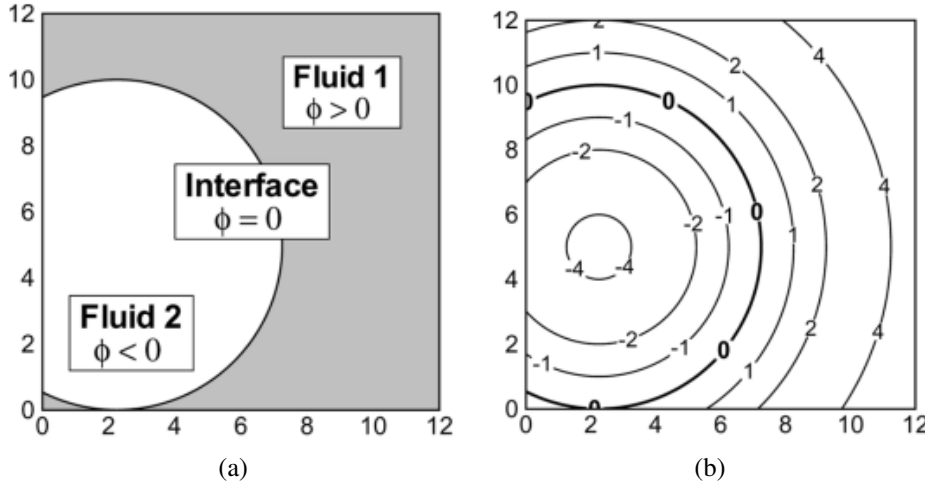


Figure 1.4: Interface representation using level set method showing (a) fluid sub-domains and interface based on level set function ϕ , and (b) various contour plot of ϕ .

level set function represents one fluid, and negative value of level set function indicates the other fluid. The interface is represented by the contour having a zero level set function value. Similar to Eq. (1.1), fluid identifier in a CV is represented as

$$\phi = \begin{cases} < 0 & \text{Grid point submerged in fluid-1} \\ > 0 & \text{Grid point submerged in fluid-2} \\ 0 & \text{Interface} \end{cases} \quad (1.3)$$

A graphical representation of the level set function is shown in Fig. 1.4, which shows a physical domain containing two fluids separated by an interface represented using ϕ . For the numerical implementation of LSM, three functions are mainly used (i) Level set function ϕ , (ii) Heaviside function $H(\phi)$ and (iii) Dirac delta function $\delta_\epsilon(\phi)$. As mentioned above, the main purpose of level set function is to identify the fluid occupying in each CV and to evolve the interface in space and time. In LSM, the interface evolution is computed using the level set advection equation, derived from the principle of conservation of mass (Gada and Sharma, 2009a), given as

$$\frac{\partial \phi}{\partial t} + u_i \frac{\partial \phi}{\partial x_i} = 0 \quad (1.4)$$

Due to the simplicity in numerical implementation and the inherent robustness to capture the interface, Level Set Method had captured the attention of researchers in this field. Moreover, the intricacies involved in interface reconstruction and computation of normal vector and curvature, which are present in the VOF are greatly curtailed in LSM.

A major challenge on how to treat surface tension which is a singular force acting only on the interface is dealt with two approaches—Diffuse Interface Level Set Method (DI-LSM) and Sharp Interface Level Set Method (SI-LSM).; presented below in separate subsection.

Diffuse Interface Level Set Method

Physically in a multi-fluid domain, the fluid properties like density, viscosity etc. varies sharply across the interface. This sharp variation of fluid properties along with the surface tension force were hard to numerically implement due to zero thickness of the interface. These difficulties made numerical modelling of capillary flows, dynamics involved in droplet, atomization of fuels etc., extremely challenging. The reconstruction of complex interface topology for flows with surface tension was a major hindrance during the early phase of multi-fluid modelling.

In order to avoid the numerical inconsistency of the property jump, diffuse interface is assumed instead of thin and massless physically relevant interface with a relatively small thickness (2ϵ), i.e., $-\epsilon \leq \phi \leq \epsilon$. Now instead of this sudden or stair-step jump, the flow properties are assumed to vary continuously across this diffuse interface. The purpose of Heaviside function is to convert the stair-step jump to a smoothly varying quantity inside the smeared interface. Sussman *et al.* (1999) defined this Heaviside function as

$$H_\epsilon(\phi) = \begin{cases} 0 & \phi < -\epsilon \\ \frac{\phi+\epsilon}{2\epsilon} + \frac{1}{2\pi} \sin\left(\frac{\pi\phi}{\epsilon}\right) & |\phi| \geq \epsilon \\ 1 & \phi > \epsilon \end{cases} \quad (1.5)$$

Existence of singular forces like surface tension is another consequence of the presence of an interface. Since these forces exist only on the interface, their proper incorporation into flow solver algorithm is not straightforward. For numerical implementation, a conventional procedure is to convert this interfacial forces into body forces which exist only in the diffuse interface region ($-\epsilon \leq \phi \leq \epsilon$). A Dirac delta function ($\delta_\epsilon(\phi)$), defined by Sussman *et al.* (1999) is used for this conversion, given as

$$\delta_\epsilon(\phi) = \frac{dH_\epsilon(\phi)}{d\phi} \begin{cases} \frac{1}{2\epsilon} + \frac{1}{2\epsilon} \cos\left(\frac{\pi\phi}{\epsilon}\right) & |\phi| \leq \epsilon \\ 0 & \text{Otherwise} \end{cases} \quad (1.6)$$

Consider the momentum equation, given as

$$\frac{\partial}{\partial t}(\rho u_i) + \frac{\partial}{\partial x_j}(\rho u_i u_j) = -\frac{\partial p}{\partial x_i} + \frac{\partial}{\partial x_j}\left[\mu\left(\frac{\partial u_i}{\partial x_j} + \frac{\partial u_j}{\partial x_i}\right)\right] + \rho g_i + F_\sigma \quad (1.7)$$

The RHS of above equation consists of pressure force, viscous force, gravity force and surface tension force (F_σ). By considering the interface as a region of finite thickness, Brackbill *et al.* (1992) proposed surface tension a body force present over diffuse region, given as

$$F_\sigma = \sigma \kappa \delta_\epsilon(\phi) n_i \quad (1.8)$$

Since a transition region is assumed to exist between the fluids rather than an actual interface, a proper estimation for thermo-physical properties of the fluids are essential in this new region. This is achieved by smoothly varying the thermo-physical properties of fluid across the interface with the help of $H_\epsilon(\phi)$.

Sharp Interface Level Set Method

A more physically realistic interface modelling approach in comparison to diffuse interface is sharp interface approach. In the diffused interface approach, the fluid properties are assumed to smoothly vary across the interface and surface tension force is assumed to act throughout the entire diffused region. Modelling of interfacial force dominant flows will result in inaccurate solutions with this approach. In SI approach, the jump in fluid properties and the singular nature of surface tension force is preserved. Thus the thermo-physical properties are defined based on Heaviside function $H(\phi)$, given as

$$H(\phi) = \begin{cases} 1 & \phi \geq 0 \\ 0 & \phi < 0 \end{cases} \quad (1.9)$$

Moreover, the surface tension force is considered as a singular force implemented as an jump-condition for pressure at the interface which prevents the smearing across the diffuse interface as in DI-LSM. This formulation was proposed as Ghost Fluid Method (GFM) using LSM by Fedkiw *et al.* (1999b) and later extended to Navier-Stokes equation by Kang *et al.* (2000). A detailed discussion of this formulation is provided in Part-I of this thesis.

1.2 Grid Systems for CmFD: Staggered and Co-located

Any grid system is the fundamental building block for CFD development. A simplest form of grid generation, consisting of uniformly spaced horizontal and vertical lines, is shown in Fig. 1.5a. This leads to sub-division of the 2-D Cartesian domain into equal sized control volumes (CV's), where the uniformly spaced grid points are located at the centroid of the CV's. Along with these uniform/internal grid points, the figure also shows the boundary grid points (at the boundary of the domain) for the implementation of boundary conditions.

Historically, a CmFD development on grid-points and control volumes (Fig. 1.5a and 1.5b) for all the flow properties (velocity, \vec{u} and pressure, p)—called as co-located grid—has led to a linear approximation of pressure and mass-flux (Sharma, 2016) based algebraic formulation, where the computation of velocity at a particular grid point does not involves pressure of the same grid point. The linear-approximation based formulations led to a *pressure-velocity decoupling* (Patankar, 1980) which results in a checker-board distribution of the velocity and pressure field, over and above the correct flow field. The physically unrealistic superimposed flow field also obeys the algebraic formulation for mass and momentum conservation and leads to an oscillatory velocity and pressure field (Sharma, 2016) as the unrealistic solution.

One of the first remedy to the pressure-velocity decoupling was proposed as a staggered grid, shown in Fig. 1.5c where the grid-points for the pressure is located at the face-centers of the momentum conservation obeying staggered velocity–CV's as shown in Fig. 1.5d. Furthermore, the figure also show that the grid points for the velocities which are normal to the surfaces are located at the face-centers of the mass conservation obeying pressure–CV's. Thus, the approximation for the normal-velocity and pressure that is required on a Co-located grid (Fig. 1.5a and 1.5b) is completely avoided on a staggered grid.

Another remedy to the pressure velocity decoupling was proposed later by Rhie and Chow (1983) for a co-located grid, where they presented a momentum-interpolation instead of the linear-interpolation for computation of mass-fluxes. Even after the proposition of momentum-interpolation, the CmFD development continued on a staggered grid for quite some time due to a numerical instability issue on a co-located grid, for the convergence of pressure equation specially for a CmFD problem with large density ratios. The numerical instability for CmFD on a co-located grid was due to improper implementation of the surface tension term, during the momentum interpolation on a Co-located grid. A momentum-interpolation that involves a proper balance between the force due to

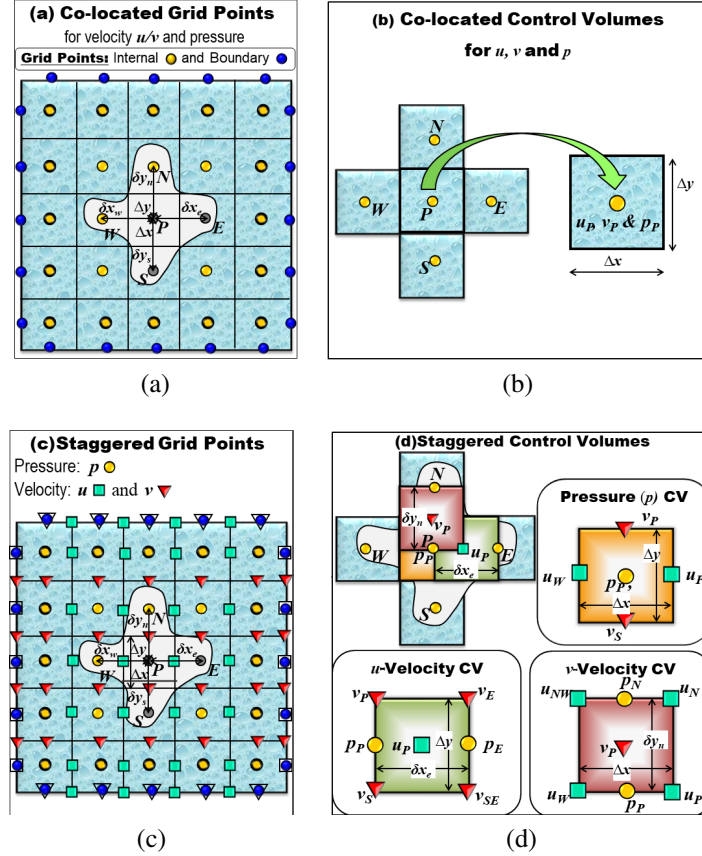


Figure 1.5: . (a) Co-located and (c) Staggered grid in a computational domain for a level set method based CMFD development. For the respective grid systems, same and different control volumes for velocity and pressure are shown in (b) and (d) (Sharma, 2016).

pressure and surface-tension, was proposed by Francois *et al.* (2006) for a volume of fluid (VOF) method.

1.3 Nucleate Boiling

A very high heat transfer capability associated with the phase change phenomenon attracts nucleate boiling for industrial applications. But considerable dependency between the solid substrate (over which boiling occurs), fluid, micro-layer (thin liquid layer trapped between the vapor and solid), and the nucleation phenomenon itself make fundamental understanding of the nucleate boiling cumbersome. Hence, for a better understanding of this process, the simplest possible nucleate boiling phenomenon should be tackled first. A typical boiling process undergoes various regimes like natural convection, partially developed nucleate boiling, fully developed nucleate boiling, transition, and film boiling. Over these existing regimes, the most sought-after regime for understanding the nucleate boiling phenomenon is the partially developed nucleate boiling regime. The initiation of

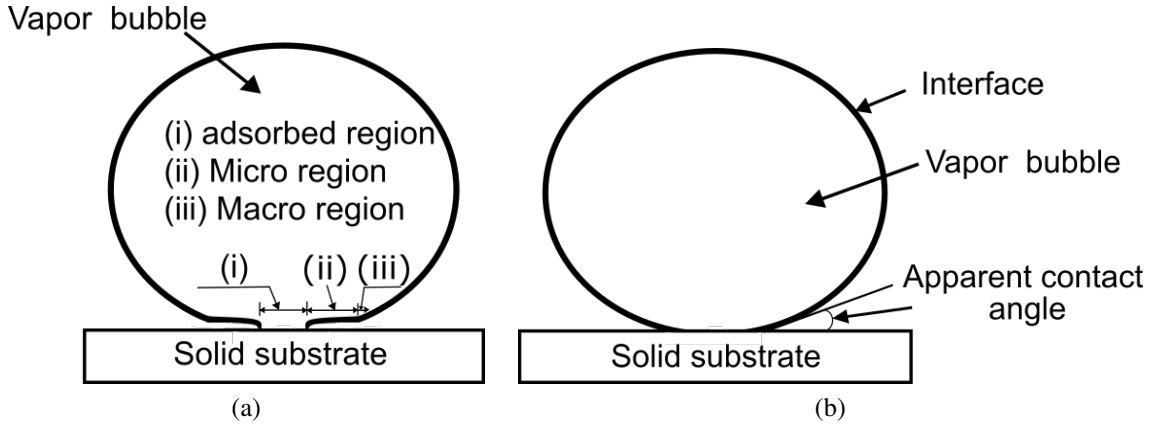


Figure 1.6: Schematic representation of (a) experimentally and (b) numerically captured vapor bubble during a single bubble nucleate boiling

this regime corresponds to the occurrence of the first bubble and terminates at the point where neighboring bubbles start interacting with each other. This independent behaviour of the individual bubble from the neighboring bubbles makes this regime ideal for fundamental investigations. Even with enormous research activities within this regime, there is still more to be understood. Hence, in view of developing a complete understanding, considerable experimental and computational investigations are still underway (especially in this regime), which are relevant to both academic and industrial community.

As shown in Fig. 1.6a, the physical bubble consists of a bulk interface (in macro regime) and the interface in micro layer. From a computational perspective, the bulk interface is modelled with several approaches. However, for capturing the interface in micro layer along with bulk interface (modelling of an entire physical bubble), the requirement of computational resources is unaffordable, due to extremely fine grid sizes needed to resolve the micro layer. Hence, a popular approach is to compute the bulk interface with an apparent contact angle as shown in Fig. 1.6b, while the micro-layer effects are considered using a suitable model without simulating it. Additionally, to capture the bubble growth accurately, the interfacial mass transfer should be evaluated with an accurate phase change model. The force due to surface tension should be evaluated adequately at this interface, or else the parasitic current generation will cause unphysical bubble deformation. All these challenges should be dealt with simultaneously for a successful simulation of single-bubble nucleate boiling

Compared to the experimental studies, starting from the pioneering work done by Nukiyama (1966), the computational studies in this regime are relatively recent. Hence in this section, a brief review regarding the progress made in numerical simulation and the challenges encountered therein, especially for the single-bubble nucleate boiling studies will be discussed. During an ebullition cycle (growth, departure, and waiting period) as-

sociated with a single bubble, the significant interaction of various multi-scale phenomena (from bulk mechanisms to micro layer) poses considerable difficulty in numerical modelling. For a better understanding, these challenges are classified into three, as follows:

- Numerical representation of bulk interface
- Surface tension and phase change modelling
- Micro-layer modelling

1.3.1 Modeling of Representation and Advection of Interface

On the basis of the scale of the heat and fluid flow physics resolved numerically, a classification of the computational methods for interface representation in single-bubble nucleate boiling simulation is presented in Fig. 1.7 which shows microscopic, mesoscopic, and macroscopic approaches. A computational method that resolves length scales in the atomic, intermediate to atomic, and continuum scales belongs to the microscopic, mesoscopic, and macroscopic approaches, respectively. With regard to single-bubble nucleate boiling simulation, the molecular dynamics (MD) method falls under the category of the microscopic approach and the lattice Boltzmann (LB) method corresponds to the mesoscopic approach. For more commonly used macroscopic methods, Fig. 1.7 shows a large variant of methodologies for representation and advection of interface in single-bubble nucleate boiling simulation. This includes Level Set Method (Son *et al.*, 1999), Volume Of Fluid (Kunkelmann and Stephan, 2009), Coupled VOF and LSM (VOSET) (Sun and Tao, 2010), Moving Particle Semi-Implicit-Meshless Advection Using Flow Directional Local Grid (MPS-MAFL) (Yoon *et al.*, 2001), Level Contour Reconstruction Method (LCRM) (Shin and Juric, 2002), Constrained Interpolation Polynomial-Conservative Semi-Lagrangian (CIP-CSL2) with Novel Interface Sharpening Scheme (Sato and Ničeno, 2012) etc. From literature, macroscopic simulation methods are the most popular due to the ability of the computational method to handle complex interface topologies with considerable ease. Although LB methods are utilized for single-bubble nucleate boiling simulation, its robustness in 3D is yet to be resolved. Whereas, in the case of MD simulation, a considerably larger computational size requirement for nucleate boiling simulation is still a stumbling block

1.3.2 Surface Tension and Phase Change Modelling

Apart from interface representation for multiphase problems with phase change (like nucleate boiling simulation), the other numerical challenges that should be taken into consideration are surface tension and phase change modelling. Accurate interface dynamics

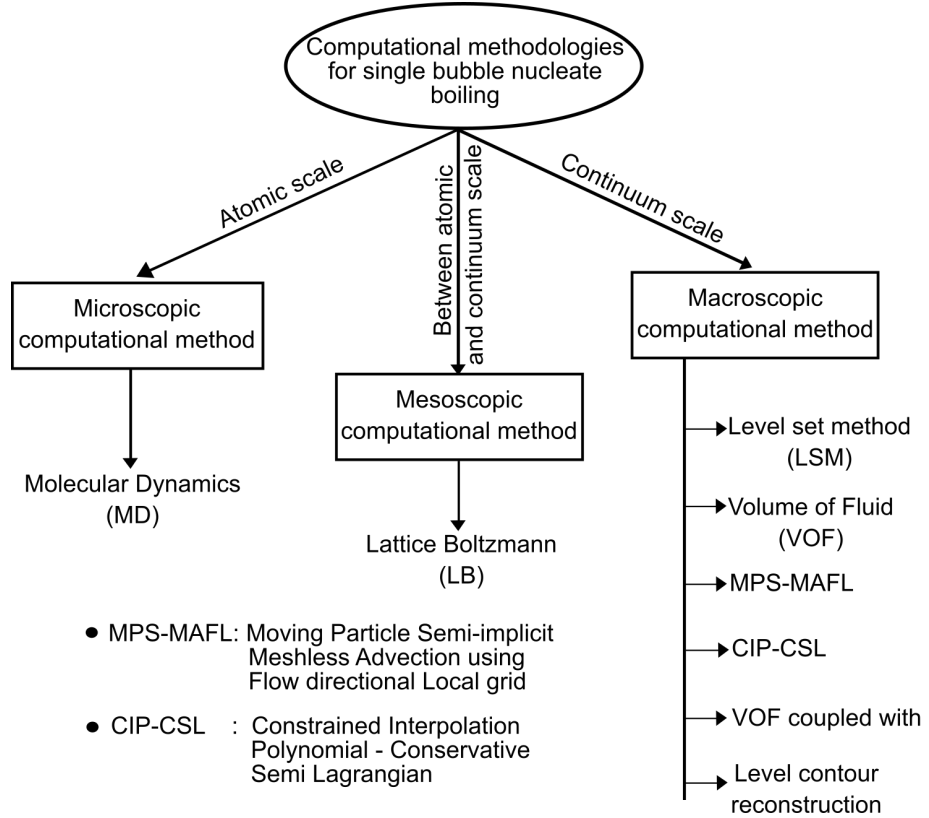


Figure 1.7: Flow diagram showing the various scales-based general classification of computational methods for nucleate boiling simulation.

could be established only by a proper numerical implementation of these phenomena. Because, if the surface tension force implementation is not proper, it will lead to improper balance between forces exerting at the interface. This force imbalance causes an artificial velocity field (known as spurious currents) to be generated near the interface vicinity, which is capable enough to significantly influence the physical solution. Similarly for the phase change modelling, inaccurate calculation of interfacial mass flux results in non-physical interface deformation. The phase change velocity of the interface, which is different from the bulk velocity is computed from the interfacial mass flux. Hence, an erroneous calculation of the will cause considerable interface deformation, since the interface is advected with the sum of phase change and bulk velocity. In this section, the computational methods that are presently available to tackle these problems from the perspective of nucleate boiling simulation are presented.

For a proper implementation of surface tension model, the two major criteria that need to be fulfilled are, an accurate computation of interface curvature (κ) and force balance at the interface. As shown in Table 1.1, several methodologies that proved accurate enough for nucleate boiling simulation are available, depending on an interface capturing method. Once the interface curvature is determined numerically, the other challenge is to

Table 1.1: Curvature calculation in various computational methodologies utilized for nucleate boiling simulation

Method	Curvature κ
LSM	$\nabla \cdot \frac{\nabla \phi}{ \nabla \phi }$ (Mukherjee and Dhir, 2004)
VOF	Height function (Jia <i>et al.</i> , 2015)
MPS-MAFL	$\frac{2\cos\theta}{r_e^{st}}$ (Nomura <i>et al.</i> , 2001)
LCRM	$\frac{F_{L\cdot G}}{\sigma G\cdot G}$ (Shin <i>et al.</i> , 2005)
CIP-CSL2	$\nabla \cdot \frac{\nabla d}{ \nabla d }$ (Sato and Ničeno, 2012)
VOF-LSM	$\nabla \cdot \frac{\nabla \tilde{c}}{ \nabla \tilde{c} }$ (Kunkelmann and Stephan, 2009)
VOSET	Height function (Ling <i>et al.</i> , 2014)

establish proper balance between forces exerted at the interface. From literature, this is achieved utilizing two methods, the diffused interface and sharp interface methods. With respect to level set method, these were referred as DI-LSM and SI-LSM in the previous section.

The fundamental objective behind the phase change models is an accurate calculation of interfacial mass flux. A popular phase change model for single bubble-based nucleate boiling simulation is the Rankine-Hugoniot jump condition (Gibou *et al.*, 2007) or energy jump condition. Another widely used approach for the phase change modelling in nucleate boiling simulation is the Hardt and Wondra method (Hardt and Wondra, 2008). In the energy jump condition model, a major assumption is that the interface temperature is at saturation temperature. However, to account for a more general condition where the interface temperature deviates from saturation condition especially for the microscale phase change problems, (Hardt and Wondra, 2008) utilized the Tanasawa model (Tanasawa, 1991) for a small jump in temperature across the interface, which is a simplified model of Schrage (Schrage, 1953). This evaporation model was developed within the VOF framework. While deriving the interfacial mass flux equation, Tanasawa (1991) considered the interface to be a part of the liquid phase (Magnini, 2012), resulting in the interface temperature to be evaluated from the liquid domain. Thus, interface temperature corresponds to the temperature calculated by solving the energy equation over the liquid domain. For numerical implementation, Hardt and Wondra (2008) considered the interfacial mass flux as a volumetric term, which resulted in an easy implementation to any computational fluid dynamics (CFD) package. This is made possible by utilizing the scalar volume fraction field. For numerical stability of the evaporation model, the phase change effect is considered to occur over a smeared interface by solving a steady diffusion equation. Further details of numerical implementation are available in the literature (Hardt and Wondra, 2008; Magnini, 2012). When (Kunkelmann and Stephan, 2009)

utilized Hardt and Wondra model for validating phase change problems, the grid size required was of the size of $1 \mu\text{m}$ to accurately capture the phase change. Hence, to obtain similar accuracy on coarser grid, an energy jump condition formulation was resorted (Kunkelmann and Stephan, 2010b).

1.4 Literature Survey

In this section literature survey for CmFD development and application perspective is presented. For CmFD development, the research gap is presented for interface capturing method with and without phase change on co-located grid. Whereas for CmFD application, the lack of numerical investigation for single bubble nucleate boiling over a base plate subjected to periodic heat-flux is presented.

1.4.1 Diffuse and sharp Interfaces-based LSM

Multi-phase flow studies using CmFD is an active area of research for past four decades. As compared to CFD for a single fluid flow, CmFD development addresses two modelling challenges: first, *sudden* variation in the thermo-physical properties *across* the interface; and second, modelling the *localized* force due to surface tension *at* the interface. To handle these modelling challenges the numerical representation of the interface should be available. This lead to the development of several numerical methodologies—Volume of Fluid (VOF) (Nichols *et al.*, 1981), *Level Set Method* (LSM) (Osher and Sethian, 1988), phase field method (Wang and Sekerka, 1996), and Front Tracking method (FT) (Juric and Tryggvason, 1996). Within the Eulerian framework, these methodologies are classified into interface tracking method and interface capturing method. The Front Tracking method is an interface tracking method with grid points on the interface evolving with time. Whereas, LSM, VOF, and phase-field method belong to interface capturing method which utilizes a suitable function to capture the interface. Among these methods, the LSM (Sussman *et al.*, 1994) is gaining acceptance and popularity due to ease in handling complex interface topology, capability for an easy extension to 3D problems, accurate calculation of interface normal and curvature, ability to impose interfacial boundary condition etc. A widely discussed limitation of the LSM is mass error, which can be reduced to acceptable limits with grid refinement or using a conservative level set method (Olsson and Kreiss, 2005).

Numerical representation of interface enables to address aforementioned first and second modelling challenges using two types of interface-treatment approaches: *Diffuse Interface* (DI) and *Sharp Interface* (SI), where the DI and SI approaches assume a finite

and infinitesimal thickness of the interface, respectively. The respective approach considers a smooth and sharp variation of the thermo-physical properties across the smooth and sharp interface for the first modelling challenge. Whereas, for the second modelling challenge, the force due to surface tension is modelled as a diffused volumetric force (across the diffused interface) in the momentum equation by the DI approach while the SI approach models it as an interfacial boundary condition (for the sharp interfacial force-induced jump of pressure) that is applied on the continuity equation. The respective surface tension models are called as *Continuum Surface Force* (CSF) model (Brackbill *et al.*, 1992) and *Sharp Surface Force* (SSF) (Kang *et al.*, 2000) model.

Historically, the study on interface commenced towards the early 18th century pioneered by Young, Laplace and Gauss. The initial approximation was to consider the interface as a region of zero thickness across which discontinuity in fluid properties exist and the interfacial forces act. Later towards the middle of 18th century, Poisson, Maxwell and Gibbs considered interface to be a region of specific thickness across which the properties vary continuously (Anderson *et al.*, 1998). A major limitation of the zero thickness model was the inability to apply to problems where the interface thickness approaches the length scale of the physical phenomenon. This diffused interface approach was later developed by Rayleigh and Van der Waals (Anderson *et al.*, 1998). Even from computational perspective, initially the diffused interface approach was preferred over sharp due to the complexities associated with sharp interface implementation. Moreover Anderson *et al.* (1998) were able to demonstrate that diffuse interface formulation asymptotically approached sharp interface limit at the condition where interface thickness reaches sharp boundary approximation. Thus, initially the diffused interface approach was preferred with the interface capturing schemes to solve CmFD problems, realizable with LSM.

The LSM was initially applied to CmFD problems with diffused interface method (Sussman *et al.*, 1994) after the formulation of CSF method (Brackbill *et al.*, 1992). This diffused interface approach utilizing LSM will be referred here as *DI-LSM*. Since the introduction of DI-LSM, several variants of this method are reported to improve the solution accuracy and robustness of the algorithm. The major developments could be attributed to the improvements on Heaviside function, advection scheme and reinitialization equation. To handle high density ratio, Chang *et al.* (1996) considered a smoothed Heaviside function instead of the initially proposed discontinuous Heaviside function (Sussman *et al.*, 1994). And the improvements with advection schemes and reinitialization equations could be attributed in dealing with mass-error associated with LSM. Upon interpreting the physical significance of Heaviside and Dirac delta function (Gada and Sharma, 2009a), Gada (2012) mentioned mass-error as an indicator showing the inaccuracy related

to the discretization involved with level set advection equation. Hence, rather than utilizing second order essentially non-oscillatory (ENO) scheme (Osher and Sethian, 1988), presently higher order schemes like third order total variation diminishing (TVD) Runge-Kutta (RK) scheme and third or fifth order weighted essentially non-oscillatory schemes (Jiang and Peng, 2000) are utilized for time and space discretization respectively in level set advection and reinitialization equations. Further to reduce the mass-error a constraint based reinitialization (Sussman *et al.*, 1998) and a time-step reinitialization (Ni *et al.*, 2006) are proposed.

These developments lead to the application of DI-LSM to problems like separated and parallel internal flow (Yap *et al.*, 2005, 2006; Datta *et al.*, 2011; Gada *et al.*, 2013), drop/bubble dynamics (Pan and Suga, 2003; Lakdawala *et al.*, 2014; Mukherjee and Kandlikar, 2005; Lakdawala *et al.*, 2015), boiling (Son and Dhir, 1998; Gada and Sharma, 2009b; Mukherjee and Kandlikar, 2005) etc. A detailed review regarding the DI-LSM is provided by Sharma (2015). Thus towards the end of 19th century, DI-LSM matured enough to handle complex CMFD problems and towards the similar time period sharp interface methodology was proposed as an alternate to DI-LSM for improving the accuracy of numerical solution. The Ghost Fluid Method (GFM) was proposed by Fedkiw *et al.* (Fedkiw *et al.*, 1999a; Liu *et al.*, 2000), to solve the interface with zero thickness by considering contact discontinuities across the interface rather than smoothening. This sharp interface method with level set method will be referred here as SI-LSM. The GFM which was initially utilized for incompressible-inviscid flows (Fedkiw *et al.*, 1999a) was also extended to account for deflagration and detonation discontinuities (Fedkiw *et al.*, 1999b). The same research group extended the GFM methodology to problems like flame front propagation (Nguyen *et al.*, 2001), multiphase flows with (Gibou *et al.*, 2007) and without (Kang *et al.*, 2000) phase change. Considering the robustness of SI-LSM, this methodology was utilized in various applications like combustion (Arienti and Sussman, 2014), vaporization (Tanguy *et al.*, 2007), film boiling (Son and Dhir, 2007), nucleate boiling (Son and Dhir, 2008) etc. Recently Shaikh *et al.* (2018) had compared both DI-LSM and SI-LSM on staggered grid, showing the improved solution accuracy obtained with sharp interface method over diffused interface method.

In the present study, one application of our interest is Nucleate Boiling with Power Transients (NBPT). Among interface capturing and interface tracking method, since nucleate boiling simulation is of interest, the interface separating superheated liquid and saturated vapor undergoes significant deformations making interface capturing method as suitable choice. Moreover, considering the ease in implementation, easy extension to 3D problems, natural handling of interface coalescence between multiple vapor bubbles, ac-

curate calculation of interface normals and curvatures, LSM is the preferred choice over VOF.

1.4.2 CmFD development on Staggered and Co-located Grid System

CmFD development involves two types of grid arrangement techniques: Staggered and Co-located, where the discrete grid points for the scalar and vector flow-properties are staggered and co-located, respectively. In the early days of CFD, the co-located grid system resulted in a checker-board velocity and pressure fields due to an improper discretization-based pressure-velocity decoupling (Sharma, 2016). The first remedy to the decoupling was the utilization of an alternate grid system, called staggered grid, proposed by Welch *et al.* (1965). Another remedy was proposed much later by Rhee and Chow (1983), which involves an alternate interpolation, called momentum interpolation method (MIM) (Rhee and Chow, 1983) for the face-center velocity on the co-located grid. However, the MIM was not correct enough for CmFD on co-located grid and led to numerical instability, especially for high density ratio, due to an improper discretization of the surface tension term. Thus, the early days of CmFD started (Nichols *et al.*, 1981) and continued with staggered grid for more than two decades after the advent of the MIM (Rhee and Chow, 1983). Table 1.2 shows the timeline associated with CMFD development on Eulerian grid.

LSM was proposed originally by Sussman *et al.* (1994) using the DI approach (DI-LSM). Later, Fedkiw *et al.* (1999a) proposed a ghost fluid method-based sharp interface level set method (SI-LSM) that was extended to Navier-Stokes equations by Kang *et al.* (2000). These DI-LSM and SI-LSM were proposed for a staggered grid system. Whereas, for CmFD on a co-located grid, a momentum-interpolation that involves a proper balance between the forces due to pressure and surface-tension, called as Balanced Force Method (BFM), was proposed by Francois *et al.* (2006) (Francois *et al.*, 2006) for a volume of fluid (VOF) method. They demonstrated stable and accurate solution for high density ratio problems on the co-located grid. This is numerically made possible by proposition of a proper MIM for two-fluid flow—23 years after the proposition of MIM for single fluid flow (Rhee and Chow, 1983)—which involves discretization of the pressure gradient and the surface tension term at identical location.

Table 1.2: Timeline associated with CmFD development on Eulerian grid.

Author	Method	Grid System	Simulation type	Contribution
Welch <i>et al.</i> (1965)	Marker and Cell Method (MAC)	Staggered	Single phase, incompressible	First staggered grid reported for single fluid system
Hirt <i>et al.</i> (1974)	Arbitrary Lagrangian-Eulerian method (ALE)	Staggered	Single phase incompressible	Overcome the limitation of MAC method by handling arbitrary confining boundaries
Hirt and Nichols (1981)	Volume Of Fluid (VOF)	Staggered	Multiphase, incompressible	First reported literature to include surface tension force in numerical algorithm
Rhie and Chow (1983)	Momentum interpolation	Co-located	Single phase, incompressible	First incompressible single phase simulation on co-located grid
Unverdi and Tryggvason (1992)	Front tracking (FT)	Staggered	Multiphase, incompressible	Front tracking method for multiphase simulation
Francois <i>et al.</i> (2006)	Balanced Force method (BFM)	Co-located	Multiphase incompressible	A comprehensive discussion on the high density ratio multiphase issues on co-located grid and proposed BFM as remedy

Table 1.3: Literatures contributing/improving the perspective of numerical methodology for diffused or sharp interface method utilizing level set method on staggered or co-located grid.

Author	DI-LSM/ SI-LSM	Grid system	Contribution
Sussman <i>et al.</i> (1994)	DI-LSM	Staggered	Utilized LSM for solving incompressible two-phase flow
Chang <i>et al.</i> (1996)	DI-LSM	Staggered	An area preserving reinitialization method by solving a perturbed Hamilton-Jacobi equation
Sussman <i>et al.</i> (1998)	DI-LSM	Staggered	A constraint based reinitialization method to preserve the individual fluid volume in each cell
Peng <i>et al.</i> (1999)	DI-LSM	Staggered	An improved reinitialization method to account flat or steep variation in level set function
Kang <i>et al.</i> (2000)	SI-LSM	Staggered	Ghost fluid method for multiphase flow
Liu <i>et al.</i> (2000)	SI-LSM	Staggered	GFM to solve Poisson equation with jump in its gradient
Gibou <i>et al.</i> (2007)	SI-LSM	Staggered	GFM extended to incompressible flows with phase change
Tanguy <i>et al.</i> (2007) Son and Dhir (2007)			
Herrmann (2008)	DI-LSM	Co-located	Extended BFM to unstructured grid
Gada and Sharma (2009a)	DI-LSM	Staggered	Physical interpretation of Heaviside and Dirac Delta function
Ningegowda and Premachandran (2014)	DI with CLSVOF	Co-located	Utilizing BFM to handle phase change problems
Montazeri <i>et al.</i> (2017)	SI-LSM (BFM approach)	Co-located	Following BFM approach a sharp interface formulation was implemented
Shaikh <i>et al.</i> (2018)	DI-LSM, SI-LSM	Staggered	Compared solution accuracy between DI-LSM and SI-LSM on staggered grid

The BFM-based VOF method, which was originally proposed for a structured grid, was later extended by Herrmann (2008) for a BFM-based DI-LSM on a co-located and unstructured grid. Similarly, Ito *et al.* (2009) modified deferred correction method for pressure gradient calculation to establish BFM criterion, on co-located non-orthogonal meshes. Montazeri *et al.* (2012) proposed an alternative formulation of BFM, which generalizes the body force components as an interfacial forcing term while maintaining force balance at the interface simultaneously. Further, they generalize body force at the faces of control volume as in a staggered approach. Ningegowda and Premachandran (2014) presented a Coupled Level Set Volume of Fluid (CLSVOF) on a co-located grid. Recently, Lin *et al.* (2019) presented BFM-based LSM for an unstructured grid. Manik *et al.* (2018) emphasised the significance of BFM for CmFD applications utilizing various test cases on three dimensional unstructured grid. Several multiphase problems like atomization process (Ruan *et al.*, 2017; Fuster *et al.*, 2009; Herrmann, 2010; Popinet, 2009; Tomar *et al.*, 2010), drop or bubble dynamics (Fuster *et al.*, 2009), gas entrainment process (Ito *et al.*, 2009) and multiphase flow in porous medium (Raeini *et al.*, 2012) are also reported for CmFD on a co-located grid. Moreover, table 1.3 shows literatures contributing to CmFD development using level set method.

1.4.3 CmFD development on co-located grid for heat transfer-induced phase change

For CmFD with phase change, boiling process is widely investigated due to its application in electronic cooling (Fan and Duan, 2020), nuclear reactors (Su *et al.*, 2016), refrigeration (Lv *et al.*, 2022), heat exchangers (El Achkar *et al.*, 2022) etc. Even though CmFD simulations for phase change applications initiated with Lagrangian methods (Welch, 1995), realizing the requirement for ease in handling interface evolution various interface capturing methods—Level Set Method (LSM), Volume of Fluid (VOF), and Couple Level Set Volume of Fluid (CLSVOF)—became popular on Eulerian grid. This is evident in the earlier work of Dhir's group for phase change simulation, initially a moving coordinate system for saturated film boiling (Son and Dhir, 1997) was utilized and realizing the requirement of a robust method for handling interface deformations diffuse interface level set method (DI-LSM) was developed for nucleate boiling simulations (Son *et al.*, 1999). Within level set method, this lead to utilization of DI-LSM for various phase change applications—flow boiling (Li and Dhir, 2007), film boiling (Gada and Sharma, 2011), nucleate boiling under normal gravity (Abarajith and Dhir, 2002; Mukherjee and Dhir, 2004) and reduced gravity (Aparajith *et al.*, 2006) conditions.

Later, for sharply enforcing the interface boundary condition to accurately model phase change, a *ghost fluid method* (GFM)-based *sharp interface level set method* (SI-LSM) was implemented for the first time by Nguyen *et al.* (2001) for capturing flame front and its merging, which was extended by various researchers for different phase change applications—film boiling (Son and Dhir, 2007; Gibou *et al.*, 2007), compressible bubble growth (Lee and Son, 2017), Leidenfrost effect (Villegas *et al.*, 2016), turbulent atomization (Desjardins *et al.*, 2008), vaporization (Tanguy *et al.*, 2007; Muramatsu *et al.*, 2022), and nucleate boiling (Son and Dhir, 2008; Lee *et al.*, 2010, 2012; Raut *et al.*, 2021). Similarly, other interface capturing methods—VOF (Malan *et al.*, 2021; Bureš and Sato, 2021; Welch and Wilson, 2000; Zhang *et al.*, 2011), CLSVOF (Ningegowda and Premachandran, 2014; Singh and Premachandran, 2018), VOSET (Cao *et al.*, 2020; Sun and Tao, 2010), and CIP-CSL2 (Sato and Ničeno, 2013)—are also utilized for phase change simulations. From the perspective of an Eulerian grid, it is interesting to observe that apart from Premachandran’s group (Ningegowda and Premachandran, 2014; Singh and Premachandran, 2018), all the above CmFD studies with phase change are performed on a *staggered grid*.

The initial modelling challenges for CmFD—localized surface tension force at the interface and sudden variation in thermo-physical properties across the interface—were resolved with Continuum Surface Force (CSF) model (Brackbill *et al.*, 1992). Later, for a more realistic mass-less interface of zero thickness the discontinuity in thermo-physical properties and localized surface tension force were preserved using Ghost Fluid Method (GFM)-based interfacial jump boundary condition formulation (Fedkiw *et al.*, 1999a; Kang *et al.*, 2000). This *smeared* and *zero* thickness interface treatment approaches are termed as *Diffuse Interface* (DI) and *Sharp Interface* (SI) approaches, respectively, were initially formulated on staggered grid Sussman *et al.* (1994); Kang *et al.* (2000).

Apart from these modelling challenges the co-located grid have two additional challenges—*pressure-velocity decoupling* (Shaikh *et al.*, 2016) and *pressure-interfacial force imbalance* (Chirammel *et al.*, 2023b; Francois *et al.*, 2006)—for CmFD. *Momentum Interpolation Method* (MIM) (Rhie and Chow, 1983) and *Balanced Force Method* (BFM) (Francois *et al.*, 2006) are the conventional methods utilized to overcome pressure-velocity decoupling and pressure-interfacial force imbalance, respectively. These challenges resulted in fewer studies of boiling and vaporization on co-located grid. Utilizing VOF on co-located grid various boiling applications—film boiling (Dixit *et al.*, 2022), flow boiling (Bahreini *et al.*, 2017; Municchi *et al.*, 2022), and nucleate boiling (Kunkelmann and Stephan, 2009, 2010b; Chen *et al.*, 2018, 2020, 2022; Bi *et al.*, 2019; Guion *et al.*, 2018)—has been investigated. Whereas Premachandrans group utilized CLSVOF

Table 1.4: Published and present work on single bubble *nucleate boiling* simulation utilizing various interface capturing methods on staggered/co-located grid.

Author	Method	Grid system	
Son <i>et al.</i> (1999, 2002)	DI-LSM	Staggered	
Abarajith and Dhir (2002); Aparajith <i>et al.</i> (2006)			
Aktinol and Dhir (2012)			
Wu <i>et al.</i> (2007); Wu and Dhir (2010)			
Dhir <i>et al.</i> (2007)			
Nam <i>et al.</i> (2011)			
Lee <i>et al.</i> (2010, 2012); Lee and Son (2011)	SI-LSM	Staggered	
Raut <i>et al.</i> (2021, 2022)			
Sato and Ničeno (2013); Sato and Niceno (2015, 2017)	CIP-CSL2		
Giustini <i>et al.</i> (2017)			
Ling <i>et al.</i> (2014)	VOSET		
Ling and Tao (2018)			
Pandey <i>et al.</i> (2018)	CLSVOF	Co-located	
Kunkelmann and Stephan (2009, 2010b)	VOF		
Kunkelmann <i>et al.</i> (2012)			
Perez-Raya and Kandlikar (2018)			
Chen <i>et al.</i> (2018, 2020, 2022)			
Bi <i>et al.</i> (2019)			
Guion <i>et al.</i> (2018)			
Kunkelmann and Stephan (2010a)	CLSVOF	Co-located	
Present	SI-LSM		

on co-located grid for film boiling simulation (Ningegowda and Premachandran, 2014, 2017; Singh and Premachandran, 2018, 2020), and other researchers coupled LSM with VOF in openFoam for nucleate boiling (Kunkelmann and Stephan, 2010a) and flow boiling simulations (Luo *et al.*, 2020). However, scarce studies are available for phase change simulations on co-located grid at high density ratio (> 1000) (Kunkelmann and Stephan, 2009; Municchi *et al.*, 2022; Chen *et al.*, 2018, 2020, 2022; Guion *et al.*, 2018).

To the authors knowledge no literatures are present for GFM-based SI-LSM on co-located grid for CmFD with phase change. Even though, Carlier and Papalexandris (2022) discussed about the absence of ghost fluid method on co-located grid for phase change, they utilized a front tracking method for interface representation. The preference of staggered grid over co-located grid is much more evident for the nucleate boiling simulations in partially developed regime (single bubble) as shown in Table 1.4, especially for high density ratio fluids. It could be further realized that for nucleate boiling simulation on co-located grid except LSM other interface capturing methods like VOF and CLSVOF has been utilized.

1.4.4 Nucleate Boiling with Power Transients

Nucleate boiling is a widely investigated phenomenon due to its application encountered in areas like immersion cooling (El-Genk, 2012; Narumanchi *et al.*, 2008), nuclear reactors (Su *et al.*, 2016), inkjet printers (Asai, 1991), MEMS (Okuyama *et al.*, 2005; Karayiannis and Mahmoud, 2017; Cornwell and Kew, 1993) etc. Typically, to establish a fundamental understanding of this complex phenomenon, the dynamics of single bubble is investigated by subjecting these bubbles to a steady heat flux. However, in practical scenarios, it is expected that the heat input is a combination of steady and transient heat flux. Improper design of the system without proper consideration of this transient behaviour could lead to catastrophic disasters as in nuclear reactors (Su *et al.*, 2016). Thus, a comprehensive understanding of *nucleate boiling with power transients* (NBPT) is essential to predict the behaviour of these systems under controlled or uncontrolled transient variation of the heat input. Moreover, with controlled power transients based on periodic heat flux, a controlled bubble dynamics (departure diameter, departure time, and bubble release frequency) could be attained—leading to *boiling-on-demand*. Currently, to investigate the effect of power transients, only experiments are conducted that has several limitations in terms of observing bubble dynamics with power transients. Thus, with the aid of numerical method, this study aims to analyse the NBPT under the effect of a periodic heat flux.

The effect of power transients on nucleate boiling gained attention since Cole (1956) studied the influence of power surge on melting of nuclear reactor fuel element, almost after two decades of nucleate boiling investigation with steady heat input (Nukiyama, 1966). The degree of subcooling and heat generation rate was found to influence the transient critical heat flux. For constant heat generation rate (degree of subcooling), the transient critical heat flux increases with degree of subcooling (heat generation rate). Largely, the effect of the heating pattern on nucleate boiling has been investigated by several studies, *i.e.*, the effect of either an exponential or linear or step variation in the heat input. Whereas, for the reactor technology (Su *et al.*, 2016; Cole, 1956), cooling of superconductors and for superconducting magnetic energy storage (SMES) (Sakurai *et al.*, 1992), the *exponential* variation in heat generation rate is of major interest that is the mode of periodic power transients considered in this study.

The common parameters that are taken into consideration while performing nucleate boiling with exponential heat input are the excursion time (parameter which controls the rate of heat generation), liquid sub-cooling, and pressure. Rosenthal (1957) investigated the effect of excursion time, liquid sub-cooling, and dissolved gas on onset of nucleate boiling phenomenon. For constant bulk temperature, it was observed that the

temperature overshoot increases as the excursion time decreases. Whereas, for constant excursion time, the temperature overshoot increases with decreasing bulk temperature. Considering excursion time, sub-cooling and pressure as parameters, Johnson (Johnson, 1971) investigated these effects on non-boiling region, boiling incipience, and nucleate boiling region. Various available steady state correlations were utilized to determine the heat transfer rate, wall superheat, and incipience conditions; and good agreement was obtained for excursion times higher than 5 ms.

Sakurai and Shiotsu (1977a) established a relation between incipience wall superheat and heat flux for nucleate boiling subjected to exponential variation in heat input by considering liquid sub-cooling and excursion time as parameters. From the superheated thermal layer and cavity model, an increase in incipience heat flux is observed with reduction of excursion time. By considering the excursion time and system pressure as the parameters, Sakurai and Shiotsu (1977b) extended their work to investigate the effect of excursion heating on boiling regimes succeeding *onset of nucleate boiling* (ONB). On comparing the steady and transient boiling curve at some transient boiling conditions, it was observed that the boiling curve intersected and not-intersected with steady boiling curve, referred as regular and irregular process, respectively. The irregular process was obtained at various conditions of exponential period and system pressures, at 30 ms for 0.196 MPa and 5 ms for 0.588 MPa. The same research group further studied the effect of exponential power transients on cryogenic liquids, LN₂ and LHe I (Sakurai *et al.*, 1996). Utilizing liquid nitrogen and liquid helium as cryogenic liquids, two types of behaviour was observed: direct transition from non-boiling regime to film boiling, and transition from non-boiling regime to fully developed nucleate boiling regime followed by film boiling. These phenomenon were assumed to occur due to *heterogeneous spontaneous nucleation* (HSN) and the latter being proposed to occur at the lower limit of HSN surface superheat. This assumption was later confirmed with a photographic study (Sakurai *et al.*, 2000) performed with liquid nitrogen and water. The same research group extended their work to determine the effect of surface condition on CHF subjected to exponential heating (Fukuda *et al.*, 2000).

Classifying the exponential period as shorter, intermediate, and longer, the effect of each category of exponential ramp rate on CHF occurring over commercial surface (CS) (Emery-3 finished rough surface (RS) and mirror finished surface (MS)) are discussed. Fitri *et al.* (2007) identified three regimes during the transition from non-boiling regime to CHF at various exponential period and system pressures with FC-72. First, transition from non-boiling regime to *fully developed nucleate boiling* (FDNB) regime; second, transition from non-boiling regime to film boiling; and third, transition from non-boiling

regime to film boiling through nucleate boiling. Park *et al.* (2009) later extended this study to compare steady and transient CHF at various system pressure, exponential period, and subcooling with water, ethanol, and FC-72.

Recently (Brown *et al.*, 2020), utilizing Laplace transform on a two-region transient conduction domain, a theoretical study was carried out to predict the *critical heat flux* (CHF) caused by HSN. During the transition from ONB to FDNB, Su *et al.* (2016) identified two phenomenon in transient heating—transition from ONB to FDNB with and without temperature overshoot, depending on the liquid subcooling and exponential period. After identifying various conditions like onset of boiling driven heat transfer (OBD), overshoot (OV) and superheated layer (SHL) depletion, it was determined that the transient boiling curve from ONB to FDNB passes through OBD, OV and SHL depletion at very high subcooling and low exponential period (75 K and 5 ms). While for low subcooling and low exponential period (25 K and 5 ms), the transient boiling curve passes from ONB to FDNB through OBD without OV and SHL depletion. Utilizing force balance approach and including the surface roughness parameters, Walunj and Sathyabhama (2018) proposed a model to predict the transient CHF and compared with the experiments performed at different pressure conditions. Shibahara *et al.* (2018) investigated the effect of exponential heat input on the heat flux at incipience condition and nucleate boiling heat transfer rate. As observed in previous study (Su *et al.*, 2016), the incipience heat flux was affected by the exponential period. But for the exponential period considered (0.35s - 19s), no difference was observed between transient and steady heat transfer.

The motivation for initiation of NBPT was exponential heat generation in nuclear reactors (Cole, 1956; Rosenthal, 1957). However, for simple analysis of transient heat flux, Lurie et al. (Lurie and Johnson, 1962) utilized step heating instead of exponential heating. On a thin metallic ribbon in water with step heating the behaviour of surface temperature and void volume were monitored. With one-dimensional transient conduction analysis, the time-wise variation in surface temperature till it reaches steady state was predicted. Nghiem *et al.* (1981) investigated onset of nucleate boiling (ONB) with step heating and observed dependency of ONB on temperature and inception time. Iida *et al.* (1994) also investigated the effect of step heating on ONB for various working fluids—ethyl alcohol, toluene, and water. An increase in temperature at boiling incipience with rate of temperature rise is observed. Okuyama et al. (Kunito *et al.*, 1988; Okuyama and Iida, 1990) performed experiments to investigate the effect of system pressure and bubble behaviour under step heating with R113 and liquid nitrogen, respectively. The transient critical heat flux—limiting value of heat flux above which the heat flux cannot exceed heat generation rate—is found to be lower than steady condition at low system pressure. Whereas,

for bubble behaviour, massive vapor bubbles are observed at low system pressure but not at high system pressure. With liquid nitrogen Okuyama and Iida (1990) were able to classify bubble behaviour into three patterns—coalescence of nucleate boiling bubbles, formation of vapor sheath along test wire, and nucleation of fine initial bubbles—based on heat generation —low, high, and extremely high.

Visentini *et al.* (2014) investigated the effect of various power ramps (step and linear) on transient ONB using a semi annulus test section to closely resemble pressurised water reactor for nuclear safety studies due to reactivity initiated accidents. Deev *et al.* (2007) were able to propose a model to predict transient critical heat flux based on experiment conducted with water as working fluid under step heating. Considering the application of step heating in inkjet printers and various other MEMS devices, the study of step heating further gained attention. The effect of surface roughness (Drach *et al.*, 1996), thick flat sample (Héas *et al.*, 2003), highly wetting fluids (Duluc *et al.*, 2004), bubble dynamic characteristics on a square platinum microheater (Li *et al.*, 2008) etc., are carried out in this regard. Apart from exponential and step heating, even though Tachibana *et al.* (1968) investigated the effect of linear power transients on critical heat flux, no further studies with linear power transients are available. Further, as shown in Table 1.5 only experiment studies are available to investigate the effect of power transients whereas the present study utilize simulation methodology to compare various modes of power transients.

1.5 Scope and Objective of Present Work

The overall scope and objective of the present work is CmFD development of novel Ghost Fluid Method-based SI-LSM on co-located grid (SI-LSM_{col}) for high density ratio problems, and then for phase change, in 2D Cartesian as well as axi-symmetric coordinate systems; and the application of SI-LSM_{col} for the analysis of single bubble nucleate boiling dynamics with various modes of power transients.

The conclusions from the literature survey and a detailed scope and objective of the series of present-work is presented below in separate subsections.

1.5.1 On Ghost Fluid Method-based Sharp Interface Level Set Method on a Co-located Grid and its comparison with Balanced Force-based Diffuse Interface Method

In literature, performance-based comparative studies of SI-versus-DI codes is available, in the VOF framework, for both staggered and co-located as shown in Table 1.6. These studies provide useful insight on applicabilities/capabilities of these codes. For

Table 1.5: Published and present work on the effect of various modes of power transients on nucleate boiling.

Author	Modes of power transients	Experiment or Simulation
Rosenthal (1957)		
Sakurai and Shiotsu (1977a,b)		
Sakurai <i>et al.</i> (2000, 1989, 1996)		
Shiotsu <i>et al.</i> (1992)		
Fukuda <i>et al.</i> (2000)	Exponential	
Fukuda and Liu (2005)		
Park <i>et al.</i> (2009)		
Su <i>et al.</i> (2016)		
Walunj and Sathyabhama (2016)		
Lurie and Johnson (1962)		
Nghiem <i>et al.</i> (1981)		Experiment
Kunito <i>et al.</i> (1988)		
Okuyama and Iida (1990)		
Shiotsu <i>et al.</i> (1992)		
Iida <i>et al.</i> (1994)		
Drach <i>et al.</i> (1996)	Step	
Héas <i>et al.</i> (2003)		
Duluc <i>et al.</i> (2004)		
Deev <i>et al.</i> (2007)		
Li <i>et al.</i> (2008)		
Visentini <i>et al.</i> (2014)		
Tachibana <i>et al.</i> (1968)	Linear	
Present work	Exponential, step, and Linear	Simulation

example, improved performance of SI over DI approach using VOF is shown on staggered (Vachaparambil and Einarsrud, 2019) and co-located grid (Renardy and Renardy, 2002). A similar SI-versus-DI comparison in the LSM framework is however available for staggered grid only (Shaikh *et al.*, 2018). Co-located grids performance for SI-LSM technique in comparison to the DI-LSM counterpart becomes important in the context of its capability for modelling complex multiphase systems with fast moving interfaces.

Based on the above conclusions from the literature survey, the present work has broadly two-objectives: first, propose a ghost fluid method-based SI-LSM on a co-located grid; second, present a comparison of numerical methodology as well as computational performance of the SI-LSM and DI-LSM on the co-located grid. For the second objective, we propose a *unified* (for the SI and DI approaches) mathematical formulation as well as numerical methodology; and a validation study, order of accuracy study, and relative performance study for diffuse and sharp interfaces-based LSMs on the co-located grid. The validation and performance studies are presented for a variety of CmFD problems on

Table 1.6: Published and present work on a comparative study for the diffuse and sharp interface-based numerical methods for CmFD, and their relative performance study.

Author	Methods	Grid system
Abadie <i>et al.</i> (2015)	LSM	Staggered
Shaikh <i>et al.</i> (2018)		
Renardy and Renardy (2002)	VOF	Co-located
Francois <i>et al.</i> (2006)		
Vachaparambil and Einarsrud (2019)	LSM	
Present work		

pressure-interfacial force balance-based static droplet problem, gravity-dominated dam break simulation, and surface tension-dominated droplet coalescence problem. Note that the last CmFD problem is solved on an *axisymmetric* coordinate while the other two-problems are on a 2D Cartesian coordinate.

1.5.2 On Comparison of Staggered and Co-located Grid-based Diffuse and Sharp Interface Level Set Method

From the above literature survey for DI and SI approaches on staggered and co-located grid, a detailed comparison of the numerical methodologies is not available. This is essential for understanding the similarity and dissimilarity in numerical formulation of the DI- and SI- approaches on both the grid systems and further to compare the relative accuracy of these methods. Thus, the scope of the present work is a detailed-presentation of numerical methodologies for diffuse-versus-sharp interface-based level set method on staggered-versus-co-located grid. This lead to the development of four in-house CmFD solvers—Diffuse interface level set method on staggered grid (DI-LSM_{stag}) (Gada, 2012), Sharp interface level set method on staggered grid (SI-LSM_{stag}) (Shaikh *et al.*, 2018), Diffuse interface level set method on co-located grid (DI-LSM_{col}) and Sharp interface level set method on co-located grid (SI-LSM_{col}) (Sanjid *et al.*, 2021b). Note that the first-two solvers on staggered grid were developed by the earlier researchers in our CFD Lab while the latter-two solvers on co-located grid are developed for this study. Further the capability of these solvers to handle various CmFD problems are established by performing capillary wave, static droplet, dam break, and Raylor-Taylor instability simulations.

1.5.3 Sharp Interface Level Set Method on a Co-located Grid for CmFD with Heat Transfer-induced Phase Change

Based on the above conclusion from literature survey, the present study has two-objectives: first, propose a ghost fluid method-based sharp interface level set method on co-located grid ($\text{SI-LSM}_{\text{col}}$) for CmFD with phase change and second, validate several benchmark problems with phase change to establish the robustness of present LSM on co-located for high density ratio problems. For the first objective, momentum interpolation method and interfacial jump condition (for pressure) is utilized to avoid pressure-velocity decoupling and pressure-interfacial force imbalance on co-located grid (Sanjid *et al.*, 2021a), respectively. Whereas for the second objective the present $\text{SI-LSM}_{\text{col}}$ is validated with solidification, 1D-moving interface, 1-D sucking interface, film boiling, growth of suspended bubble in superheated liquid and nucleate boiling simulations. Further note that growth of suspended bubble in superheated liquid and nucleate boiling are performed on *axisymmetric* coordinate, while the other problems are simulated on 2D Cartesian coordinate.

1.5.4 Single bubble nucleate boiling over a base plate, subjected to Power Transients

Conclusions drawn from the above literature survey is that, for exponential mode of power transients, mainly the effect on boiling curve, ONB, and CHF are investigated with excursion time. Whereas the influence on bubble dynamic parameters—bubble departure diameter D_d , bubble growth period t_g , and bubble departure frequency f —are not found in the literatures. Clarity on the complex boiling phenomenon due to power transients could be obtained with proper understanding of the single bubble dynamics. Further, the understanding from single bubble dynamics perspective is essential since they are responsible for heat removal, bubble coalescence which could be detrimental to the system, and controllability of boiling phenomenon. A proper parametrization of the exponential heat flux is also vital to achieve these, which are not available currently. Thus, the focus of the present study is on two objectives: first, to propose a numerical methodology with proper parametrization of the input transient heat flux which enables numerical simulation of the NBPT; and the second on investigation on effect of a periodic exponential heat flux on the single bubble dynamics parameters. These objectives are setup such that they have the future scope to fulfil our motivation to control the bubble dynamics (with heating pattern) and enable boiling-on-demand.

1.5.5 Effect of Heating Patterns on Single bubble nucleate boiling over a base plate

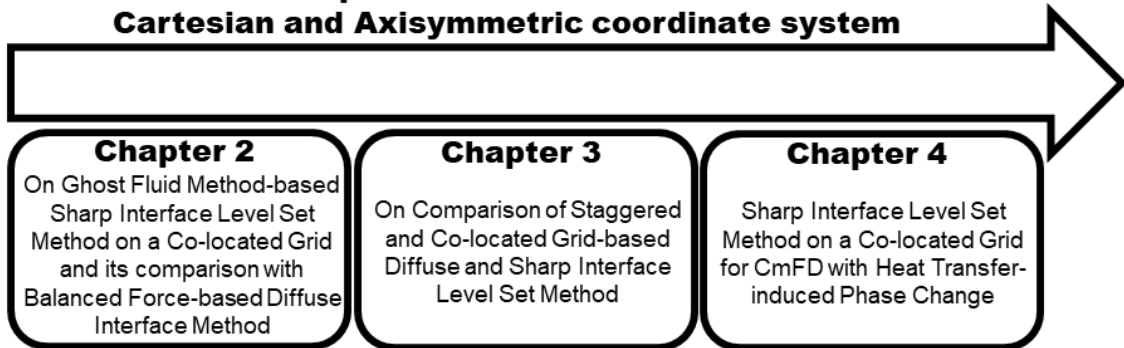
Conclusions drawn from the above literature survey is that apart from the time-wise exponential variation another commonly utilized power transients is step heating. Similar to the exponential power transients the studies with step heating also focus mainly on ONB and CHF without much attention on bubble dynamic parameters—bubble departure diameter, bubble growth period, and bubble departure frequency. Moreover, there is no comparison between the effect of various modes of power transients on nucleate boiling. Thus the objective of the present study is to utilize previously proposed solution methodology to investigate other modes of power transients—step and linear—for comparison on their effect on single bubble nucleate boiling.

1.6 Organization of report

This report present seven chapters. Chapter-1 as introduction, Chapter-2 on a comparative study on numerical methodology along with computational performance for GFM-based SI-LSM and BFM-based DI-LSM, Chapter-3 on further comparative study on numerical methodology of sharp-versus-diffuse interface based LSM on staggered-versus-co-located grid, Chapter-4 on extension of the present GFM-based SI-LSM to CmFD problems with phase change on co-located grid, Chapter-5 on CmFD analysis for the effect of exponential power transients on single bubble nucleate boiling, Chapter-6 on CmFD analysis for the effect of various modes of power transients on single bubble nucleate boiling, and Chapter-7 on conclusions and future scope for present work. Overall, apart from Chapter-1 on introduction and Chapter-7 on conclusion and future scope, this report is divided into two parts—Part I on CmFD development and Part II on CmFD application and analysis. All the CmFD development associated with present SI-LSM and DI-LSM are presented in chapters 2-4 of the Part I of this report, whereas the CmFD analysis of the nucleate boiling with power transients—proposition of a simulation methodology and effect of various power transients on single bubble during nucleate boiling—is presented in chapter 5-6 of the Part II.

PART-I

CmFD Development on Co-located Grid for 2D Cartesian and Axisymmetric coordinate system



This part discuss about SI-LSM-based and DI-LSM-based CmFD development on co-located grid and its comparison with staggered grid, and further the extension of present GFM-based SI-LSM on co-located for heat transfer-induced phase change. Each chapter is organized such that initially numerical methodology—consisting of discretization, solution method and solution algorithm—is discussed and ending with validation and performance study of utilized methodologies. In Chapter 1, the discretization using physical law-based FVM, the semi-explicit projection method-based unified solution method for present GFM-based SI-LSM and BFM-based SI-LSM are presented followed with their solution algorithm. In Chapter 2, similarly the discretization, solution method, and solution algorithm are compared in detail for present sharp-versus-diffuse approach on staggered-versus-co-located grid. In Chapter 3, present SI-LSM on co-located grid is extended for heat transfer-induced phase change, establishing the capability of present numerical methodology on co-located grid for complex multi-physics. For evaluating the computational performance, in Chapter-2 and Chapter-3, sufficiently different CmFD benchmark problems (surface tension force dominant and gravity dominant) are utilized, which required the development of present in-house codes on 2D Cartesian and Axisymmetric coordinate systems. Whereas in Chapter 4, various CmFD benchmark problems for phase change with increased complexity on both 2D Cartesian and Axisymmetric coordinate systems are presented.

Chapter 2

On Ghost Fluid Method-based Sharp Interface Level Set Method on a Co-located Grid and its comparison with Balanced Force-based Diffuse Interface Method

This study on Computational multi-Fluid Dynamics (CmFD) development, presents an extension of the Ghost Fluid Method (GFM)-based Sharp Interface Level Set Method (SI-LSM) (originally proposed on a staggered grid) for a co-located grid system. Further, a comparative study for the GFM-based SI-LSM and a balanced force method (BFM)-based Diffuse Interface Level Set Method (DI-LSM). The BFM-based DI-LSM avoids a pressure-interfacial force decoupling, during the implementation of the Momentum Interpolation Method (MIM) by a proper-discretization of the surface tension term; not needed for the single-phase flow. Whereas, the GFM-based SI-LSM implicitly couples two immiscible, incompressible fluids via interface jump condition, which makes the MIM for the two-fluid flow *same* as that for a single-fluid flow. A *unified*, for both SI-LSM and DI-LSM, mathematical and numerical formulations are presented.

2.1 Unified mathematical formulation for SI-LSM and DI-LSM

For both DI-LSM and SI-LSM, instead of using separate equations for each of the two-fluid flow, a *single field formulation* is used which involves a single governing equa-

tion for both the fluids along with an appropriate thermo-physical property. The formulation leads to a single-field for the two-fluid flow, where the interfacial force due to surface-tension is modelled as a volumetric force in the momentum conservation equation, for the DI-LSM, whereas, the SI-LSM models it separately as an interfacial jump boundary condition (BC) for pressure, during the solution of the mass conservation equation. Further, for phase change problems, interfacial mass transfer is also modelled as another volumetric term in the DI-LSM (Gada and Sharma, 2011) and as the interfacial jump BC for pressure in the SI-LSM (Shaikh *et al.*, 2019); both the modelling are for the mass conservation equation.

Figure 2.1 shows a schematic representation of present DI-LSM and SI-LSM with various types of grid points and control volumes (CVs). For DI-LSM, Fig. 2.1(a) shows a computational domain consisting of numerically smeared interface, interior and interfacial grid points, and fully or partially filled CVs. For single field formulation, the thermo-physical properties are assumed to vary continuously in the diffuse interfacial region between numerically relevant interface ($-\epsilon \leq \phi \leq \epsilon$), shown in Fig. 2.1(a). The *volumetric force* due to surface tension force is also modelled in this region. Further, partially filled CVs are shown in Fig. 2.1(b) and Fig. 2.1(c) with main grid point (P) inside Fluid-1 and Fluid-2, respectively; corresponding stencils shown in Fig. 2.1(a). Similarly, for SI-LSM, Fig. 2.1(d) shows computational domain with various grid points and control volumes which are demarcated with a zero thickness or physically relevant interface ($\phi = 0$). Unlike single-field formulation in DI-LSM, since no artificial smearing of interface is involved in SI-LSM, Fig. 2.1(d) shows no diffuse interface region but only a physically relevant interface separating the subdomains Ω_1 and Ω_2 for Fluid-1 and Fluid-2, respectively. Since the interfacial forces are modelled by a jump condition formulation in the SI-LSM, major difference could be seen in partially filled control volumes for the SI-LSM (Fig. 2.1(e,f)) and DI-LSM (Fig. 2.1(b,c)). These formulations are further discussed below in the unified numerical methodology section.

In this section, for both DI-LSM and SI-LSM methods, conservation and subsidiary equations are presented in separate subsection below. Although the level set function—defined as a normal distance function—is used to capture the interface, it is also used to easily implement the force due to surface tension and the variation of thermo-physical properties across the interface; presented below. A comprehensive discussion on the mathematical formulation along with the various functions in the LSM are presented in a previous work (Shaikh *et al.*, 2018); from our research group for a staggered grid. Here, for a co-located grid, note that the mathematical formulation is unified for both SI-LSM and DI-LSM; not found in the literature.

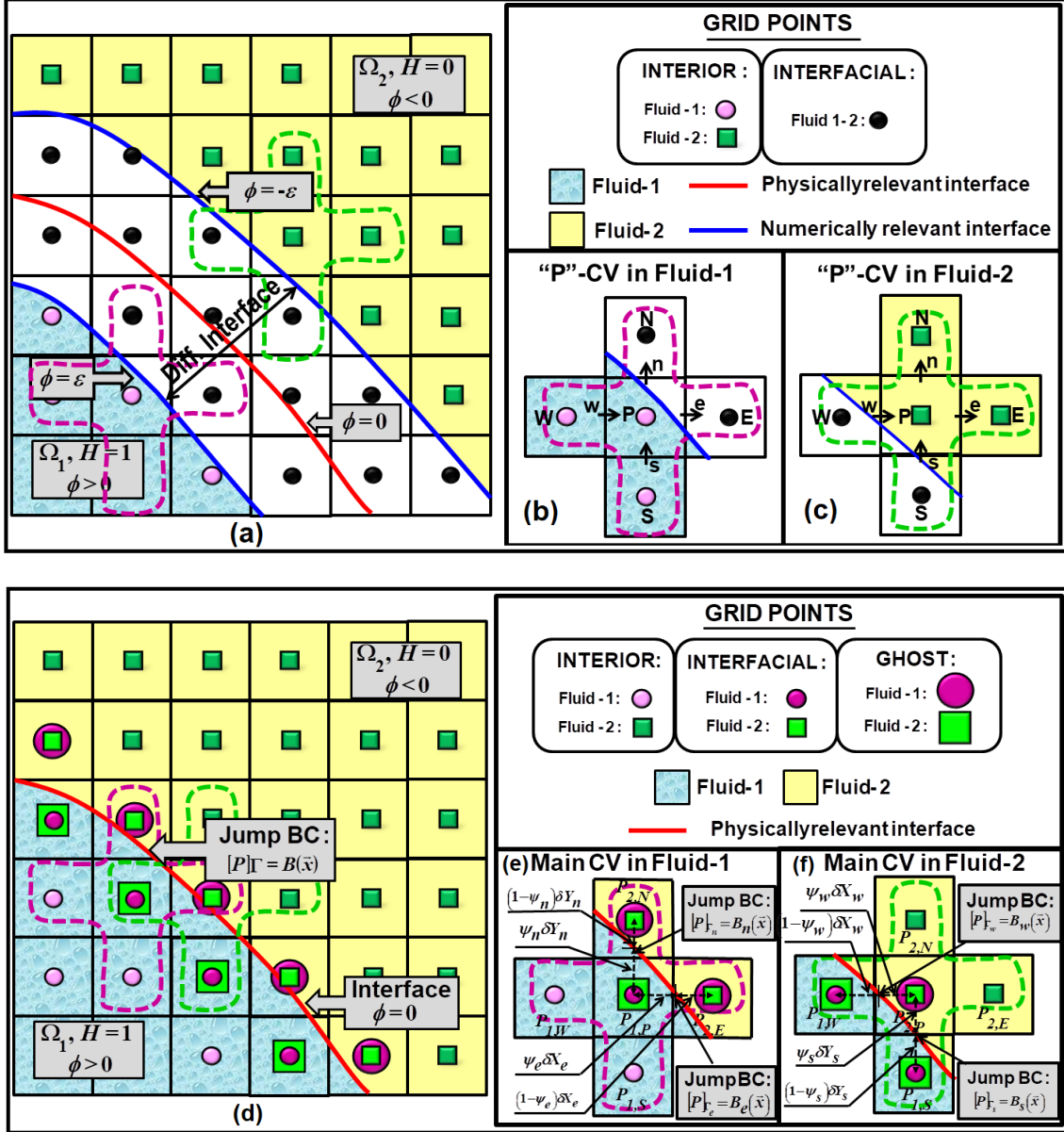


Figure 2.1: Schematic of a representative computational domain along with the various types of grid points for a two-fluid flow, with the fluids separated by a (a) diffuse interface ($-\epsilon \leq \phi \leq \epsilon$) for the DI-LSM and (d) sharp interface $\Gamma(\phi = 0)$ for the SI-LSM. For a representative partially-filled Cartesian control volume (CV), the associated interfacial grid point “P” in the (b, e) fluid-1, and (c, f) fluid-2 inside the Ω_1 and Ω_2 subdomains, respectively.

The present unified formulation assumes constant fluid properties but unequal in each fluid, i.e., the bulk fluids are incompressible. Further, the interface is assumed as thin and massless, with no-slip in tangential velocity. The surface tension coefficient is assumed to be constant all along the interface.

2.1.1 Conservation Equations

Gada and Sharma (2009a) proposed physical interpretations of Heaviside and Dirac-delta functions for the LSM, which were used to present a control volume-based derivation of the continuity equation and level-set advection equation, from volume conservation and mass conservation laws, respectively. Here, for both DI-LSM and SI-LSM, the conservation laws-based single-field conservation equations are presented below in a non-dimensional form. For the SI-LSM, non-dimensional interfacial jump boundary conditions are also presented. Further, for both DI-LSM and SI-LSM, various level set functions-based formulations are presented for the computations of non-dimensional thermo-physical properties, and normal as well as curvature of the interface.

Volume Conservation Law-based Continuity Equation:

$$\nabla \cdot \vec{U} = 0 \quad (2.1)$$

Mass Conservation Law-based Level-Set Advection Equation:

$$\frac{\partial \phi}{\partial \tau} + \vec{U}_a \cdot \nabla \phi = 0 \quad (2.2)$$

where \vec{U}_a is the bulk velocity, obtained by solving the below momentum equation, for the advection of the level set function ϕ .

Momentum Equation:

$$\frac{\partial(\rho^* \vec{U})}{\partial \tau} + \nabla \cdot (\rho^* \vec{U} \vec{U}) = -\nabla P + \frac{1}{Re} \nabla \cdot (\mu^* [\nabla \vec{U} + \nabla \vec{U}^T]) + \rho^* \frac{1}{Fr^2} \hat{j} + \bar{F}_{\vec{U}}^{ST} \quad (2.3)$$

where $\bar{F}_{\vec{U}}^{ST}$ is the non-dimensional volumetric force, due to surface tension, for the DI-LSM; given as

$$\bar{F}_{\vec{U}}^{ST} = \frac{1}{We} \kappa \delta_\epsilon \hat{N} \text{ for DI-LSM and } \bar{F}_{\vec{U}}^{ST} = 0 \text{ for SI-LSM} \quad (2.4)$$

where δ_ϵ is a smoothed Dirac delta function, and \hat{N} is non-dimensional unit normal vector. Note that the $\bar{F}_{\vec{U}}^{ST}$ is zero (not considered) in SI-LSM. Instead, the force due to

surface tension is incorporated as an interfacial jump boundary condition; given (Shaikh *et al.*, 2018) as

$$[P] = \frac{2}{Re_1} [\eta] \hat{N} \cdot (\nabla U \cdot \hat{N}, \nabla V \cdot \hat{N}) + \frac{\kappa}{We} \text{ for SI-LSM} \quad (2.5)$$

For the above non-dimensional formulation, considering l_c as length scale, v_c as velocity scale, t_c as time scale, and fluid-1 as the reference fluid, the non-dimensional variables and governing parameters are given as

$$\vec{X} = \frac{\vec{x}}{l_c}; \tau = \frac{tu_c}{l_c}; \vec{U} = \frac{\vec{u}}{u_c}; P = \frac{p}{\rho_1 u_c^2}$$

$$Re = \frac{\rho_1 l_c u_c}{\mu_1}; Fr = \frac{u_c}{\sqrt{gl_c}}; We = \frac{\rho_1 u_c^2 l_c}{\sigma}$$

where \vec{X} , τ , \vec{U} and P are non-dimensional Cartesian coordinate, time, velocity, and pressure, respectively. Further, Re is Reynolds number, Fr is Froude number, and We is Weber number. Finally, the non-dimensional density ρ^* and dynamic viscosity μ^* in the above conservation equations are represented in terms of a Heaviside function $H(\phi)$ as

$$\rho^* = H(\phi) + \frac{\rho_2}{\rho_1}(1 - H(\phi)) \quad (2.6)$$

$$\mu^* = H(\phi) + \frac{\mu_2}{\mu_1}(1 - H(\phi)) \quad (2.7)$$

Here, the subscript ‘1’ and ‘2’ corresponds to the properties associated with the Fluid-1 and Fluid-2 (Fig. 2.1), respectively. The Heaviside function $H(\phi)$ is given as

For DI-LSM: Smoothed or Diffused Heaviside function

$$H(\phi) = H_\epsilon(\phi) = \begin{cases} 0 & \phi < -\epsilon \\ \frac{\phi+\epsilon}{2\epsilon} + \frac{1}{2\pi} \sin\left(\frac{\pi\phi}{\epsilon}\right) & |\phi| \geq \epsilon \\ 1 & \phi > \epsilon \end{cases} \quad (2.8)$$

For SI-LSM: Sharp-Heaviside function

$$H(\phi) = \begin{cases} 0 & \phi < 0 \\ 1 & \phi \geq 0 \end{cases} \quad (2.9)$$

where $\epsilon = 1.5\Delta X$ is the thickness of the diffuse interface, with ΔX as the uniform grid size. Note that the smoothed $H_\epsilon(\phi)$ in the DI-LSM and the sharp $H(\phi)$ in the SI-LSM

leads to a gradual/smooth and sharp variation of the thermo-physical properties, across the finite (but small 2ϵ) and zero thicknesses of the diffuse and sharp interface (Fig. 2.1), respectively.

Further, for Eq. (2.4) on DI-LSM and Eq. (2.5) on SI-LSM, the non-dimensional unit normal vector \hat{N} and curvature κ of the interface are given as

$$\hat{N} = \nabla\phi/|\nabla\phi| \text{ and } \kappa = -\nabla \cdot \hat{N} \quad (2.10)$$

2.1.2 Subsidiary Equation

Apart from the above conservation equations, a reinitialization equation is needed to re-establish the advected level set function ϕ as normal distance function. The subsidiary equation is given (Sussman *et al.*, 1994) as

Reinitialization Equation:

$$\frac{\partial\phi}{\partial\tau_s} = S_\epsilon(\phi_0)(1 - |\nabla\phi|) \quad (2.11)$$

where $\tau_s (= \Delta x/10)$ is a pseudo time step, and $S_\epsilon(\phi_0) (= \phi_0/\sqrt{\phi_0^2 + \Delta x^2})$ is a smoothed sign function.

2.2 Unified numerical methodology for DI-LSM and SI-LSM on a co-located grid

In this section, for both DI-LSM and SI-LSM, a unified numerical methodology is presented for the solution of the unified mathematical formulation; presented in the previous section. For the discretization of the above equations, a *physical law-based Finite Volume Method* (FVM) (Sharma, 2016) is used for the continuity and momentum equations (Eq. 2.1 and Eq. 2.3) while a finite difference method is used for the level-set advection and reinitialization equations (Eq. 2.2 and Eq. 2.11). The physical law-based FVM uses a discrete-form of the conservation laws (instead of the continuous differential equation) and discrete-math (independent of continuous-math)—proposed in a text book on CFD by Sharma (2016). The resultant systems of linear algebraic equations (LAEs), for the flow field, are solved by using a *semi-explicit pressure projection method* as a solution method. The discretization method, solution method, and solution algorithm are presented in separate subsections below. The present SI-LSM is efficiently parallelized

and extended for CmFD with phase change problem (nucleate boiling) and will be presented in our future work. Further for DI-LSM, this is presented in a previous work of our research group (Aggarwal *et al.*, 2013).

2.2.1 Discretization method: Physical law-based FVM

For the volume and momentum conservation (Eq. (2.1) and (2.3)) in a 2D Cartesian coordinate system and a *uniform* Cartesian grid, the physical law-based FVM or algebraic formulation are given (Sharma, 2016), in a non-dimensional form, as

$$(U_e^{n+1} - U_w^{n+1})\Delta Y + (V_n^{n+1} - V_s^{n+1})\Delta X = 0 \quad (2.12)$$

$$\begin{aligned} \rho_P^{*,n} \frac{U_P^{n+1} - U_P^n}{\Delta \tau} \Delta V_P + A_{U,P}^n &= \frac{P_W^{n+1} - P_E^{n+1}}{2} \Delta Y + D_{U,P}^{n+1} + \bar{F}_{U,P}^{ST,n} \Delta V_P \\ \rho_P^{*,n} \frac{V_P^{n+1} - V_P^n}{\Delta \tau} \Delta V_P + A_{V,P}^n &= \frac{P_S^{n+1} - P_N^{n+1}}{2} \Delta X + D_{V,P}^{n+1} - \frac{1}{Fr^2} \Delta V_P + \bar{F}_{V,P}^{ST,n} \Delta V_P \end{aligned} \quad (2.13)$$

where U and V are the velocities in the X- and Y-directions, respectively. Further, the subscript ‘ P ’ represents a flow property at the cell-center of a representative CV while that at the east, west, north and south face-centers of the CV are represented by subscript e , w , n and s , respectively; refer Fig. 2.1(b). Further, $A_{\vec{U},P}$ and $D_{\vec{U},P}$ are the FVM-based discretized form of the non-dimensional advection and diffusion terms in momentum equation (Eq. 2.3), respectively. They are given (Sharma, 2016), in a vector form, as

$$\begin{aligned} A_{\vec{U},P}^n &= [M_{X,e}^n \vec{U}_e^n - M_{X,w}^n \vec{U}_w^n] \Delta Y + [M_{Y,n}^n \vec{U}_n^n - M_{Y,s}^n \vec{U}_s^n] \Delta X \\ D_{\vec{U},P}^{n+1} &= \frac{1}{Re} \left(\mu_e^* \frac{\vec{U}_E^{n+1} - \vec{U}_P^{n+1}}{\delta X_e} \Delta Y - \mu_w^* \frac{\vec{U}_P^{n+1} - \vec{U}_W^{n+1}}{\delta X_w} \Delta Y \right. \\ &\quad \left. + \mu_n^* \frac{\vec{U}_N^{n+1} - \vec{U}_P^{n+1}}{\delta Y_n} \Delta X - \mu_s^* \frac{\vec{U}_P^{n+1} - \vec{U}_S^{n+1}}{\delta Y_s} \Delta X \right) \end{aligned}$$

where $M_X (= \rho^* U)$ and $M_Y (= \rho^* V)$ represent non-dimensional mass-fluxes in the X- and Y-directions, respectively. Also, for the DI-LSM, the discretized form of the surface tension term (Eq. 2.4) in the momentum equation (Eq. (2.13)) is given as

$$\begin{aligned} \bar{F}_{U,P}^{ST,n} &= \left(\bar{F}_{U,e}^{ST,n}, \bar{F}_{U,w}^{ST,n} \right) \text{ and} \\ \bar{F}_{V,P}^{ST,n} &= \left(\bar{F}_{V,n}^{ST,n}, \bar{F}_{V,s}^{ST,n} \right) \end{aligned} \quad (2.14)$$

where overbar represents linear interpolation of the surface tension term from neighbouring face-centers. Further, $\bar{F}_{U,P}^{ST,n}$ and $\bar{F}_{V,P}^{ST,n}$ are horizontal and vertical components of the volumetric surface tension force at cell-center ($\bar{F}_{U,P}^{ST,n}$), respectively.

2.2.2 Solution method: Semi-explicit pressure projection method

Semi-explicit method (Sharma, 2016), based on the pressure *projection method*, is considered here as the solution method for the solution of the above algebraic equation, where the mass conservation equation (Eq. 2.12) is implicit while all the terms are considered as explicit for the momentum equation (Eq. 2.13); except the diffusion and pressure terms. The Semi-Explicit projection method involves two-step predictor-corrector approach, involving first a prediction of a cell-center velocity \vec{U}_P^* and then its correction \vec{U}'_P . This leads to the new time level ($n + 1$) velocity $\vec{U}_P^{n+1} = \vec{U}_P^* + \vec{U}'_P$.

For a co-located grid based on the momentum interpolation method, along with the cell-center velocity \vec{U}_P^* , the face-centers normal-velocity also needs the prediction (U_e^* , U_w^* , V_n^* , and V_s^*) and correction (U'_e , U'_w , V'_n , and V'_s). Thus, for both cell-center and face-center velocities, the predictor step and corrector step are presented below in separate subsections for a 2D Cartesian coordinate system; similar to that presented in a CFD book by Sharma (2016) for a single phase flow.

Predictor step

Prediction of the velocity at the Cell-Center:

For the pressure projection method, a predicted velocity \vec{U}_P^* is obtained by ignoring the pressure term from the original proposition in Eq. (2.13); given in a vector form as

$$\rho_P^{*,n} \frac{\vec{U}_P^* - \vec{U}_P^n}{\Delta\tau} \Delta V_P + A_{\vec{U},P}^n = D_{\vec{U},P}^{n+1} + \bar{F}_{\vec{U},P}^{ST,n} \Delta V_P - \frac{1}{Fr^2} \Delta V_P \hat{j} \quad (2.15)$$

Further,

$$\vec{U}_P^* = \vec{U}_P + \frac{\Delta\tau}{\rho_P^{*,n} \Delta V_P} \left(\bar{F}_{\vec{U},P}^{ST,n} \Delta V_P - \frac{1}{Fr^2} \Delta V_P \hat{j} \right) \quad (2.16)$$

where \vec{U}_P is a *provisional* velocity at the cell center P, used for the prediction of the face-center normal-velocities, is given as

$$\vec{U}_P = \vec{U}_P^n + \frac{\Delta\tau}{\rho_P^{*,n}} (D_{\vec{U},P}^{n+1} - A_{\vec{U},P}^n) \quad (2.17)$$

Prediction of normal-velocity at the Face-Centers:

At the east face-center of the 2D Cartesian control volume (Fig. 2.1(b)), the predicted normal-velocity U_e^* in the X-direction is given (similar to Eq. 2.16) as

$$\rho_e^{*,n} \frac{U_e^* - U_e^n}{\Delta\tau} \Delta V_e + A_{U,e}^n = D_{U,e}^{n+1} + \bar{F}_{U,e}^{ST,n} \Delta V_e \quad (2.18)$$

Further,

$$U_e^* = \tilde{U}_e + \frac{\Delta\tau}{\rho_e^{*,n} \Delta V_e} \left(\bar{F}_{U,e}^{ST,n} \Delta V_e \right) \quad \left\{ \tilde{U}_e = U_e^n + \frac{\Delta\tau}{\rho_e^{*,n} \Delta V_e} (D_{U,e}^{n+1} - A_{U,e}^n) \right\} \quad (2.19)$$

where, the *provisional* normal-velocity \tilde{U}_e at the east face center is approximated as

$$\tilde{U}_e \approx \overline{(\tilde{U}_P, \tilde{U}_E)} = 0.5 \times (\tilde{U}_P + \tilde{U}_E) \quad (2.20)$$

where the \tilde{U}_e from a linear interpolation of the neighbouring cell-center provisional-velocities (\tilde{U}_P^* and \tilde{U}_E^*); and the surface tension term at the east face-center $\bar{F}_{U,e}^{ST,n}$ in the Eq. 2.19 is given (from Eq. 2.14) as

$$\bar{F}_{U,e}^{ST,n} = \begin{cases} \frac{1}{W_e} \kappa_e \delta_e(\phi_e) \hat{N}_e \Delta V_e & \text{for DI-LSM} \\ 0 & \text{for SI-LSM} \end{cases} \quad (2.21)$$

Although Eq. (2.19) involves ΔV_e , the volume of the staggered CV at east face-center, it cancels out (refer Eq. (2.19)) and the computation of the ΔV_e is avoided for the present co-located grid. Further, note that the Eq. (2.19) is for the east face-center normal-velocity U_e^* on the staggered grid. However, the above approximation (Eq. 2.20) for \tilde{U}_e nicely avoid the computation of geometric parameters (surface-area and volume) of the staggered CV, which is difficult to implement specially for complex geometric problems on a curvilinear structured and unstructured grid.

For a single-phase flow, Eq. (2.16) reduces to $\vec{U}_P^* = \vec{U}_P$ and Eq. (2.19) to $U_e^* = \overline{(U_P^*, V_E^*)}$ for the projection method. This continued for two-phase flow in the early days of CmFD development on a co-located grid, considering the discretized surface tension term $F_{\vec{U},P}^{ST}$ as a part of the provisional velocity \vec{U}_P along with the advection-diffusion term in Eq. (2.17). This cell-center discretization of the surface tension term is avoided in the above Eq. (2.19) for U_e^* , by defining the provisional velocity \tilde{U}_P without the surface tension term in Eq. (2.16). Thus, the definition of \tilde{U}_P in Eq. (2.17), for the two-phase flow, is same as that for the single phase flow. This ensures that the surface tension term $\bar{F}_{\vec{U},e}^{ST,n}$ is discretized at the east face-center. Thus, the discretization of both surface tension and pressure terms (presented below in Eq. 2.25) at the identical face-center locations avoid the pressure-interfacial force imbalance as in the balanced force method (Francois *et al.*, 2006).

The BFM is not relevant to the present SI-LSM since it does not consider the surface tension term ($\bar{F}_{\vec{U}}^{ST} = 0$) in the momentum equation. Instead, the SI-LSM considered

the surface tension term as an interfacial boundary condition for the continuity equation; its solution method is presented below.

Similar to Eq. (2.19), predicted normal-velocity at the other face-centers (U_w^* , V_n^* , and V_s^*) can be obtained; and the predicted volume source $S_{vol,P}^*$ is given (similar to Eq. 2.12) as

$$S_{vol,P}^* = (U_e^* - U_w^*)\Delta Y + (V_n^* - V_s^*)\Delta X \quad (2.22)$$

Corrector step

Since the above predicted normal-velocity $\vec{U}_{f=e,w,n,s}^*$ does not satisfy the mass conservation, $S_{vol,P}^* \neq 0$ (Eq. 2.22), an equation for velocity correction equation \vec{U}' is obtained by subtracting the above equation for prediction with that for the original proposition.

Correction of velocity at cell-center:

Subtracting Eq. (2.15) from Eq. (2.13), and assuming $D_{U,P}^{n+1} - D_{U,P}^n \approx 0$ (Patankar, 1980), the cell-center velocity correction \vec{U}'_P is given as

$$U'_P = U_P^{n+1} - U_P^* = -\frac{\Delta\tau}{\rho_P^{*,n}} \frac{(P_E^{n+1} - P_W^{n+1})}{2\Delta X}; \quad V'_P = -\frac{\Delta\tau}{\rho_P^{*,n}} \frac{(P_N^{n+1} - P_S^{n+1})}{2\Delta Y} \quad (2.23)$$

Correction of normal-velocity at Face-center:

Similar to the original proposition of cell-center velocity \vec{U}_P^{n+1} (Eq. 2.13), the original proposition for the east face-center normal-velocity U_e^{n+1} is given as

$$\rho_e^{*,n} \frac{U_e^{n+1} - U_e^n}{\Delta\tau} \Delta V_e + A_{U,e}^n = (P_P^{n+1} - P_E^{n+1})\Delta Y + D_{U,e}^{n+1} + \bar{F}_{U,e}^{ST,n} \Delta V_e \quad (2.24)$$

Subtracting the prediction equation (Eq. 2.18) from the above equation, and assuming $D_{U,e}^{n+1} - D_{U,e}^n \approx 0$ (Patankar, 1980), correction equation for the normal-velocity V'_e at the east face-center and similar equations for the other face-centers are given as

$$\begin{aligned} U'_e &= U_e^{n+1} - U_e^* = \beta_e \frac{P_P^{n+1} - P_E^{n+1}}{\delta X_e}; \quad U'_w = \beta_w \frac{P_W^{n+1} - P_P^{n+1}}{\delta X_w} \\ V'_n &= \beta_n \frac{P_P^{n+1} - P_N^{n+1}}{\delta Y_n}; \quad V'_s = \beta_s \frac{P_S^{n+1} - P_P^{n+1}}{\delta Y_s} \end{aligned} \quad (2.25)$$

where $\beta = \Delta\tau/\rho^{*,n}$. Note that ρ^* is the non-dimensional (not predicted) density and is equal to 1 and ρ_2/ρ_1 (Eq. 2.6), for an interior CV in the fluid-1 and fluid-2, respectively; refer Fig. 2.1 for the interior and interfacial CV. This is also true for an interfacial CV in the

SI-LSM while ρ^* varies smoothly in-between 1 and ρ_2/ρ_1 for the interfacial CV in DI-LSM (Eq. 2.8).

Pressure Equation

Algebraic formulation for the pressure involves an algebraic formulation for the volume conservation (Eq. 2.12), where the normal-velocity $U'_{\eta'}$ at the new time-level is given as $U'^{n+1}_{\eta',f} = U^*_{\eta',f} + U'_{\eta',f}$. Substituting the equation for $U'^{n+1}_{\eta',f=e,w,n,s}$ to Eq. (2.12) results in an algebraic form of the volume-conservation equation, involving both predicted and correction normal-velocity; given as

$$(U'_e - U'_w)\Delta Y + (V'_n - V'_s)\Delta X = -[(U^*_e - U^*_w)\Delta Y + (V^*_n - V^*_s)\Delta X] \equiv S_{vol}^* \quad (2.26)$$

For the DI-LSM, substitution of Eq. (2.25) for the normal-velocity correction $U'_{\eta',f}$ of the above equation results in an algebraic formulation for pressure, called pressure equation, as

$$a_P P_P^{n+1} = a_E P_E^{n+1} + a_W P_W^{n+1} + a_N P_N^{n+1} + a_S P_S^{n+1} + b \quad (2.27)$$

where

$$a_E = \frac{\beta_e \Delta S_e}{\delta X_e}, \quad a_W = \frac{\beta_w \Delta S_w}{\delta X_w}, \quad a_N = \frac{\beta_n \Delta S_n}{\delta Y_n}, \quad a_S = \frac{\beta_s \Delta S_s}{\delta Y_s}, \\ \beta = \Delta \tau / \rho^*, \quad a_P = \sum_{NB=E,W,N,S} a_{NB} \text{ and } b = -S_{vol,P}^*$$

Whereas, for the ghost fluid-based SI-LSM, Eq. 2.25 for $U'_{\eta',f}$ consists of a neighbouring (E/W/N/S) cell-center values from the other fluid for an interfacial control volume P (Fig. 2.1(e)-(f))). The involvement of both the fluids cell-center values in the $U'_{\eta',f}$ is avoided in the SI-LSM, by a sub-cell discretization, given for the face-centers of an interfacial CV “ P ” in the fluid-2 (shown in Fig. 2.1(f)) as

$$U'_e = \beta_e \frac{P_{2,P}^{n+1} - P_{2,E}^{n+1}}{\delta X_e}; \quad U'_w = \beta_w \frac{P_{2,\Gamma_w}^{n+1} - P_{2,P}^{n+1}}{\psi_w \delta X_w} \\ V'_n = \beta_n \frac{P_{2,P}^{n+1} - P_{2,N}^{n+1}}{\delta Y_n}; \quad V'_s = \beta_s \frac{P_{2,\Gamma_s}^{n+1} - P_{2,P}^{n+1}}{\psi_s \delta Y_s} \quad (2.28)$$

Similarly, the cell-center velocity correction \vec{U}'_P (Fig. 2.1(f)) for the interfacial CV “ P ” is given as

$$U'_P = \beta_P \frac{(P_{2,E}^{n+1} - P_{2,\Gamma_w}^{n+1})}{(1 + \psi_w) \Delta X} \\ V'_P = \beta_P \frac{(P_{2,N}^{n+1} - P_{2,\Gamma_s}^{n+1})}{(1 + \psi_s) \Delta Y} \quad (2.29)$$

where the pressure P_{2,Γ_w} and P_{2,Γ_s} at the interface Γ are obtained by solving a discretized form of an interfacial jump boundary condition for pressure $[P]_\Gamma$ (Eq. 2.5) and considering the zero normal-velocity correction at face-centers $[U'_{\eta',f}]_\Gamma = 0$. This is presented in detail in a previous work from our research group (Shaikh *et al.*, 2018), which results in the interfacial pressure in Eq. (2.29) as

$$P_{2,\Gamma_w} = \frac{\beta_1 \psi_w P_{1,w} + (1 - \psi_w) \beta_2 P_{2,P} - \beta_1 \psi_w B_w}{(1 - \psi_w) \beta_2 + \psi_w \beta_1}$$

$$P_{2,\Gamma_s} = \frac{\beta_1 \psi_s P_{1,s} + (1 - \psi_s) \beta_2 P_{2,P} - \beta_1 \psi_s B_s}{(1 - \psi_s) \beta_2 + \psi_s \beta_1}$$

Finally, substituting the above equation in Eq. (2.28) and the resulting $\vec{U}'_{\eta',f}$ in Eq. (2.26), Shaikh *et al.* (2018) presented a finite volume method-based *generalized* algebraic formulation that results in a pressure equation for the SI-LSM that is same as above (Eq. 2.27) for the DI-LSM. However, for the SI-LSM the source term b in Eq. (2.27) gets modified (Shaikh *et al.*, 2018) as

$$b = S_{vol,P}^* + m_1 S_{jump,int} \left\{ S_{jump,int} = \sum_{f=e,w,n,s} \Phi_f S_{jump,f} \right\} \quad (2.30)$$

where $S_{jump,int} = S_{jump,w} + S_{jump,s}$, $m_1 = -\frac{\phi_P}{|\phi_P|}$, and Φ_f is a variable for numerical identification with $\Phi_f = 1$ for an interfacial cell and $\Phi_f = 0$ for interior cells; given as

$$\Phi_f = max \left[\left(\frac{-\phi_P \phi_{NB=E,W,N,S}}{|\phi_P \phi_{NB}|} \right), 0 \right]$$

Thus, the source term $S_{jump,f}$ in Eq. (2.30) is given (Shaikh *et al.*, 2018) as

$$S_{jump,f=e,w} = \frac{\hat{\beta}_f B_f \Delta S_f}{\delta X_f} \text{ and } S_{jump,f=n,s} = \frac{\hat{\beta}_f B_f \Delta S_f}{\delta Y_f}$$

where,

$$\hat{\beta}_f = \frac{\beta_1 \beta_2}{\beta_1 (1 - \psi_f) + \beta_2 \psi_f}, \quad \psi_f = \frac{|\phi_P|}{|\phi_P| + |\phi_{NB}|}, \quad B_f = \frac{B_P |\phi_{NB}| + B_{NB} |\phi_P|}{|\phi_P| + |\phi_{NB}|}$$

$$\text{and } B(X, Y) = [P]_\Gamma = \frac{2}{Re_1} [\eta] \hat{N} \cdot (\nabla U \cdot \hat{N}, \nabla V \cdot \hat{N}) + \frac{\kappa}{We} \quad (2.31)$$

Further, for SI-LSM with fluid-1 as the reference fluid, $\beta_1 = \Delta\tau$ and $\beta_2 = (\Delta\tau\rho_1)/\rho_2$. Also, $S_{jump,f}$ term is zero in DI-LSM and non-zero for the SI-LSM; only for those faces of the interfacial cells which are in the other fluid. For example, $S_{jump,e}$ and $S_{jump,n}$ are non-zero and $S_{jump,w}$ and $S_{jump,s}$ are zero for an interfacial cell “P” in fluid-1 (Fig. 2.1(e));

vice-versa, for the cell “ P ” in fluid-2 (Fig. 2.1(f)). Moreover, depending on the fluid in which an interfacial grid point is submerged, the sign of the $S_{jump,f}$ term changes, that is implemented numerically by a variable m_1 in Eq. (2.30); defined as $m_1 = -\phi_P/|\phi_P|$. The above formulation of pressure equation is presented in-detail by Shaikh *et al.* (2018) for the SI-LSM on the staggered grid which is extended here for the SI-LSM on the co-located grid.

Ghost Fluid Method (GFM)-based SI-LSM is presented here for the first time on co-located grid, even though initially proposed on staggered grid (Fedkiw *et al.*, 1999a; Kang *et al.*, 2000). On comparison with staggered grid, along with challenges for single phase flow other challenges need to overcome for multiphase flow on co-located grid. Apart from establishing aforementioned pressure-interfacial force balance while solving pressure Poisson equation the major difference on co-located grid from staggered grid is in velocity correction equation. On a staggered grid, while correcting face-center normal-velocity of the main-CV only adjacent pressure grid points are involved. Whereas on co-located grid, for correcting cell-center velocity of the main-CV alternate pressure grid points are involved. Thus for an interfacial cell, presence of interface is computed only between adjacent pressure grid point towards one and two side of “ P ” grid point at main CV on staggered and co-located grid, respectively. For example, Fig. 2.1(e) shows pressure grid point at cell-center of interior and interfacial cells with interfacial cell in fluid-1 and neighboring grid points—“ E ” and “ N ”—in other fluid. Thus, for correcting cell-center velocity \vec{U}_P interfacial jump boundary condition for pressure is utilized along east and north direction from “ P ” grid point on co-located grid. For the same computational stencil on staggered grid, since correction of velocity are the face-centers of main control volume, similar interfacial jump condition for pressure east and north direction is utilized. Whereas, to generalize the discretization of velocity correction equation, since alternate and adjacent pressure grid points are involved on co-located and staggered grid, respectively, the sub-domain (Ω_1 or Ω_2) of alternate grid points with respect to main grid point need to be evaluated on co-located grid whereas only between adjacent pressure grid points on staggered grid.

For both DI-LSM and SI-LSM on the co-located grid, non-dimensional time step is chosen based on a criterion (Shaikh *et al.*, 2018) that is given as

$$\Delta\tau = 0.025 \min(\Delta\tau_{CFL}, \Delta\tau_{CAP}, \Delta\tau_{GFN})$$

where $\Delta\tau_{CFL}$, $\Delta\tau_{CAP}$, and $\Delta\tau_{GFN}$ are the time step due to CFL, capillary, and grid Fourier number conditions.

2.2.3 Solution algorithm

Solution algorithm, which is unified for the DI-LSM and SI-LSM on a co-located grid, is as follows:

1. Define computational domain by specifying the Cartesian domain size ($L \times H$) and the uniform grid size (ΔX and ΔY).
2. Define the initial interface configuration, utilizing the level set function ϕ and calculate geometric properties (\hat{N} and κ) of the interface.
3. Initialize fluid properties (ρ^* and μ^*) and flow properties (\vec{U} and P) in the computational domain.
4. Apply the required boundary conditions for the flow properties and the level set function ϕ .
5. Calculate the Heaviside function $H(\phi)$, using Eq. (2.8) for the DI-LSM and Eq. (2.9) for the SI-LSM.
6. Using the Heaviside function $H(\phi)$, determine the thermo-physical properties of the two fluid (Eqs. 2.6 and 2.7) in the computational domain.
7. Predict the cell-center velocity \vec{U}_P^* , after computing the advection and diffusion term along with $\bar{F}_{\vec{U}}^{ST}$, for the DI-LSM (Eq. 2.16).
8. Predict the face-center normal-velocity $U_{\eta',f}^*$ at all the faces of the control volume; presented for the east face in Eq. (2.19).
9. Solve the pressure poisson equation, Eq. (2.27), iteratively as discussed in the previous section; with a modified “ b ” term for the interfacial CVs in the SI-LSM.
10. Compute the cell-center velocity correction \vec{U}'_P (Eq. 2.23) and add it with \vec{U}_P^* (obtained in the step 7), resulting in the velocity field for the new time level \vec{U}_P^{n+1} .
11. Advect the interface by solving level set advection equation, Eq. (2.2), using the velocity field \vec{U}_P^{n+1} .
12. Solve the reinitialization equation, Eq. (2.11).
13. Check for the unsteady stopping criterion of the CmFD simulation. If satisfied, terminate the simulation or else go to step 4.

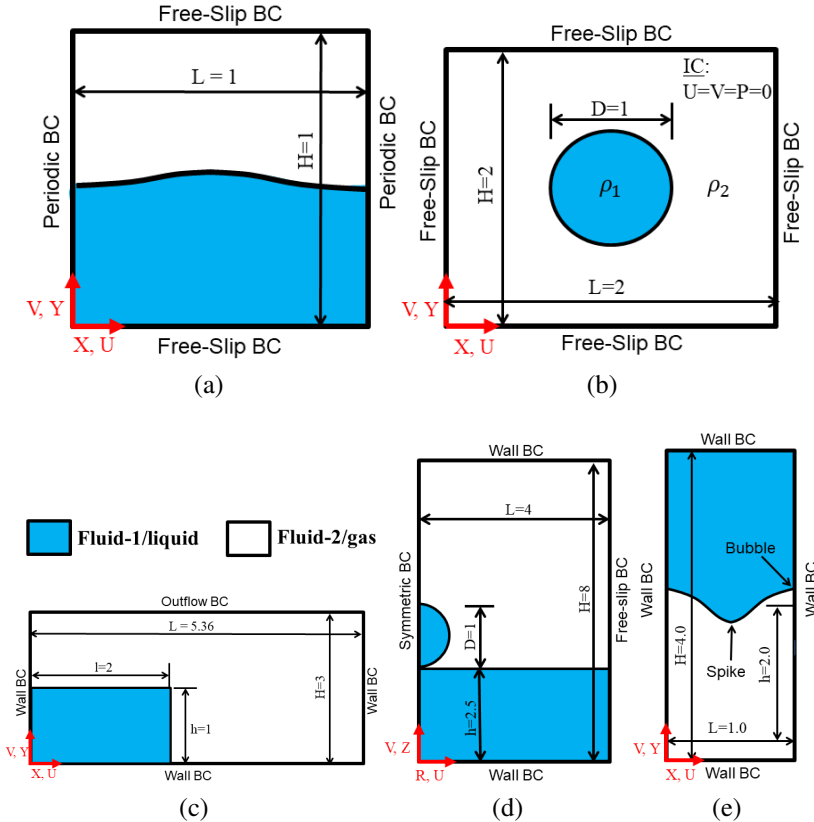


Figure 2.2: Computational setup of the sufficiently different CmFD problems: (a) capillary wave, (b) static droplet, (c) dam break, (d) droplet coalescence, and (e) Rayleigh-Taylor instability; considered for the present validation and performance study.

2.3 Validation and Performance Study for the BFM-based DI-LSM and GFM-based SI-LSM on a Co-located Grid

In this section, sufficiently different CmFD problems such as static droplet (Young-Laplace law), dam break (gravity dominant), droplet coalescence (surface tension dominant), and Rayleigh-Taylor instability (buoyancy driven) are simulated by the present GFM-based SI-LSM and BFM-based DI-LSM on the co-located grid system. The results obtained, for the various CmFD problems, are presented in a validation and performance study. Also, order of convergence study (of the SI-LSM and DI-LSM) are presented for a capillary wave problem. For the five CmFD problems considered here, the computational setup is shown in Fig. 2.2.

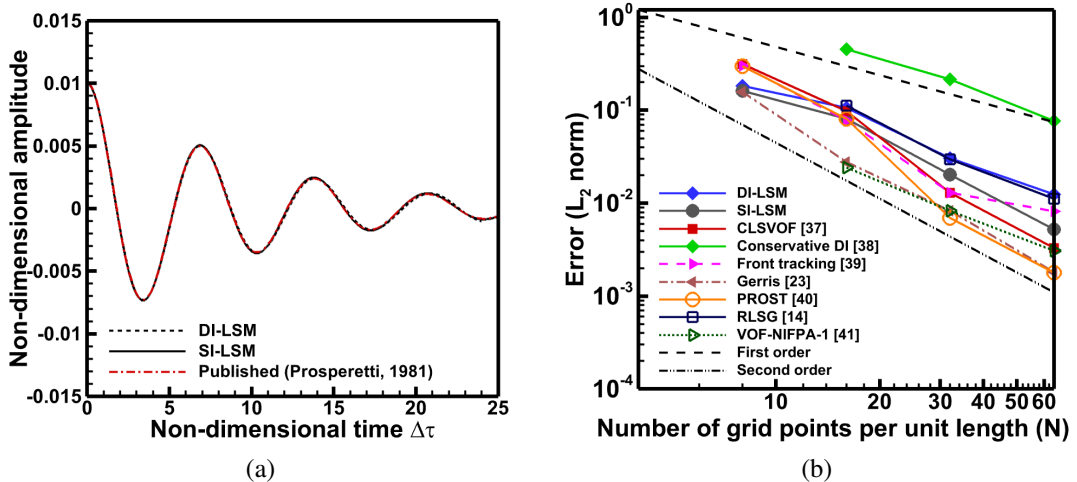


Figure 2.3: (a) Computation of the present LSMs with the analytical solution (Prosperetti, 1981) for the temporal variation of non-dimensional amplitude simulated with grid size of 64×64 and (b) L_2 norm of the error-based order of accuracy study for the present LSMs along with that reported for various multiphase solvers.

2.3.1 Capillary wave

For a problem on decaying oscillations of a Capillary wave that has an analytical solution; presented by Prosperetti (1981), order of accuracy study is widely reported for the various numerical methods in CmFD. The problem corresponds to a sinusoidal perturbed interface between initially static fluid, with $\chi = 1$ and $\eta = 1$, which results in a time-wise varying amplitude of the interface-oscillation around its equilibrium position; where, χ and η denotes density ratio and viscosity ratio, respectively with fluid-1 being the reference fluid. Figure 2.2(a) shows the present non-dimensional computational set-up, similar to that presented by Gerlach *et al.* (2006), where the wavelength λ of the wave is considered as the length scale l_c and the inverse of oscillation frequency ($1/\omega_0$) is the time scale t_c .

Figure 2.3(a) shows an excellent agreement of the present SI-LSM as well as DI-LSM with the analytical solution for the time-wise variation in the amplitude of the oscillating wave. After the validation study, order of accuracy study is done by computing the L_2 norm of the error of the time-wise variation of the non-dimensional amplitude as compared to the analytical solution (Prosperetti, 1981); obtained on various uniform grid size. The order of accuracy study is shown in Fig. 2.3(b), for the present LSMs as compared to the other multiphase solvers—coupled level-set volume-of-fluid (CLSVOF) (Gerlach *et al.*, 2006), conservative diffuse-interface (Mirjalili *et al.*, 2020), front tracking (Popinet and Zaleski, 1999), Gerris flow solver (Popinet, 2009), parabolic reconstruction of surface tension for the volume-of-fluid (PROST) (Renardy and Renardy, 2002), bal-

anced force refined level set grid (RLSG) (Herrmann, 2008) and non-intersecting flux polyhedron advection-VOF advection scheme (VOF-NIFPA-1) (Ivey and Moin, 2017). The figure shows that the order of accuracy of the present LSMs is in-between first and second order, which is similar to that seen for the other multiphase solver in the literatures; except by Gerris (Popinet, 2009), PROST (Renardy and Renardy, 2002), and CLSVOF (Gerlach *et al.*, 2006), which are seen as second order accurate. Note from the figure that the present error for DI-LSM almost overlaps with that reported for the DI-based RLSG method by (Herrmann, 2008). Also note from the figure that the accuracy of the present LSMs, on various grid sizes, lies in-between that for the various CmFD methods in the literature.

2.3.2 Static Droplet

Static droplet is a classical test case, for the various CmFD methodologies, to evaluate the *pressure-interfacial force balance*. A series of test cases on the static droplet is presented below in separate subsections, which are adapted from a detailed study by Francois *et al.* (2006) for the VOF method. Whilst their results on various errors were presented for a particular time-instance, a temporal variation of the errors are also presented in this study.

For a suspended static drop under equilibrium, the exact difference in pressure between the fluid inside the drop and the surrounding fluid is given as

$$\Delta p_{exact} = p_1 - p_2 = \sigma \kappa_{exact} \quad (2.32)$$

where subscript 'exact', 1, and 2 corresponds to the analytical solution, fluid-1, and fluid-2, respectively. Further, p is the dimensional pressure and κ_{exact} is the dimensional exact-curvature. For a circular interface of radius r , solved in 2D Cartesian coordinate, κ_{exact} is given as

$$\kappa_{exact} = \frac{1}{r} \quad (2.33)$$

Ideally, while simulating this test case, a CmFD methodology should maintain the initial circular configuration, by establishing exact balance between the forces due to pressure and surface tension, and should not lead to spurious current near the interface. This is tested for the present SI-LSM and DI-LSM on a co-located grid, utilizing the computational set-up of Francois *et al.* (2006) *in dimensional units*. This is shown in Fig. 2.2(b), where a drop with radius $r = 2$ is placed at the center of the 2D Cartesian domain of size 8×8 . The thermo-physical properties of the fluid are density of fluid-1 $\rho_1 = 1$, density of fluid-2 $\rho_2 = 1 - 10^{-5}$, and surface tension coefficient $\sigma = 73$. The drop is considered as

inviscid unless specified. The exact pressure jump across the drop is 36.5 for the present computational set-up. Further, the present flow field is initialized with zero values and free-slip boundary condition is used on the boundary of the computational domain (Fig. 2.2(b)). Although various grid size of 20×20 , 40×40 , 80×80 and 160×160 are considered, unless specified, a grid size of 40×40 is used for all the simulations with a capillary time step criterion as

$$(\Delta t)_{crit} = \sqrt{\frac{0.5(\rho_1 + \rho_2)\Delta x^3}{2\pi\sigma}}$$

The present LSMs-based jump in pressure is computed in two different ways as follows:

$$\begin{aligned}\Delta p_{total} &= p_{av,1} - p_{av,2} \\ \Delta p_{max} &= p_{max} - p_{min}\end{aligned}\tag{2.34}$$

Thereafter, for the above pressure jumps, the relative error $E(\Delta p)_{total/max}$ is computed as

$$E(\Delta p)_{total/max} = \frac{|\Delta p_{total/max} - \Delta p_{exact}|}{\Delta p_{exact}}\tag{2.35}$$

For the error in velocity, we employ L_∞ norm as follows

$$E(\vec{u}_{max}) = |\vec{u}|_{max} = max(|\vec{u}|)\tag{2.36}$$

where Δp_{total} is the difference in average pressure between fluid-1 and fluid-2, Δp_{max} is the difference in maximum and minimum pressure (p_{max} and p_{min}) in the computational domain, and $E(\vec{u}_{max})$ is the magnitude of maximum spurious current that is desired to be zero. Note that all the values, presented in this subsection, are dimensional.

DI-LSM and SI-LSM with exact curvature

In this section, using the exact curvature $\kappa_{exact} = 0.5$, our DI-LSM is tested for the coupling between the surface tension force and pressure gradient, while the SI-LSM is tested for pressure-interfacial force balance. The time step, grid size, and convergence tolerance for the pressure Poisson iterative loop are 10^{-6} , 40×40 , and 10^{-12} , respectively.

Table 2.1 shows a comparison of the various errors for the present DI-LSM and SI-LSM. As the density ratio ρ_1/ρ_2 increases from 1 to 10^5 , the table shows that the maximum spurious current-based $|\vec{u}|_{max}$ increases from $O(10^{-6})$ to $O(10^{-3})$ for the DI-LSM and from $O(10^{-17})$ to $O(10^{-11})$ for the SI-LSM. Further, the error $E(\Delta p_{total})$ for the DI-LSM is $O(10^{-2})$ while it is much smaller $O(10^{-13})$ for the SI-LSM. Similar larger reduction in $E(\Delta p_{max}) = O(10^{-11})$ for the SI-LSM is seen in the table as compared to $O(10^{-3})$ for the DI-LSM. Thus, by comparing various Δp -based errors and maximum spurious currents

Table 2.1: For the static droplet problem comparison of errors for the spurious current and pressure-jump across the interface for the present DI-LSM and SI-LSM. The results are obtained for an inviscid static droplet with $r=2$ placed at the center of computational domain of size 8×8 with *exact curvature* specified. The simulations are performed on a grid 40×40 ($r/h = 10$ or $h = 0.2$), time step $\Delta t = 10^{-6}$ and convergence tolerance as 10^{-12} for pressure. The values are taken after one time-step and all values are dimensional.

LSM	ρ_1/ρ_2	$E(\vec{u}_{max}) = \vec{u} _{max}$	$E(\Delta p_{total})$	$E(\Delta p_{max})$
DI-LSM	1	2.66×10^{-6}	4.21×10^{-2}	1.24×10^{-2}
	10^3	3.74×10^{-4}	4.35×10^{-2}	6.57×10^{-3}
	10^5	1.11×10^{-3}	4.41×10^{-2}	3.56×10^{-3}
SI-LSM	1	7.97×10^{-17}	9.39×10^{-14}	1.29×10^{-11}
	10^3	1.99×10^{-13}	1.00×10^{-13}	2.64×10^{-11}
	10^5	1.99×10^{-11}	1.00×10^{-13}	2.64×10^{-11}

for various density ratios, the table shows that the accuracy of the SI-LSM is better as compared to that for the DI-LSM.

Figure 2.4 shows a scatter plot of the pressure distribution, for the DI-LSM and SI-LSM at various density ratios. The figure shows a gradual and sudden variation of pressure during the pressure jump, across the diffuse and sharp interface, for the DI-LSM and SI-LSM, respectively. The difference is due to the difference in the surface tension models—CSF model and SSF model for the respective LSMs. Moreover, the density ratio does not seem to have an appreciable effect on the accuracy of the pressure-jump since no appreciable change is noticed with increasing ρ_1/ρ_2 , for both the LSMs; also demonstrated quantitatively by the errors ($E(\Delta p)_{total}$ and $E(\Delta p_{max})$) in Table 2.1. Further, SI-LSM retains the expected pressure jump across the interface. Whereas, for the error in spurious current, Table 2.1 shows the $E(\vec{u}_{max})$ depends on both surface tension model and density ratio, with a reasonable increase in the $E(\vec{U}_{max})$ with increasing ρ_1/ρ_2 .

Figure 2.5 shows a surface plot for the pressure distribution after 1000 time steps, with spikes in pressure near the interface for DI-LSM. Further, with increasing ρ_1/ρ_2 , the figure shows an increase in the spikes for DI-LSM while SI-LSM reproduces almost same sharp-jump in the pressure. For this exact curvature case, probably the spikes (or oscillation) in pressure near the interface for DI-LSM could be attributed to the Dirac delta-based formulation of surface tension model. This is because, using gradient in volume fraction instead of Dirac Delta, no such spikes are seen in the work of Francois *et al.* (2006). Further, since the present SI-LSM does not involve Dirac delta, no such spikes are seen here for the SI-LSM on co-located grid. Interestingly, for SI-LSM on staggered grid, Dirac delta-base formulation does not result in such spikes in pressure but

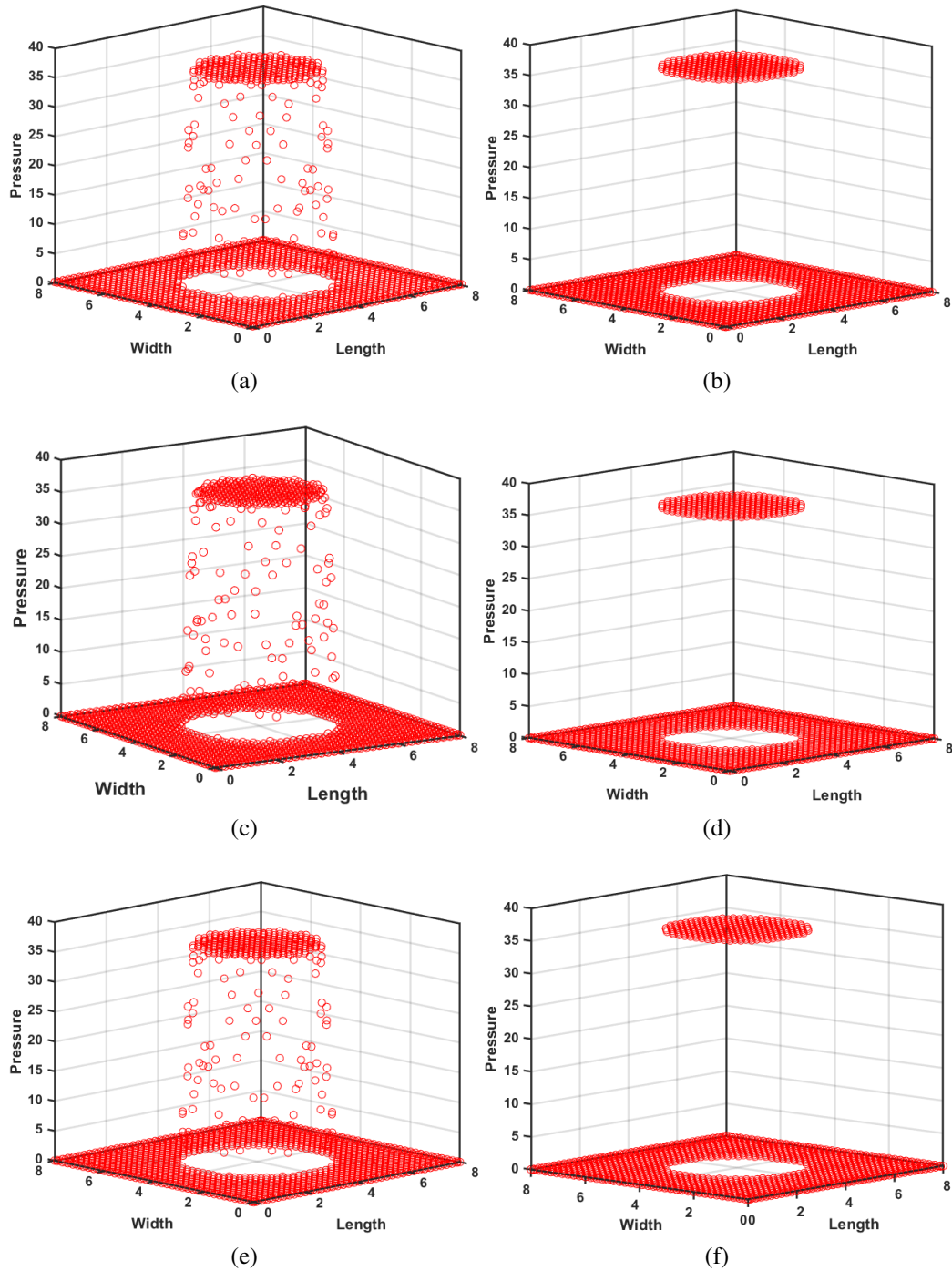


Figure 2.4: Comparison of computed pressure field for (a, c, e) DI-LSM and (b, d, f) SI-LSM at density ratio ρ_1/ρ_2 of (a, b) 1, (c,d) 10^3 , and (e,f) 10^5 , for an inviscid static droplet of radius $r=2$ placed at the center of computational domain of size 8×8 with *exact curvature* κ_{exact} specified. The simulations are performed on a grid 40×40 ($r/h = 10$ or $h = 0.2$), time step $\Delta t = 10^{-6}$, and convergence tolerance 10^{-12} for pressure. Results are plotted after one time-step and all values are dimensional.

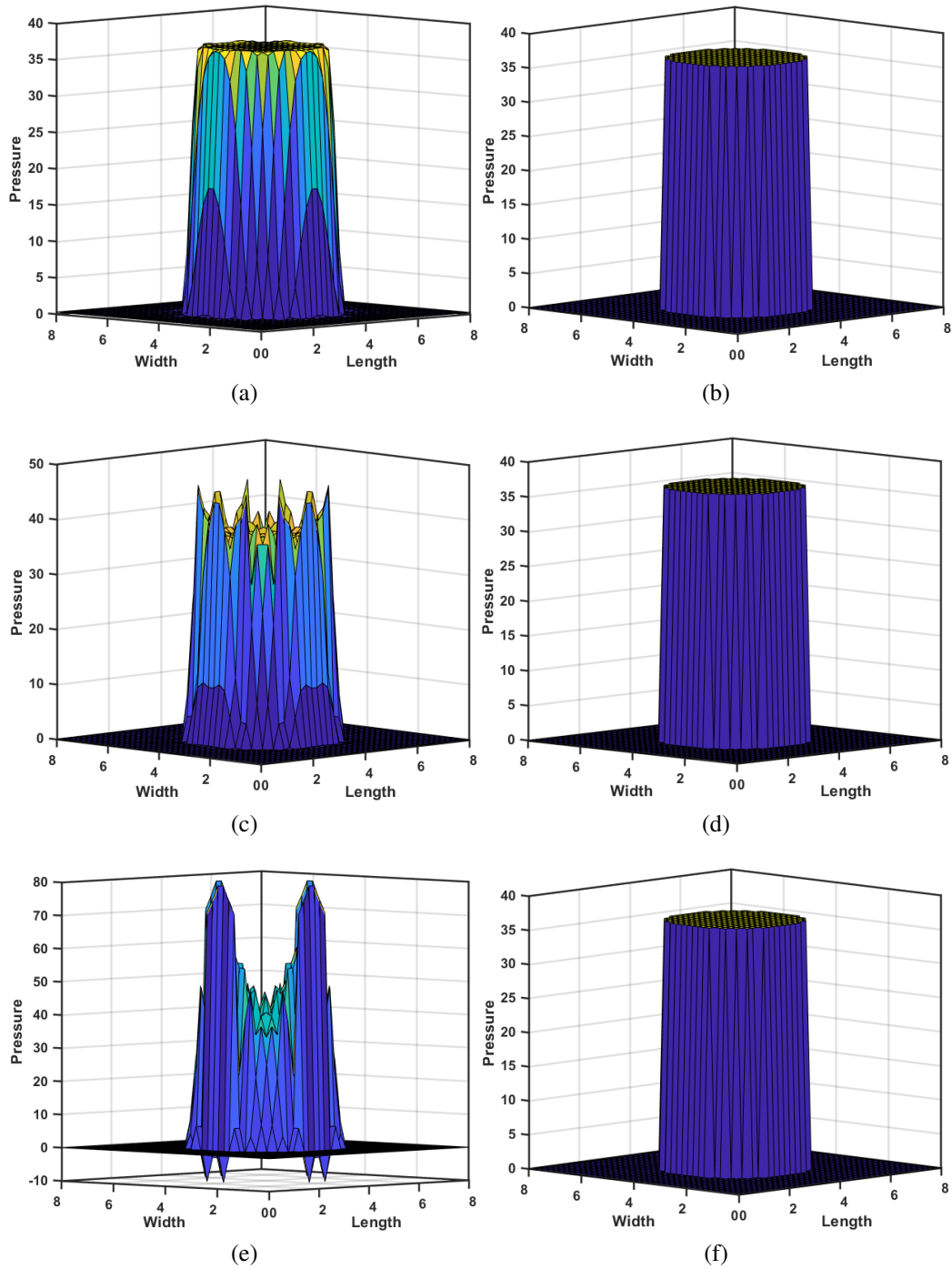


Figure 2.5: Comparison of computed pressure field (a, c, e) DI-LSM and (b, d, f) SI-LSM at density ratio ρ_1/ρ_2 of (a, b) 1, (c, d) 10^3 , and (e, f) 10^5 , for an inviscid static droplet of radius $r=2$ placed at the center of computational domain of size 8×8 with *exact curvature* κ_{exact} specified. The simulations are performed on a grid 40×40 ($r/h = 10$ or $h = 0.2$), time step $\Delta t = 10^{-6}$, and convergence tolerance 10^{-12} for pressure. Results are plotted after 1000 time-step and all values are dimensional.

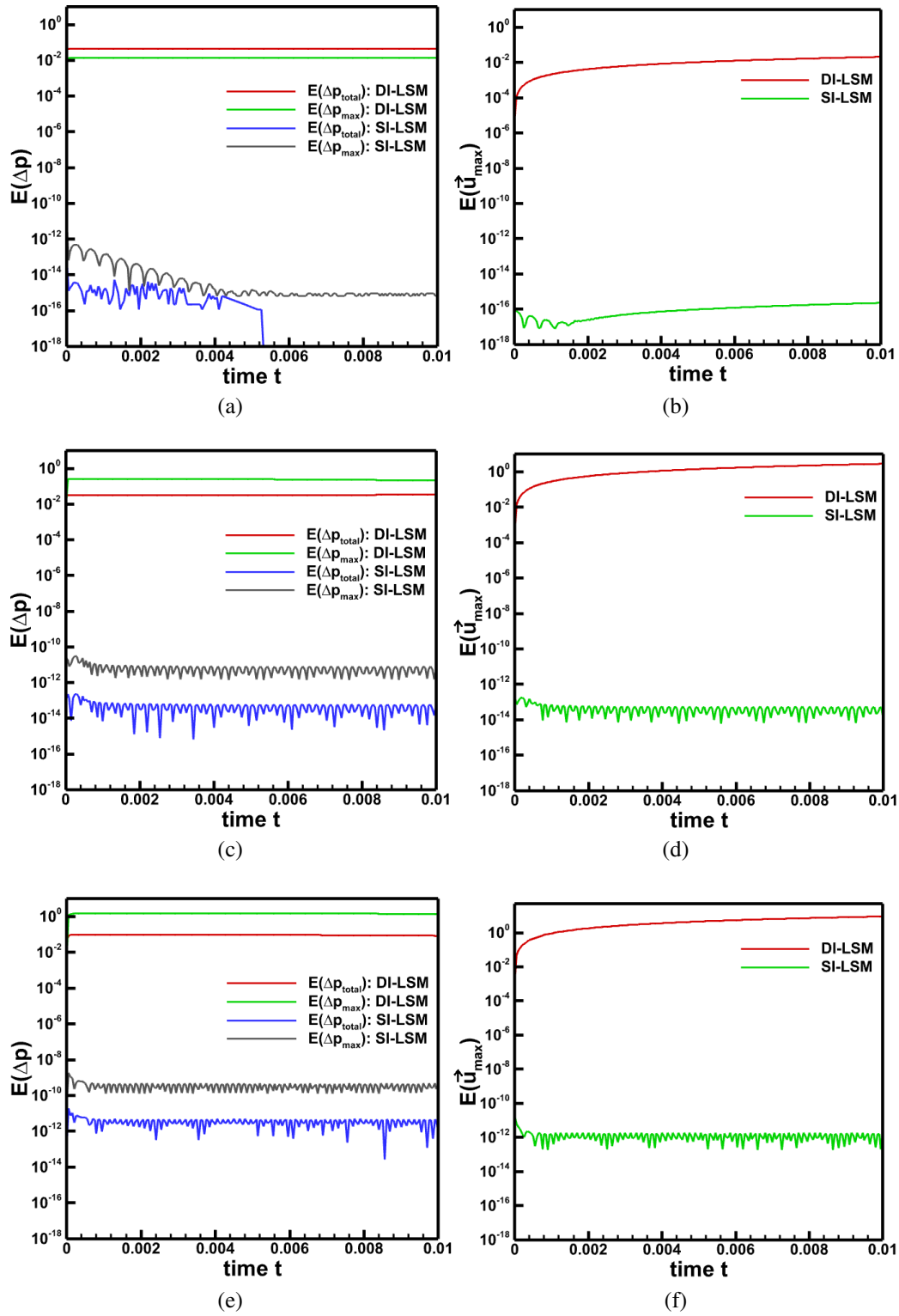


Figure 2.6: For exact curvature κ_{exact} case, time-wise variation of the error in (a, c, e) pressure $E(\Delta P)$ and (b, d, f) maximum magnitude of spurious currents $E(\vec{U}_{max})$ at density ratio ρ_1/ρ_2 of (a, b) 1, (c, d) 10^3 , and (e,f) 10^5 . Computational set-up is similar to Fig. 2.4 and 2.5.

Table 2.2: For the static droplet problem, comparison of errors for the spurious current and pressure-jump across the interface for the present DI-LSM and SI-LSM. The results are obtained for an inviscid static droplet with $r=2$ placed at the center of computational domain of size 8×8 with *computed* curvature κ_{comp} . The simulations are performed on a grid 40×40 ($r/h = 10$ or $h = 0.2$), time step $\Delta t = 10^{-6}$ and convergence tolerance as 10^{-12} for pressure. The values are taken after one step and all values are dimensional.

LSM	ρ_1/ρ_2	$E(\vec{u}_{max}) = \vec{u} _{max}$	$E(\Delta p_{tot})$	$E(\Delta p_{max})$
DI-LSM	1	2.69×10^{-6}	4.19×10^{-2}	1.46×10^{-2}
	10^3	3.32×10^{-4}	4.34×10^{-2}	9.37×10^{-3}
	10^5	9.67×10^{-4}	4.39×10^{-2}	6.70×10^{-3}
SI-LSM	1	1.43×10^{-7}	2.39×10^{-3}	4.45×10^{-3}
	10^3	2.29×10^{-7}	2.42×10^{-3}	4.60×10^{-3}
	10^5	2.29×10^{-7}	2.42×10^{-3}	4.60×10^{-3}

results in increased magnitude of spurious current (Shaikh *et al.*, 2018). Similar to the above results for one time-instant, the time-wise variation in Fig. 2.6 shows a substantially smaller error for the SI-LSM as compared to the DI-LSM for various time-instants. However, it can also be seen that the temporal variation of the various errors is slightly fluctuating for the SI-LSM while it is smooth and time-wise invariant Δp -based errors for the DI-LSM. Moreover, the time-wise evolution of spurious currents in Fig. 2.6 shows an increasing trend with the DI-LSM as compared to almost constant spurious velocity field of SI-LSM. This generation of spurious currents as simulation progress could be attributed to the usage of Dirac Delta function in the DI-LSM which also causes spikes in pressure near the interface, discussed above. Recent studies (Abu-Al-Saud *et al.*, 2018; Popinet, 2018) shows that within DI-LSM, a well-balanced surface tension model can converge spurious currents to machine zero. The increasing maximum magnitude of spurious current with time as well as with density ratio for present DI-LSM on a co-located grid indicates scope for future work on well-balanced surface tension model; instead of present Dirac delta-based formulation.

DI-LSM and SI-LSM with computed curvature

As compared to the previous subsection with exact curvature ($\kappa_{exact} = 0.5$), this subsection presents the relative performance study for the curvature κ_{comp} that is computed from the level set function ϕ (Eq. 2.10). The problem set-up is similar to that discussed in the previous subsection.

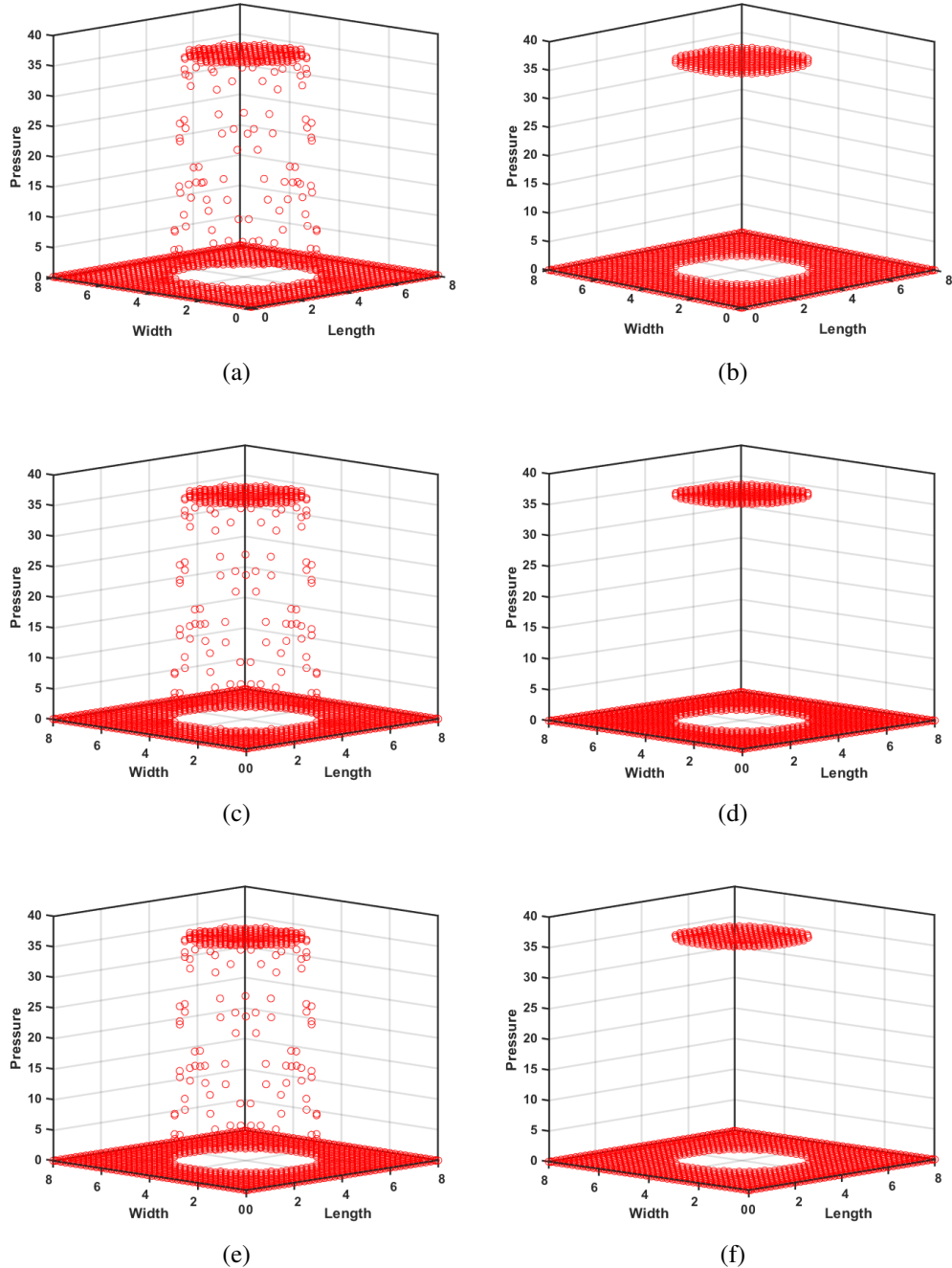


Figure 2.7: Comparison of computed pressure field for a) DI-LSM ($\chi = 1$), b) SI-LSM ($\chi = 1$), c) DI-LSM ($\chi = 10^3$), d) SI-LSM ($\chi = 10^3$), e) DI-LSM ($\chi = 10^5$), and f) SI-LSM ($\chi = 10^5$) for an inviscid static droplet with $r=2$ placed at the center of computational domain of size 8×8 with *computed curvature* κ_{comp} . The simulations are performed with $\chi = 1$ on a grid 40×40 ($r/h = 10$ or $h = 0.2$), time step $\Delta t = 10^{-6}$ and pressure convergence tolerance 10^{-12} . Results are plotted after one time-step and all values are dimensional.

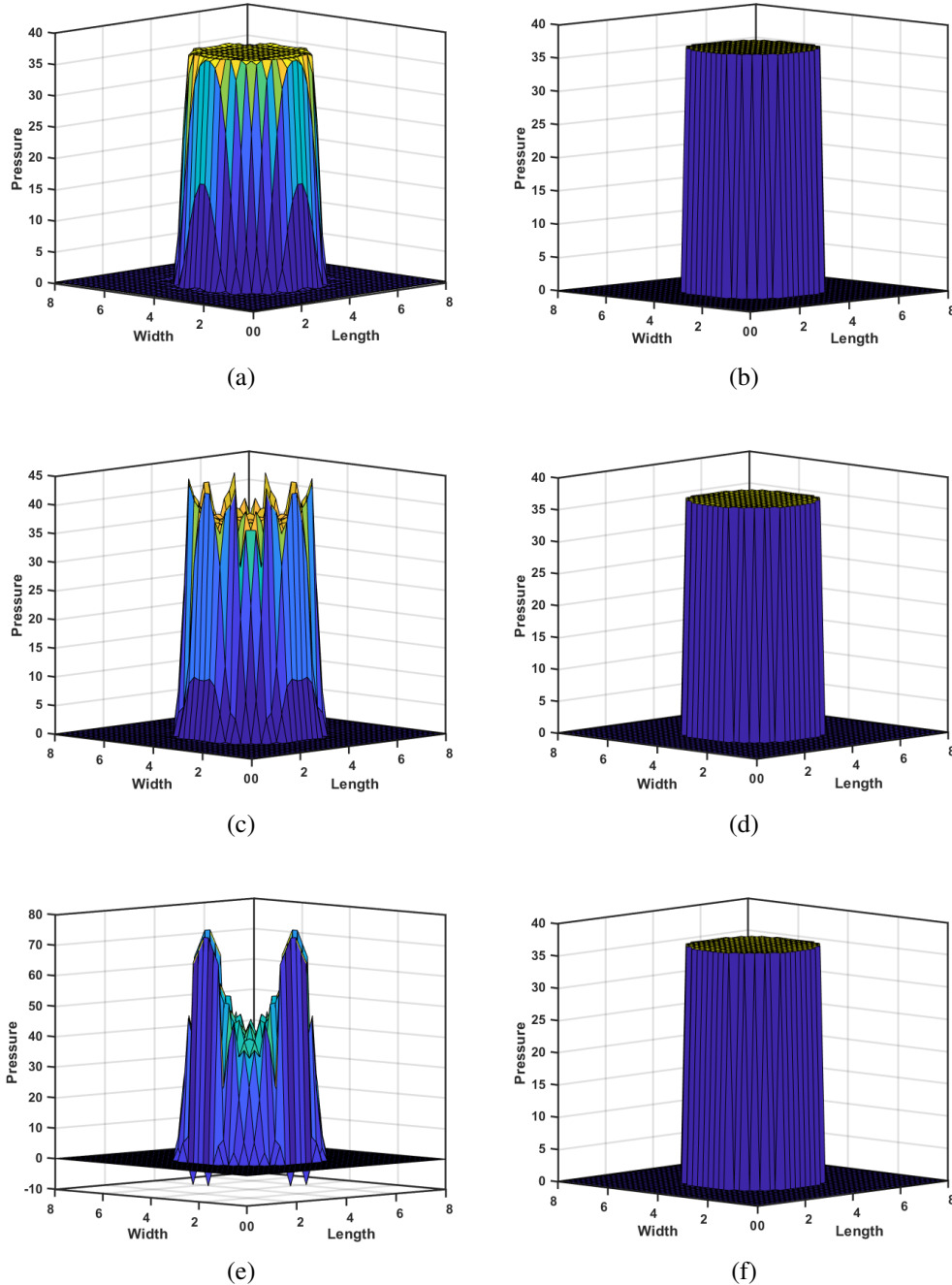


Figure 2.8: Comparison of computed pressure field for a) DI-LSM ($\chi = 1$), b) SI-LSM ($\chi = 1$), c) DI-LSM ($\chi = 10^3$), d) SI-LSM ($\chi = 10^3$), e) DI-LSM ($\chi = 10^5$), and f) SI-LSM ($\chi = 10^5$) for an inviscid static droplet with $r=2$ placed at the center of computational domain of size 8×8 with *computed curvature* κ_{comp} . The simulations are performed with $\chi = 1$ on a grid 40×40 ($r/h = 10$ or $h = 0.2$), time step $\Delta t = 10^{-6}$ and pressure convergence tolerance 10^{-12} . Results are plotted after 1000 time-step and all values are dimensional.

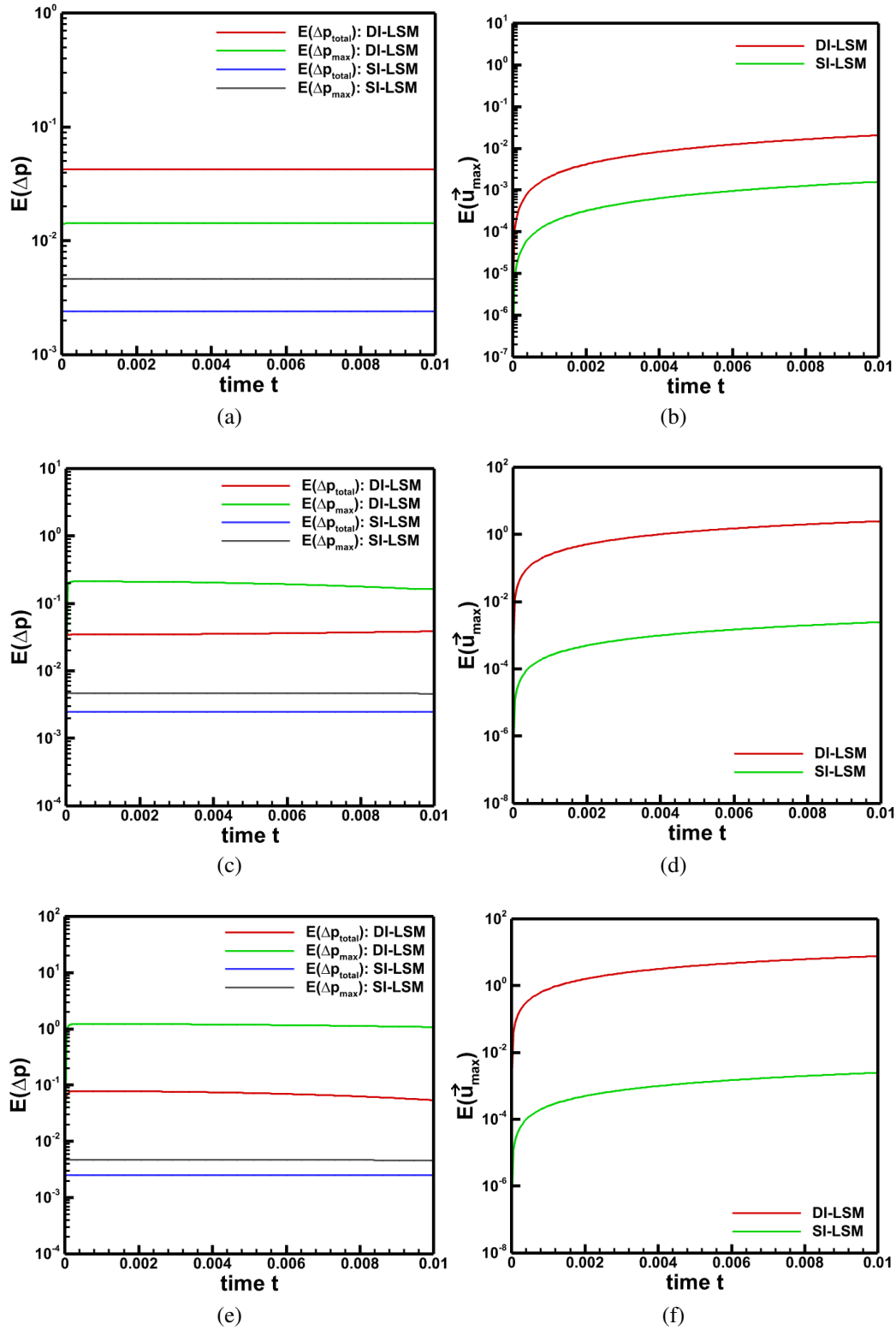


Figure 2.9: For computed curvature κ_{comp} case, time-wise variation of the error in (a, c, e) pressure $E(\Delta P)$ and (b, d, f) maximum magnitude of spurious currents $E(\vec{U}_{max})$ at density ratio ρ_1/ρ_2 of (a, b) 1, (c, d) 10^3 , and (e,f) 10^5 . Computational set-up is similar to Fig. 2.7 and 2.8.

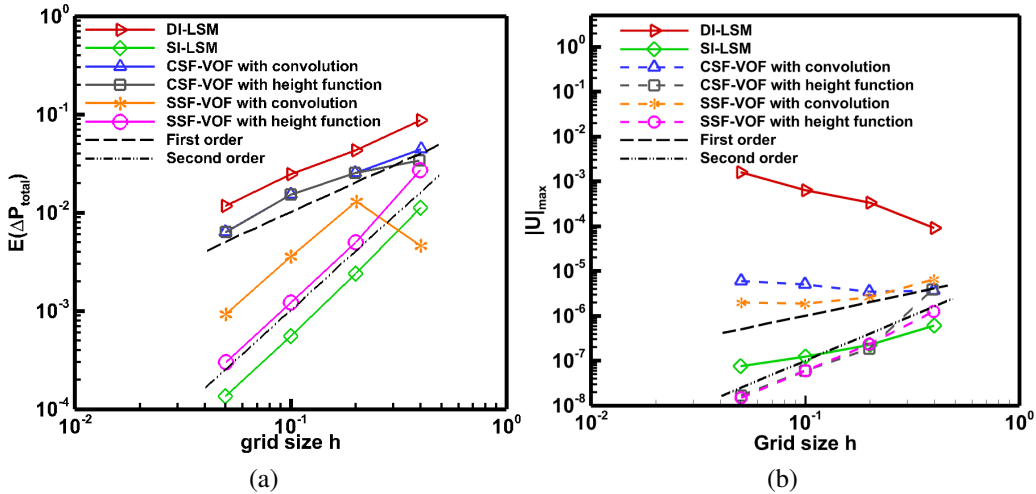


Figure 2.10: Variation in (a) error in ΔP_{tot} and (b) maximum magnitude of spurious current with grid size for the present CSF model-based DI-LSM and SSF model-based SI-LSM as compared to the CSF and SSF models-based VOF methods with various curvature estimations (Francois *et al.*, 2006). An inviscid static droplet with $r = 2$ at the center of computational domain 8×8 is simulated with κ_{comp} . The density ratio $\chi = 10^3$, time step $\Delta t = 10^{-6}$ and pressure tolerance 10^{-12} . All the values are taken after one time-step and dimensional.

After one time step, similar to Table 2.1 for the κ_{exact} , Table 2.2 for the κ_{comp} shows the various errors. It is interesting to notice that the various errors are of almost same order of magnitude for the DI-LSM in both the table while, for the SI-LSM, the errors increases in the range of four to ten orders of magnitude under the effect of the computed curvature κ_{comp} . Inspite of this, with κ_{comp} , the errors in Table 2.2 are smaller for the SI-LSM as compared that for the DI-LSM as in Table 2.1 for the κ_{exact} . Similar results are reported by Francois *et al.* (2006) for the SSF and CSF models-based VOF methods. Thus, the computed curvature κ_{comp} diminishes the superiority (in terms of the smallness in the errors of the SSF model as compared to the CSF model). For SI-LSM, note from Table 2.1 that the maximum spurious current $E(\vec{U}_{\max})$ varies with the density ratio for κ_{exact} but not for κ_{comp} (Table 2.2). Whereas, $E(\Delta p)$ is almost constant with the density ratio for both κ_{exact} and κ_{comp} cases.

Similar to Figs. 2.4 and 2.5 for κ_{exact} , Fig. 2.7 shows a scatter plot and Fig. 2.8 shows a surface plot for the pressure field with the κ_{comp} . Near the interface, the pressure fields after 1 time-step in Figs. 2.4 and 2.7 shows a gradual variation. Whereas, the field after 1000 time-steps in Figs. 2.5 and 2.8 shows spikes; and sharp or sudden variation, of the pressure near the interface, for the DI-LSM and SI-LSM, respectively.

Thus, the computed curvature does not affect the nature of pressure jump across the interface for both CSF and SSF models-based level-set and VOF methods but leads

to a larger error for SSF models-based methods for the κ_{comp} as compared to κ_{exact} . An improved curvature model can reduce this increased error for the present SI-LSM.

After presenting the above results after 1 and 1000 time-steps, for various density ratios Fig. 2.9 shows that the time-wise variation of error is almost constant for $E(\Delta P)$ and increases asymptotically for the maximum spurious current $E(\vec{U}_{max})$. For the SI-LSM, it is interesting to notice the smooth variation of both the types of errors for the κ_{comp} case (Fig. 2.9) as compared to the oscillating-errors, around almost constant value, for the κ_{exact} case (Fig. 2.6). Further, as compared to Fig. 2.6(b), 2.6(d), and 2.6(e) which shows an increase in time-wise evolution of spurious current for DI-LSM only for the *constant* curvature. Figure 2.9 (b,d,f) shows similar trend for both DI-LSM and SI-LSM with *computed* curvature. Thus there is a scope for future on the improvement of curvature model for the SI-LSM. Finally, for the κ_{comp} case with the results after one time-step, the effect of mesh convergence on the various errors for the DI-LSM and SI-LSM is studied. This is shown in Fig. 2.10, for various grid size $\Delta x = \Delta y = h = 0.4, 0.2, 0.1$, and 0.05. The figure also shows the variation in the various error reported by (Francois *et al.*, 2006) for the CSF and SSF models-based VOF method; with the same grid sizes h and the same computational setup. Their results were reported for various curvature estimation techniques like convolution and height function while Eq. (2.10) is used for curvature estimation in the present LSMs.

Figure 2.10(a) shows that the order of convergence of the error $E(\Delta p_{total})$ on the pressure jump is smaller for the present SI-LSM while that for the present DI-LSM is larger as compared to the errors for the various VOF methods (Francois *et al.*, 2006). Further, the figure shows that the DI-LSM and the CSF model-based VOF methods exhibit first-order convergence while the present SI-LSM and the SSF model-based VOF methods exhibit second-order convergence for the pressure jump. Whereas, for the maximum magnitude of spurious currents, 2.10(b) shows no convergence with *diffuse* approaches in the present DI-LSM and the CSF-VOF method with convolution (Francois *et al.*, 2006). Whereas, for the sharp approaches, the figure shows almost first-order convergence for both SI-LSM and SSF-VOF approach with convolution while the SSF-VOF approach with height function exhibit a second-order convergence.

Effect of fluid properties and integration time step with computed curvature

In this subsection with κ_{comp} , Fig. 2.11 shows the effect of thermo-physical properties (σ , μ_1/μ_2 , μ_1 , and ρ_1) and the time-step Δt on the various errors after one time-step. The figure shows almost no effect of the thermo-physical properties and time-step on the various errors; except for the error $E(\vec{U}_{max})$, on the spurious velocity, under the effect of

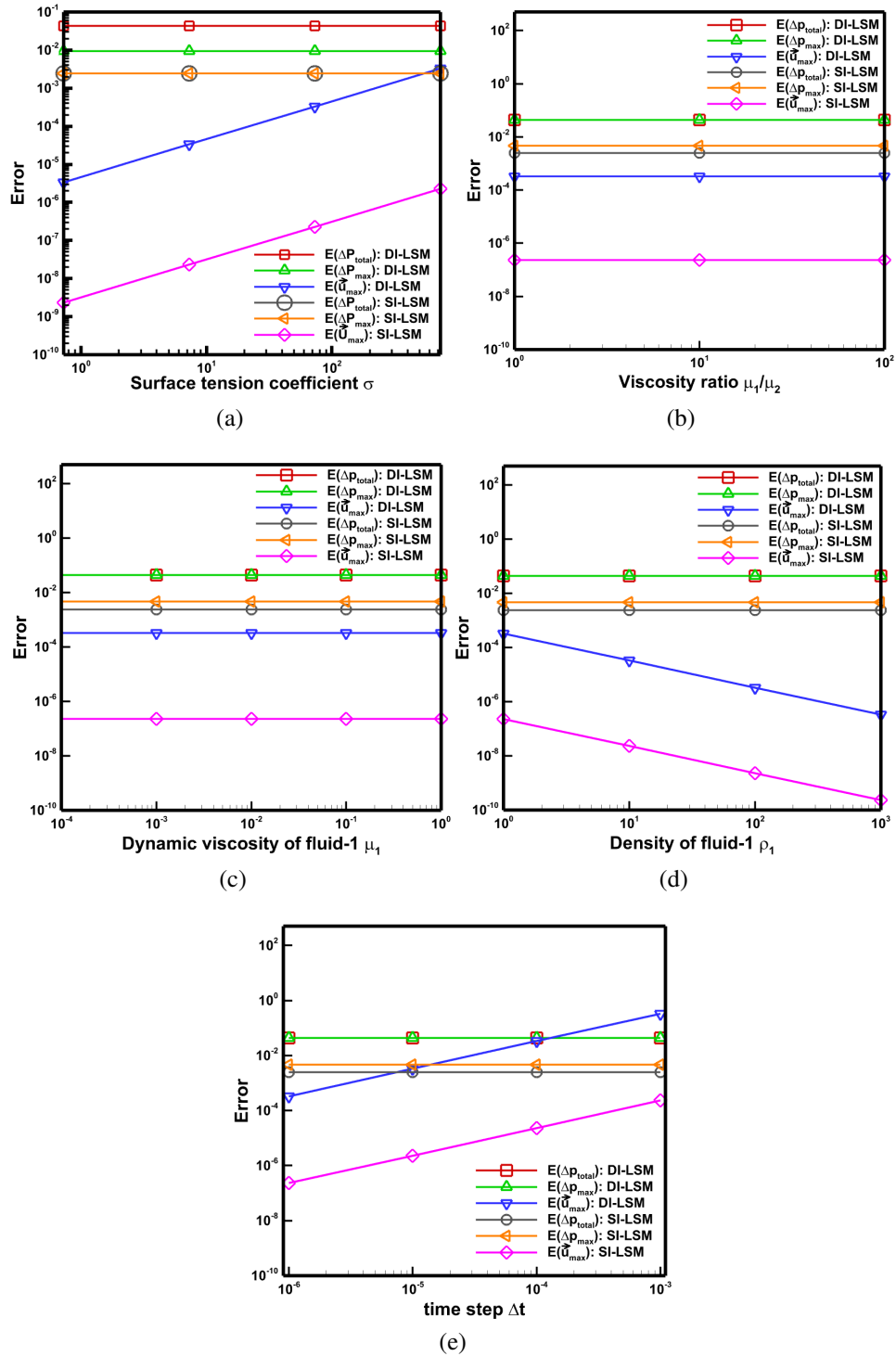


Figure 2.11: Effect of various thermo-physical properties a) surface tension coefficient σ , b) viscosity ratio μ_1/μ_2 , c) dynamic viscosity of fluid μ_1 , d) density of fluid-1 ρ_1 , and e) time-step Δt on errors for total pressure $E(\Delta p_{total})$, maximum pressure $E(\Delta p_{max})$, and maximum velocity $E(\vec{U}_{max})$. Results are plotted after one time-step and all values are dimensional.

σ , ρ_1 , and Δt . The figure also shows that the $E(\vec{U}_{max})$ increases with increasing surface tension coefficient σ and time-step Δt while it decreases with increasing density ρ_1 of

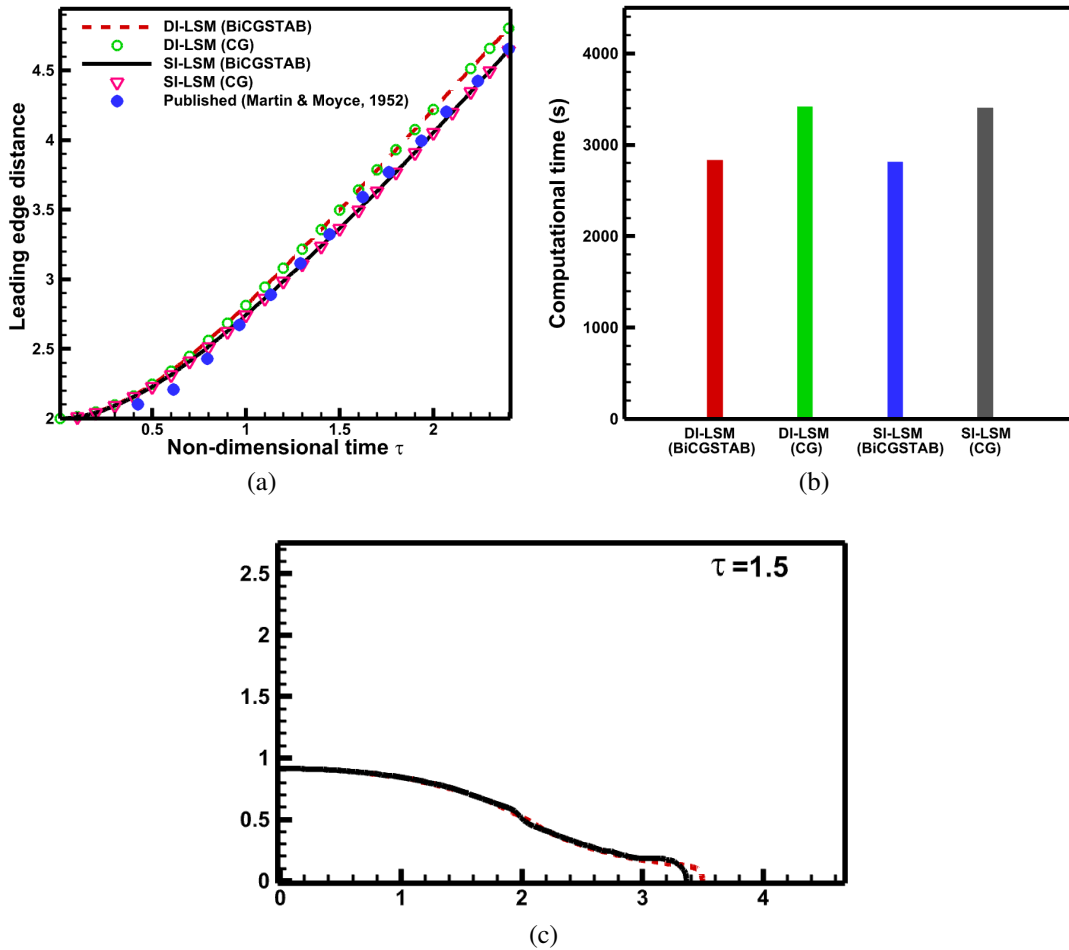


Figure 2.12: Comparison of the (a) present LSM-based results and published experimental results (Martin and Moyce, 1952), for the temporal variation of leading edge distance (of the interface at the bottom wall) for a water column and (b) instantaneous interface obtained from the present DI-LSM (dashed line) and SI-LSM (solid line) at a non-dimensional time $\tau = 1.5$, and (c) computational time taken till $\tau = 2.4$ on grid size of 144×80 . For each LSMs, the results are presented for Conjugate Gradient (CG) and BiCGSTAB solvers for the pressure Poisson equation.

the fluid-1. However, note from the figure that the errors for the SI-LSM is smaller than that for the DI-LSM. Similar results was reported by Francois *et al.* (2006) for the VOF method. Thus, for both VOF and LSM, spurious current is directly proportional to surface tension and time-step; and inversely proportional to ρ_1 .

2.3.3 Dam break simulation

In this widely used gravity dominated test-problem for CmFD development, an initially static rectangular water column is allowed to collapse under gravity. The present computational setup, shown in Fig. 2.2(c), is similar to the experimental set-up of Martin and Moyce (1952), with the size of the water column and the computational domain as

$l \times h$ and $L \times H$, respectively. Considering initial height h of the water column as length scale l_c , and $\sqrt{gl_c}$ as velocity scale u_c , various non-dimensional thermo-physical properties are density ratio (ρ_2/ρ_1) = 1.27×10^{-3} , viscosity ratio (μ_2/μ_1) = 1.56×10^{-2} , Weber number (We) = 1.35×10^5 , Reynolds number (Re_1) = 2.75×10^6 , and Froude number (Fr) = 1. The simulation is performed for a grid size of 144×80 and non-dimensional time-step $\Delta\tau = 10^{-3}$. Finally, to account for the evolution of interface near the boundary, a zero gradient boundary condition is utilized for level set function which corresponds to 90° contact angle of the interface with the south and west walls.

Figure 2.12(a) shows an excellent agreement between the results obtained by the present LSMs and the published experimental results, for the time-wise variation of the leading edge distance, with a maximum error of 5.37% for the SI-LSM and 6.54% for the DI-LSM; as compared to the experimental results. Further, as expected, Fig. 2.12(a) shows almost same results by the two different pressure Poisson solvers—Biconjugate Gradient Stabilized (BiCGSTAB) and Conjugate Gradient (CG). Also, for comparison of computational performance Fig. 2.12(b) shows that the computational time taken by BiCGSTAB is 17% smaller than that by CG solver. However, for a particular pressure solver, the figure shows almost same computational time by the present DI-LSM and SI-LSM. Further, for a comparison between the present SI-LSM and DI-LSM Fig. 2.12(c) shows almost same instantaneous interface; except near the bottom wall.

2.3.4 Droplet coalescence over a horizontal pool

For this surface tension dominant CmFD problem, an ethanol droplet of initial diameter D , placed over an initially stagnant ethanol, pool of height $2.5D$ (in Fig. 2.2(d)), undergoes coalescence over a horizontal interface. For both SI-LSM and DI-LSM note that this problem is solved in an *axisymmetric* coordinate system, as compared to the Cartesian coordinates for the above problems. Considering the diameter D as the length scale l_c and capillary velocity ($\sqrt{\sigma/\rho_1 l_c}$) as the velocity scale u_c , non-dimensional parameters are $\chi = 0.0636$, $\eta = 0.0476$, $We = 1$, $Re_1 = 128.52$, and $Fr = 1.57$. The present problem is simulated on a computational domain of size $4D \times 8D$, shown in Fig. 2.2(d), using a grid size of 120×240 and a non-dimensional time step $\Delta\tau = 10^{-4}$.

Figure 2.13(a) shows an excellent agreement between the present SI-LSM-based and published experiment (Blanchette and Bigioni, 2006) results, for the temporal variation of non-dimensional height H of the droplet. As compared to the experiment result by Blanchette and Bigioni (2006), the maximum error for $H(\tau)$ is 1.94% for the SI-LSM and 6.54% for the DI-LSM. For computational time, similar to dam break problem, Fig. 2.13(b) shows almost same computational time by the present DI-LSM and SI-LSM and a

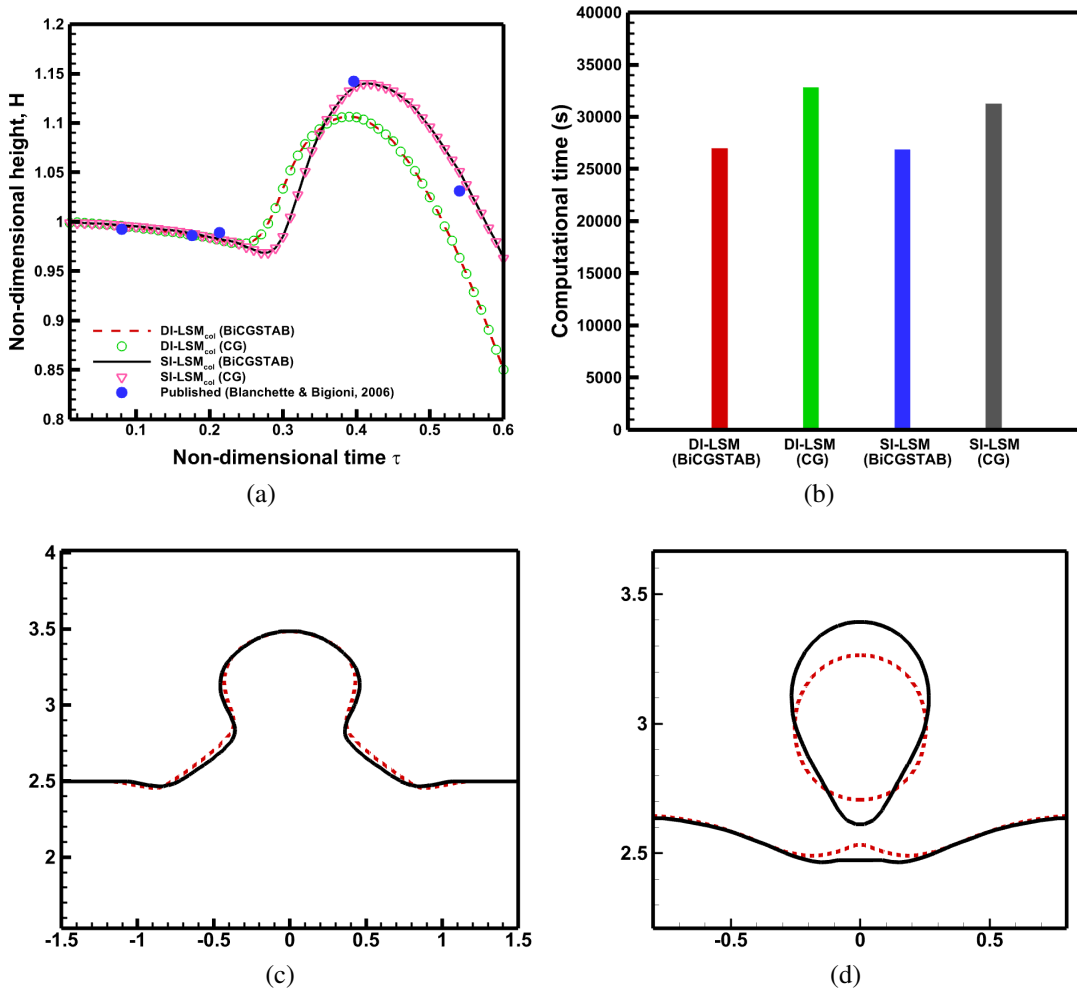


Figure 2.13: For droplet coalescence, a) temporal variation of non-dimensional height H of the top of the droplet, obtained from the two different pressure solvers for present LSMs and a published experimental result (Blanchette and Bigioni, 2006) and b) computational time taken till $\tau = 0.6$ on grid size of 120×240 . Further, instantaneous interface obtained from the present DI-LSM (dashed line) and SI-LSM (solid line), c) during the initial stage of coalescence ($\tau = 0.2$) and d) after the formation of secondary droplet ($\tau = 0.64$).

18% (14%) reduction in the time for BiCGSTAB as compared to CG solver for DI-LSM (SI-LSM). Further, for a comparison between the present results based on the SI-LSM and DI-LSM instantaneous interfaces in Fig. 2.13(c) shows a good agreement between the instantaneous interface during the early stage of coalescence; and after the formation of secondary droplet (not shown here). Whereas, once secondary droplet is formed, Fig. 2.13(d) shows a difference in the instantaneous interfaces predicted by the SI-LSM and DI-LSM. The remarkable differences, with a much more accurate result by the SI-LSM, for this problem (as compared to the other problems presented here) is due to the fact that the droplet coalescence involves a more stronger dominance of the surface tension force.

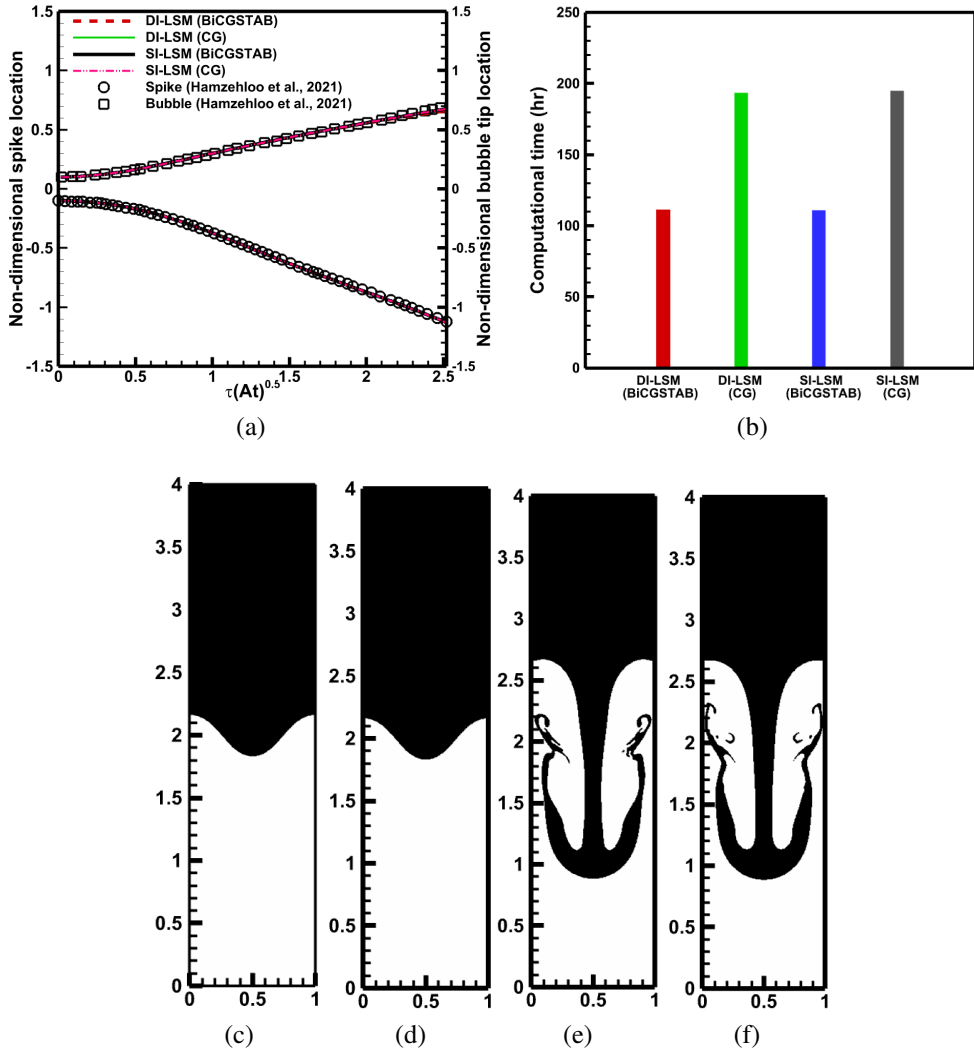


Figure 2.14: For Rayleigh-Taylor, a) temporal variation of non-dimensional spike and bubble location, obtained from the present LSMs and a published numerical result (Huang *et al.*, 2020) and b) computational time taken till $\tau\sqrt{At}=2.5$ on a grid size of 150×600 . Further, instantaneous interface obtained at $\tau\sqrt{At} = 0.5$ and 2.5 with (c,e) DI-LSM and (d,f) SI-LSM are shown for BiCGSTAB. Similar results are obtained with CG.

Thus, the relative accuracy study for this problem clearly demonstrates the superiority of the interfacial jump condition-based surface tension model in the SI-LSM.

2.3.5 Rayleigh-Taylor instability

For this buoyancy driven CmFD problem, heavier fluid is kept over lighter fluid (separated with an initially perturbed interface) that results in an interpenetration of both fluids due to instability. Both the present LSMs are solved on a 2D Cartesian coordinate system for this problem, and Fig. 2.2(e) shows the present computational set-up on a computational domain $L \times H$. The initially perturbed interface is defined as,

$$Y_0 = h + A \cos(k) \quad (2.37)$$

where $h (= 2)$, $A (= 0.1)$, and $k (= 2\pi X)$ are the initial mean position of perturbed interface, non-dimensional amplitude, and wave number. Considering L as length scale l_c and $\sqrt{gl_c}$ as velocity scale u_c , non-dimensional parameters are $\chi = 0.333$, $\eta = 1$, $Re_1 = 3000$, $Fr = 1$, and Atwood number $At = 0.5$. The present problem is simulated on computational domain of size 1×4 using a grid size of 150×600 , and a non-dimensional time step $\Delta\tau = 10^{-4}$.

Figure 2.14(a) shows an excellent agreement between the present LSMs and published numerical results, for the time-wise variation in bubble (spike), with a maximum error of 2.94%(3.35%) for SI-LSM and 3.36%(5.67%) for DI-LSM. For computational time, Fig. 2.14(b) shows a similar results as discussed above for dam break (Fig. 2.12b) and droplet coalescences (Fig. 2.13b) problem, with a 42% reduction in computational time by BiSCGSTAB as compared to that for CG solver. Further, for comparison of present LSMs, Fig. 2.14 (c,d) show almost same interface during initial stage of simulation for DI-LSM and SI-LSM. Whereas, a small difference in the instant interface could be observed towards the later stages of simulation in Fig. 2.14 (e,f) for the DI-LSM and SI-LSM.

2.4 Closure

In this chapter, GFM-based SI-LSM, referred as SI-LSM_{col} and BFM-based DI-LSM, referred as DI-LSM_{col}, in-house CmFD codes are developed. The present unified formulation enhanced and differentiated understanding of conventional BFM and GFM on co-located grid system. Further, the present BFM-based numerical methodology establish uniformity with conventional numerical methodology utilized for single-phase solution on co-located grid. Moreover, the ability of present GFM-based SI-LSM to handle CmFD problems are established utilizing various CmFD benchmark test cases.

Chapter 3

On Comparison of Staggered and Co-located Grid-based Diffuse and Sharp Interface Level Set Method

3.1 Introduction

For interface capturing methods, the basic frameworks for the discrete grid points, for the flow variables, in CFD/CmFD are the staggered and co-located grid system. In the early days of CFD, the progress with the obviously chosen co-located grid halted due to an improper discretization-based pressure-velocity decoupling (Sharma, 2016), with first remedy was an alternate grid system, called staggered grid, and another remedy more than a decade later was an alternate interpolation, called momentum interpolation method (MIM) (Rhie and Chow, 1983). The MIM was not sufficient enough for CmFD on a co-located grid, especially for high density ratios; and the CmFD, as compared CFD, continued on a staggered grid for more than two decades.

At high density ratios, MIM-based CMFD codes diverged due to deformations of the interface as a result of spurious currents or velocity fields generated near the interface. The main cause was identified (Francois *et al.*, 2006) as improper discretization-based imbalance between two surface forces: pressure and interfacial forces, called here as pressure-interfacial force imbalance. This was overcome by a balanced force method (BFM), where the interfacial forces are evaluated at the faces of the control volume Francois *et al.* (2006). The above discussed MIM-based and BFM-based CmFD was for a diffuse interface level set method (DI-LSM). However, for a more realistic sharp interface level set method (SI-LSM), the MIM is sufficient enough as presented in chapter 2. In the SI-LSM, the interfacial force is formulated as an interfacial boundary condition while

solving the Pressure Poisson equation (Kang *et al.*, 2000; Liu *et al.*, 2000). This formulation automatically ensures balance between the interfacial force and pressure force by considering the interfacial forces as surface force at the interface. Hence the BFM for the pressure-interfacial force balance is not required in the SI-LSM. However, for a DI-LSM on a co-located grid, the surface tension forces are considered as a body force on the diffuse interface that requires BFM for discretizing the interfacial forces at the faces of the control volume. Thus for CMFD on a co-located grid, SI-LSM requires MIM only while DI-LSM needs both MIM and BFM. Although both DI-LSM and SI-LSM have been compared previously on a staggered grid (Shaikh *et al.*, 2018), there are no studies showing the comparison of numerical methodology and computational performance for various multiphase problems of DI-LSM versus SI-LSM on a staggered versus co-located grid. This is the objective of the present work, considering the four possible combinations—Diffuse Interface Level Set Method on Staggered grid (DI-LSM_{stag}), Diffuse Interface Level Set Method on Co-located grid (DI-LSM_{col}), Sharp Interface Level Set Method on Staggered grid (SI-LSM_{stag}) and Sharp Interface Level Set Method on Co-located grid (SI-LSM_{col}).

3.2 Mathematical formulation

This section presents a mathematical formulation that is based on a *whole-domain* and a *sub-domain* conservation law for the DI-LSM and SI-LSM, respectively, shown in Fig 3.1. Thus, the conservation equations presented here will be applicable to *both* the fluids in the whole computational domain for the DI-LSM while that for the SI-LSM is applicable to *individual* fluid-based sub-domains.

The sub-domain approach in the SI-LSM requires an additional boundary condition for pressure-jump that balances with the force due to surface tension at the interface. Such interfacial boundary condition is not required in the DI-LSM since the interfacial tension is modelled as a volumetric body force, using the CSF model (Brackbill *et al.*, 1992). Note that the SI-LSM models the force due to surface tension as a more realistic sharp surface force (SSF) while the DI-LSM approximates it as the CSF model-based volumetric force that is diffused over a finite (but small) thickness of the diffused-interface. Further, over the diffused-interface in the DI-LSM, the thermo-physical properties is also diffused by smoothening its sharp change across the realistic sharp-interface; which is not the case for the SI-LSM.

Although the SI-LSM uses the individual fluid-based sub-domain approach, a *single-field formulation* leads to a single-set of conservation equation applicable to both the fluids in the SI-LSM; similar to that in the DI-LSM. This section presents the single field

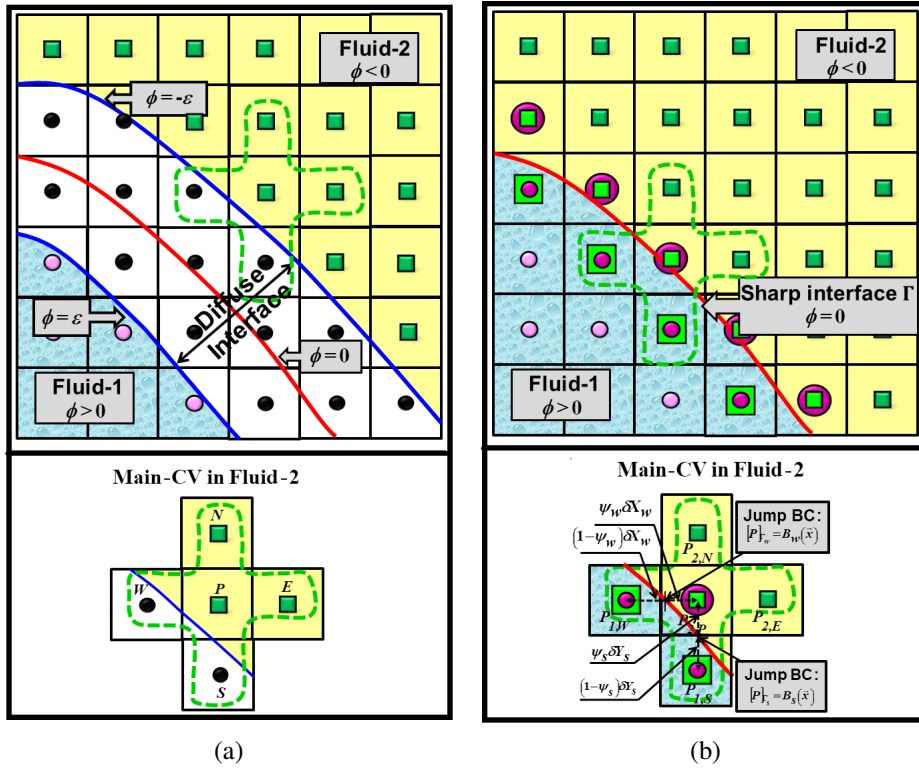


Figure 3.1: Schematic representation of interface treatment for (a) DI-LSM ($-\epsilon \leq \phi \leq \epsilon$) with a diffused interface of thickness ϵ and (b) SI-LSM $\Gamma(\phi = 0)$ with an interface of zero thickness utilized on both staggered and co-located grid.

mathematical formulation for both DI and SI approaches, and the next section presents a numerical methodology for each approach on the staggered as well as co-located grid system.

3.2.1 Conservation equations

For both DI-LSM and SI-LSM on the staggered as well as co-located grid, instead of solving the conservation equations for each fluid separately, the single-field formulation-based *single set* of non-dimensional form of conservation equations are solved, throughout the computational domain, by considering a level set function ϕ -based Heaviside function $H(\phi)$; presented below. The level set function ϕ is used for the two-fluid-interface representation, with $\phi = 0$ as the interface along with a change in the *sign* of ϕ across the interface.

The present formulation assume both the fluids as incompressible, the interface as thin, massless and no-slip, and a constant surface tension coefficient over the interface. Here, the continuity and level set advection equations are presented as volume and mass conservation equations, respectively. This is based on a conservation law-based deriva-

tion—proposed by Gada and Sharma (2009a), using their physical interpretation of the Heaviside H_ϵ and a Dirac delta function δ_ϵ .

Volume Conservation Law-based Continuity Equation:

$$\nabla \cdot \vec{U} = 0 \quad (3.1)$$

Mass Conservation Law-based Level Set Advection Equation:

$$\frac{\partial \phi}{\partial \tau} + \vec{U}_a \cdot \nabla \phi = 0 \quad (3.2)$$

where \vec{U}_a is the bulk velocity, for advecting the level set function ϕ -based interface, obtained by solving momentum equation shown below.

Momentum Equation:

For the DI-LSM

$$\frac{\partial(\rho^* \vec{U})}{\partial \tau} + \nabla \cdot (\rho^* \vec{U} \vec{U}) = -\nabla P + \frac{1}{Re_1} \nabla \cdot (2\mu^* D) - \frac{\rho^*}{Fr^2} \hat{j} + \frac{1}{We} \kappa \hat{N} \delta_\epsilon(\phi) \quad (3.3)$$

For the SI-LSM

$$\frac{\partial(\rho^* \vec{U})}{\partial \tau} + \nabla \cdot (\rho^* \vec{U} \vec{U}) = -\nabla P + \frac{1}{Re_1} \nabla \cdot (2\rho^* D) - \frac{\rho^*}{Fr^2} \hat{j} \quad (3.4)$$

where the *difference* in above equations, for the DI-LSM and SI-LSM, corresponds to the treatment of the surface tension term. Equation (3.3) shows $\kappa \hat{N} \delta_\epsilon(\phi)/We$ as the non-dimensional surface tension force, modelled by as a diffused body force in the DI-LSM by the CSF model (Brackbill *et al.*, 1992). Whereas, for the SI-LSM, the surface tension is not considered in Eq. (3.4); Instead, it is represented as the SSF model-based interfacial boundary condition (Shaikh *et al.*, 2018) for a jump in pressure, which is balanced by a jump of normal viscous stress and interfacial stress; given as

$$[P] = \frac{2}{Re_1} [\eta] \hat{N} \cdot (\nabla U \cdot \hat{N}, \nabla V \cdot \hat{N}) + \frac{\kappa}{We} \quad (3.5)$$

Considering l_c as length scale, u_c as velocity scale, and t_c as time scale, the resulting non-dimensional variables in the above equations are given as

$$\vec{X} = \frac{\vec{x}}{l_c}; \tau = \frac{tu_c}{l_c}; \vec{U} = \frac{\vec{u}}{u_c}; P = \frac{p}{\rho_1 u_c^2}$$

$$We = \frac{\rho_1 u_c^2 l_c}{\sigma}; Re = \frac{\rho_1 l_c u_c}{\mu_1}; Fr = \frac{u_c}{\sqrt{gl_c}}$$

where $\vec{x}, \vec{u}, t, p, g$ and σ represents dimensional Cartesian-coordinate, velocity, time, pressure, acceleration due to gravity, and surface tension coefficient, respectively. Further, We is Weber number, Re is Reynolds number, and Fr is Froude number—the non-dimensional governing parameters for the CmFD.

3.2.2 Subsidiary Equation

Apart from the above conservation equations, the LSM requires a reinitialization equation (Sussman *et al.*, 1994) to re-establish the advected level set function ϕ as the normal distance function; given (Sussman *et al.*, 1994) as

Reinitialization Equation:

$$\frac{\partial \phi}{\partial \tau_s} = S_\epsilon(\phi_0)(1 - |\nabla \phi|) \quad (3.6)$$

where $\tau_s (= \Delta x / 10)$ is pseudo time step and $S_\epsilon (= \phi_0 / \sqrt{\phi_0^2 + \Delta x^2})$ is a smoothed sign function.

3.2.3 Thermo-physical properties

Apart from the above presented difference on modelling of surface tension for the DI-LSM and SI-LSM, further difference exist in the treatment of thermo-physical properties—implemented more realistically as the sharp change across the sharp interface in the SI-LSM while the property variation is smoothed, across the diffused interface, in the DI-LSM; given as

$$\rho^* = H(\phi) + \frac{\rho_2}{\rho_1}(1 - H(\phi)); \mu^* = H(\phi) + \frac{\mu_2}{\mu_1}(1 - H(\phi)) \quad (3.7)$$

where, considering the fluid-1 as the reference fluid, the ρ_2/ρ_1 and μ_2/μ_1 in Eq. (3.7) are the non-dimensional density and viscosity, respectively. Further, $H(\phi)$ is a sharp Heaviside function that is diffused $H_\epsilon(\phi)$ for the DI-LSM. These Heaviside functions are given as

For DI-LSM: Diffuse or smoothed Heaviside function

$$H(\phi) = H_\epsilon(\phi) = \begin{cases} 0 & \phi < -\epsilon \\ \frac{\phi + \epsilon}{2\epsilon} + \frac{1}{2\pi} \sin\left(\frac{\pi\phi}{\epsilon}\right) & |\phi| \geq \epsilon \\ 1 & \phi > \epsilon \end{cases} \quad (3.8)$$

For SI-LSM: Sharp Heaviside function

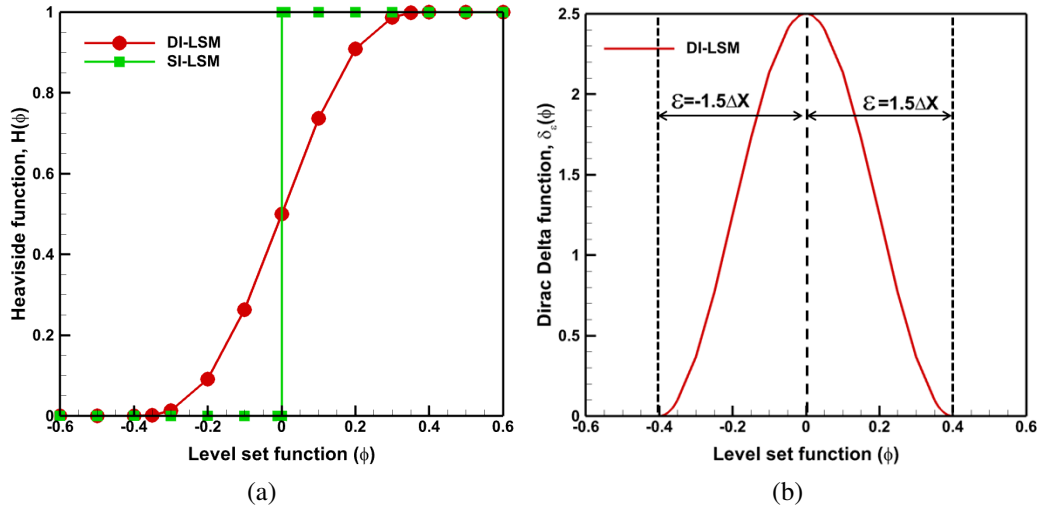


Figure 3.2: Schematic representation showing the variation of (a) Heaviside function and (b) Dirac Delta function across the interface for diffuse and sharp interface method.

$$H(\phi) = \begin{cases} 0 & \phi < 0 \\ 1 & \phi \geq 0 \end{cases} \quad (3.9)$$

A schematic variation of the sharp $H(\phi)$ and diffuse $H_\epsilon(\phi)$ Heaviside function are shown in Fig. 3.2a. Further, for the DI-LSM, Fig. 3.2b shows a smoothed Dirac delta function $\delta_\epsilon(\phi)$, physically interpreted as interfacial area-concentration inside a control volume (Gada and Sharma, 2009a), given as

$$\delta_\epsilon(\phi) = \frac{dH_\epsilon(\phi)}{d\phi} = \begin{cases} \frac{1}{2\epsilon} + \frac{1}{2\epsilon} \cos\left(\frac{\pi\phi}{\epsilon}\right) & \text{if } |\phi| < \epsilon \\ 0 & \text{otherwise} \end{cases} \quad (3.10)$$

Finally, the non-dimensional unit normal vector \hat{N} and curvature κ , which appears during the implementation of the interfacial force (Eq. 3.3 for the DI-LSM and Eq. 3.5 for the SI-LSM), are given as

$$\hat{N} = \frac{\nabla\phi}{|\nabla\phi|}; \quad \kappa = -\nabla \cdot \hat{N} \quad (3.11)$$

3.3 Numerical methodology

This section presents the numerical methodology in three-steps (Sharma, 2016): Discretization of the domain/equations, solution method, and solution algorithm; presented below in separate subsection. For the fluid flow, a *semi-explicit projection method* is used as a solution method. For high density-ratio multiphase simulations on a co-located grid, along with the momentum-interpolation method (MIM), the balanced force

method (BFM) is also needed to avoid the pressure-interfacial force imbalance for the DI-LSM; as discussed above. Thus, during the solution methodology for the discretized momentum equations, this section presents both MIM and BFM for the DI-LSM while only MIM is presented for the SI-LSM.

Mostly, a solution methodology in CFD follows a predictor-corrector two-step approach, where velocities are first predicted and then corrected—at the face-centers of the main/scalar CVs in a staggered grid and at both cell-centers and face-centers in a co-located grid. Note that the prediction and correction of the normal-velocities at the face-centers of a co-located grid ensures the pressure-velocity coupling by the MIM, which are used in the discretized mass conservation equation to obtain the equation for pressure.

For CmFD development on a staggered grid, the forces due to the surface tension and pressure are discretized at the cell-center of the staggered velocity-CV for the momentum conservation. Thus, the discretization of both the forces are at *identical* staggered grid points, which automatically ensures the pressure-interfacial force balance on the staggered grid system. This is not the case for a co-located grid system, where a *proper* MIM is needed for the discretization of both the forces at identical grid points otherwise it leads to the pressure-interfacial force imbalance; presented below.

The above discussed proper MIM-based force balance on the co-located grid is relevant to the DI-LSM, but not for the SI-LSM. This is because the force due to surface tension is not considered in the momentum equation (Eq. 3.4) for the SI-LSM. Further, the pressure-interfacial force imbalance is ensured during the solution of the continuity equation (Eq. 3.1), where both pressure and surface tension (in the interfacial boundary condition; Eq. (3.5)) terms are discretized at the face-centers of the co-located CV; presented below. Unlike DI-LSM, the SI-LSM considers both pressure and surface tension forces at the interface for solving the discretized pressure equation. This ensures proper balance between pressure and interfacial force, which is an essential criterion for the CmFD numerical methodology, and only MIM is required for the SI-LSM, on the co-located grid.

3.3.1 Discretization of Computational Domain and Governing Equations

For the present DI-LSM and SI-LSM, Fig. 3.3(a) shows a staggered grid points, for the normal-velocity at the face-centers, for the staggered grid system; and Fig. 3.3(b) shows the co-located grid points (at the same location, cell-centers) for both velocity and pressure, , for the co-located grid system. For both the grid arrangements, the figure shows that the grid points, for the level set function, are defined at the corners of the main

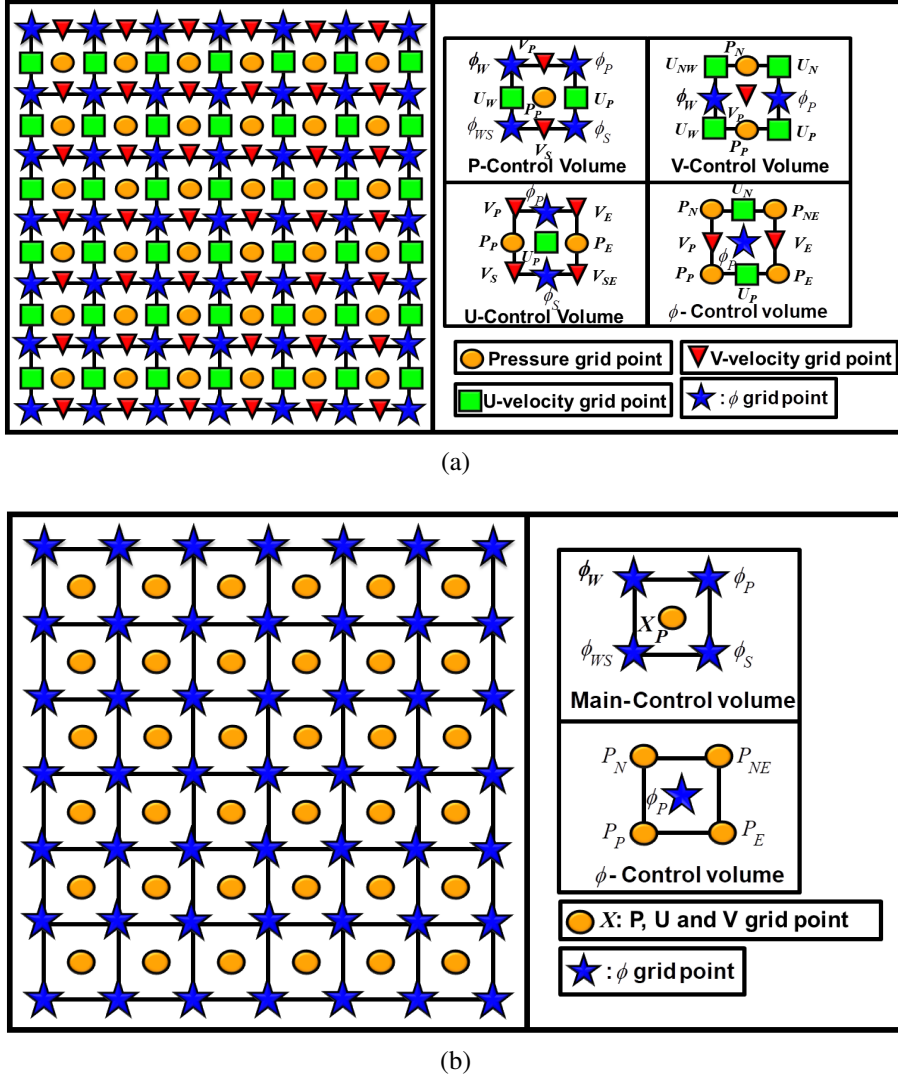


Figure 3.3: Schematic for the: (a) staggered and b) co-located grid systems, showing the arrangement of grid points for pressure and velocity along with the level set function (ϕ). The control volumes of the different variables are also shown.

control volume. Thus, a space-wise averaging is done to determine the level set function that are needed at the grid points for the pressure/velocity.

For the discretization or algebraic-formulation of the governing equations presented above, a *physical law-based finite volume method* (Sharma, 2016) is used for the fluid flow equations (Eqs. (3.1), (3.3), and (3.4)) while a *finite difference method* is used for the interface-capturing level set equations (Eqs. (3.2) and (3.6)). Further, the advection and diffusion terms in the momentum equation are discretized by 3rd order Lin-Lin TVD (Total Variation Diminishing) (Date, 2005) and central differencing scheme (Sharma, 2016), respectively. For the level set equations, 3rd order Runge-Kutta method is used for the temporal term and 5th order upwind weighted essentially non-oscillatory (WENO) scheme is used for the advection term.

3.3.2 Solution method for the Flow properties: Semi-Explicit Pressure Projection Method

In this section, a solution methodology is presented for two types of interface (diffuse and sharp) and grid systems (staggered and co-located) that corresponds to the level set methods of four-types: DI-LSM_{stag}, SI-LSM_{stag}, DI-LSM_{col} and SI-LSM_{col}. The methodology uses a predictor-corrector method, with a momentum equation-based prediction and correction equation. These equations are presented for both velocities at cell-center and mass-fluxes at face-centers in the co-located grid system. Whereas, for the staggered grid system, they are presented for only normal-velocity or mass-fluxes at the face-centers of the main CV.

For the solution of discretized governing equations of the various CmFD solvers, the Semi-explicit method (Sharma, 2016), based on pressure projection method, considers the continuity equation as implicit while all the terms in the momentum equation are explicit except the diffusion and pressure terms; presented below.

Original-proposition for the Continuity Equation:

$$\nabla \cdot \vec{U}^{n+1} = 0 \quad (3.12)$$

Original-proposition for the Momentum Equation:

The original-proposition for the momentum equation. unified for both DI-LSM and SI-LSM, is given as

$$\vec{U}_P^{n+1} = \tilde{\vec{U}}_P + S_P^n \quad (3.13)$$

where $\tilde{\vec{U}}_P$ is a *provisional* velocity (without the source term S_P^n), given as

$$\tilde{\vec{U}}_P = \vec{U}_P^n - \Delta\tau \nabla \cdot (\vec{U}^n \vec{U}^n)_P + \frac{1}{\rho_m^n Re_1} \nabla \cdot (2\mu_m^n D^{n+1})_P \quad (3.14)$$

and then S_P is given as

$$S_P^n = \begin{cases} -\frac{1}{Fr^2} + \left(\frac{\kappa \hat{\delta}_e(\phi)}{\rho_m^n We} \right)_P^n & \text{for DI-LSM} \\ -\frac{1}{Fr^2} & \text{for SI-LSM} \end{cases} \quad (3.15)$$

Momentum Equation-based Predictor step

The Semi-explicit method is a predictor-corrector approach which involves the prediction and followed by the correction of the velocities. In this section, for both DI-LSM

and SI-LSM the prediction of the face-center normal-velocities at the main-CV are presented for both staggered and co-located grid systems. Whereas, as discussed above, only co-located grid requires the prediction of cell-center velocity. The prediction equations are presented for both DI-LSM and SI-LSM as follows:

Prediction of Cell-Center velocity for the co-located grid system:

The prediction equation, unified for both DI-LSM and SI-LSM, is given as

$$\vec{U}_P^* = \tilde{\vec{U}}_P^n + S_P^n \quad (3.16)$$

where

$$\tilde{\vec{U}}_P^n = \vec{U}_P^n - \Delta\tau \nabla \cdot (\vec{U}^n \vec{U}^n)_P + \frac{1}{\rho_m^n R e_1} \nabla \cdot (2\mu_m^n D^*)_P \quad (3.17)$$

whereas, the source S_P^n is same as given above in Eq. (3.15).

Prediction of Face-Center Normal-velocity for both Staggered and Co-located Grid systems:

Similarly, the *unified* (for both the grid systems) prediction equation for the *normal-velocity* at the east face-center of the Cartesian CV (main CV for the staggered grid) is given as

$$U_e^* = \tilde{U}_e^n + S_e^n \quad (3.18)$$

where the provisional velocity is given as

$$\tilde{U}_e^n = U_e^n - \Delta\tau \nabla \cdot (U^n U^n)_e + \frac{1}{\rho_m^n R e_1} \nabla \cdot (2\mu_m^n D^*)_e \quad (3.19)$$

and the source term is given as

$$S_e^n = \begin{cases} -\frac{1}{Fr^2} + \left(\frac{\kappa \hat{N} \delta_e(\phi)}{\rho_m^n W_e} \right)_e^n & \text{for DI-LSM} \\ -\frac{1}{Fr^2} & \text{for SI-LSM} \end{cases} \quad (3.20)$$

Similarly, for the other face-centers, the predicted normal-velocity are given as

$$U_w^* = \tilde{U}_w^n + S_w^n; \quad V_n^* = \tilde{V}_n^n + S_n^n; \quad \text{and} \quad V_s^* = \tilde{V}_s^n + S_s^n;$$

Although the above equation for the prediction of face-center normal-velocity $U_{f=e,w,n,s}$ is applied for both staggered and co-located grid system, the computation of the advection

and diffusion term in \tilde{U}_e^n (Eq. 3.19) involves the geometric parameters (surface and volume) of the staggered CVs in the staggered grid system. This is avoided in the co-located grid system, since the calculation of geometric properties for the staggered CVs gets complicated; specially for a complex geometric problem on a curvilinear-structured and unstructured grid. Instead, the provisional velocity \tilde{U}_e is obtained by a linear interpolation—called momentum interpolation—of the provisional U -velocity at neighbouring cell centers \tilde{U}_P and \tilde{U}_E (obtained from Eq. 3.17) for the co-located grid; given for a uniform grid as

$$\tilde{U}_e^n = \left(\overline{\tilde{U}_P^n + \tilde{U}_E^n} \right) = 0.5(\tilde{U}_P^n + \tilde{U}_E^n) \quad (3.21)$$

Similarly, for the other face centers, the provisional velocities are given as

$$\tilde{U}_w^n = \left(\overline{\tilde{U}_W^n + \tilde{U}_P^n} \right); \quad \tilde{V}_n^n = \left(\overline{\tilde{V}_P^n + \tilde{V}_N^n} \right); \quad \text{and} \quad \tilde{V}_s^n = \left(\overline{\tilde{V}_S^n + \tilde{V}_P^n} \right);$$

Further, for the DI-LSM on the co-located grid, the cell-centered surface tension term in S_P is considered separately from the \tilde{U}_P during the prediction of U_P^* (Eq. 3.17). Thus, the linear interpolation of the cell-center surface tension term (Eq. 3.21) is avoided and it is computed at the face-center (Eq. 3.20). The *separate* consideration of the surface tension term from the provisional velocity \tilde{U}_P (Eq. 3.17) in S_P is the *key idea* of the BFM (Francois *et al.*, 2006) for a diffuse interface based VOF method or LSM on the co-located grid system. Whereas, for a sharp interface-based CmFD method, this is not needed; presented above.

Momentum Equation-based Corrector step

Correction of face-center normal-velocity for both staggered and co-located grid systems:

As the predicted velocities does not satisfy the continuity equation (Eq. 3.12), these predicted velocities need to be corrected to calculate the actual velocity. This involves the correction of face-center normal-velocity ($U'_{f=e,w}$ and $V'_{f=n,s}$) for both the grid systems, and the cell-center velocity \vec{U}'_P only for the co-located grid system. For the east face-center normal-velocity, the *original proposition* on both the grid systems are given for DI-LSM as well as SI-LSM as

$$U_e^{n+1} = \tilde{U}_e^n + S_e^n - \frac{\Delta\tau}{\rho^{*,n}} \frac{P_E^{n+1} - P_P^{n+1}}{\delta X_e} \quad (3.22)$$

Subtracting the above original proposition from the predicted east face-center normal-velocity (Eq. 3.18) and using the assumption $D^{n+1} - D^* \approx 0$ (Patankar, 1980), the correc-

tion equation for the east face-center normal-velocity U'_e is given for both the grid systems as

$$U_e^{n+1} - U_e^* = U'_e = -\frac{\Delta\tau}{\rho_{*,n}} \frac{P_E^{n+1} - P_P^{n+1}}{\delta X_e} \quad (3.23)$$

similarly,

$$\begin{aligned} U'_w &= -\frac{\Delta\tau}{\rho_{*,n}} \frac{P_P^{n+1} - P_W^{n+1}}{\delta X_w}; \quad V'_s = -\frac{\Delta\tau}{\rho_{*,n}} \frac{P_P^{n+1} - P_S^{n+1}}{\delta Y_s} \\ V'_n &= -\frac{\Delta\tau}{\rho_{*,n}} \frac{P_N^{n+1} - P_P^{n+1}}{\delta Y_n}; \end{aligned} \quad (3.24)$$

Correction of the cell-center velocity for the co-located grid:

The cell-center velocity correction \vec{U}'_P is obtained by subtracting the cell-center velocity prediction (Eq. 3.16) from original proposition (Eq. 3.13 for both DI-LSM and SI-LSM) and using the assumption $D^{n+1} - D^* \approx 0$; given as

$$\vec{U}_P^{n+1} - \vec{U}_P^* = \vec{U}'_P = -\frac{\Delta\tau}{\rho_{*,n}} \nabla P^{n+1} \quad (3.25)$$

Continuity Equation-based Pressure Equation

Using the normal-velocity $U_{e/w}^*/V_{n/s}^*$ at the face-centers of the CVs, from the above prediction step (Eq. 3.18) and U'_e/V'_n from the above correction step (Eq. 3.23), the FVM-based discretized continuity equation (Eq. 3.12) results in a pressure equation; given as

$$a_P P_P^{n+1} = a_E P_E^{n+1} + a_W P_W^{n+1} + a_N P_N^{n+1} + a_S P_S^{n+1} + b \quad (3.26)$$

where a_P , a_E , a_W , a_N and a_S are the coefficients of the linear algebraic equation for the pressure, which are given as

$$\begin{aligned} a_E &= \frac{\Delta\tau \Delta S_e}{\rho_e^{*,n} \delta X_e}, \quad a_W = \frac{\Delta\tau \Delta S_w}{\rho_w^{*,n} \delta X_w}, \quad a_N = \frac{\Delta\tau \Delta S_n}{\rho_n^{*,n} \delta Y_n}, \quad a_S = \frac{\Delta\tau \Delta S_s}{\rho_s^{*,n} \delta Y_s}, \\ a_P &= a_E + a_W + a_N + a_S \\ b &= \begin{cases} S_{vol,P}^* & \text{for DI-LSM} \\ S_{vol,P}^* + S_{jump,int} & \text{for SI-LSM} \end{cases} \end{aligned} \quad (3.27)$$

where the predicted volumetric source $S_{vol,P}^*$ and the interfacial source $S_{jump,int}$ are given as

$$S_{vol,P}^* = (U_w^* - U_e^*) \Delta Y + (V_s^* - V_n^*) \Delta X \text{ and}$$

$$S_{jump,int} = S_{jump,e} + S_{jump,w} + S_{jump,n} + S_{jump,s}$$

The interfacial source term $S_{jump,f}$ is non-zero only for an interfacial cell and zero for an interior cell; given (Shaikh *et al.*, 2018) as

$$\begin{aligned} S_{jump,e} &= \frac{\hat{\beta}_e B_e \Delta S_e}{\Delta X} S_{jump,w} = \frac{\hat{\beta}_w B_w \Delta S_e}{\Delta X} \\ S_{jump,n} &= \frac{\hat{\beta}_n B_n \Delta S_n}{\Delta Y} S_{jump,s} = \frac{\hat{\beta}_s B_s \Delta S_s}{\Delta Y} \end{aligned} \quad (3.28)$$

where

$$\hat{\beta}_f = \frac{\beta_1 \beta_2}{\beta_1(1 - \psi_f) + \beta_2 \psi_f}; \left\{ \frac{|\phi|_P}{|\phi|_P + |\phi|_{NB}} \text{ and } \beta_i = \frac{\Delta\tau}{\chi_i} \right\}$$

$$B_f = \frac{B_P |\phi_{NB}| + B_{NB} |\phi_P|}{|\phi_P| + |\phi_{NB}|}; \left\{ B(X, Y) = [P]_\Gamma = \frac{2}{Re_1} [\eta] \hat{N} \cdot (\nabla U \cdot \hat{N}, \nabla V \cdot \hat{N}) + \frac{\kappa}{We} \right\}$$

where NB is the neighbouring cell center (E, W, N , and S) for a control volume with cell-center P and f is an interfacial face-center. For an interior grid point with a neighbouring interfacial grid, as shown with a stencil in Fig. 3.1(a) for the DI-LSM (on both the grid systems), the source term in Eq. (3.27) is given as,

$$b = S_{vol,P}^* = \begin{cases} U_w^* \Delta S_w - U_e^* \Delta S_e + V_s^* \Delta S_s - V_n^* \Delta S_n & \text{for staggered} \\ (\overline{U_w^*, U_P^*}) \Delta S_w - (\overline{U_P^*, U_E^*}) \Delta S_e + (\overline{V_S^*, V_P^*}) \Delta S_s \\ - (\overline{V_P^*, V_N^*}) \Delta S_n & \text{for co-located} \end{cases} \quad (3.29)$$

where the above “overbar” for the co-located grid corresponds to linear interpolation, which is not needed for the staggered grid system. Similarly for an interfacial grid point, shown in Fig. 3.1(b) for the SI-LSM on both the grid systems, the source term in Eq. (3.27) is given as,

$$b = S_{vol,P}^* + S_{jump,w} + S_{jump,s}$$

Detailed discussion of the above implementation details for $SI-LSM_{stag}$ can be found in a previous work (Shaikh *et al.*, 2018) from our research group.

3.3.3 Solution algorithm

Solution algorithm, unified for the present $DI-LSM_{stag}$, $SI-LSM_{stag}$, $DI-LSM_{col}$ and $SI-LSM_{col}$, is as follows:

1. Discretize the computational domain with suitable grid arrangement (staggered or co-located) and grid size (ΔX and ΔY).

2. Using the level set function ϕ , initialize the interface and calculate interface normal (\hat{N}) and curvature (κ).
3. Calculate Heaviside function, $H(\phi)$ from Eq. (3.8) and Eq. (3.9) for DI-LSM and SI-LSM, respectively. Further, for DI-LSM, calculate the Dirac delta function $\delta_\epsilon(\phi)$ from Eq. (3.10) .
4. Initialize the thermo-physical properties in the computational domain, using Eq. (3.7) for the DI-LSM and SI-LSM, on both the grid systems. Also, initialize the flow properties (\vec{U} and P).
5. For the co-located grid, predict the cell-center velocity \vec{U}_P^* (Eq. 3.16) for both DI-LSM and SI-LSM. Thereafter, for staggered and co-located grid systems, predict the face-center normal-velocity (Eq. 3.18) for the DI-LSM and SI-LSM.
6. For the SI-LSM on staggered and co-located grid, calculate the interfacial source term $S_{jump,f}$ (Eq. 3.28).
7. Solve the pressure Poisson equation (Eq. 3.26) with suitable modification of the coefficients and source term for the DI-LSM and SI-LSM.
8. Correct the face-center normal-velocity $U'_{e/w}/V'_{n,s}$ (Eq. 3.23 and 3.24) and cell-center velocity \vec{U}'_P (Eq. 3.25).
9. Compute the velocity at the new time level: $U_{e/w}^{n+1} = U_{e/w}^* + U'_{e/w}$ and $V_{n/s}^{n+1} = V_{n/s}^* + V'_{n/s}$ for the staggered grid; and $\vec{U}_P^{n+1} = \vec{U}_P^* + \vec{U}'_P$ for the co-located grid.
10. Using the velocity at the new time-level, solve the level set advection and reinitialization equation (Eqs. (3.2) and (3.6)) for the level set function ϕ .
11. Using the ϕ calculate the $H(\phi)$ (Eq. 3.8 and 3.9 for DI-LSM and SI-LSM, respectively) and $\delta_\epsilon(\phi)$ (Eq. 3.10) to determine the thermo-physical properties of fluid.
12. Check the unsteady stopping criterion, if satisfied terminate the program or go to step 5.

3.4 Validation and relative accuracy study

In this section, for the present sharp and diffuse interfaces-based LSMs on a staggered and co-located grid systems, validation and relative accuracy are presented for our

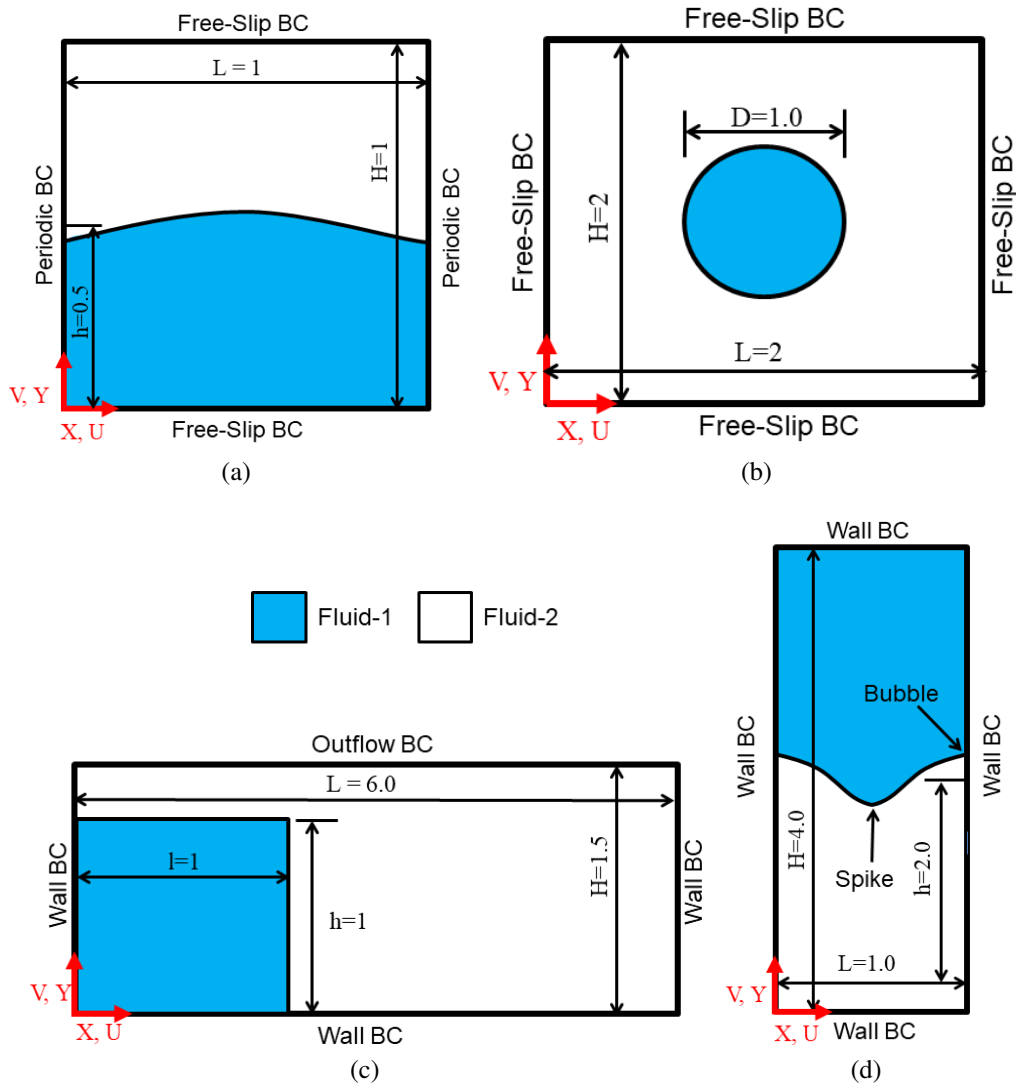


Figure 3.4: Computational setup for (a) capillary wave, (b) static droplet, (c) dam break simulation, and (d) Rayleigh-Taylor instability. All geometrical values are non-dimensional.

four different LSMs-based in house codes—($\text{DI-LSM}_{\text{stag}}$, $\text{SI-LSM}_{\text{stag}}$, $\text{DI-LSM}_{\text{col}}$, and $\text{SI-LSM}_{\text{col}}$). For this exercise, four commonly used CmFD problems are chosen: capillary wave, static droplet, dam break, and Raynor-Taylor instability. Capillary wave and static droplet are numerically relevant problems to test the ability of the code to capture the pressure-interfacial force balance. Capillary problem evaluates the pressure-interfacial force along with simple interface dynamics making it suitable for order of accuracy studies. Whereas, the static droplet problem focuses on pressure-interfacial force balance without any interface dynamics and as an ideal problem to test a co-located grid based numerical methods prediction capability. The dam break (gravity dominated) and Raynor-Taylor instability (buoyancy driven) are physically relevant CmFD problems with significant interface deformation. Thus, for our four LSMs-based in-house codes, relative

accuracy of the present CSF and SSF surface tension models on both the grid systems are presented.

3.4.1 Capillary wave: Order of Accuracy Study

In this problem, a sinusoidal perturbation results in a damped oscillation of an interface that separates viscous fluids. Figure 3.4(a) shows the present computational set-up, similar to Gerlach *et al.* (2006), with a computational domain of non-dimensional size 1×1 and the fluids are separated by a sinusoidal interface. Considering wavelength λ as length scale l_c , and inverse of oscillation frequency ω_0 as the time scale t_c , the non-dimensional thermo-physical properties of the fluid are $\rho_1/\rho_2 = 1$, $\mu_1/\mu_2=1$, $Re_1 = 609.98$, and $We = 124$.

Figure 3.5 shows the variation of L_2 error norm with grid size in comparison to that reported by various multiphase solvers—coupled level-set volume-of-fluid (CLSVOF) (Gerlach *et al.*, 2006), conservative diffuse-interface (conservative DI) (Mirjalili *et al.*, 2020), Front tracking (FT) (Popinet and Zaleski, 1999), Gerris flow solver (Popinet, 2009), Parabolic reconstruction of surface tension for the volume-of-fluid (PROST) (Renardy and Renardy, 2002), balanced force refined level set grid (RLSG) (Herrmann, 2008), and non-intersecting flux polyhedron advection - VOF advection scheme (VOF-NIFPA-1)(Ivey and Moin, 2017). Here, considering the present LSMs-based solution and analytical solution Prosperetti (1981), the error corresponds to L_2 norm for the time-wise evolution of the amplitude of interface-oscillation. The figure shows that the order of accuracy of the present LSMs is in-between first and second order, which is similar to that seen for the other multiphase solver in the literatures; except by second order solver —Gerris (Popinet, 2009), PROST (Renardy and Renardy, 2002), and CLSVOF (Gerlach *et al.*, 2006). Note from the figure that the present error for DI-LSM_{col} almost overlap with RLSG method (Herrmann, 2008). Among the present LSMs, note from the figure that even though almost similar accuracy is obtained on the coarser grid (smaller N), SI as compared to DI approach results in smaller error as the number of grid points N increases; with lowest error for SI-LSM_{col}. Also note from the figure that the accuracy of the present LSMs, on various grid sizes, lies in-between that for the various CmFD methods in the literatures.

3.4.2 Static Droplet

Static droplet is a classical test case to evaluate the pressure-interfacial force balance of various CmFD solvers. For an initially inviscid static droplet with circular configuration under zero gravity, the pressure jump across the interface, called as Laplacian

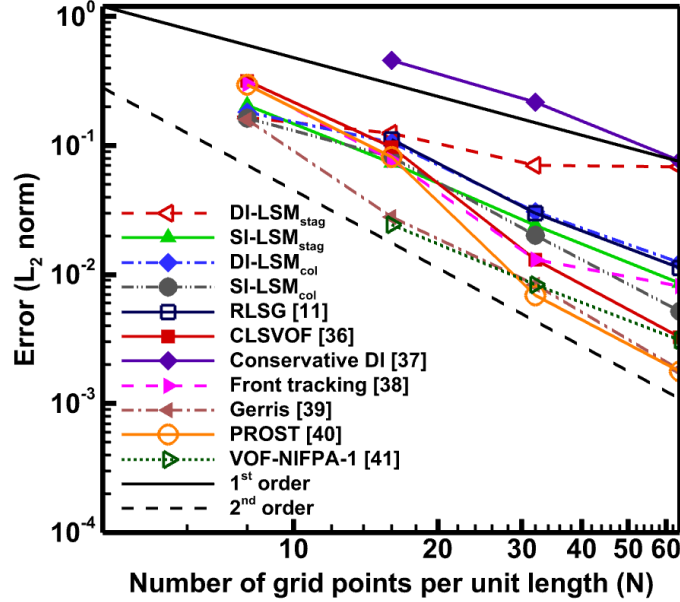


Figure 3.5: Variation of L_2 norm of the error with grid size for the present LSMs as compared to the various multiphase solvers-based published results.

pressure-jump is available from analytical study (Butt *et al.*, 2013) as $\Delta p_{exact} = \sigma\kappa_{exact}$. Here, Δp , σ , and κ are dimensional pressure jump across the interface, surface tension coefficient and curvature, respectively, and the subscript *exact* corresponding to the analytical solution.

For simulation of the suspended droplet under equilibrium, the problem set-up of Francois *et al.* (2006) is utilized here. For the present two-dimensional simulation in Cartesian coordinate, Fig. 3.4(b) shows a droplet of size D placed at the center of computational domain of size $L \times H$. Considering D as length scale l_c and $\sqrt{\sigma/\rho_1 l_c}$ as velocity scale u_c , the non-dimensional geometric dimensions are shown in Fig. 3.4(b). Further, the non-dimensional thermo-physical properties are considered as $\chi = 10^3$ and $We = 1$, which results in non-dimensional pressure jump across the interface $\Delta P_{exact} = 2$. The density ratio $\chi = 10^3$ is obtained with $\rho_1 = 1$ and $\rho_2 = 10^{-3}$. Unless specified all simulations are performed on a grid size of 40×40 , non-dimensional time step $\Delta\tau = 1.07 \times 10^{-6}$, and convergence tolerance $\epsilon = 10^{-12}$ for pressure.

The accuracy of present LSMs are determined by evaluating the ability to simulate exact pressure jump along with a negligible maximum magnitude of spurious current

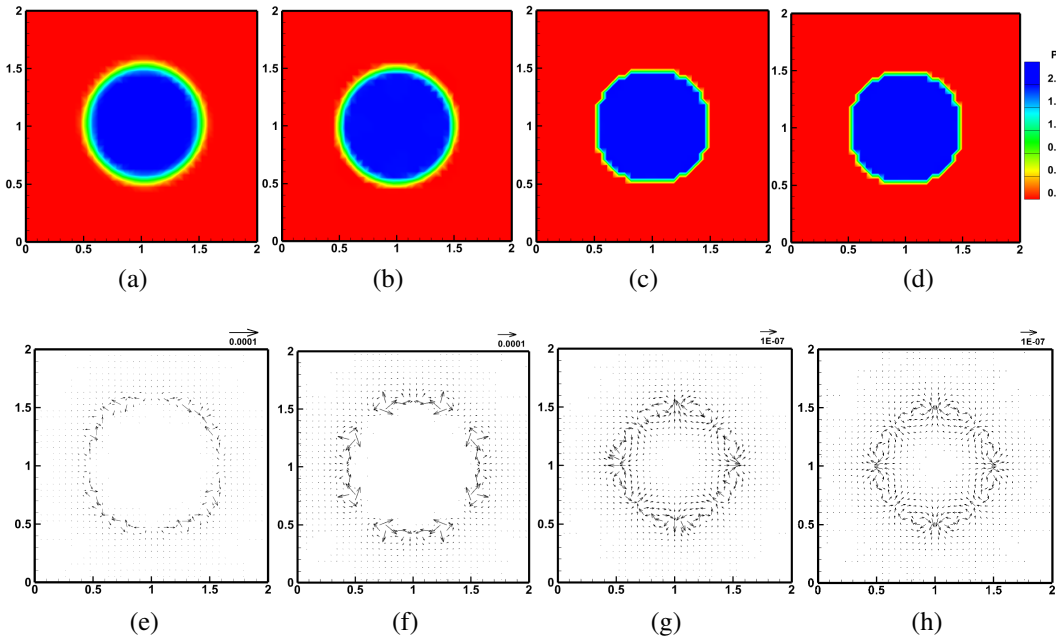


Figure 3.6: Pressure contour and velocity vector plot, obtained after one time step, at density ratio $\chi = 10^3$ for (a, e) $DI - LS M_{stag}$, (b, f) $DI - LS M_{col}$, (c, g) $SI - LS M_{stag}$, and (d, h) $SI - LS M_{col}$.

($|\vec{U}|_{max}$). The associated errors are given as

$$\begin{aligned} E(\Delta P_{total}) &= \frac{|\Delta P_{total} - \Delta P_{exact}|}{\Delta P_{exact}} \\ E(\Delta P_{max}) &= \frac{|\Delta P_{max} - \Delta P_{exact}|}{\Delta P_{exact}} \\ L_\infty(\vec{U}) &= |\vec{U}|_{max} \end{aligned} \quad (3.30)$$

Table 3.1: Comparison of various errors obtained after one time-step for the static droplet problem with $\chi = 10^3$ utilizing present LSMs.

Error	$DI - LS M_{stag}$	$DI - LS M_{col}$	$SI - LS M_{stag}$	$SI - LS M_{col}$
$E(\Delta P_{total})$	5.71×10^{-2}	4.34×10^{-2}	2.42×10^{-3}	2.42×10^{-3}
$E(\Delta P_{max})$	1.12×10^{-2}	9.54×10^{-3}	4.60×10^{-3}	4.60×10^{-3}
$L_\infty(\vec{U})$	1.76×10^{-5}	7.78×10^{-5}	6.12×10^{-8}	5.37×10^{-8}

where $E(\Delta P_{total})$, is the error for *total* pressure jump ΔP_{total} , $E(\Delta P_{max})$ is the error for *maximum* pressure jump, and $L_\infty(\vec{U})$ is the L_∞ error-norm for the velocity vector. Further, the jump in total pressure ΔP_{total} and maximum pressure ΔP_{max} are given as

$$\Delta P_{total} = P_{av,1} - P_{av,2}$$

$$\Delta P_{max} = P_{max,1} - P_{max,2}$$

where $P_{av,1}$, $P_{av,2}$, $P_{av,3}$ and $P_{av,4}$ are the non-dimensional average pressure in fluid-1, average pressure in fluid-2, maximum pressure in the fluid-1, and maximum pressure in fluid-2, respectively.

For the static droplet droplet problem with density ratio $\chi = 10^3$, Fig. 3.6 shows pressure contour and velocity vector; obtained from the present LSMs. For the SI-LSM, the figures show almost same results on staggered and co-located grid. Whereas, for the DI-LSM, Fig. 3.6(b) and 3.6(f) shows a reasonable difference in the results on staggered and co-located grid for the velocity field; but not for the pressure.

For staggered-versus-co-located grid, almost same errors are seen in Table 3.1 for DI-LSM/SI-LSM; except a smaller $E(\Delta p_{max})$ for the DI-LSM_{col} as compared to DI-LSM_{stag}. Whereas, for sharp-versus-diffuse interface LSMs, the maximum magnitude of spurious current or $L_\infty(\vec{U})$ is $O(10^{-5})$ for DI-LSM and is much smaller $O(10^{-8})$ for the SI-LSM. Further, for $E(\Delta P_{max})$, the table shows a smaller error for the SI-LSM as compared to DI-LSM on both the grid systems. Thus, the table shows that the accuracy of the SI-LSM is better than DI-LSM without appreciable difference between the two grid systems.

3.4.3 Dam break simulation

Dam break is a gravity dominated benchmark problem for multiphase flow solvers, where the experimental results of Martin and Moyce (1952) is used for a validation study. For the present two-dimensional simulation on Cartesian coordinate, Fig. 3.4(c) shows a rectangular water column of size $l \times h$, which is stationary (initially) in a computational domain of size $L \times H$. Considering initial height h of water column as length scale l_c , $(gl)^{0.5}$ as velocity scale u_c , and l_c/u_c as time scale t_c the non-dimensional geometric dimension of the fluid column and computational domain are shown the figure. Further, the non-dimensional thermo-physical properties are $\rho_1/\rho_2 = 819.67$, $\mu_1/\mu_2 = 64.1$, $Re_1 = 2.75 \times 10^6$, $We = 1.35 \times 10^5$, and $Fr = 1$. For the present unsteady simulations upto a maximum non-dimensional time $\tau_{max} = 2.5$, a uniform grid size 200×50 and non-dimensional time step $\Delta\tau = 10^{-3}$ is considered.

Figure 3.7(a) shows a good agreement between the present LSMs-based simulations and the experimental results (Martin and Moyce, 1952) for the timewise variation of the leading edge distance and the column height. The instantaneous leading edge distance is measured along the bottom boundary while the instantaneous column height is considered along the left boundary of the computational domain. As compared to the experiment results (Martin and Moyce, 1952), on the variation of leading edge distance (column height), the maximum errors are 3.82% (6.49%), 3.10% (5.75%), 3.94% (6.51%), and

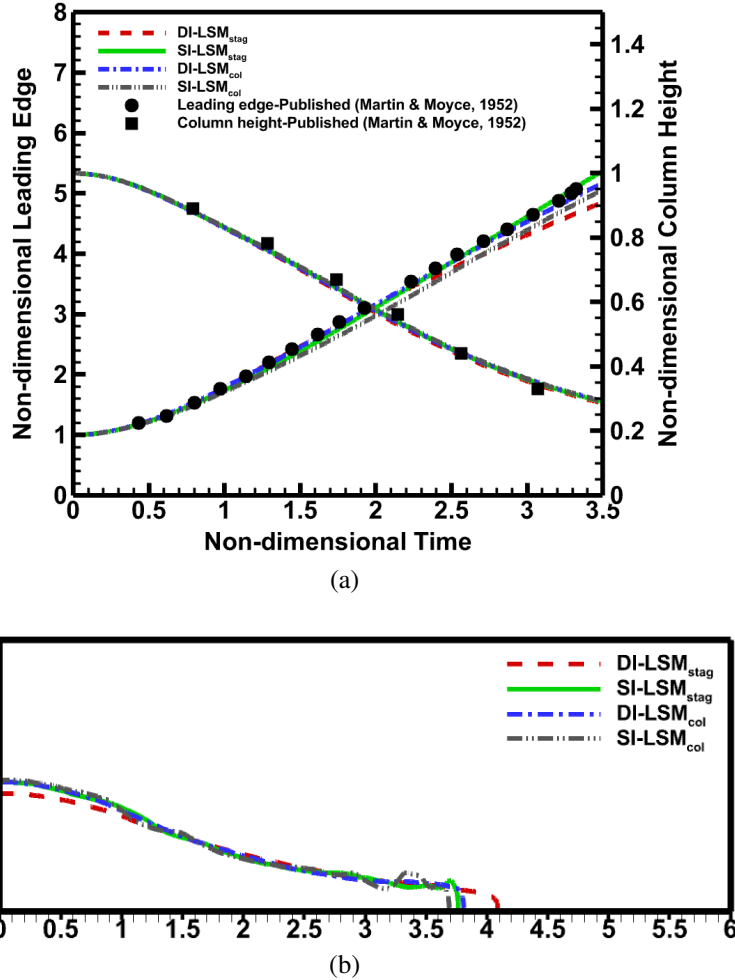


Figure 3.7: For the present LSMS-based dam break simulations on a staggered and co-located grid systems, (a) time-wise variation of leading edge distance and column height as compared to the published experimental results (Martin and Moyce, 1952), and (b) instantaneous interface at $\tau = 2.4$.

4.61% (3.24%) for the $\text{DI-LSM}_{\text{stag}}$, $\text{SI-LSM}_{\text{stag}}$, $\text{DI-LSM}_{\text{col}}$, and $\text{SI-LSM}_{\text{col}}$ are, respectively. For globally mass conservative Phase-Field method, Huang *et al.* (2020) reported the maximum error as 4.36% for the leading edge distance and 2.34% for the column height.

For the various LSMS, Fig. 3.7(b) shows almost coinciding instantaneous interface; except a slightly different interface for the DI-LSM on a staggered grid.

3.4.4 Rayleigh-Taylor instability

Rayleigh-Taylor instability is an instability of an interface due to a buoyancy induced phenomenon, which occurs when a heavier fluid is kept above a lighter-fluid. An initially perturbed interface causes the instability, resulting in an inter-penetration of both the fluids that leads to a complex interface dynamics. For a validation and prediction accuracy study

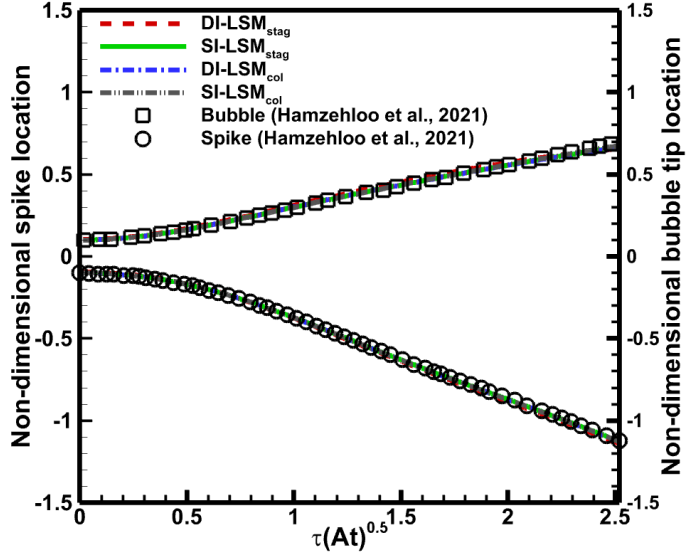


Figure 3.8: Verification of Rayleigh-Taylor instability showing the comparison of present LSMs with published numerical result (Huang *et al.*, 2020) for the temporal variation of non-dimensional bubble and spike distance.

of the present LSMs-based solvers, a 2D Rayleigh-Taylor instability with Atwood number $At = 0.5$ and Reynolds number $Re = 3000$ is considered.

Figure 3.4d shows a computational domain of size $L \times H$, with a perturbed interface separating a heavier fluid and a lighter fluid. The position of this perturbed interface along the vertical direction is defined as

$$Y_0 = h + A\cos(k)$$

where $A (= 0.1)$, $k (= 2\pi X)$, and $h (= 2)$ are the non-dimensional amplitude, wave number, and initial mean position of the cosine function respectively. For the present non-dimensional study L and $\sqrt{gl_c}$ are considered as length scale l_c and velocity scale u_c , respectively. Further, the non-dimensional thermo-physical properties are considered as $\rho_1/\rho_2 = 3$, $\mu_1/\mu_2 = 1$, $Re_1 = 3000$, $We = 3 \times 10^5$, and $Fr = 1$. All the simulations are performed upto a maximum non-dimensional time $\tau_{max} \sqrt{At} = 2.5$ on a grid size of 150×600 , non-dimensional time step $\Delta\tau = 10^{-4}$.

For validation, the time-wise evolution of the location of spike and bubble (marked in Fig. 3.4(d)) are measured along the vertical centerline of computational domain and vertical boundary, respectively. Figure 3.8 shows a good agreement between the present LSMs and published numerical result (Huang *et al.*, 2020), with a maximum error in the location of spike (bubble) as 4.44% (6.62%), 2.98% (4.87%), 3.36% (5.67%), and 2.94% (3.35%) for $DI-LSM_{stag}$, $SI-LSM_{stag}$, $DI-LSM_{col}$, and $SI-LSM_{col}$, respectively. Thus, among the present LSMs, $SI-LSM_{col}$ results in the smallest error for both spike and bubble

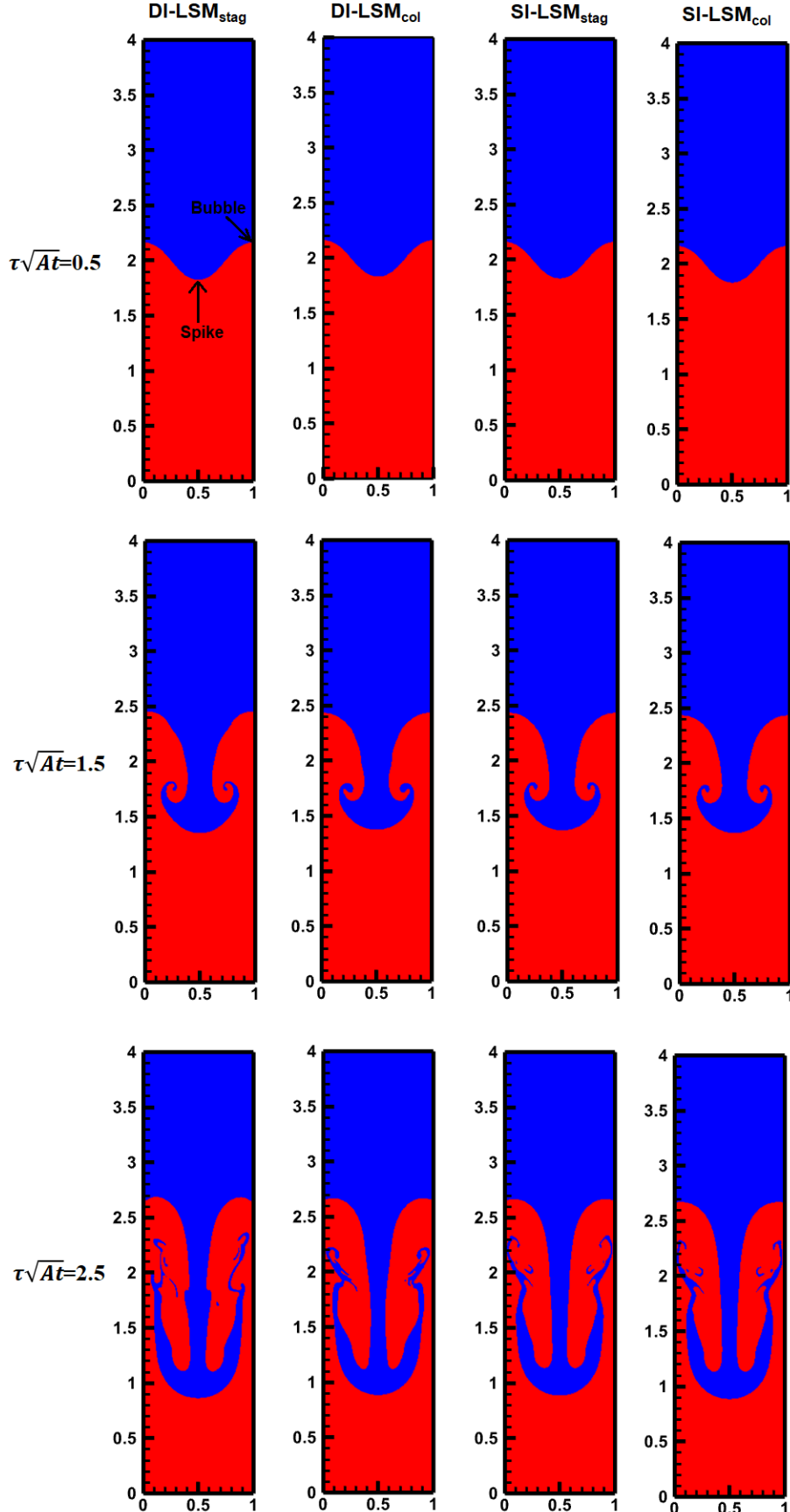


Figure 3.9: For the present LSMs-based simulation of the Rayleigh-Taylor instability on a staggered and co-located grid systems, comparison of instantaneous interface at various time instants.

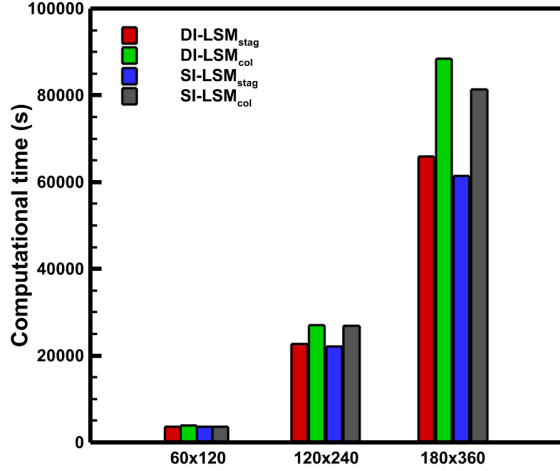


Figure 3.10: Computational time taken by various LSMs for droplet coalescence till non-dimensional time $\tau = 0.6$ with various grid sizes.

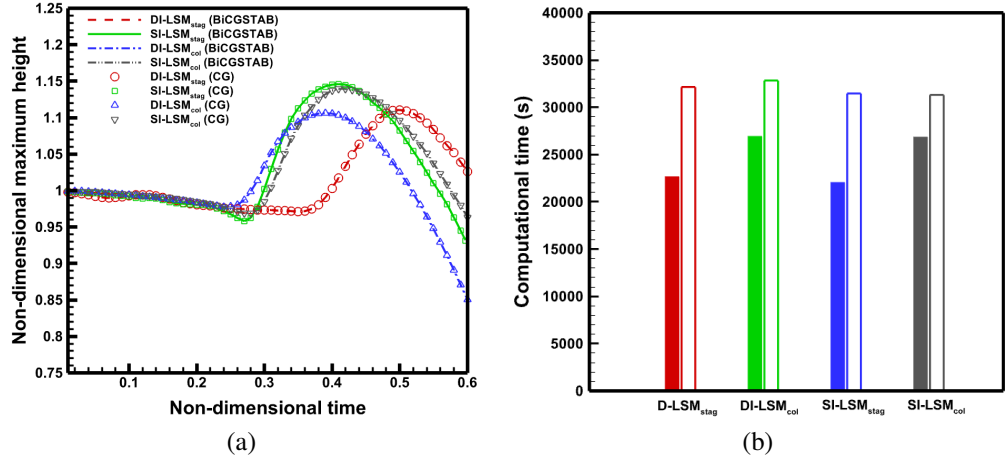


Figure 3.11: Comparison of BiCGSTAB and CG iterative methods for pressure Poisson equation simulating droplet coalescence showing (a) time-wise evolution of non-dimensional maximum height and (b) computational time till $\tau = 0.6$ on grid size of 120×240 .

locations. Further, the SI-LSM as compared to DI-LSM leads to a smaller error on both the grid system.

For various LSMs, Fig. 3.9 shows almost same instantaneous interfaces for SI-LSM on both the grid system while a slight difference in the interfaces are seen for the DI-LSM on the co-located as compared to staggered grid. However, the results for DI-LSM_{col} are in better agreement with the results for SI-LSM_{stag} and SI-LSM_{col}.

3.4.5 Computational time

For a comprehensive comparison of various solvers performance it is essential to compare the total computational time also apart from solution accuracy or relative error.

This is performed in this section by comparing the computational time taken by various LSMs for a specified problem. Among the various CmFD problems validated since the computational time taken for droplet coalescence is higher as compared to other problems—capillary wave, static droplet, dam break, Rayleigh-Taylor, and rising bubble—the same is utilized here for the study of computational time.

Figure 3.10 shows the computational time obtained for droplet coalescence with pressure Poisson iterative loop solved using BiCGSTAB and tolerance of 1e-5. Thermo-physical properties and computational set-up is similar to the validation case utilized in the previous section. Even though on coarser grid no significant variation is obtained between various LSMs as the grid becomes finer LSMs on staggered grid takes lesser computational time as compared to LSMs on co-located grid. For the present pressure Projection method since pressure Poisson iterative loop contribute significantly to the total computational time, hence Conjugate Gradient (CG) method was also utilized instead of BiCGSTAB for comparison. Figure 3.11(a) shows similar variation in time-wise evolution of non-dimensional maximum height between BiCGSTAB and CG method. Whereas for computational time as shown in Fig. 3.11(b), for various LSMs CG takes more time as compared to BiCGSTAB with least time taken by SI-LSMs as compared to DI-LSMs on both the grid systems.

Thus, overall this study shows that present LSM's on co-located grid is a suitable substitute for LSMs on staggered grid with respect to solution accuracy and comparable computational time.

3.5 Closure

In previous chapter for development of GFM-based SI-LSM on co-located and its comparison with BFM-based DI-LSM resulted into $\text{SI-LSM}_{\text{col}}$ and $\text{DI-LSM}_{\text{col}}$, respectively. While in this chapter, apart from the solvers on co-located grid previously published solvers on staggered grid— $\text{DI-LSM}_{\text{stag}}$ and $\text{SI-LSM}_{\text{stag}}$ —are utilized. A detailed comparison of numerical methodology and computational performance is further presented for various LSMs on staggered and co-located grid.

Chapter 4

Sharp Interface Level Set Method on a Co-located Grid for CmFD with Heat Transfer-induced Phase Change

For the successful simulation of CMFD problems - accurate capturing of interface, treatment of discontinuities in fluid and flow properties across the interface, handling singular forces etc. are essential. Additionally, on co-located grid it is essential to avoid pressure-velocity decoupling and pressure-interfacial force imbalance. Review of literatures dealing with phase change problems, will lead to the conclusion that staggered grid is the widely used grid system as compared to co-located grid. For heat transfer induced phase change problems on complex geometries it is essential to require a numerical methodology for high density ratio simulations on co-located grid. From the previous chapters, considering the robustness and computational performance of present GFM-based SI-LSM on co-located, is extended to phase change problems in this chapter. This enable us to utilize a robust CmFD solver on co-located grid for nucleate boiling with power transients—a complex multiphysics problem.

4.1 Mathematical formulation

For the present Ghost Fluid Method (GFM)-based SI-LSM_{col}, this section presents a sub-domain conservation law-based mathematical formulation—the conservation equations are applicable for individual fluids in the sub-domain. The interfacial jump condition for pressure and velocity are considered in GFM using ghost cells as shown in Fig. 4.1. The present formulation further avoids pressure-interfacial force imbalance along with pressure-velocity decoupling for a co-located grid. Although the sub-domain approach is

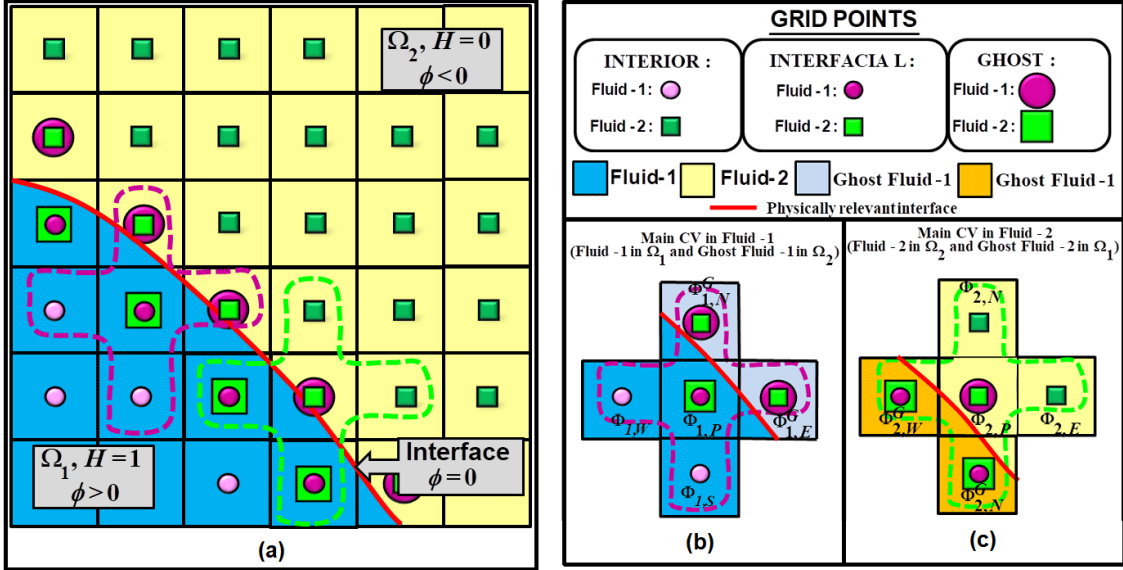


Figure 4.1: Schematic of a representative computational domain along with the various types of grid points for a two-fluid flow showing (a) various grid points for flow field $\Phi (= P, \vec{U}, \theta)$ and various interfacial CV's filled with real and ghost fluid for b) main CV filled with fluid-1 in Ω_1 sub-domain and ghost fluid-1 in Ω_2 sub-domain, whereas c) shows main CV filled with fluid-2 in Ω_2 sub-domain and ghost fluid-2 in Ω_1 sub-domain.

used here for individual fluids a *single-field formulation* enables a single set of conservation equations that results in a single flow-field for both the fluids are used; presented below.

4.1.1 Conservation equations

The sub-domain conservation law and single-field formulation-based conservation equations in non-dimensional form are presented below. Based on the physical interpretations of Heaviside function and Dirac-delta function for LSM and its application for a conservation law-based derivations of conservation equation by Gada and Sharma (2009a), continuity equation and level set advection equation presented here are based on volume conservation law and mass conservation law, respectively. For the present SI-LSM, the interfacial jump condition-based formulation for pressure is also presented, which avoids pressure-interfacial force imbalance on co-located grid for CmFD with phase change.

Volume Conservation Law-based Continuity Equation:

$$\nabla \cdot \vec{U} = 0 \quad (4.1)$$

Mass Conservation Law-based Level Set Advection Equation:

$$\frac{\partial \phi}{\partial \tau} + \vec{U}_a \cdot \nabla \phi = 0 \quad (4.2)$$

where \vec{U}_a is the non-dimensional velocity with which interface is advected, defined as the sum of non-dimensional bulk velocity (\vec{U}_{bulk}) and non-dimensional phase change velocity (\vec{U}_{PC}).

Momentum Equation:

$$\frac{\partial(\chi_i \vec{U})}{\partial \tau} + \nabla \cdot (\chi_i \vec{U} \vec{U}) = -\nabla P + \frac{1}{Re_1} \nabla \cdot (2\eta_i D) - \frac{\chi_i}{Fr^2} \hat{j} \quad (4.3)$$

Energy Equation:

$$\frac{\partial \theta}{\partial \tau} + \nabla \cdot (\vec{U}_{bulk} \theta) = \frac{1}{\chi_i \gamma_i Re_1 Pr_1} \nabla \cdot (\zeta_i \nabla \theta) \quad (4.4)$$

For the above equations, considering l_c as length scale, u_c as velocity scale, and t_c as time scale, the resulting non-dimensional variables with fluid-1 as the reference fluid, given as

$$\vec{X} = \frac{\vec{x}}{l_c}; \vec{U} = \frac{\vec{u}}{u_c}; \tau = \frac{tu_c}{l_c}; P = \frac{p}{\rho_1 u_c^2}; \theta = \frac{T - T_{sat}}{T_{wall} - T_{sat}};$$

where \vec{X} , \vec{U} , τ , P , and θ are non-dimensional Cartesian coordinate, velocity, time, pressure, and temperature, respectively. The resulting non-dimensional parameters are given as

$$Re = \frac{\rho_1 l_c u_c}{\mu_1}; We = \frac{\rho_1 u_c^2 l_c}{\sigma}; Fr = \frac{u_c}{\sqrt{g l_c}}; Pr = \frac{\mu_1 c_{p,1}}{k_1};$$

Also, the non-dimensional thermo-physical properties are given as

$$\chi_i = \frac{\rho_i}{\rho_1}; \eta_i = \frac{\mu_i}{\mu_1}; \gamma_i = \frac{c_{p,i}}{c_{p,1}}; \zeta_i = \frac{k_i}{k_1}$$

where χ_i , η_i , γ_i , and ζ_i are the non-dimensional density, dynamic viscosity, specific heat, and thermal conductivity, respectively. Further, We is Weber number, Re is Reynolds number, Fr is Froude number, and Pr is Prandtl number.

For the above single-field formulation, the non-dimensional thermo-physical properties are defined using Heaviside function $H(\phi)$; given as

$$\begin{aligned}\chi_i &= H(\phi) + \chi(1 - H(\phi)); \quad \eta_i = H(\phi) + \eta(1 - H(\phi)) \\ \gamma_i &= H(\phi) + \gamma(1 - H(\phi)); \quad \zeta_i = H(\phi) + \zeta(1 - H(\phi))\end{aligned}\tag{4.5}$$

where

$$\chi = \frac{\rho_2}{\rho_1}; \quad \eta = \frac{\mu_2}{\mu_1}; \quad \gamma = \frac{c_{p,2}}{c_{p,1}}; \quad \zeta = \frac{k_2}{k_1}$$

and the Heaviside function is given as

$$H(\phi) = \begin{cases} 0 & \Omega_1(\phi < 0) \\ 1 & \Omega_2(\phi \geq 0) \end{cases}\tag{4.6}$$

For example, considering fluid-1 as reference fluid and the sub-domains Ω_1 for fluid-1 and Ω_2 for fluid-2 Eq. (4.5) results in $\chi_i = 1$, $\eta_i = 1$, $\gamma_i = 1$, and $\zeta_i = 1$ for Ω_1 and $\chi_i = \chi$, $\eta_i = \eta$, $\gamma_i = \gamma$, and $\zeta_i = \zeta$ for Ω_2 .

4.1.2 Subsidiary Equation

Apart from the above conservation equations, reinitialization and an extrapolation equation need to be solved. The reinitialization equation establish the advected ϕ as normal distance function. Whereas, extrapolation equation extends values from sub-domain Ω_1 (Ω_2) to other sub-domain Ω_2 (Ω_1) for the calculation of ghost value.

Reinitialization Equation:

$$\frac{\partial \phi}{\partial \tau_s} = S_\epsilon(\phi_0)(1 - |\nabla \phi|)\tag{4.7}$$

where $\tau_s (= \Delta X / 10)$ is pseudo time step and $S_\epsilon (= \phi_0 / \sqrt{\phi_0^2 + \Delta X^2})$ is a smoothed sign function (Sussman *et al.*, 1994).

Extrapolation Equation:

The sub-domain conservation law-based solution of above conservation equations with interfacial jump condition-based formulation involve jump in pressure, velocity, and temperature across the interface for heat transfer-induced phase change in multiphase flow. For the solution of this flow field utilizing GFM-based SI-LSM, ghost grid points are essential to avoid discontinuity during discretization of the non-dimensional flow field

variable Φ (pressure P , velocity \vec{U} , and temperature θ). These grid points in a real fluid correspond to the Φ value of the other fluid across the interface.

Figure 4.1(b) shows a computational stencil for the solution of $\Phi_{1,P}$ in Ω_1 sub-domain filled with fluid-1. For this interfacial CV, instead of using $\Phi_{2,S}$ and $\Phi_{2,E}$ (real values of Φ in fluid-2 subdomain Ω_2) ghost values of fluid-1 in sub-domain Ω_1 are utilized ($\Phi_{1,S}^G$ and $\Phi_{1,E}^G$). This avoid discontinuous fluid values during discretization on interfacial CV's. Similarly for computational stencils shown in Fig. 4.1(c) to compute $\Phi_{2,P}$, instead of using $\Phi_{1,N}$ and $\Phi_{1,W}$ (real values of Φ in fluid-1 in Ω_1) ghost values of fluid-2 in Ω_2 are utilized ($\Phi_{2,N}^G$ and $\Phi_{2,W}^G$).

The ghost values, at ghost grid points, are calculated by solving a constant-extrapolation equation, given as

$$\frac{\partial \Phi_N}{\partial \tau_s} + H_G(\phi) \hat{N} \cdot \nabla \Phi_N = 0 \quad (4.8)$$

where Φ_N is the variable extrapolated in normal direction across the interface, τ_s is pseudo time step, and \hat{N} is the unit normal vector. Since Eq. (4.8) is solved on ghost grid points $H_G(\phi)$ in the above equation should be suitably considered. For example, in Fig. 4.1(b) to calculate $\Phi_{1,S}^G$ and $\Phi_{1,E}^G$, the extrapolation equation is solved in Ω_2 and results in $H_G(\phi)$ that is defined as

$$H_G(\phi) = \begin{cases} 0 & \phi < 0 \\ 1 & \phi \geq 0 \end{cases} \quad (4.9)$$

Whereas, since the extrapolation equation is solved in Ω_1 in Fig. 4.1(c), $H_G(\phi)$ is defined as unity in $\phi < 0$ and zero in $\phi \geq 0$. Although the higher order linear and quadratic-extrapolation methods are available (Aslam, 2004), in the present study considers constant extrapolation for interfacial mass flux since it leads to almost same accuracy in less computational time as compared to the higher order extrapolation methods.

For the heat transfer induced phase change problems, a jump in heat flux also occur across the interface due to interfacial mass transfer phenomenon. Utilizing Stefan condition involving energy conservation and mass conservation (Shaikh *et al.*, 2019; Tanguy *et al.*, 2007), the non-dimensional interfacial mass flux is given as

$$\vec{M} = \frac{Ja}{\gamma Re_1 Pr_1} (\nabla \theta)_1 - \zeta (\nabla \theta)_2 \quad (4.10)$$

and implemented as

$$\vec{M} = \frac{Ja \left(\left(\frac{\partial \theta}{\partial N} \right)_{1,\Gamma} - \zeta \left(\frac{\partial \theta}{\partial N} \right)_{2,\Gamma} \right)}{\gamma Re_1 Pr_1} \quad (4.11)$$

where $\partial\theta/\partial N$ is the non-dimensional normal temperature gradient at the interface, and its subscript $(1, \Gamma)$ and $(2, \Gamma)$ denotes that the gradient is evaluated at interface along fluid-1 and fluid-2, respectively. Further, Jacob number Ja is given as

$$Ja = \frac{c_{P,2}(T_w - T_{sat})}{h_{lv}}$$

For the heat transfer induced-phase change problems, non-dimensional phase change velocity \vec{U}_{PC} for advecting the level set function, given as

$$\vec{U}_{PC} = \vec{M}$$

4.1.3 Interfacial boundary condition

Conservation equations for the present SI-LSM are solved using interfacial jump condition for Φ —a sub-domain conservation law-based formulation. To account for surface tension force and interfacial mass transfer, the jump in pressure $[P]_\Gamma$, velocity $[\vec{U}]_\Gamma$, and non-dimensional heat flux $[q^*]_\Gamma$ are considered while solving continuity-based pressure Poisson, momentum, and energy equations, respectively. The jump in their values across the interface Γ is represented as $[\cdot]_\Gamma = (\cdot)_{1,\Gamma} - (\cdot)_{2,\Gamma}$, where $(\cdot)_{1,\Gamma}$ and $(\cdot)_{2,\Gamma}$ represents a value or its gradient at the interface in Ω_1 and Ω_2 , respectively.

The surface tension term, which is not present in the momentum equation (Eq. 4.3), is modelled as an interfacial boundary condition for pressure along with normal component of viscous stress and recoiling pressure due to phase change (Shaikh *et al.*, 2018; Tanguy *et al.*, 2014); given as

$$[P] = \frac{\kappa}{We} + \frac{2}{Re_1} [\eta] \hat{N} \cdot (\nabla U \cdot \hat{N}, \nabla V \cdot \hat{N}) - \dot{M}^2 \left(1 - \frac{1}{\chi}\right) \quad (4.12)$$

Non-dimensional form of interfacial jump BC in velocity is given as (Tanguy *et al.*, 2007)

$$[\vec{U}]_\Gamma = B_2 = \vec{M} \left[\frac{1}{\chi} \right] \quad (4.13)$$

For the solution of energy equation due to phase change, the jump in non-dimensional heat flux across the interface is given as

$$[q^*]_\Gamma = B_3 = \left[\zeta \frac{\partial \theta}{\partial N} \right]_\Gamma = \left(\frac{\partial \theta}{\partial N} \right)_{1,\Gamma} - \zeta \left(\frac{\partial \theta}{\partial N} \right)_{2,\Gamma} = \vec{M} \quad (4.14)$$

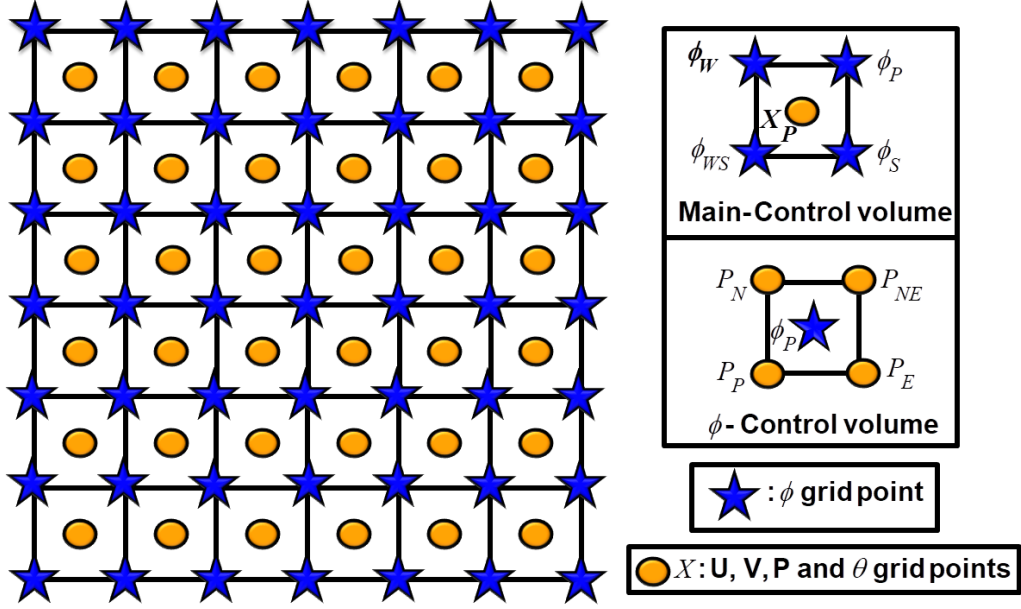


Figure 4.2: Schematic for the co-located grid system, showing grid point arrangement for pressure (P), velocities (U and V), and temperature (θ) along with level set function ϕ and their respective control volumes.

Assuming a thermal equilibrium condition at the interface (Gibou *et al.*, 2007), continuity in temperature field is obtained at the interface; given as

$$\theta_1 = \theta_2 = \theta_{sat} \implies [\theta]_\Gamma = 0$$

Further, for Eq. (4.12) and (4.1.2), the non-dimensional unit normal vector \hat{N} and curvature κ are given as

$$\hat{N} = \frac{\nabla\phi}{|\nabla\phi|}; \quad \kappa = -\nabla \cdot \hat{N} \quad (4.15)$$

4.2 Numerical methodology

For multiphase simulation on co-located grid with phase change, apart from common multiphase modelling challenges—interface, surface tension, and phase change—the *pressure-interfacial force imbalance* is also involved. Improper balance of pressure and interfacial force results in numerical instability at high density ratio (Francois *et al.*, 2006). This is avoided here using the interfacial jump condition for pressure, which establish interfacial force balance even at numerically discretized level; discussed for CmFD with phase change. Thus, this section presents numerical methodology in separate subsections on discretization of computational domain and governing equations, solution method, and solution algorithm.

4.2.1 Discretization of Computational Domain and Governing Equations

For the present SI-LSM_{col}, Fig. 4.2 shows the co-located arrangement for pressure, velocity and temperature. Whereas, level set function (ϕ) is defined at the corners of the control volume. To evaluate ϕ at the cell-center, a spatial averaging is performed from corners of the respective control volume (CV). Similarly, to calculate flow variables at face-centers or corners of main-CV, suitable spatial averaging is performed.

Physical law-based FVM (Sharma, 2016) is used for fluid flow for the discretization of the mass, momentum, and energy conservation equations, (Eqs. 4.1 4.3, and 4.4), while a finite difference method is used for the level set equation: for the discretization of advection equation: (Eq. 4.2), reinitialization equation (Eq. 4.7) and extrapolation equation (Eq. 4.8). For the diffusion and advection terms in both momentum and energy equations, central difference (Sharma, 2016) and 3rd order Lin-Lin TVD (Total Variation Diminishing) (Date, 2005) are utilized, respectively. For level set advection (Eq. 4.2) and reinitialization equations (Eq. 4.7), temporal and advection terms are discretized with 3rd order RK and 5th order WENO scheme, respectively. While for the extrapolation equation (Eq. 4.8), first order forward Euler and first order upwind is used for discretization of temporal and spatial term (Tanguy *et al.*, 2014), respectively.

4.2.2 Solution method: Semi-Explicit Pressure Projection Method

In this section, for LSM-based CmFD with phase change on co-located grid a predictor-corrector approach which involves momentum equation-based prediction and correction equation is discussed for the solution of the conservation equations. These equations are presented for a co-located distribution of flow field (\vec{U} , P , and θ). Further, to account for discontinuous pressure, velocity, and heat flux for SI-LSM on co-located grid, the interfacial jump condition-based formulation is also discussed.

For the solution of discretized governing equations, semi-explicit method based on pressure Projection considers all the terms as explicit except diffusion and pressure term for momentum equation and the continuity equation as implicit. Similarly for energy equation all terms are explicit expect diffusion term; presented below.

Original-proposition for the Continuity Equation:

$$\nabla \cdot \vec{U}^{n+1} = 0 \quad (4.16)$$

Original-proposition for the Momentum Equation:

$$\vec{U}_P^{n+1} = \vec{U}_P^n - \Delta\tau \nabla \cdot (\vec{U}^n \vec{U}^n) - \frac{\Delta\tau}{\chi_i^n} \nabla P^{n+1} + \frac{1}{\chi_i^n Re_1} \nabla \cdot (2\eta_i^n D^{n+1}) + \frac{1}{Fr^2} \hat{j} \quad (4.17)$$

Original-proposition for the Energy Equation:

$$\theta_P^{n+1} = \theta_P^n - \Delta\tau \nabla \cdot (\vec{U}^n \theta^n) - \frac{1}{\chi_i^n \gamma_i^n Re_1 Pr_1} \nabla \cdot (\zeta_i^n \nabla \theta) \quad (4.18)$$

Solution for Conservation of Momentum Equation

The semi-explicit method, which is a two-step predictor-corrector approach, which involves first prediction and then correction of velocities. In this section, these steps are discussed in-detail for CmFD with phase change problems similar to that presented in a book on CFD by Sharma (2016) for single phase flow.

Prediction of Cell-Center velocity:

In semi-explicit pressure projection method, the cell-center velocity is first predicted by neglecting the pressure term from original proposition (Eq. 4.17); given as

$$\vec{U}_P^* = \vec{U}_P^n - \Delta\tau \nabla \cdot (\vec{U}^n \vec{U}^n) + \frac{1}{\chi_i^n Re_1} \nabla \cdot (2\eta_i^n D^*) + \frac{1}{Fr^2} \hat{j} \quad (4.19)$$

Correction of Cell-Center velocity:

Since the predicted velocity does not satisfy continuity equation (Eq. 4.16), it is required to correct the predicted velocity. Hence, to calculate actual velocity field, the velocity correction equation is obtained by subtracting predicted velocity (Eq. 4.19) from original proposition (Eq. 4.17) and assuming $D^{n+1} - D^* \approx 0$ (Patankar, 1980); given as

$$\vec{U}_P^{n+1} - \vec{U}_P^* = \vec{U}'_P = \frac{\Delta\tau}{\chi_i^n} \nabla P^{n+1} \quad (4.20)$$

For CmFD with phase change, the jump in velocity as well as the jump in pressure need to be accounted while solving Eq. (4.19) and Eq. (4.20), respectively. Whereas for CmFD without phase change, only discontinuity in pressure is involved and considered for Eq. (4.20) while the solution of Eq. (4.19) is straightforward. For example, consider the computational stencil in Fig. 4.1(b) that consist of cells “E” and “N” in fluid-2 whereas cell “P” in fluid-1. For this cell, the discretization of advection and diffusion terms in Eq. (4.19) requires grid points across the interface ($\vec{U}_{2,E}$ and $\vec{U}_{2,N}$) and taken directly for CmFD without phase change. While for phase change problems, the velocity jump across interface results in discontinuous velocity field that prevents utilization of neighboring real velocity field values ($\vec{U}_{2,E}$ and $\vec{U}_{2,N}$).

In the present GFM-based SI-LSM on co-located, the jump in velocity (Eq. 4.13) is utilized to establish a continuous velocity field across the interface by considering ghost fluid-1 (ghost fluid-2) in the sub-domain Ω_2 (Ω_1) of real fluid-2 (real fluid-1). Thus, using Eq. 4.13, ghost velocity field of fluid-2 in fluid-1 (\vec{U}_2^G) and of fluid-1 in fluid-2 (\vec{U}_1^G) are given as

$$\begin{aligned}\vec{U}_1^G &= \vec{U}_2 + \vec{M}^* \left(1 - \frac{1}{\chi_2} \right) \left\{ \phi < 0 \right\} \\ \vec{U}_2^G &= \vec{U}_1 - \vec{M}^* \left(1 - \frac{1}{\chi_2} \right) \left\{ \phi > 0 \right\}\end{aligned}\quad (4.21)$$

For the computational stencil shown in Fig. 4.1, thus instead of real velocity field of fluid-2, the ghost values at the respective grid points are utilized while discretizing the advection and diffusion terms in velocity prediction equation. Thus, the purpose of the ghost cells are to isolate divergence free velocity field for each subdomain from *discontinuous* actual velocity field. For numerical implementation this is made possible by defining ghost cells, shown in Fig. 4.1(b), within a region of $3\Delta X$ on either side of the physically relevant interface ($\phi = 0$). The specified thickness $\epsilon = 6\Delta X$ across the interface is chosen due to the requirement of three grid points to one side of interface by 5th order WENO scheme used in level set equations (Eq. 4.2 and 4.7).

Pressure Poisson equation:

Once the velocity prediction equation (Eq. 4.19) is solved with interfacial jump condition for velocity, the predicted velocity need to be corrected using velocity correction equation (Eq. 4.20) with actual pressure field. On co-located grid, the jump condition formulation avoids pressure-interfacial force imbalance that is essential to perform high density ratio phase change simulations. Using the normal predicted velocities from Eq. (4.19) and corrected velocities from Eq. (4.20), the FVM-based discretized continuity equation (Eq. 4.16) results in a linear algebraic equation for pressure; given as

$$a_P P_P^{n+1} = a_W P_W^{n+1} + a_S P_S^{n+1} + a_E P_E^{n+1} + a_N P_N^{n+1} + b \quad (4.22)$$

where the coefficients a_P , a_W , a_S , a_E , and a_N are given as

$$\begin{aligned}a_W &= \frac{\beta_w \Delta S_w}{\delta X_w}, \quad a_S = \frac{\beta_s \Delta S_s}{\delta Y_s}, \\ a_E &= \frac{\beta_e \Delta S_e}{\delta X_e}, \quad a_N = \frac{\beta_n \Delta S_n}{\delta Y_n},\end{aligned}$$

$$a_P = \sum_{NB=E,W,N,S} a_{NB} = a_E + a_W + a_N + a_S$$

$$b = S_{vol,P}^* + S_{jump,int}$$

where

$$S_{vol,P}^* = (U_w^* - U_e^*)\Delta Y + (V_s^* - V_n^*)\Delta X \text{ and}$$

$$S_{jump,int} = \sum_{f=e,w,n,s} S_{jump,f} = S_{jump,e} + S_{jump,w} + S_{jump,n} + S_{jump,s}$$

where

$$\begin{aligned} S_{jump,e} &= \frac{\hat{\beta}_e B_e \Delta S_e}{\Delta X} \quad S_{jump,w} = \frac{\hat{\beta}_w B_w \Delta S_e}{\Delta X} \\ S_{jump,n} &= \frac{\hat{\beta}_n B_n \Delta S_n}{\Delta Y} \quad S_{jump,s} = \frac{\hat{\beta}_s B_s \Delta S_s}{\Delta Y} \\ \hat{\beta}_f &= \frac{\beta_1 \beta_2}{\beta_1(1 - \psi_f) + \beta_2 \psi_f}; \left\{ \psi_f = \frac{|\phi|_P}{|\phi|_P + |\phi|_{NB}} \text{ and } \beta_i = \frac{\Delta \tau}{\chi_i} \right\} \\ B_f &= \frac{B_P |\phi_{NB}| + B_{NB} |\phi_P|}{|\phi_P| + |\phi_{NB}|}; \left\{ B_1(\vec{X}) = [P]_\Gamma = \frac{2}{Re_1} [\eta] \hat{N} \cdot (\nabla U \cdot \hat{N}, \nabla V \cdot \hat{N}) \right. \\ &\quad \left. + \frac{\kappa}{We} - \dot{M}^2 \left(1 - \frac{1}{\chi} \right) \right\} \end{aligned} \quad (4.23)$$

For the stencil shown in Fig. 4.1(c), for pressure, since interface is present between “P” and “E”, and also between “P” and “N” grid points, $S_{jump,int}$ becomes

$$S_{jump,int} = S_{jump,e} + S_{jump,n} \quad \{S_{jump,w} = S_{jump,s} = 0\}$$

and thus the source term (b) in Eq. (4.22) is given as

$$b = S_{vol,P}^* + S_{jump,e} + S_{jump,n}$$

The above formulation, for energy and species equations are presented in detail by Shaikh *et al.* (2019) from our research group for SI-LSM on staggered grid, which is extended here on co-located grid for SI-LSM.

For the computational stencil shown in Fig. 4.1(b), for an interfacial cell in fluid-1 with fluid-1 being reference fluid, various non-dimensional parameters are given as

$$\zeta_1 = \gamma_1 = \chi_1 = 1$$

Moreover, $S_{jump,\Gamma}$ term is non-zero only for the faces of interfacial CV in other fluid. For example, S_{jump,Γ_w} and S_{jump,Γ_s} are zero and, S_{jump,Γ_e} and S_{jump,Γ_n} terms are non-zero for the interfacial cell shown in Fig. 4.1(b).

Solution for Conservation of Energy Equation

Using the real velocity field (\vec{U}_1 and \vec{U}_2) and its ghost field (\vec{U}_1^G and \vec{U}_2^G), the FVM-based discretization of energy equation (Eq. 4.18) results in linear algebraic equation for non-dimensional temperature θ as

$$a_P^\theta \theta_P^{n+1} = a_W^\theta \theta_W^{n+1} + a_S^\theta \theta_S^{n+1} + a_E^\theta \theta_E^{n+1} + a_N^\theta \theta_N^{n+1} + b^\theta \quad (4.24)$$

where a_P^θ , a_E^θ , a_W^θ , a_N^θ , and a_S^θ are the coefficients of above LAE, which are given as

$$\begin{aligned} a_W^\theta &= \frac{\alpha_w \Delta S_w}{\delta X_w}, \quad a_S^\theta = \frac{\alpha_s \Delta S_s}{\delta Y_s}, \\ a_E^\theta &= \frac{\alpha_e \Delta S_e}{\delta X_e}, \quad a_N^\theta = \frac{\alpha_n \Delta S_n}{\delta Y_n}, \end{aligned}$$

$$a_P^\theta = aP^0 + \sum_{(NB=E,W,N,S)} a_{NB}^\theta = aP^0 + a_E^\theta + a_W^\theta + a_N^\theta + a_S^\theta$$

where

$$a_P^0 = \frac{\Delta V_P}{\tau}; \quad \alpha_f = \frac{\zeta_{i,f}}{\chi_i \gamma_i Re_1 Pr_1}$$

and

$$b = ap^0 \theta_P^n - A_{\theta,P}^n + S_{jump,\Gamma} / \chi_i \gamma_i Re_1 Pr_1$$

where the advection term $A_{\theta,P}^n$ and interfacial source term $S_{jump,\Gamma}$ are given as

$$A_{\theta,P}^n = \sum_{f=e,n} U_f^n \theta_f^n \Delta S_f - \sum_{f=w,s} V_f^n \theta_f^n \Delta S_f$$

and

$$S_{jump,\Gamma} = \sum_{f=e,w,n,s} \Phi_f S_{jump,\Gamma_f} \quad (4.25)$$

where Φ_f is a variable to identify interfacial CV and interior CV, given as

$$\Phi_f = \begin{cases} 0 & \text{Interior CV} \\ 1 & \text{Interfacial CV} \end{cases}$$

Further, source term S_{jump,Γ_f} in Eq. (4.25) is given as (Shaikh *et al.*, 2019)

$$\begin{aligned} S_{jump,\Gamma_e} &= \hat{\zeta}_e M_{X,\Gamma_e}^* (1 - \psi_e) \Delta S_e; \quad S_{jump,\Gamma_w} = \hat{\zeta}_w M_{X,\Gamma_w}^* (1 - \psi_w) \Delta S_w; \\ S_{jump,\Gamma_n} &= \hat{\zeta}_n M_{Y,\Gamma_n}^* (1 - \psi_n) \Delta S_n; \quad S_{jump,\Gamma_s} = \hat{\zeta}_s M_{Y,\Gamma_s}^* (1 - \psi_s) \Delta S_s \end{aligned}$$

where

$$\hat{\zeta}_f = \frac{\zeta}{\psi_f + \zeta(1 - \psi_f)} \text{ and } \psi_f = \frac{|\phi_P|}{|\phi_P| + |\phi_{NB}|}$$

where $NB (= E, W, N, S)$ denotes cell-center value of neighboring CV. M_X^* and M_Y^* are the Cartesian components of non-dimension interfacial mass flux \vec{M}^* . The above equation is applicable for an interior ($\hat{\zeta}_f = \zeta_f$ and $S_{jump,\Gamma} = 0$) and interfacial CV.

Calculation of Interfacial Mass Flux

Accurate calculation of interfacial mass flux is essential in multiphase simulations with phase change otherwise it results in unphysical interface. In this section, the calculation of interfacial mass flux is presented with the help of Fig. 4.1, for a simple phase change problem assuming fluid-1 as superheated and fluid-2 under saturated condition. The figure shows an interfacial CV in fluid-1 and interface passing through east and north face of the main CV. Since fluid-2 is saturated, the non-dimensional interfacial mass flux from Eq. (4.11) is given as

$$\vec{M}^* = \frac{Ja}{\gamma Re Pr} (\nabla \theta)_{1,\Gamma} \quad (4.26)$$

where $(\nabla \theta)_{1,\Gamma}$ is the non-dimensional normal temperature-gradient at the interface Γ ; given as

$$(\nabla \theta)_{1,\Gamma} = \frac{\partial}{\partial X} \left(\frac{\partial N}{\partial X} \right) + \frac{\partial}{\partial Y} \left(\frac{\partial N}{\partial Y} \right) \quad (4.27)$$

Since \vec{M} requires ' $3\Delta X$ ' thickness on either side of interface for proper interface advection, due to non-availability of $(\nabla \theta)_{1,\Gamma}$ in Ω_2 sub-domain, only \vec{M} for the grid points in $\Omega_{1,\Gamma}$ sub-domain can be directly calculated from Eq. (4.26). The ghost grid point values of $(\nabla \theta)_{1,\Gamma}$ of fluid-1 in Ω_2 sub-domain is computed by solving constant extrapolation equation—Eq. (4.8) with $\Phi_N = \nabla \theta$. Once \vec{M} is calculated on grid points near the interface ($2\epsilon \leq 6\Delta X$), the phase change velocity \vec{U}_{PC} is computed and utilized for advecting the interface in Eq. 4.2. Similar numerical methodology can be extended if temperature gradient exists on both fluids due to either superheated or sub-cooled conditions.

4.2.3 Solution algorithm

The solution algorithm for the present SI-LSM_{col} is as follows:

1. Discretize the computational domain with co-located grid arrangement and suitable grid size (ΔX and ΔY).
2. Initialize interface, and calculate \hat{N} and κ of interface (Eq. 4.15) using level set function ϕ .

3. Calculate Heaviside function $H(\phi)$ throughout the computational domain using Eq. (4.6)
4. Using Eq. (4.5), define spatial distribution of thermo-physical properties in the computational domain. Also initialize the flow field variables (\vec{U} , P , and θ).
5. Apply boundary conditions for U , V , P , θ , and ϕ
6. Solve energy equation for temperature field in the computational domain after computing advection and diffusion term (Eq. 4.24).
7. Calculate normal temperature gradient (Eq. 4.27) and populate it at ghost cells using extrapolation equation (Eq. 4.8).
8. Calculate interfacial mass flux using Eq. (4.10) and compute phase change velocity at the ghost cells (Eq. 4.1.2).
9. Predict the cell-center velocity \vec{U}_P^* after computing advection and diffusion term (Eq. 4.19).
10. Calculate interfacial pressure jump condition (Eq. 4.12).
11. Iteratively solve the pressure Poisson equation to compute actual pressure for next time level (Eq. 4.22).
12. Correct the cell-center velocity by solving velocity correction equation (Eq. 4.19).
13. Based on actual velocity and phase change velocity at new time level, solve level set advection (Eq. 4.2) and reinitialization equation (Eq. 4.7).
14. Check stopping criterion, if satisfied terminate the program execution or else go to step 3.

4.3 Validation of present SI-LSM_{col} for benchmark CmFD problems with heat transfer-induced phase change

In this section, a validation study is presented for the present SI-LSM on a co-located grid, for various phase change problems: solidification, 1-D moving interface, 1-D sucking interface, growth of suspended bubble in superheated liquid, film boiling, and single bubble nucleate boiling. Here, the growth of suspended bubble in superheated liquid and

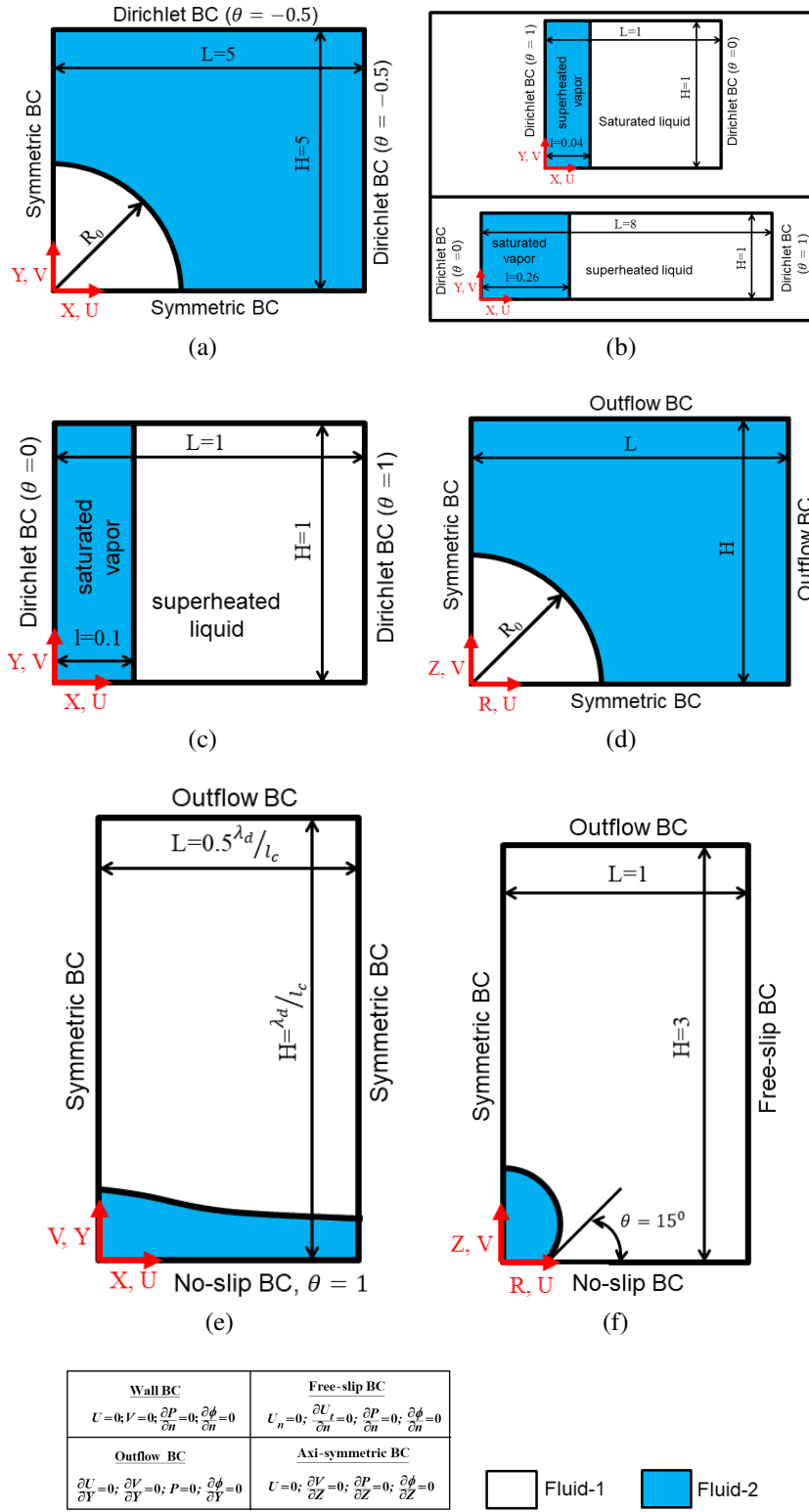


Figure 4.3: Computational setup of different CmFD phase change problems: (a) solidification, (b) one-dimensional moving interface, (c) one-dimensional sucking interface, (d) growth of suspended bubble in superheated liquid, (e) film boiling, and (f) single bubble nucleate boiling.

nucleate boiling simulations are performed on axisymmetric coordinate, and the other phase change problems are simulated on 2D-Cartesian coordinate system.

4.3.1 Solidification problem

A special class of Stephan problem i.e., cylindrical solidification is simulated, where a solid nuclei is allowed to undergo solidification due to the presence of surrounding sub-cooled liquid. Due to uniform temperature distribution along the interface, the solid domain grows maintaining its cylindrical configuration. For the present two-dimensional simulation on Cartesian coordinate, Fig. 4.3(a) shows the computational set-up with an initial solid nuclei with non-dimensional radius $r_0 = 1.56$ (Shaikh *et al.*, 2016). Due to the symmetric nature of problem, the figure shows only a quarter of the physical domain, considered for simulation, which results in symmetric boundary conditions at west and south walls along with Dirichlet boundary conditions at north and east walls. To initialize the temperature field, analytical solution for Stefan problem (Carslaw, 1959) is utilized; given as

$$T(r, t) = T(s) = \begin{cases} T_\infty \left(1 - \frac{F(s)}{F(s_0)}\right) & s > s_0 \\ 0 & s \leq s_0 \end{cases} \quad (4.28)$$

where $s = \frac{r}{\sqrt{t}}$, $F(s) = E_1(s^2/4)$, $E_1(z) = \int_z^\infty \frac{\exp(\zeta)}{\zeta} d\zeta$ and $T_\infty = \frac{1}{2} \frac{s_0 F(s_0)}{F'(s_0)}$. Further, the temporal variation in the radius of the solid (Carslaw, 1959) is given as

$$R_\Gamma(t) = s_0 \sqrt{t} \quad (4.29)$$

where s_0 corresponds to initial radius of solid nuclei. Considering unit length scale (l_c), l_c^2/α as time scale (t_c), and l_c/t_c as velocity scale (u_c), the non-dimensional geometric properties of computational domain is shown in Fig. 4.3(a). Further, the thermo-physical properties are taken as density $\rho = 1$, thermal conductivity $k = 1$, specific heat $c = 1$, and latent heat of solidification [h] = 1. The simulation is performed on a grid size 100×100 and non-dimensional time step $\Delta\tau = 10^{-3}$ till maximum non-dimensional time $\tau_{max} = 1.5$. Figure 4.4 shows the time-wise evolution of the radius of the cylindrical interface, with good agreement between the present SI-LSM_{col} and the analytical solution (Carslaw, 1959).

4.3.2 One-dimensional moving interface problem

One-dimensional moving interface is a simple test case to evaluate the phase change module with various thermo-physical properties for fluid, unlike unit value considered in previous solidification. In this problem, initially a vertical interface will be separating two

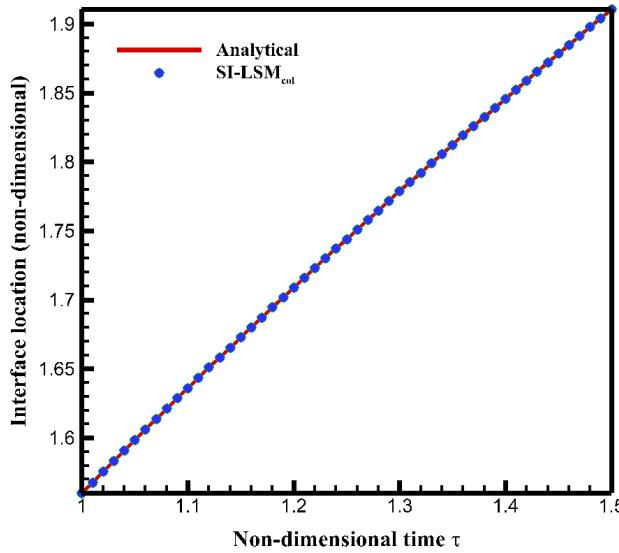


Figure 4.4: Solidification problem simulated with present SI-LSM_{col} showing time-wise evolution of interface and compared with analytical solution (Carslaw, 1959).

fluids (liquid and vapour), with one being at saturation and the other at superheated condition. Due to the superheat from one fluid, vaporization occurs that results in a movement of interface by maintaining its initial straight line configuration. Depending on the superheated fluid, two types of problems are available: superheated vapour and saturated liquid (sup-vap/sat-liq); and saturated vapour and superheated liquid (sat-vap/sup-liq). For these problems, an analytical expression is available (Perez-Raya and Kandlikar, 2016) for the time-wise evolution of interface $x(t)$ and instantaneous temperature distribution $T(x, t)$ in superheated fluid; given as

$$x(t) = \begin{cases} 2\lambda_v \sqrt{\alpha_v t} & \text{sup-vap/sat-liq} \\ 2\lambda_l \sqrt{\alpha_l t} & \text{sat-vap/sup-liq} \end{cases} \quad (4.30)$$

and,

$$T(x, t) = \begin{cases} T_{sup} - (T_{sup} - T_{sat}) \frac{\operatorname{erf}(\frac{x}{2\sqrt{\alpha_v t}})}{\operatorname{erf}(\lambda_v)} & \text{sup-vap/sat-liq} \\ T_{sup} - (T_{sup} - T_{sat}) \frac{\operatorname{erf}(\frac{x}{2\sqrt{\alpha_l t}})}{\operatorname{erf}(\lambda_l)} & \text{sat-vap/sup-liq} \end{cases} \quad (4.31)$$

where α , T_{sup} , and T_{sat} corresponds to thermal diffusivity, superheated temperature, and saturation temperature, respectively. Here, the subscript ‘l’ and ‘v’ corresponds to properties associated with liquid and vapor, respectively. Whereas λ_v and λ_l are constants evaluated by solving transcendental equation, given as

$$\lambda_v h_v = \frac{c_v(T_{sup} - T_{sat})}{\sqrt{\pi} \exp(\lambda_v^2) \operatorname{erf}(\lambda_v)} ; \lambda_l h_l = \frac{\rho_l}{\rho_v} \frac{c_l(T_{sup} - T_{sat})}{\sqrt{\pi} \exp(\lambda_l^2) \operatorname{erfc}(\lambda_l)}$$

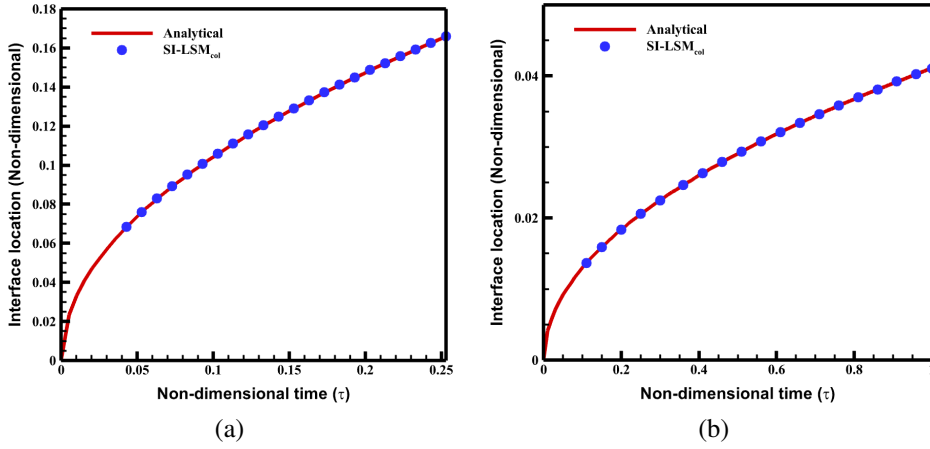


Figure 4.5: For one-dimensional moving interface problems, (a) superheated vapor-saturated liquid and (b) saturated vapor-superheated liquid, comparison of present SI-LSM_{col} and analytical solution (Perez-Raya and Kandlikar, 2016) for the time-wise evolution of interface.

For the present simulation on Cartesian coordinate, Fig. 4.3(b) shows computational domain of non-dimensional size 1×1 and 8×1 with a vertical interface for sup-vap/sat-liq and sat-vap/sup-liq, respectively. For initiating the temperature distribution in vapor (liquid) sub-domain for sup-vap/sat-liq (sat-vap/sup-liq) configuration, the simulation is initiated from non-dimensional physical time τ_0 of 0.033 (0.1), and wall superheat of 10 K for both simulations. Further, the thermo-physical properties for sup-vap/sat-liq (sat-vap/sup-liq) are $\rho_l/\rho_v = 60.37$ (1), $k_l/k_v = 5.28$ (10), $c_l/c_v = 1.34$ (1), $\mu_l/\mu_v = 22.22$ (100), and $h_{lv} = 3.29 \times 10^5$ (10⁴). Simulations are performed with grid size 100×100 till maximum non-dimensional time $\tau_{max} = 0.26$ for sup-vap/sat-liq, and 160×20 grid size till $\tau_{max} = 1$ for sat-vap/sup-liq; with non-dimensional time step $\Delta\tau = 10^{-3}$ for both simulations. Figure (4.5a) and (4.5b) shows a good agreement is obtained between present simulation and analytical for the time-wise evolution of the interface for sup-vap/sat-liq and sat-vap/sup-liq simulations.

4.3.3 One-dimensional sucking interface problem

One-dimensional sucking interface problem consist of interfacial mass transfer due temperature gradient at liquid phase. This results in propagation of the interface towards liquid phase due to volume expansion of generated vapor. For present validation, available analytical solution (Irfan and Muradoglu, 2017) for time-wise evolution of interface ($x_\Gamma(t)$) and instantaneous temperature distribution in liquid ($T_l(x, t)$) are utilized; given as

$$x_\Gamma(t) = 2\beta \sqrt{\alpha_v t} \quad (4.32)$$

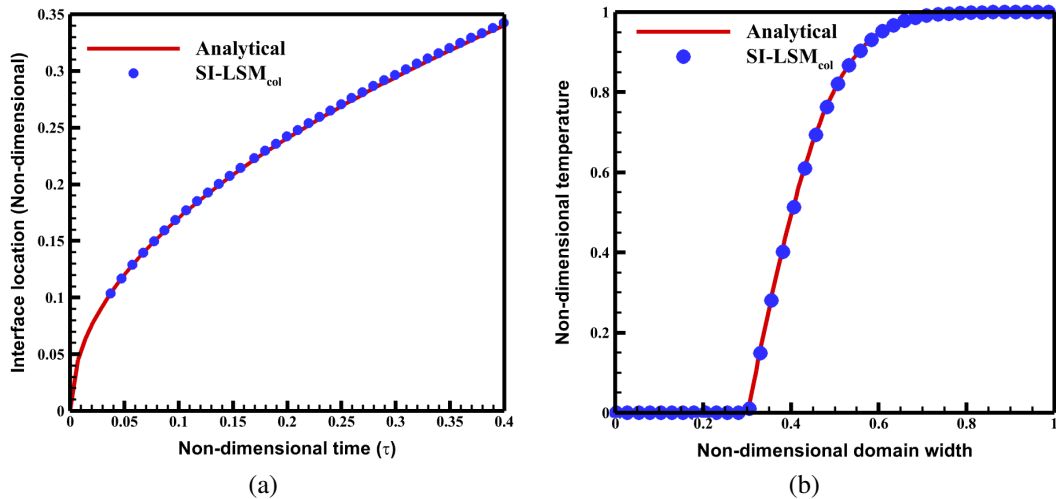


Figure 4.6: One-dimensional sucking interface problem simulated with present SI-LSM_{col} showing (a) time-wise evolution of interface and (b) temperature distribution at $\tau = 0.24$, and compared with analytical solution (Irfan and Muradoglu, 2017).

and,

$$T_l(x, t) = T_\infty - \left[\frac{T_\infty - T_w}{erfc(\beta \frac{\rho_v \sqrt{\alpha_v}}{\rho_l \sqrt{\alpha_l}})} \right] erfc\left(\frac{x}{2\sqrt{\alpha_l}t} + \frac{\beta(\rho_v - \rho_l)}{\rho_l} \sqrt{\frac{\alpha_v}{\alpha_l}} \right) \quad (4.33)$$

To solve Eq. (4.32) and (4.33) constant β is required, obtained by solving transcendental equation, given as

$$\exp(\beta^2) \operatorname{erf}(\beta) \left[\beta - \frac{(T_\infty - T_{sat}) c_{p,v} k_l \sqrt{\alpha_v} (-\beta^2 \frac{\rho_v^2 \alpha_v}{\rho_l^2 \alpha_l})}{h_l k_v \sqrt{\pi \alpha_l} \operatorname{erfc}(\beta \frac{\rho_v \sqrt{\alpha_v}}{\rho_l \sqrt{\alpha_l}})} \right] = \frac{c_{p,v} (T_w - T_{sat})}{h_l v \sqrt{\pi}}$$

For the present simulation on Cartesian coordinate, Fig. 4.3(c) shows a computational domain of size 1×1 with superheated liquid and saturated vapour separated by an initial vertical interface. To initiate the temperature field, simulation is commenced from non-dimensional time of 0.035, and resultant interface location and temperature distribution are evaluated using Eq. (4.32) and (4.33), respectively. The height of computational domain (h) is length scale (l_c), l_c^2/α is time scale (t_c), and α/l_c is velocity scale. Further, the thermo-physical properties are $\rho_l/\rho_v = 10$, $k_l/k_v = 0.43$, $c_l/c_v = 1$, $\mu_l/\mu_v = 14$, and $h_{lv} = 100$. The simulation is executed till non-dimensional time 0.4 with grid size of 200×200 . Figure 4.6 shows good agreement between present simulation and analytical solution for the time-wise evolution of interface and instantaneous temperature distribution.

4.3.4 Growth of suspended bubble in superheated liquid

Growth of suspended bubble in superheated liquid is a widely utilized test case for phase change solver coupled with Navier-Stokes equation. In this problem, initially a vapour bubble at saturation condition is placed inside a superheated liquid with uniform temperature distribution along the interface. Heat flux from the superheated layer results in vaporization, causing the initially spherical vapour to expand by maintaining the circular geometric characteristic of the interface. An analytical solution is available (Scriven, 1962) for the time-wise evolution of this radius and the instantaneous temperature distribution, given as

$$r(t) = 2\beta_g \sqrt{\frac{k_l}{c_{p,l}\rho_l} t} \quad (4.34)$$

and,

$$T = T_\infty - 2\beta_g^2 \left(\frac{\rho_v(H_{lv} + (c_{p,l} - c_{p,v})\Delta T)}{\rho_l c_{p,l}} \right) \times \\ \int_{1-\frac{R}{r}}^1 \exp \left(-\beta_g^2 ((1-\zeta)^{-2} - 2(1 - \frac{\rho_v}{\rho_l})\zeta - 1) \right) d\zeta \quad (4.35)$$

Here, β_g is growth constant evaluated from expression given as

$$\frac{\rho_l c_{p,l} \Delta T}{\rho_v (H_{lv} + (c_{p,l} - c_{p,v}) \Delta T)} = \\ 2\beta_g^2 \int_0^1 \exp \left(-\beta_g^2 ((1-\zeta)^{-2} - 2(1 - \frac{\rho_v}{\rho_l})\zeta - 1) \right) d\zeta \quad (4.36)$$

For the present two-dimensional simulation on Cylindrical coordinates, two test-cases with different thermo-physical properties are selected. To initiate temperature field, a vapor bubble of initial non-dimensional radius $R_0 = 0.5$ is selected and time required for bubble to grow till R_0 is calculated using Eq. (4.34). Further, Eq. (4.35) is solved for initial temperature distribution, and velocity is initialized with zero field. For case-1 (Malan, 2018), the thermo-physical properties are $\rho_l/\rho_v = 10$, $k_l/k_v = 10$, $c_l/c_v = 2.5$, $\mu_l/\mu_v = 10$, $h_{lv} = 100$, $\sigma = 10^{-3}$, and wall superheat $\Delta T = 3$. Whereas for case-2 (Sato and Ničeno, 2013), $\rho_l/\rho_v = 1605$, $k_l/k_v = 27.16$, $c_l/c_v = 2.07$, $\mu_l/\mu_v = 22.22$, $h_{lv} = 2.26 \times 10^6$, $\sigma = 0.059$, and wall superheat $\Delta T = 5$. Considering diameter of the initial vapor bubble (D_0) as length scale (l_c), l_c^2/α_l as time scale (t_c), and α/l_c as velocity scale, the non-dimensional geometric properties are shown in Fig. 4.3(d). The simulations are performed on grid 80×80 (400×400) till maximum non-dimension time $\tau_{max} = 0.8$ (1.1×10^{-3}) for the case-1 (case-2). Figure 4.7(a) and 4.7(b) shows good agreement is obtained between present simulation and analytical solution for the time-wise evolution of interface in both the cases.

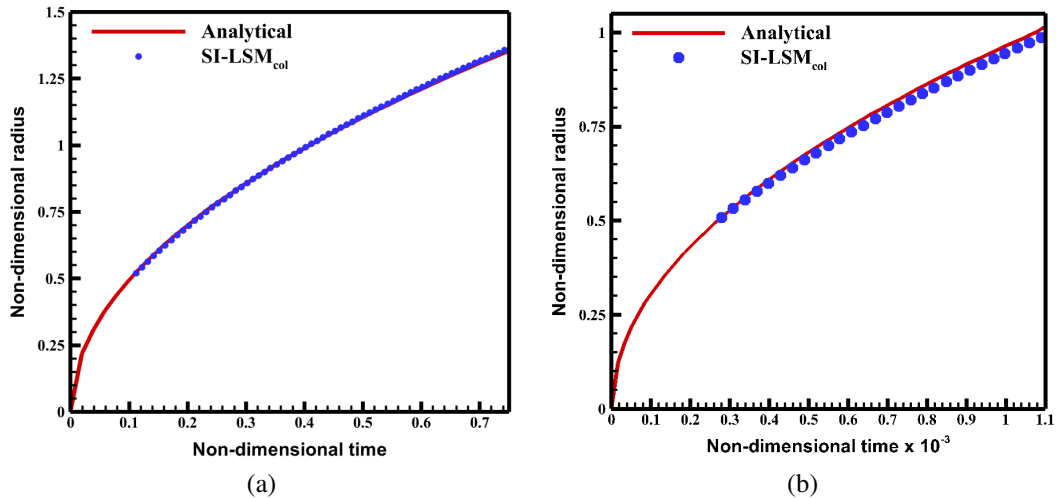


Figure 4.7: Growth of suspended bubble in superheated liquid simulated with present SI-LSM_{col} showing time-wise evolution of interface for (a) case-1 ($\rho_2/\rho_1 = 10$) and (b) case-2 ($\rho_2/\rho_1 = 1605$), and compared with analytical solution (Scriven, 1962).

4.3.5 Film boiling

Film boiling is an excellent test case of physical relevance to evaluate the performance of phase change solver coupled with conservation equations. In this problem, the saturated liquid is separated by superheated vapour which is in contact with a heated wall by an initially perturbed interface. Due to the instability associated with density gradient, caused by heavier saturated liquid at the top and lighter superheated vapour at the bottom, leads to a periodic bubble detachment at the node and anti-node locations. For the present two-dimensional simulation on Cartesian coordinate, Fig. 4.3(e) shows a computational domain of non-dimensional size $l \times h$. To initialize the flow field, velocity and pressure are taken as zero, whereas the temperature is varied linearly from initially perturbed interface to the bottom wall in the vapour domain and constant saturation temperature throughout liquid. The initially perturbed interface is given as

$$\phi = Y_{int} - Y = 0.025(\lambda_d/l_c) + 0.0025(\lambda_d/l_c)\cos\left(\frac{\pi X}{0.5\lambda_d}\right) - Y \quad (4.37)$$

Considering $\sqrt{\sigma/g(\rho_l-\rho_v)}$ as length scale (l_c), $\sqrt{gl_c}$ as velocity scale (u_c), l_c/u_c as time scale, and ΔT as temperature scale, width and height of computational domain are taken as $l = 0.5\lambda_d/l_c$ and $h = \lambda_d/l_c$, respectively; where λ_d is the most critical Taylor wavelength defined as $\lambda_d = 2\pi\sqrt{3\sigma/g(\rho_l-\rho_v)}$. Further, the non-dimensional thermo-physical properties (Tomar *et al.*, 2005) are $\rho_l/\rho_v = 1.66$, $k_l/k_v = 1.01$, $c_l/c_v = 0.62$, $\mu_l/\mu_v = 1.44$, $h_{lv} = 276400$, $\sigma = 7 \times 10^{-5}$, and wall superheat $\Delta T = 5$. The simulation is performed on a grid size of 150×300 till a maximum non-dimensional time $\tau_{max} = 400$.

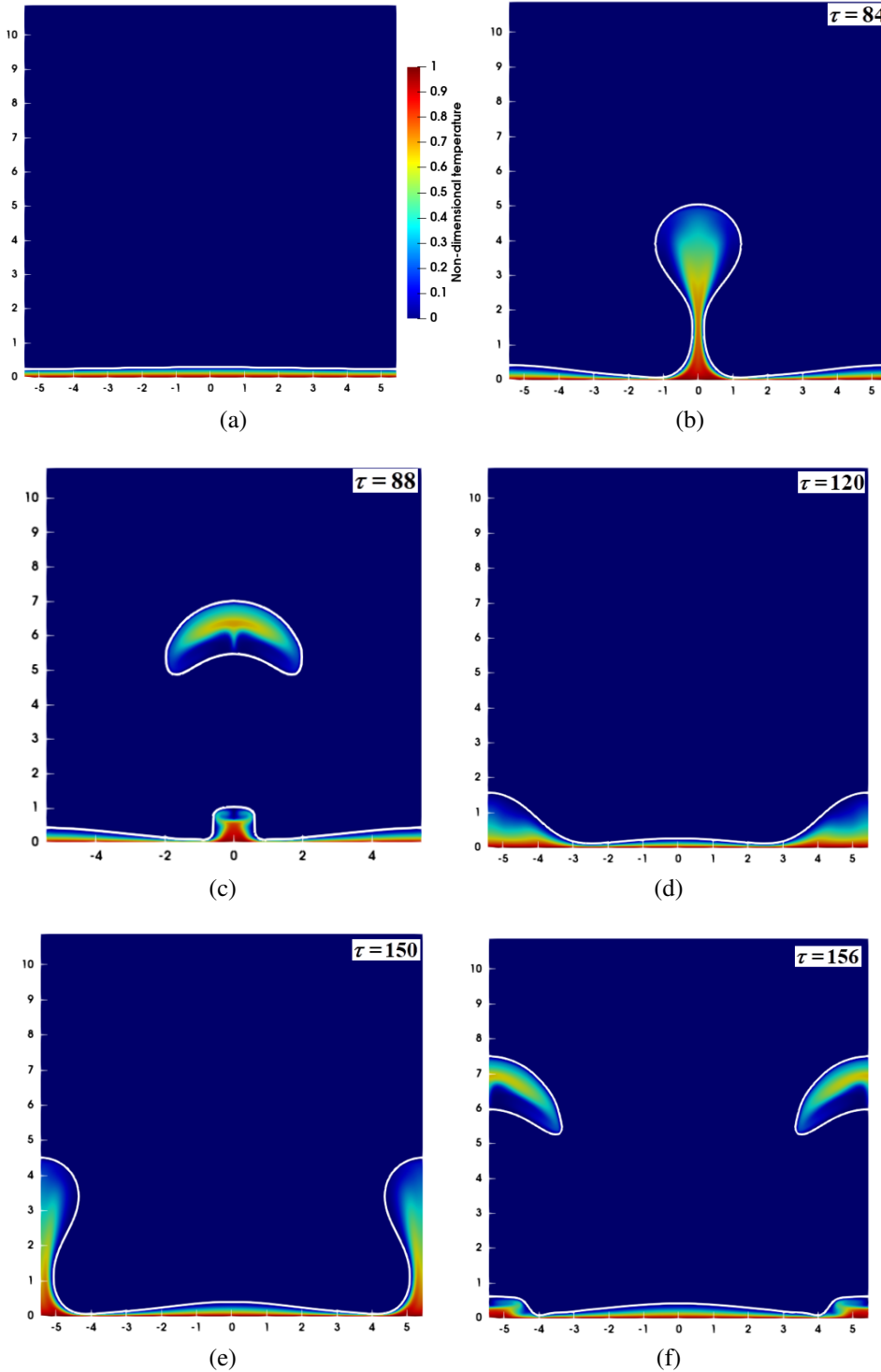


Figure 4.8: Bubble dynamics in film boiling simulation obtained with present SI-LSM_{col}, observed at various non-dimensional time (a) $\tau=0$, (b) $\tau=84$, (c) $\tau=88$, (d) $\tau=120$, (e) $\tau=150$ and (f) $\tau=156$. The colour contour shows the non-dimensional temperature distribution within the vapour.

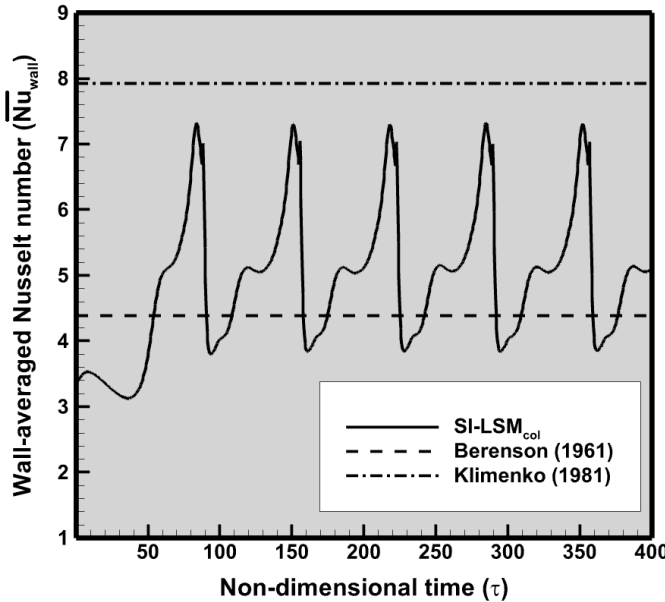


Figure 4.9: Film boiling simulated with present SI-LSM_{col} showing time-wise evolution of wall averaged Nusselt number \bar{Nu}_{wall} and compared with the correlations of Berenson (Berenson, 1961) and Klimenko (Klimenko, 1981).

Using the above mentioned parameters Fig. 4.8 shows SI-LSM_{col}-based results on bubble dynamics during film boiling simulation. The Fig. 4.8(a) shows the initial configuration of the perturbed interface, defined using Eq. (4.37). Due to the wall superheat and the associated interfacial mass transfer, the generated vapour accumulates at the node location. The increased buoyancy, due to the gravitational field, dominates the interfacial forces resulting in the departure of the bubble from the node location as shown in Fig. 4.8(b). Once the bubble departure occurs as in Fig. 4.8(c), Fig. 4.8(d) shows that the remaining vapour film recoils leading to the vapour accumulation at the anti-node location. Similar to the phenomenon in the node location, Fig. 4.8(e,f) shows the bubble departure from the anti-node. This process continuous and results in the periodic bubble release from node and anti-node. For the validation study, the wall averaged Nusselt number (\bar{Nu}_{wall}) is evaluated, given as

$$\bar{Nu}_{wall} = \frac{1}{L} \int_0^L Nu_{wall} dY$$

where L is the domain width and $Nu_{wall}(= \left. \frac{\partial \theta}{\partial Y} \right|_{Y=0})$ is the local Nusselt number computed at the superheated wall. Figure 4.9 show a temporal evolution of \bar{Nu}_{wall} for the various cycles of vapour bubble release, with a dynamic steady state condition achieved from the second cycle onwards. The figure also shows that the present SI-LSM-based computed \bar{Nu}_{wall} lies in-between the \bar{Nu}_{wall} obtained from the Berenson (Berenson, 1961) and Klimenko (Klimenko, 1981) correlations. Further, the maximum and minimum \bar{Nu}_{wall} in a cycle is

compared with the simulation results of Gada (2012). This is shown in Table 4.1 with good agreement between the present SI-LSM_{col} and that obtained by Gada (2012) for DI-LSM on a staggered grid.

Table 4.1: Film boiling simulated with present SI-LSM_{col} showing minimum and maximum wall averaged Nusselt number ($\overline{Nu}_{wall,min}$ and $\overline{Nu}_{wall,max}$) , and compared with results of Gada (2012) simulated with diffuse interface level set method on staggered grid.

Simulation	$\overline{Nu}_{wall,min}$	% error ($\overline{Nu}_{wall,min}$)	$\overline{Nu}_{wall,max}$	% error ($\overline{Nu}_{wall,max}$)
Gada (2012)	3.86		7.60	
Present	3.79	1.77	7.30	3.94

4.3.6 Single bubble dynamics in nucleate boiling

Single bubble nucleate boiling simulation is a physically relevant and computationally challenging problem due to the complex interaction between interfacial forces, mass flux due to phase change, contact line dynamics, micro-layer etc. On co-located grid, algorithms capable to avoid both pressure-velocity decoupling and pressure-interfacial force imbalance simultaneously will be able to perform nucleate boiling simulation, especially for high density ratio cases. Hence, nucleate boiling simulation with water and its vapour $\chi = 1605$ is an ideal test case to demonstrate the robustness of present SI-LSM_{col} in handling the high density ratio CmFD problems with phase change. Further, to validate nucleate boiling, experiment performed with distilled water by Siegel and Keshock (1964) is utilized. In their experiment, for single bubble formed during nucleate boiling its growth rate, departure diameter, contact angle etc., are compared between normal and reduced gravity conditions. In this study, a commonly utilized computational set-up with wall superheat ($T_{wall} - T_{sat}$) of 6.2 K and contact angle with 38° under normal gravity condition is considered.

For the present two-dimensional simulation on Cylindrical coordinate, Fig. 4.3(f) shows the computational domain and boundary conditions. As shown in figure, the domain is initialized with a vapor seed at saturation condition surrounded with superheated liquid due to the presence of superheated wall. To initialize the temperature distribution in liquid, turbulent natural convection boundary thickness is utilized, given as

$$\delta_{TBL} = 7.14(\nu_l \alpha_l / g \beta_T \Delta T)^{1/3}$$

where δ_{TBL} , ν_l , α_l , and β_T represents initial thermal boundary layer thickness, kinematic viscosity, thermal diffusivity, and coefficient of thermal expansion, respectively. To ini-

tialize non-dimensional temperature field, it is assumed to vary linearly from $\theta = 1$ to $\theta = 0$ across δ_{TBL} , and with zero value above δ_{TBL} and in vapor. Since vapor is assumed to be at saturation energy equation is solved only on liquid. Considering $\sqrt{\sigma/g(\rho_l - \rho_v)}$ as length scale (l_c), $\sqrt{gl_c}$ as velocity scale (u_c), l_c/u_c as time scale, and ΔT as temperature scale the non-dimensional geometric properties of computational domain are shown in Fig. 4.3(f). Further, since water and its vapor is the working fluid, non-dimensional thermo-physical properties is similar to case-2 set-up in previous subsection for growth of suspended bubble in superheated liquid. The simulations are performed on grid 100×300 and non-dimensional time step $\Delta\tau = 10^{-5}$, till bubble growth rate attains dynamics steady condition.

Apart from numerical modelling for above macro scale phenomenon, for nucleate boiling simulation a micro-layer model is required to capture interfacial mass-flux from thin liquid layer beneath the bubble. Since, length scale of micro-layer is much smaller than grid size, a micro-layer model of Utaka *et al.* (2013) is utilized here, which was numerically implemented by Sato and Niceno (2015) as depletable micro-layer model. In this model, the thickness of micro-layer is assumed to vary linear from the nuclei location (seed location) to the triple point, given a

$$\delta_{ml} = C_{slope} r_{ml} \quad (4.38)$$

where δ_{ml} is micro-layer thickness, C_{slope} is a constant assumed to depend on heater material, its surface roughness and system pressure (Sato and Niceno, 2015), and r_{ml} is the radial distance from seed location to cell-center of control volume. Once δ_{ml} is defined, assuming Peclet number (Pe) less than unity (dominance of thermal diffusion over advection) in the micro-layer, the heat flux in the micro-layer (q_{ml}) is given as

$$q_{ml} = k_l \left(\frac{T_{wall} - T_{sat}}{\delta_{ml}} \right) \quad (4.39)$$

Further, the interfacial mass flux (\dot{m}_{ml}) is given as

$$\dot{m}_{ml} = q_{ml}/h_b \quad (4.40)$$

Assuming one-dimensional model for vaporization phenomenon from micro-layer (Sato and Niceno, 2015), the reduction in micro-layer thickness is given as

$$\frac{d\delta}{dt} = -\frac{1}{\rho_l} \dot{m}_{ml} \quad (4.41)$$

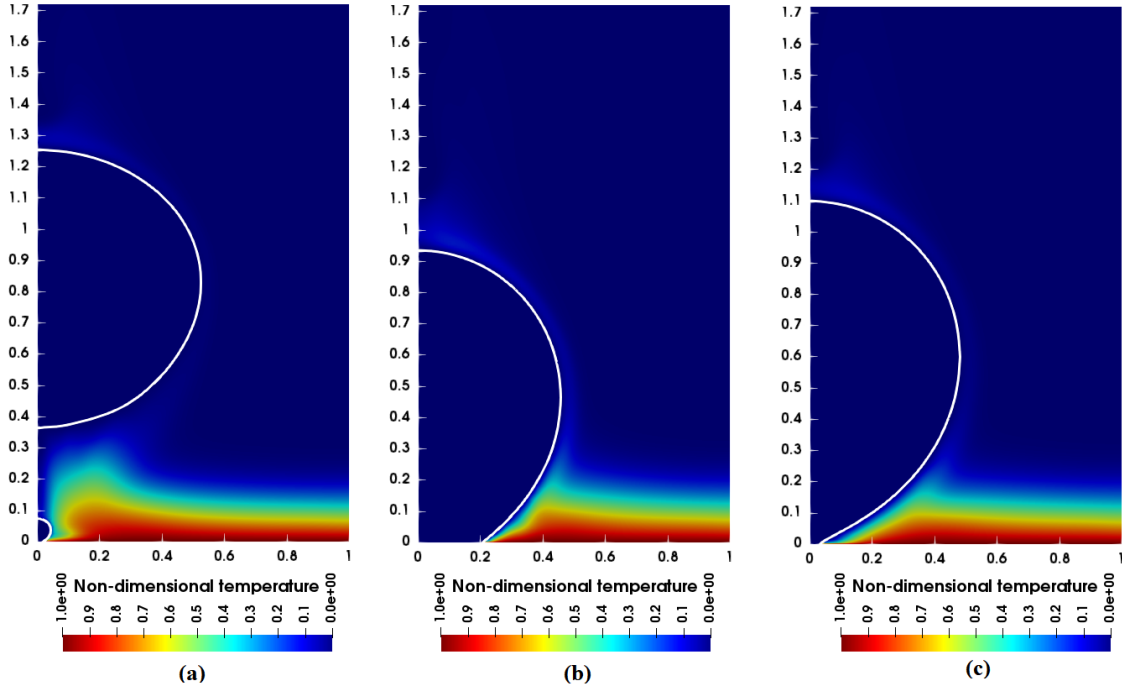


Figure 4.10: Single bubble nucleate boiling simulated with present SI-LSM_{col} for wall superheat of 6.17 K and static contact angle of 38°. The figure shows the bubble shape and temperature distribution at various instances of ebullition cycle, (a) seeding of a new bubble (b) maximum base area covered during growth phase and (c) at the instance prior to bubble departure.

Utilizing Euler explicit method for time, the above equation is discretized as

$$\delta^{n+1} = \delta^n - \frac{\Delta t}{\rho_l} \dot{m}_{ml}^n \quad (4.42)$$

The depletable micro-layer is implemented into present SI-LSM_{col} and the single bubble nucleate boiling is simulated. Figure 4.10 shows the ebullition cycle obtained with C_{slope} value of 2.2×10^{-2} and with aforementioned parameters. Figure 4.10(a) shows the instance in an ebullition cycle in which new bubble seed is placed and the associated temperature distribution in the liquid phase. Since a constant wall temperature boundary condition is specified in this problem, the waiting time between the departed bubble and the seeded bubble is assumed to be constant to prevent interaction between departed bubble and seeded bubble. The bubble grows due to the interfacial mass flux from bulk liquid and micro-layer causing the base area of the bubble to increase to a maximum value and remains stagnant prior to receding phase, which is shown in Fig. 4.10(b). Once the buoyancy force overcomes the forces holding the bubble to the wall, the bubble base area reduces indicating beginning of receding phase. Finally as shown in Fig. 4.10(c) the bubble departure occurs and leaves the wall surface causing the liquid to fill the vacant region. To validate the growth rate of the bubble, several cycles of ebullition cycle is

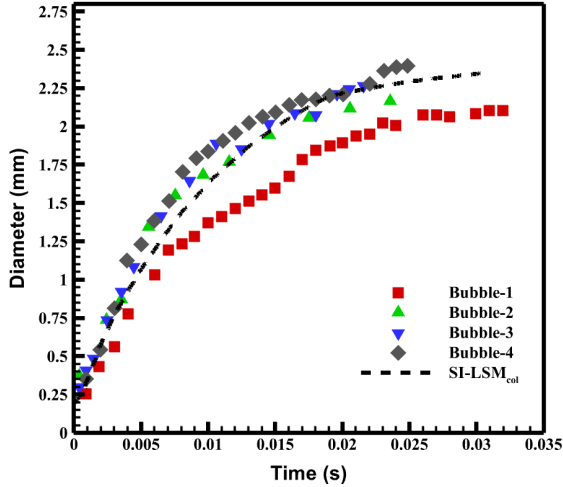


Figure 4.11: Single bubble nucleate boiling simulation with present $\text{SI-LSM}_{\text{col}}$ showing the time-wise evolution of apparent diameter of bubble from seeding to departure and compared with published experiment (Siegel and Keshock, 1964). The simulation corresponds to wall superheat value of 6.17 K and a static contact angle of 38° .

simulated and the results are taken once a dynamic steady condition is observed. Figure 4.11 shows the validation of bubble growth with the experimental of Siegel and Keshock (1964). In their experiment, four different bubbles were measured from a single nucleation site under similar conditions, marked as Bubble-1, Bubble-2, Bubble-3 and Bubble-4 in the Fig. 4.11. The comparison shows good agreement between present $\text{SI-LSM}_{\text{col}}$ and published experiment (Siegel and Keshock, 1964).

4.4 Closure

From the previous chapters, the benefit of GFM-based SI-LSM over conventional methodologies are presented. Further, utilizing variety of CmFD solvers the computational performance and robustness of present $\text{SI-LSM}_{\text{col}}$ are evaluated. Considering this, phase change model was added to the solver and tested with several benchmark CmFD problems. Good agreement is obtained with various analytical, numerical, and experimental results compared. Moreover, validation of complex multiphase phenomenon like single bubble nucleate boiling shows the robustness and accuracy of present in-house solver utilized to perform NBPT discussed in following chapters.

PART-II

CmFD Application and Analysis of Single Bubble Nucleate Boiling with Power Transients

Chapter 5

Single bubble nucleate boiling over a base plate, subjected to Power Transients

Chapter 4

Effect of Heating Patterns on Single Bubble Nucleate Boiling over a Base Plate

This part consist of two chapters, discuss about the CmFD application and analysis—single bubble nucleate boiling with power transients. In chapter 5, the numerical methodology formulated to perform study on NBPT is discussed along with parametrization of periodic exponential heat flux. Utilizing the same, effect of exponential power transients on single bubble dynamics—bubble departure diameter, bubble growth period, and bubble departure frequency—are discussed. Realizing the requirement of understanding the effect of other modes of power transients, in chapter 6, variation of bubble dynamics parameter for various power transients are investigated. The numerical formulation developed in chapter 5 with exponential power transients is utilized in chapter 6 for different power transients.

Chapter 5

Single bubble nucleate boiling over a base plate, subjected to Power Transients

5.1 Introduction

Nucleate Boiling with Power Transients (NBPT) is a prominent research area with significant industrial application, but not yet utilized the potential of numerical investigation. Power transients have significant effect on nucleate boiling phenomenon as compared to steady heating (Rosenthal, 1957). Thus, relevant to various industries like nuclear reactor, electronic cooling etc. Because in nuclear reactors, the control rod withdrawal can lead to exponential heat generation which can further lead to accidents if not properly controlled (Su *et al.*, 2016). In electronic industries for cooling application, the working load on the components can generate transient heat inputs which alter the performance of cooling system if not designed accordingly. Considering these implications, numerous experimental studies have been conducted in NBPT, discussed earlier in literature survey. From these literatures it could be inferred that currently in the field of NBPT, the trend is to determine the effect of power transients on either boiling curve, ONB or CHF without any attention on bubble dynamics. Hence, this study investigates the effect of power transients on bubble dynamic parameters in the regime of partially developed nucleate boiling (single bubble) which is established utilizing developed SI-LSM_{col}.

5.2 Mathematical and Numerical Details

A sharp interface Level Set Method (Chirammel *et al.*, 2023a), based on a jump condition formulation and implemented on a co-located grid, is utilized for the single bubble nucleate boiling simulation subjected to power transients. This methodology follows a sub-domain conservation law-based formulation, where the conservation equations are solved for each fluid by considering the interfacial jump as a boundary condition while solving the pressure Poisson equation. The non-dimensional form of these conservation equations and subsidiary equations are given as

Volume conservation or Continuity equation:

$$\nabla \cdot \vec{U} = 0 \quad (5.1)$$

Mass-conservation or Level set advection Equation:

$$\frac{\partial \phi}{\partial \tau} + \vec{U}_a \cdot \nabla \phi = 0 \quad (5.2)$$

Momentum equation:

$$\frac{\partial (\chi_i \vec{U})}{\partial \tau} + \nabla \cdot (\chi_i \vec{U} \vec{U}) = -\nabla P + \frac{1}{Re_1} \nabla \cdot (2\eta_i D) - \frac{\chi_i}{Fr^2} \hat{J} \quad (5.3)$$

Energy equation:

$$\frac{\partial \theta}{\partial \tau} + \nabla \cdot (\vec{U} \theta) = \frac{1}{Re_i Pr_i} \nabla \cdot (\nabla \theta) \quad (5.4)$$

where τ , \vec{U} , P , θ , and D are non-dimensional time, velocity, pressure, temperature, and rate of deformation tensor. Further, χ is density ratio, η is viscosity ratio; and Re is Reynolds number, Fr is Froude number, and Pr is Prandtl number respectively, in the non-dimensional form.

Apart from the above conservation equations (Gada and Sharma, 2009a), subsidiary equations are also involved; given as

Reinitialization equation:

$$\frac{\partial \phi}{\partial \tau_s} = S_\varepsilon(\phi_0)(1 - |\nabla \phi|) \quad (5.5)$$

Extrapolation equation:

$$\frac{\partial F}{\partial \tau_s} + \hat{N} \cdot \nabla F = 0 \quad (5.6)$$

where τ_s , $S_\varepsilon(\phi_0)$, and F represents pseudo time step, smoothed sign function (Sussman *et al.*, 1994), and variable extrapolated in the normal direction across the interface. Here,

F corresponds to the normal temperature gradient $\partial\theta/\partial N$, which is utilized to compute the interfacial mass flux.

A semi-explicit method (Sharma, 2016) based on Projection method is utilized for solving the conservation equations on a co-located grid system. The algebraic formulation of the conservation equations (Eq. 5.1, 5.3 and 5.4) are derived utilizing a physical law-based finite volume method (Sharma, 2016). Whereas the level set advection (Eq. 5.2), reinitialization (Eq. 5.5) and the extrapolation (Eq. 5.6) equations are discretized with finite difference method. In the momentum as well as energy equation, the diffusion and advection term are discretized with central difference method and 3rd order Lin-Lin total variation diminishing scheme (Date, 2005), respectively. Whereas for the level set equations, the temporal and advection terms are discretized with 3rd order Runge-Kutta method and 5th order WENO (weighted essentially non-oscillatory) scheme. A detailed discussion of the present mathematical formulation and numerical methodology is provided in Part I of the thesis.

5.3 Validation study: Single bubble Nucleate Boiling over a plate

Even though water is commonly utilized to investigate nucleate boiling phenomenon, Ethanol is also considered as a viable working fluid (Kalani and Kandlikar, 2013) for thermal management of electronic components. Recent studies also focus significantly on Ethanol due to its lower boiling point at atmospheric conditions, high latent heat of vaporization, and heat transfer performance (Kalani and Kandlikar, 2013; Utaka *et al.*, 2014; Zakšek *et al.*, 2020) as compared to the other refrigerants. Thus, in the present study, ethanol and its vapor are used as the working fluid. Moreover, considering the applicability for thermal management in electronic devices, a contact angle of 15° is utilized throughout this study; corresponding to contact angle between ethanol and silicon (Spencer *et al.*, 2013). The capability of the present SI-LSM_{col} to simulate nucleate boiling is demonstrated by a validation study with water and ethanol as working fluid. Previously published experimental results of Siegel and Keshock (1964) is utilized for the water and that of Bovard *et al.* (2017) for the ethanol as working fluid. Their thermo-physical properties are shown in Table 5.1.

For simulation, Fig. 5.1 shows a two-dimensional *axisymmetric* domain, with a symmetric, no-slip, free-slip, and an outflow boundary conditions at the west, south, east, and north boundaries of the computational domain, respectively. For the initial condition, a zero velocity field, a linearly varying temperature field (inside thermal boundary layer

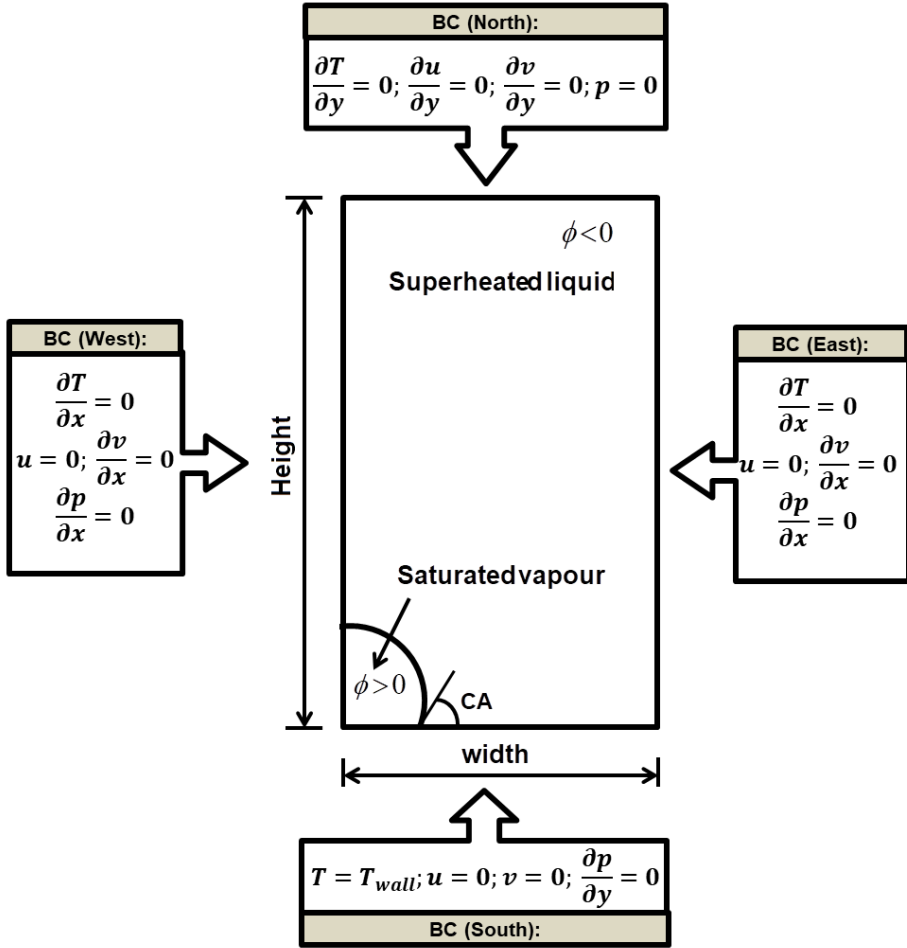


Figure 5.1: Schematic of computational domain and boundary conditions utilized for validation with experimental results of Siegel and Keshock (1964), and Bovard *et al.* (2017).

thickness, specified utilizing turbulent natural convection boundary layer thickness, with a constant temperature outside the boundary layer), and a specified initial seed size (Son *et al.*, 1999) are considered. The axisymmetric computational domain is of size 1×3 (non-dimensional with length scale, $l_c = \sqrt{\sigma/g(\rho_1 - \rho_v)}$ and velocity scale, $u_c = \sqrt{gl_c}$) with grid size 100×300 . A static contact angle of 38° and a *constant wall superheat* of 6.17 K are considered for water. Whereas, for ethanol a static contact angle of 22° (ethanol-copper) and *steady heat flux* value of 9540 W/m^2 are considered in our validation study.

For water as working fluid, Fig. 5.2 shows a good agreement between experiment and present SI-LSM_{col}-based results for the temporal variation of the apparent diameter of vapor bubble. The lower limit and upper limit in the Figure 5.2 corresponds to the minimum and maximum apparent diameter, respectively; among various reported diameter of nucleated single bubble, under same operating conditions in experiment (Siegel and Keshock, 1964). For ethanol with steady heat flux boundary condition, a departure

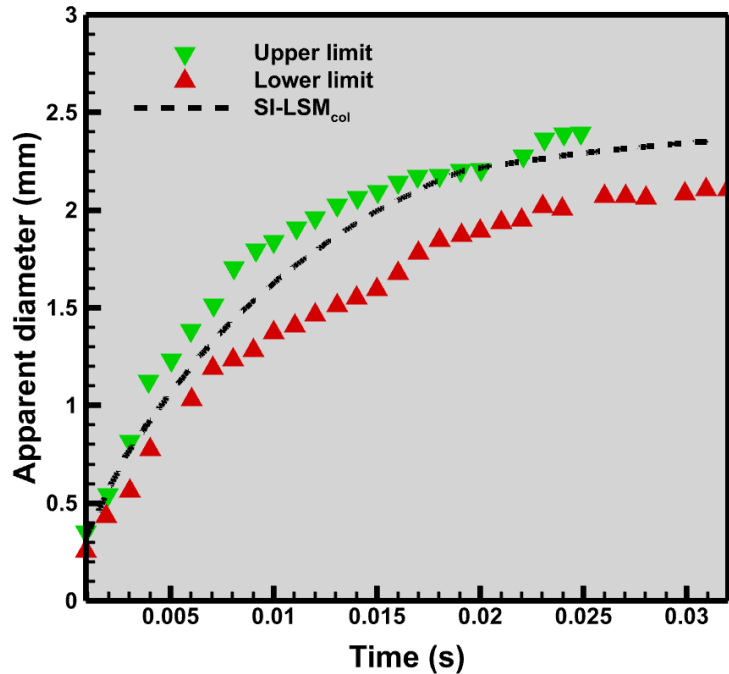


Figure 5.2: Validation of present in-house code $\text{SI-LSM}_{\text{col}}$ for single bubble dynamics in nucleate boiling utilizing Siegel and Keshock (1964).

Table 5.1: Thermo-physical properties of water and ethanol, utilized for the single bubble nucleate boiling simulation.

Fluid		ρ (kg/m^3)	k (W/mK)	c_p (J/kgK)	μ (Ns/m^2)	σ (N/m)	h (J/kg)
Water	Liquid	958.4	0.679	4216	2.8×10^{-4}	0.059	2.26×10^6
	Vapor	0.597	0.025	2030	1.26×10^{-5}		
Ethanol	Liquid	757.8	0.154	3000	4.29×10^{-4}	0.018	9.63×10^5
	Vapor	1.435	0.020	1830	1.04×10^{-5}		

diameter of 1.01 mm was obtained with present simulation whereas Bovard *et al.* (2017) reported 0.97 mm for surface roughness of $0.03 \times 10^{-3} \text{ m}$ on copper substrate, with a deviation of 4.12% between the present simulation and the published experiment (Bovard *et al.*, 2017).

5.4 Computational Modelling: Nucleate Boiling over a base plate, subjected to a periodic Heat-Flux

Two major constraints for performing the single bubble nucleate boiling simulation with power transients are computational setup for the initial condition and parametrization of transient heat flux. Thus, to initialize the simulation in this study, *a prevailing physical condition* on boiling with power transients is resorted. In practical scenarios, a *sudden*

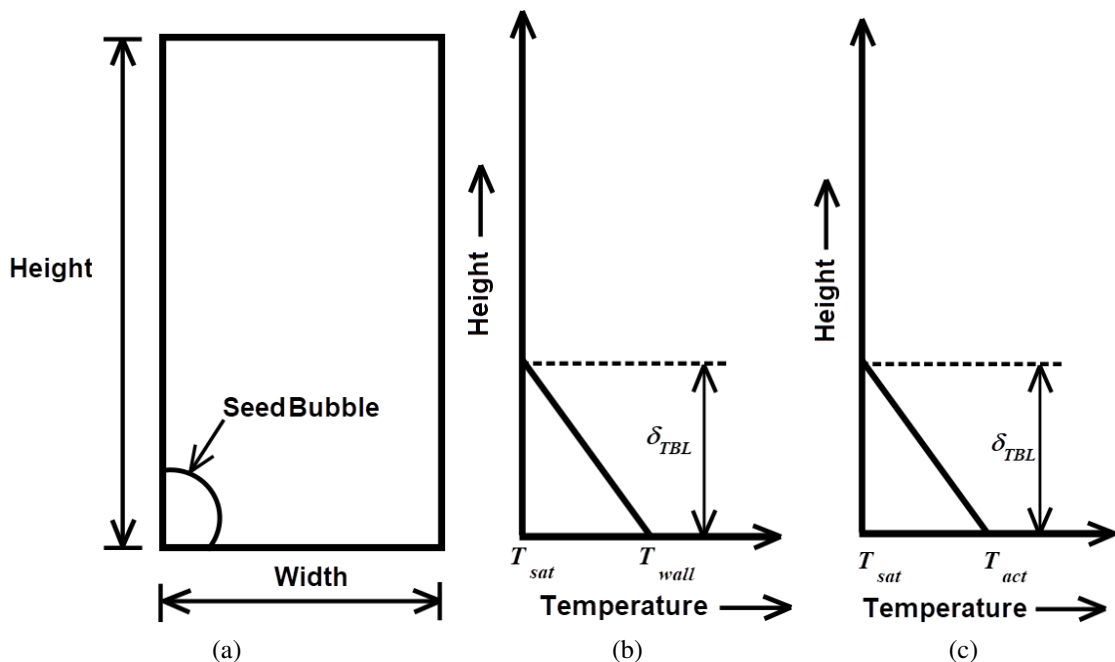


Figure 5.3: For the nucleate boiling simulation subjected to steady heating conditions, with (a) showing the computational domain with initial bubble seed, and schematic of initial temperature distribution in the near-wall liquid region for (b) constant wall temperature T_W and (c) uniform heat flux boundary condition for the base plate.

shift from steady heating condition to power transients could be seen in nuclear reactors and electronic devices during instantaneous removal of control rods in nuclear reactors (Su *et al.*, 2015) and while performing process intensive applications on electronic devices (Mathew and Krishnan, 2022). This is implemented in our computational methodology presented below. Whereas, the parametrization of the transient heat flux is carried out by varying the time wise evolving heat flux in *cyclic* manner and also ensuring the total heat input during each cycle remains *constant*. This mode of heat flux variation enables us to compare steady and transient heat flux conditions and perform parametric investigation on the effect of various parameters associated with transient heat flux on single bubble dynamics. A detailed formulation of the present problem is presented below.

5.4.1 Designing of input heat flux for power transients with periodic exponential heating

In macroscopic nucleate boiling simulations, the initial condition for the flow field variables like velocity, pressure and temperature need to be specified. Commonly, a zero field variables are defined for velocity and pressure. While for temperature, the thermal boundary layer thickness calculated based on turbulent natural convection heat transfer is

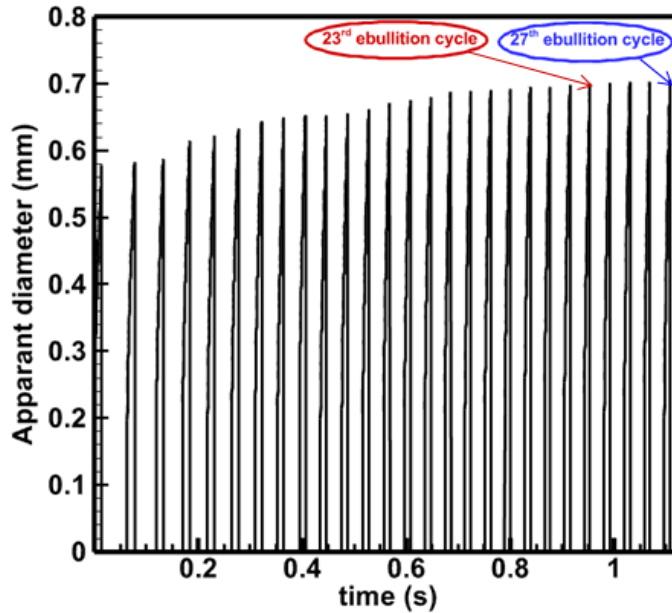


Figure 5.4: Evolution of ebullition cycle with time for an ethanol vapor bubble subjected to steady heat flux $q_{steady} = 5000 \text{ W/m}^2$. No appreciable difference in bubble departure diameter D_d , bubble growth period t_g and bubble waiting period t_w of the vapor bubble between 23rd and 27th ebullition cycle could be noticed.

utilized (Son *et al.*, 1999); given as

$$\delta_{TBL} = 7.14(\mu_l \alpha_l / g \beta_T \Delta T)^{1/3} \quad (5.7)$$

where δ_{TBL} is the thermal boundary layer thickness. Further, μ_l , α_l , g , β_T and ΔT corresponds to dynamic viscosity of liquid, thermal diffusivity of liquid, acceleration due to gravity, coefficient of thermal expansion and wall superheat, respectively.

Under saturated boiling condition with constant wall temperature T_W , the initial temperature field is assumed to vary linearly across this layer from $T(x, \delta_{TBL}) = T_{sat}$ to $T(x, 0) = T_W (> T_{sat})$ and the fluid above this superheated layer is assumed to be at T_{sat} . The schematic of this initial temperature distribution in the computational domain is shown in Fig. 5.3, where Fig. 5.3(a) represents the schematic of the computational domain with the initial bubble seed. This procedure is followed if the bottom wall of the computational domain is maintained at constant wall temperature T_W , as shown in Fig. 5.3(b). Whereas, in the case of constant heat flux boundary condition as in Fig. 5.3(b), the δ_{TBL} from Eq. 5.7 is calculated (Sato and Niceno, 2015) by considering ($\Delta T = T_{act} - T_{sat}$), where T_{act} is the activation temperature at which the seed-bubble gets activated from the cavity.

Further, for power transients simulation, the periodic heat flux variation is assumed here to initiate after steady heating; as mentioned previously. Thus, the initial condition

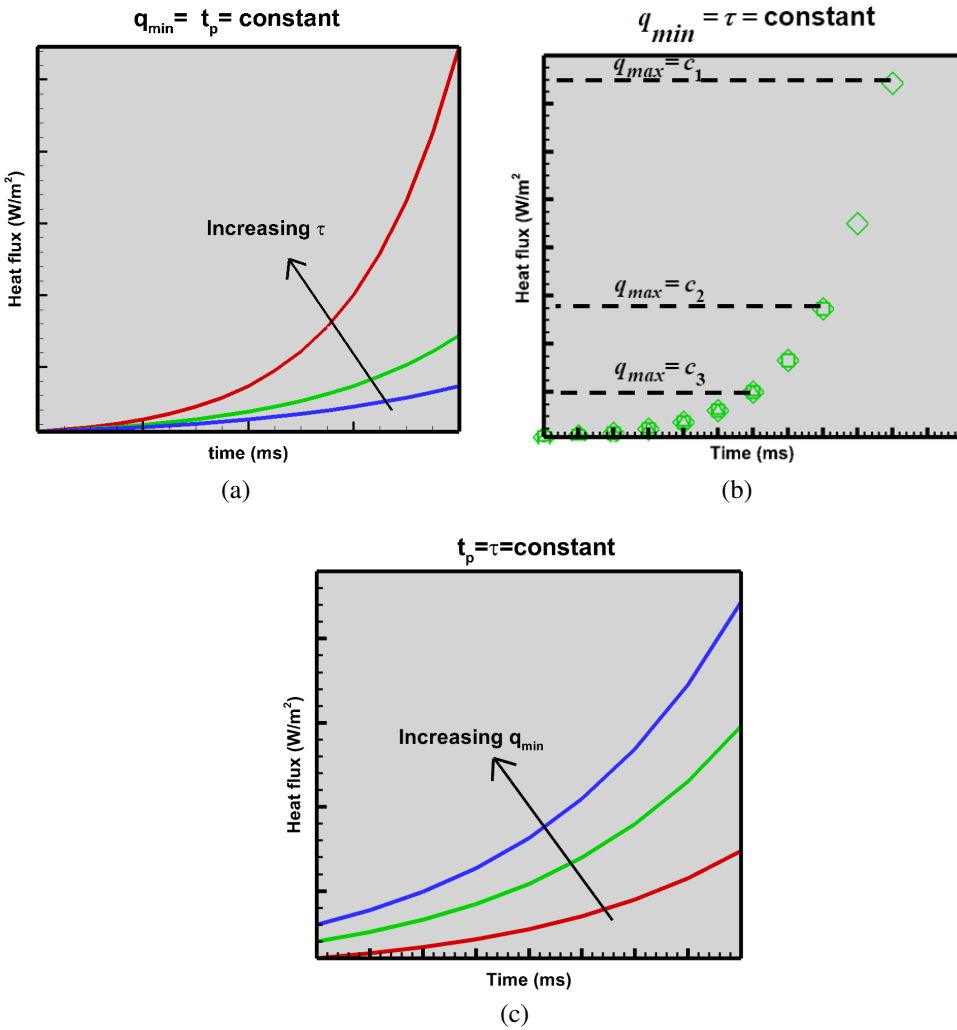


Figure 5.5: Variation of heat flux with time during exponential mode of heating when (a) q_{\min} and t_p are constant, (b) q_{\min} and τ are constant, and (c) t_p and τ are constant.

for the periodic heat flux corresponds to the velocity, pressure and temperature field that is obtained from a steady heat flux BC; after the boiling reaches a periodic state. For example, the time-wise growth of an ethanol vapor bubble is computed with steady heat flux $q_{\text{steady}} = 5000 \text{ W/m}^2$ (for initial condition), activation temperature $T_{act} = 83.3 \text{ K}$, grid size 100×300 , initial seed radius of $100 \mu\text{m}$, and static contact angle $\theta = 15^\circ$. The criterion for the selection of these parameters are discussed later.

For the steady heat-flux BC, Fig. 5.4 shows the initial transients in departure diameter of the released vapor bubble and finally achieving dynamic steady state condition. Between 23rd and 27th ebullition cycle the bubble departure diameter (D_d), bubble growth period (t_g), and bubble waiting period (t_w) shows an increase of 0.78%, 0.72%, and 0.30%, respectively. Once such a dynamic steady state condition is established, then the required

periodic heat-flux could be initiated and the behaviour of vapor bubble under such transients is investigated.

Since the present study is on the effect of an exponential mode of power transients, the transient variation in heat flux is considered as in published literatures (Su *et al.*, 2016; Walunj and Sathyabhamma, 2016), given as

$$q(t) = q_{min} \exp(t/\tau) \quad (5.8)$$

where $q(t)$, q_{min} , t and τ denotes transient heat flux, minimum heat flux from which exponential transient initiates, time associated with heating, and exponential or excursion time, respectively. Further, for a periodic exponential heating between minimum and maximum heat fluxes (q_{min} and q_{max}), the time period of heating cycle is varied periodically between $t = 0$ and $t = t_p$, where t_p is the time period of the periodically varying exponential heat-flux boundary condition. Thus, for the exponential heat flux as shown in Eq. (5.8) q_{min} , t_p , and τ characterises the input periodic heat flux whereas only excursion time τ has been investigated in literatures. To understand the dependency between each of these parameters, a schematic representation is plotted in Fig. 5.5 by varying one of the parameter and keeping the other parameters as constant. Fig. 5.5(a) shows the effect of excursion time τ on transient heat flux $q(t)$ while keeping q_{min} and t_p as constant. When the τ decreases, there is a sharper increase in the transient heat flux since lower excursion time (τ) lead to a higher ramp rate ($1/\tau$). Further, in Fig. 5.5(b) q_{min} and τ are kept constant and the time period t_p is varied. This causes the heat flux curve to follow the same path resulting in increase maximum heat flux with the time period t_p of periodic heating. Finally, in Fig. 5.5(c) t_p and τ are held constant and q_{min} is varied. The figure shows an increase in q_{max} with increasing q_{min} . Hence, for the periodic exponential heat-flux, q_{min} , t_p and τ have significant influence on the heat input, that need to be accounted.

In the present study, the design of power transients is based on two objectives—comparison of vapor bubble between the steady and periodic heating conditions and influence of the various parameters governing the periodic heat-flux. Now that we have identified the parameters which govern the periodic exponential heat-flux, one would have to bring it to a proper *basis* of comparison for the present parametric study on periodic heating. Moreover, we also need a proper basis for comparison of the present periodic heat flux results with those for the steady heat-flux cases. Thus, a common parameter for such a comparison is chosen as the average heat flux. Thus, for a proper basis of comparison, Eq. 5.8 is expressed in terms of the time-averaged heat flux (q_{avg}) in an exponential cycle that is made equal to the steady heat flux q_{steady} . This leads to a modified-form of

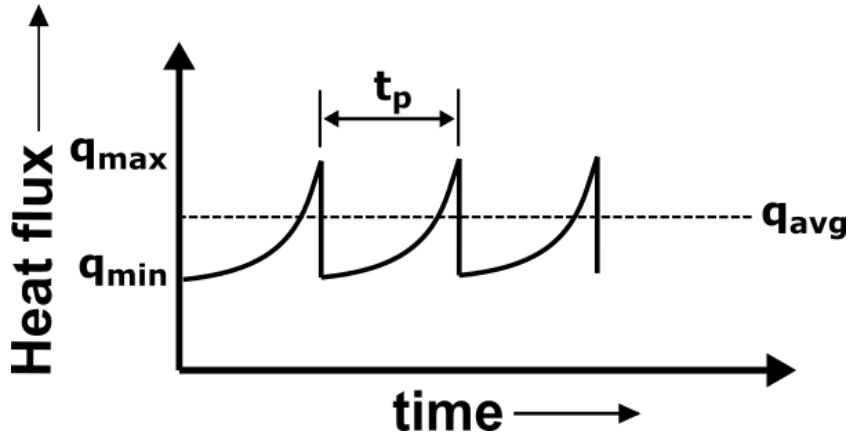


Figure 5.6: Schematic of power transients with exponential heating pattern utilized in this study. The q_{\max} and q_{\min} are the minimum heat flux occurring during an exponential power cycle. While t_p is the time period of the periodic exponential power cycle and q_{avg} corresponds to the time averaged heat flux during a power cycle.

Eq. 5.8 as

$$q(t) = \frac{q_{\text{avg}}(t_p/\tau)}{[\exp(\frac{t_p}{\tau}) - 1]} \exp(t/\tau) \quad (5.9)$$

where

$$q_{\text{steady}} = q_{\text{avg}} = \frac{\int_0^{t_p} q(t) dt}{t_p}$$

This constraint enables us to compare the present periodic heat flux-based results with those for steady heat flux-based results. Thus, for the present parametric study for the periodic heat-flux BC and its comparison with the results for steady heat-flux, the three input parameters are q_{avg} , τ , and t_p .

For a constant q_{avg} using Eq. 5.9, Fig. 5.7(a) shows a schematic of the variation in the heating cycle with increasing τ and increasing t_p ; based on the exponential heating cycle in Fig. 5.6. Thus, for constant t_p and q_{avg} , Fig. 5.7(a) shows that if the excursion time τ is increased then q_{\max} associated with the heating cycle decreases while q_{\min} increases to satisfy the constant q_{avg} condition. Thus, as the excursion time τ increases, the q_{\min} and q_{\max} approaches q_{avg} resulting in reduced exponential heating effect. In contrast, for increasing time period t_p with a constant τ and q_{avg} , Fig. 5.7(b) shows that q_{\max} increase and q_{\min} decreases to ensure same q_{avg} .

5.4.2 Parametric Details associated with input heat flux

Once the initial condition is defined for simulating the nucleate boiling with periodic heat flux BC, the next procedure is the suitable selection of input heat flux characteristics for the cyclic exponential variation. As mentioned previously, the parameters associated

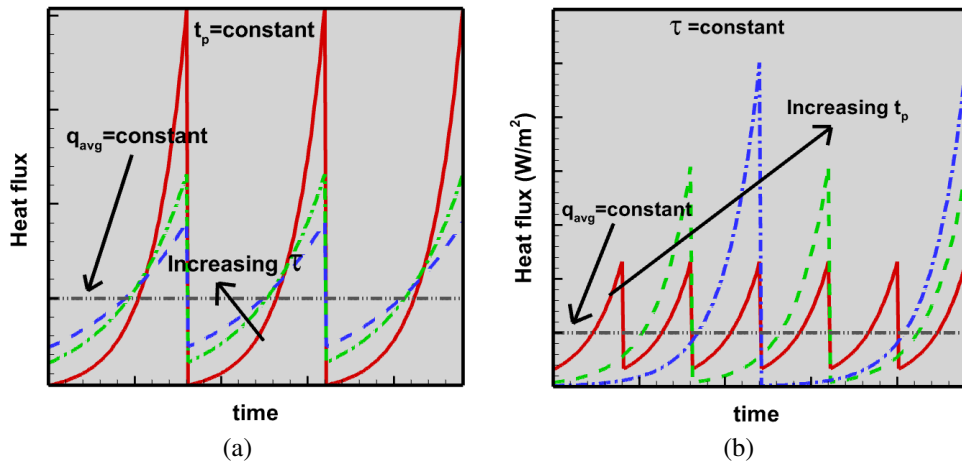


Figure 5.7: Schematic of heat flux variation with time for (a) various excursion time with time period of periodic heat flux to be constant and (b) various exponential time period of periodic heat flux for a constant excursion time.

with the heat flux variation shown in Fig. 5.6 are the excursion time τ , time-period t_p , and time averaged heat flux (q_{avg}). Among these parameters, the q_{avg} value is identified to be of significant importance since the comparison with steady heat flux is possible and moreover the sole effect of other parameters (τ and t_p) could be evaluated. Since partially developed nucleate boiling regime (isolated bubble) is the region of our interest in the current investigation, the q_{avg} value is selected such that the supplied heat flux leads to a rise in the wall temperature, which is smaller than the temperature that leads to the deviation from partially developed nucleate boiling regime to fully developed nucleate boiling regime.

In a recent study of Huber et al. (Huber *et al.*, 2017), for isolated bubbles with negligible micro-region effects, the Jakob number (Ja) is identified to be in moderate range ($Ja < 50$). Thus, to ensure partially developed nucleate boiling regime the same condition is utilized here to fix the upper limit of q_{avg} considered here. Whereas, the minimum value for q_{avg} is considered based on the experiment of Zakšek et al. (Zakšek *et al.*, 2020) with ethanol on smooth surface. Thus, once the q_{avg} value is specified, then the instantaneous heat flux values during cyclic variation need to be fixed. For the same, the maximum heat flux reported in literature ($q_{max,high} = 143 \text{ kW/m}^2$) (Utaka *et al.*, 2014) during partially developed nucleate boiling regime is utilized. This formulation ensures the heat flux values associated with exponential variation to be in partially developed nucleate boiling regime.

Apart from the heat flux values, the other parameters are the excursion time τ and heating time-period t_p . The lower limit of excursion time τ is decided such that the q_{max} associated with the heating cycle does not exceed the aforementioned $q_{max,high}$, while its

Table 5.2: For the present parametric study, on the effect of periodic heat-flux on the nucleate boiling, range of values chosen for various exponential heating cycle parameters.

Parameter	Range
Time-averaged heat flux	$q_{avg} = 5000-15000 \text{ (W/m}^2\text{)}$
Excursion time	$\tau = 0.2-8 \text{ ms}$
Heating time period	$t_p = 4-16 \text{ ms}$

higher limit is chosen such that there is no effect of ramping on ebullition cycle. Once these values are determined, then the heating time-period t_p is varied such that the above mentioned conditions are fulfilled. Here, since ethanol and its vapor are considered as the working fluid, the range of the input parameters chosen here, based on the aforementioned discussion, are shown in Table 5.2.

5.4.3 Simulation methodology and parameters monitored

In this section, for simulating single bubble nucleate boiling dynamics with exponential function-based periodic heat-flux, the numerical methodology utilized and the monitored parameters associated with single bubble dynamics are discussed. Once the heating pattern as shown in Fig. 5.6 is designed and the parameters of exponential heat flux input (Table 5.2) is decided, the next step is the formulation of solution procedure for the power transients simulation. Even though the present study focus is on exponential power transients, the proposed solution procedure shown in Fig. 5.8 is a generalized approach applicable to any power transients.

The single bubble nucleate boiling simulation is initiated with a steady heat flux replicating the steady operating condition in which nucleate boiling is utilized. Once the periodic bubble departure-based nucleate boiling has been reached as shown in Fig. 5.4 the transient flow field variables stabilizes with a periodic bubble dynamics. This is evident from various bubble dynamics parameters— D_d , t_g and t_w —which shows almost same values as from the previous ebullition cycle. In this study, once no appreciable difference is observed for subsequent three to four ebullition cycles then the power transients is initiated from the seeding of vapor bubble for next ebullition cycle. If no such variations are observed the simulation continues with steady heat flux boundary condition. The bubble dynamic parameters are evaluated as the ebullition cycle is allowed to reach dynamic steady condition with the provided periodic heat flux. This solution methodology is thus utilized to evaluate the effect of q_{avg} , t_p and τ on bubble dynamic parameters which are essential to model the nucleate boiling (Hazi and Markus, 2009). Although numerous literatures are available with steady heating conditions for evaluating the bubble dynamic parameters, no literatures are available with transient heating conditions. This

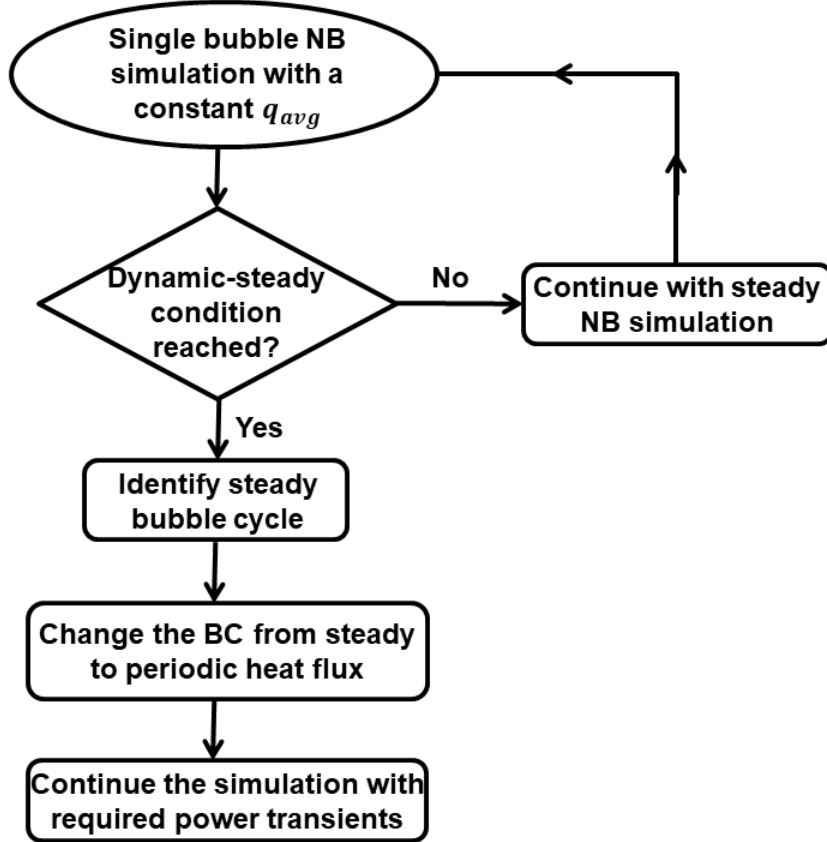


Figure 5.8: Simulation methodology utilized for initializing the temperature and velocity field required for nucleate boiling simulation subjected to power transients.

study aims to investigate in this direction by evaluating how power transients influence departure diameter, departure time and bubble release frequency with various parameters of exponential power transients; challenging to determine from experiments.

5.5 Effect of Periodic-versus-Steady Heat Flux BC on the Bubble Dynamics during the Nucleate Boiling

In this section, the effect of various input parameters— q_{avg} , τ , t_p (Table 5.2)—associated with the periodic heating cycle on bubble departure diameter D_d , bubble growth period t_g , and bubble departure frequency f that characterises the periodically departing vapor bubble during the nucleate boiling are presented. Further, by keeping $q_{avg} = q_{steady}$, the deviation of aforementioned bubble dynamic parameters with steady heating condition is discussed. This section also presents a vertical coalescence phenomenon for certain transient heating cases, where a trailing seed-bubble coalesce with the leading departed-bubble.

5.5.1 Bubble departure diameter (D_d) and bubble growth period (t_g)

Utilizing the time wise cyclic variation of exponential heating pattern as shown in Fig. 5.6, the effect of t_p , τ and q_{avg} on bubble departure diameter D_d and bubble growth period t_g of the vapor bubble, and comparison with q_{steady} are discussed in this section. The bubble departure diameter D_d corresponds to the apparent diameter of the vapor bubble at the instance it detaches from the solid wall, whereas the bubble growth period t_g is the time interval between seeding of a vapor bubble and departure from solid wall. Figure 5.9 shows the effect of various heating parameters on D_d and t_g along with their deviation from steady heating condition.

Fig. 5.9(a) shows the effect of excursion time τ for different heating time period t_p on bubble departure diameter D_d at $q_{avg} = 5000 \text{ W/m}^2$. For plotting Fig. 5.9(a) initially single bubble nucleate boiling simulation is performed with $q_{steady} = 5000 \text{ W/m}^2$. once the bubble reaches a dynamic steady condition as in Fig.5.4 i.e., 27th ebullition cycle, the departure diameter of the bubble is evaluated by averaging from previous five ebullition cycle. Now to investigate the transient effects, the steady heat flux is replaced with transient heat flux boundary condition which requires t_p , τ , and q_{avg} as input (Eq. 5.9). Thus, simulation is continued with exponential heating cycle from the onset of vapor seeding, i.e, while placing the seed bubble for 28th ebullition cycle. The bubble is allowed to grow and depart with usual ebullition cycle till a periodic condition is reached with the periodic heat flux. Once the same has been attained, the bubble departure diameter D_d of the bubble is evaluated by averaging from previous five ebullition cycles, which corresponds to the D_d obtained for an exponential heating cycle with $t_p = 8 \text{ ms}$, $\tau = 8 \text{ ms}$ and $q_{avg} = 5000 \text{ W/m}^2$. Now two departure diameters are available, one corresponding to $q_{steady} = 5000 \text{ W/m}^2$ and other for $q_{avg} = 5000 \text{ W/m}^2$ with heating time period of 8 ms and excursion time of 8 ms. This establishes our first objective of comparing bubble dynamics between steady and transient heat flux condition formulated while designing the heat flux pattern.

The next objective is to investigate the effect of various parameters associated with heating pattern. For example, to determine the effect of excursion time on bubble departure diameter D_d , the exponential heating cycle is considered with $t_p = 8 \text{ ms}$, $\tau = 6 \text{ ms}$, and $q_{avg} = 5000 \text{ W/m}^2$. Comparing with aforementioned heating cycle the excursion time τ is reduced from 8 ms to 6 ms keeping all other parameters similar. The transient heat flux replaces steady heat flux boundary condition once the steady boiling reaches to a periodic state; with $t_p = 8 \text{ ms}$, $\tau = 6 \text{ ms}$, and $q_{min} = 2386.4 \text{ W/m}^2$. The simulation continues with the periodic heat flux until periodic condition is achieved, resulting in the bubble departure diameter D_d for the varied excursion time τ . Similarly to evaluate the effect of heating time period t_p , the τ and q_{avg} are kept constant by varying t_p and the corresponding departure

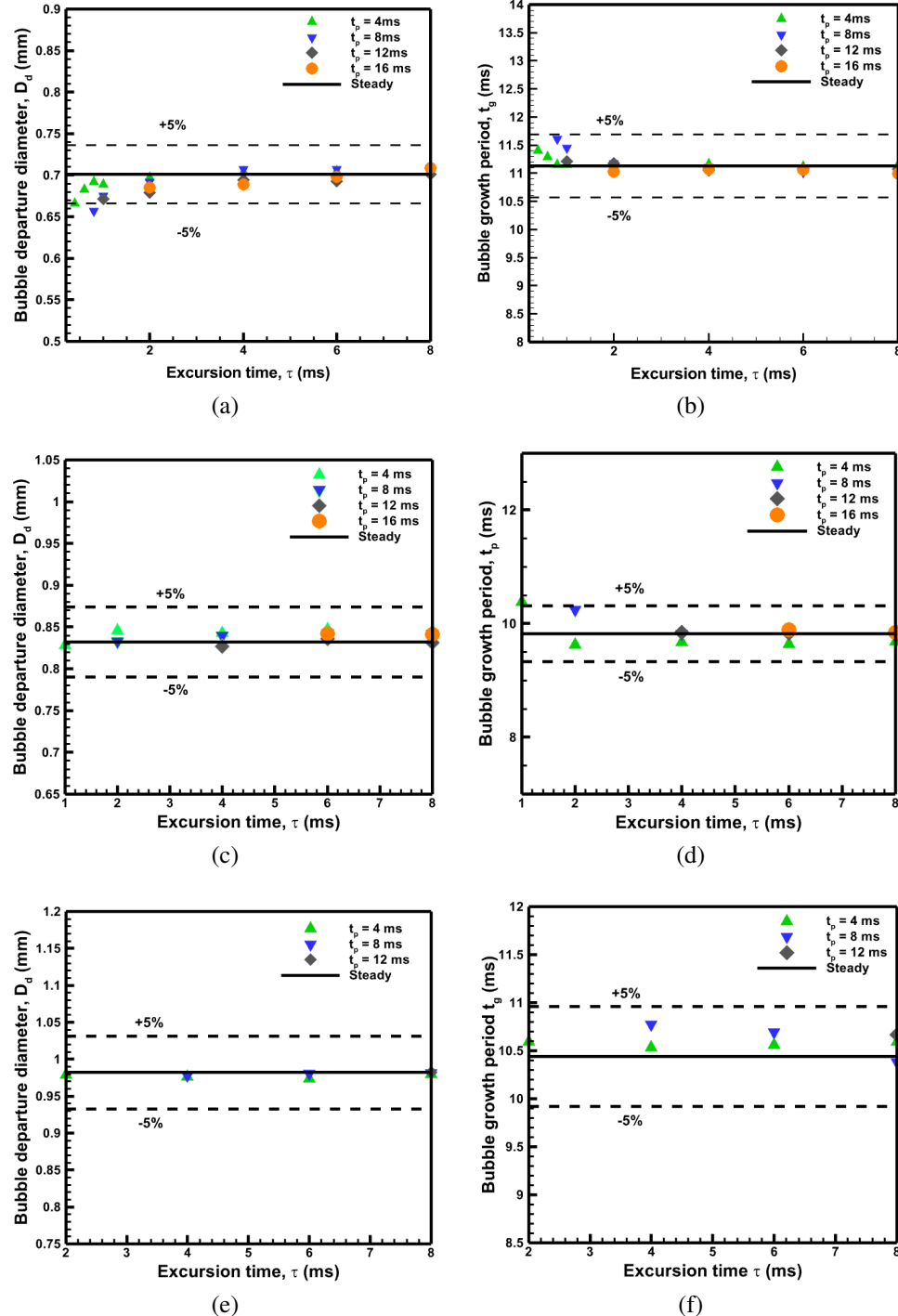


Figure 5.9: Effect of heating time period (t_p) and excursion time (τ) on the bubble departure diameter and bubble growth period for, (a), (b) $q_{\text{avg}} = 5000 \text{ W/m}^2$, (c), (d) $q_{\text{avg}} = 10000 \text{ W/m}^2$, and (e), (f) $q_{\text{avg}} = 15000 \text{ W/m}^2$, compared with their corresponding bubble departure diameter at $q_{\text{steady}} = q_{\text{avg}}$. For larger t_p note that the above results are not shown for smaller τ value since the cases correspond to vertical coalescence.

diameter is determined. It could be observed from Fig. 5.9 for various q_{avg} that t_p and τ is having a slight influence on the departure diameter D_d from the steady heating condition as the data obtained under the periodic heating is within $\pm 5\%$ of the data corresponding to q_{steady} value.

An interesting phenomenon observed during this study was coalescence of seeded bubble with departed bubble from previous ebullition cycle. For a constant q_{avg} , this phenomenon observed for τ lower than certain constant value and τ values above resulted in ebullition cycles without coalescence. Fig. 5.11 shows a schematic of this phenomenon, termed as *vertical coalescence*; with a detailed discussion in the following section. Thus in 5.9 the bubble departure diameter are plotted for ebullition cycles without vertical coalescence. Figure 5.9 also shows the effect of various heating parameters on bubble growth period and comparison with steady heating condition. The effect of various heating parameters and its comparison is made possible as shown in Fig. 5.9(b) for $q_{avg} = 5000 \text{ W/m}^2$. Moreover, Fig. 5.9(d) and 5.9(f) corresponds to $q_{avg} = 10000 \text{ W/m}^2$ and $q_{avg} = 15000 \text{ W/m}^2$, respectively. Similar to bubble departure diameter, the t_p and τ are not having any influence on bubble growth period for constant q_{avg} . The obtained values from transient heat flux condition are within $\pm 5\%$ to the departure time from steady heat flux condition.

5.5.2 Bubble departure frequency

Bubble departure frequency f is another important parameter which characterises bubble dynamics. It is defined as the number of ebullition cycles occurring in a unit time, given as

$$f = \frac{1}{t_g + t_w} \quad (5.10)$$

where t_g and t_w are the bubble growth period and bubble waiting period, respectively. As presented above, the bubble growth period t_g corresponds to the time taken by a bubble to depart from the wall from the instance at which it is seeded, whereas the bubble waiting period t_w is the time interval between bubble departure and the instance of seeding bubble for subsequent ebullition cycle. Higher the f value, higher will be the number of ebullition cycle resulting in efficient heat removal from the wall (Walunj and Sathyabhamma, 2018). As discussed in previous sections for D_d and t_g , in this section the effect of various exponential heating parameters are investigated and also compared with steady heating condition.

For various constant heating time period t_p at $q_{avg} = 5000 \text{ W/m}^2$ Fig. 5.10(a) shows reduction in excursion time τ results in increased bubble departure frequency f , evident for all the heating time period except 16 ms. For constant heating time period and q_{avg} ,

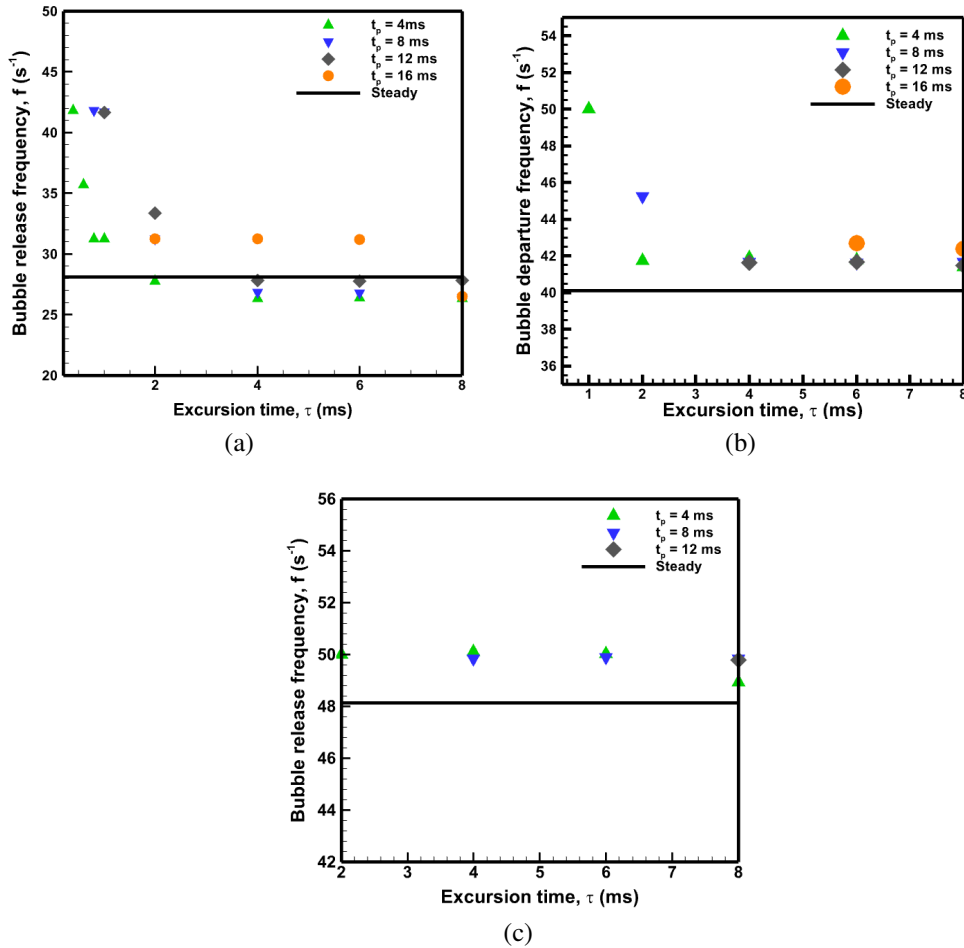


Figure 5.10: Effect of heating time-period t_p and excursion time τ on the bubble departure frequency f for (a) $q_{avg} = 5000 \text{ W/m}^2$, (b) $q_{avg} = 10000 \text{ W/m}^2$, and (c) $q_{avg} = 15000 \text{ W/m}^2$, and compared with their corresponding bubble departure frequency f at $q_{steady} = q_{avg}$. For larger t_p note that the above results are not shown for smaller τ value since the cases correspond to vertical coalescence.

reduction in τ causes the q_{max} value to increase based on Eq. (5.9). Higher the q_{max} , lesser is the time required for the cavity to be activated at T_{act} temperature. The general trend of the curve is in such a way that bubble departure frequency f reduces with increasing τ and reaches saturation value after a particular τ . This is due to the lesser fluctuation of heat flux value closer to the q_{avg} value due to increased τ . Because when τ value is increased keeping t_p and q_{avg} constant, increase in τ causes q_{min} to increase and q_{max} to reduce that results in fluctuation of heat flux value near q_{avg} , which causes the system to behave similar to steady heating condition. Similarly, if τ is fixed, an increase in t_p results in an increased q_{max} which also leads to rise in f . In Fig. 5.10(a), no increase in f is observed for $t_p = 16 \text{ ms}$. This is because for a constant q_{avg} and t_p , below a minimum τ value, vertical coalescence is observed due to increased q_{max} . As the heating time period increases, it could be observed that this lower limit in τ also increases. Thus, vertical

coalescence occur at higher τ value for higher heating time period. Like a minimum τ value will limit the increase in f , there is a maximum τ associated with every constant heating time period curve which does not cause any increase in f . This is because an increase in τ with constant q_{avg} and t_p , causes q_{min} and q_{max} to fluctuate in closer proximity to q_{avg} resulting in a steady behaviour.

The same trend could be realized in Fig. 5.10(b) and Fig. 5.10(c) for $q_{avg} = 10000 \text{ W/m}^2$ and 15000 W/m^2 , respectively. Moreover as the q_{avg} value increases, the lower limit in τ causing vertical coalescence increases significantly with t_p . Thus no appreciable increase in bubble departure frequency f is observed for $q_{avg} = 15000 \text{ W/m}^2$ as shown in Fig. 5.10(b). Hence higher the q_{avg} value higher is the chance of vertical coalescence which will be detrimental to the thermal management systems utilizing nucleate boiling as a means of heat removal. Further, at lower q_{avg} exponential heat flux with lower heating time period is preferred over higher heating time period due to increased chance of vertical coalescence. Overall, lower q_{avg} with lesser heating time period significantly increase the bubble departure frequency f with reduced chance of vertical coalescence favourable to the thermal management systems. In the published experiment, Johnson (Johnson, 1971) was able to obtain good prediction using steady state correlations for nucleate boiling under the effect of exponential heating with excursion time greater than 5 ms . Similar results are also observed in this numerical study for ethanol with similar behaviour between exponential and steady heating above 5 ms for all q_{avg} values considered, whereas the published experiment was with water and thin metallic ribbon as heater.

5.5.3 Vertical coalescence

For the application of nucleate boiling as a thermal management solution, critical heat flux (CHF) is still a concern which leads to a substantial increase in the surface temperature with degraded heat removal. Recently in published literature (Walunj and Sathyabhamma, 2018), it was observed that early coalescence of bubble occurs with increasing excursion time τ . This boiling mechanism is considered as a limiting criterion for efficient heat removal and an indication of onset of CHF. In the present numerical study, coalescence between subsequent bubbles released from the cavity is also observed for exponential heating, called as vertical coalescence. This phenomenon occurs once the bubble nucleating from a cavity coalesces with a previously departed bubble from the same cavity. Another mode of coalescence in nucleate boiling is horizontal coalescence in which bubble coalesce in horizontal direction that is not investigated here. The bubble seeding for the succeeding ebullition cycle is performed when the seed location reaches a specific activation temperature T_{act} . This seed location is considered as the center of

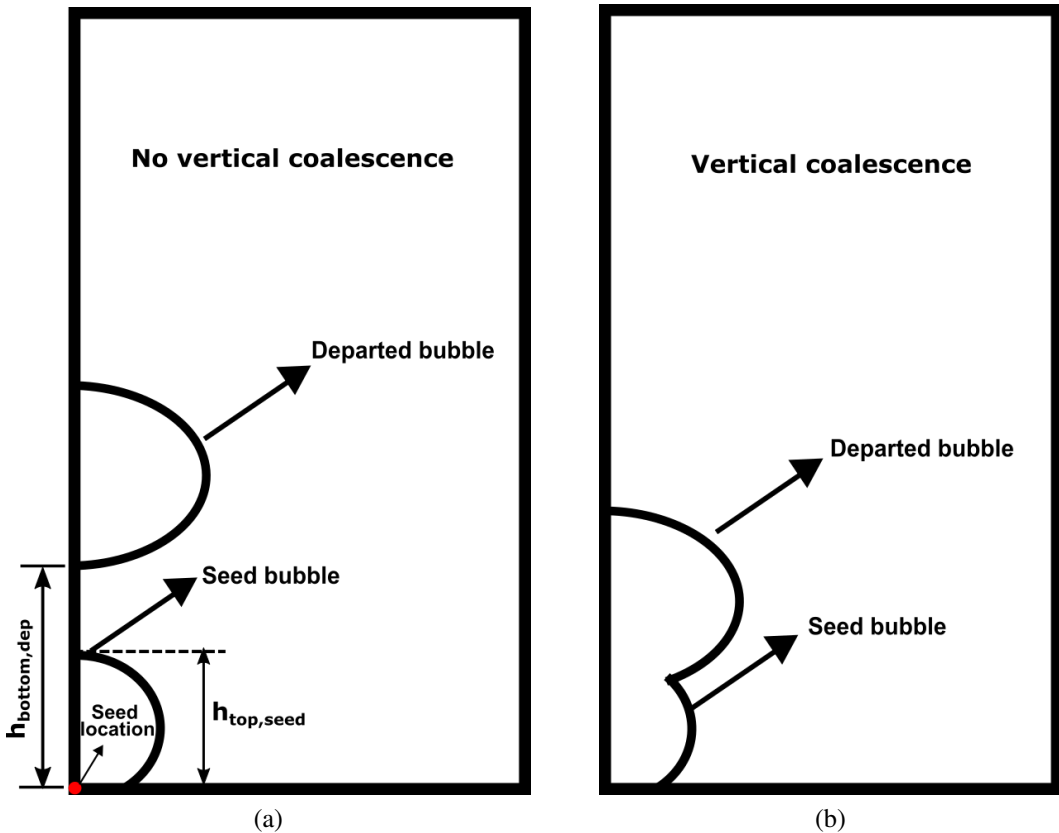


Figure 5.11: Schematic representation showing an ebullition cycle (a) without and (b) with vertical coalescence. The seed location (shown with red colour marking) is the point at which activation temperature is monitored for seeding the bubble. Here, $h_{top,seed}$ corresponds to height of the seed bubble from seed location while $h_{bottom,dep}$ corresponds to the distance from the bottom of the departed bubble to seed location.

bubble base from which the nucleated vapor bubble grows symmetrically outwards. Depending on the transient heat flux provided it is found from simulations that it is not the bubble growth period t_g but bubble waiting period t_w significantly changes. Smaller is the t_w , higher is the chance for vertical coalescence since the departed bubble will be near the vicinity of nucleating bubble as shown in Fig. 5.11.

Figure 5.11 shows a schematic representation of the non-occurrence and occurrence of vertical coalescence during a bubble ebullition cycle. The physical phenomenon of vertical coalescence could be described based on the distance from the top of the seed bubble to the solid wall ($h_{top,seed}$) and distance from the bottom of the departed bubble to the solid wall ($h_{bottom,dep}$). As shown in Fig. 5.11a, if $h_{bottom,dep} > h_{top,seed}$ at any instance, then vertical coalescence does not occur. And the instance at which $h_{bottom,dep}$ becomes equal with $h_{top,seed}$ then vertical coalescence occur.

The objective of this section is to investigate the criterion required for vertical coalescence for various parameters associated with transient heat flux. Hence for the same,

Table 5.3: Input parameters associated with exponential heating cycle for $q_{avg} = 5000 \text{ W/m}^2$ and $t_p = 8 \text{ ms}$ to determine the occurrence and non-occurrence of vertical coalescence. The ✓ and ✗ symbol shows the values for which vertical coalescence is observed and not observed, respectively.

τ (ms)	q_{min} (W/m ²)	q_{max} (W/m ²)	Vertical coalescence
0.2	8.49×10^{-13}	200000	✓
0.4	0.000206115	100000	✓
0.6	0.107973294	66666.77	✓
0.61	0.132149552	65573.9	✗
0.62	0.160645889	64516.29	✗
0.8	2.27009955	50002.27	✗
1.0	13.42300803	40013.42	✗
2.0	373.1472073	20373.15	✗
4.0	1565.176427	11565.18	✗
6.0	2386.349029	9053.016	✗
8.0	2909.883534	7909.884	✗

initially q_{avg} and t_p are kept constant and τ is varied to determine the critical τ at which vertical coalescence is observed. For $q_{avg} = 5000 \text{ W/m}^2$ and $t_p = 8 \text{ ms}$ and various values of τ , Table 5.3 presents the various q_{min} and q_{max} as well as occurrence and non-occurrence of vertical coalescence. The table shows that vertical coalescence occur when the τ value is reduced below 0.61 ms . Since vapor coalescence could be detrimental for efficient heat removal, the lowest τ value for a constant q_{avg} and t_p at which vertical coalescence does not occur is called here as $\tau_{safe,vc}$. Thus $\tau \leq \tau_{safe,vc}$ and $\tau > \tau_{safe,vc}$ implies the occurrence and non-occurrence of vertical coalescence, respectively. The q_{max} corresponding to $\tau_{safe,vc}$ will be thus referred as $q_{safe,vc}$. For efficient heat removal, thus vertical coalescence is considered as a limiting criterion (Walunj and Sathyabhama, 2018).

The effect of q_{avg} and t_p on $\tau_{safe,vc}$ (or $q_{safe,vc}$) is also studied. Figure 5.12 shows the variation of the $\tau_{safe,vc}$, required to prevent vertical coalescence, for different operating conditions. Any input condition below (above) of a line in the figure corresponds to the occurrence and non-occurrence of vertical coalescence. This is because, for a constant heating time period curve, any τ value below (above) the curve results in a higher (lower) q_{max} value in the heating cycle. For a constant heating time period as shown in Fig. 5.12(a), shows that $\tau_{safe,vc}$ increases with q_{avg} . For example, at $t_p = 4 \text{ ms}$ the $\tau_{safe,vc}$ increases by 400% for $q_{avg} = 5000 \text{ W/m}^2$ to 15000 W/m^2 , and the increase is more (481%) for $t_p = 16 \text{ ms}$. Thus, from Fig. 5.12(a), it could be inferred that the possibility of vertical coalescence is lesser at lower q_{avg} value for a constant heating time period t_p . Similarly, for a constant q_{avg} value, the possibility of vertical coalescence is lesser if the heating time period of the power cycle reduces.

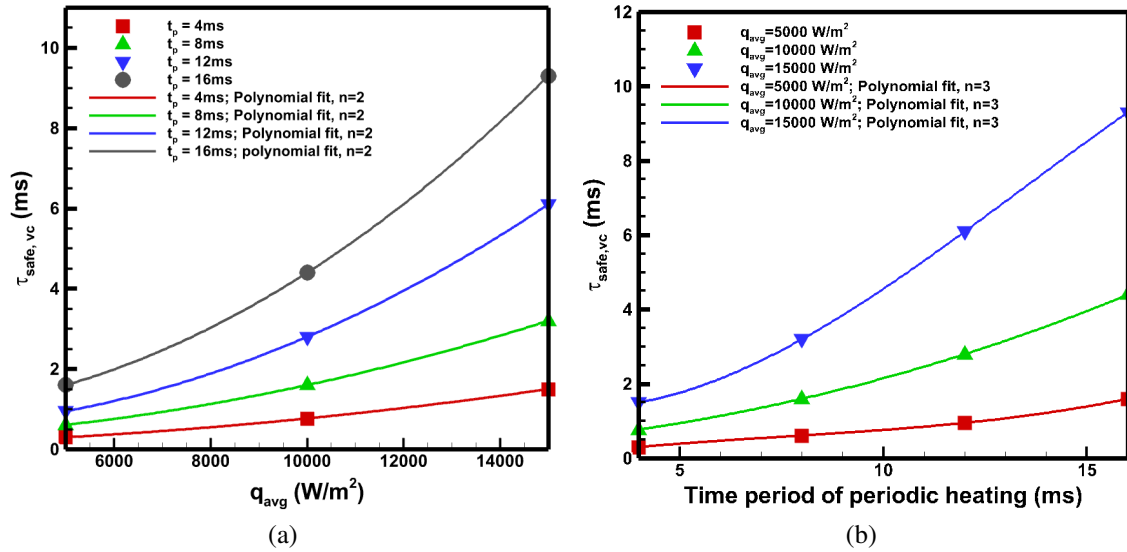


Figure 5.12: Variation in (a) minimum excursion time with q_{avg} for various constant heating time and (b) minimum excursion time with heating time period for various q_{avg} constant values. The symbols correspond to numerical data and the solid line indicates curve fitted with a polynomial function with order n .

The same result has been plotted by showing the variation of $\tau_{safe,vc}$ with heating time period for various q_{avg} value as shown in Fig. 5.12(b). The variation of $q_{safe,vc}$ with various input parameters is shown in Fig. 5.13. Physically, higher $q_{safe,vc}$ indicates the ability to sustain single bubble ebullition cycle without vertical coalescence at higher instantaneous heat flux. From Fig. 5.13(a), it could be seen that for a constant q_{avg} , vertical coalescence occur at lesser $q_{safe,vc}$ value at higher heating time period in comparison with lower heating time period. Similarly, Fig. 5.13(b) shows that the heat flux required for vertical coalescence is higher at lower q_{avg} value in comparison with higher q_{avg} if the heating time period of the exponential heating cycle is constant.

Necessary and sufficient condition for vertical coalescence

In the previous section, 16 ms is the maximum heating time period utilized to investigate the effect of vertical coalescence. Further, when the heating time period was increased to 20 ms interestingly no vertical coalescence was obtained for very high ramp rates or lower excursion time. Thus, even with such a significantly higher q_{max} value, the absence of vertical coalescence lead to the conclusion that $q_{max} > q_{safe,vc}$ is not the sufficient condition for vertical coalescence. From physical perspective, for the occurrence of vertical coalescence, the nucleation should occur such that the previously departed bubble should be in touch with the nearby seeded bubble. If one were to prevent coalescence, then a time delay between two exponential heating spikes is likely to delay coalescence. To

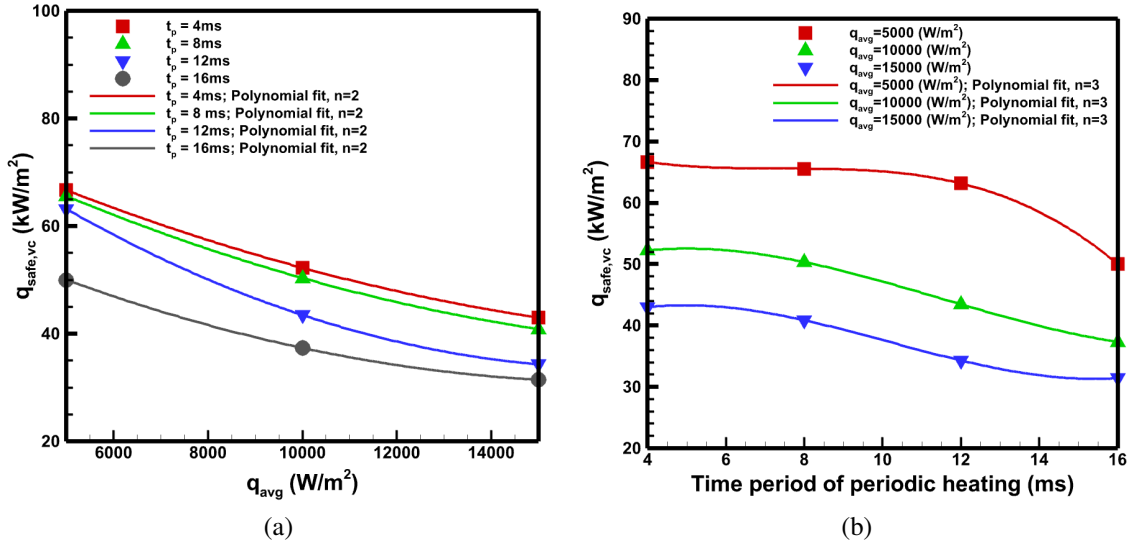


Figure 5.13: Variation in maximum heat flux at which vertical coalescence is not observed under various operating condition with (a) q_{avg} for various constant heating time period and (b) heating time period for different constant q_{avg} values. The symbols correspond to numerical data and the solid line indicates curve fitted with polynomial function with order n .

Table 5.4: Input parameters of heating cycle for the heat flux pattern shown in Fig. 5.14 to evaluate the necessary and sufficient condition for vertical coalescence with $q_{avg} = 5000\text{ W/m}^2$.

Ramp rate (ms)	t_1 (ms)	t_2 (ms)	q_{min} (W/m ²)	q_{max} (W/m ²)	Vertical coalescence
0.6	10	13	1.11×10^{-2}	191666.4	✗
0.6	15	8	2.66×10^{-6}	191666.4	✓

achieve this objective, a delay period is introduced between exponential cycles as shown in Fig. 5.14 such that q_{min} controls the activation of cavity. Hence, this modified heating pattern consists of two regions: an exponential rise and a delay region. During the exponential rise, the heat flux is varied from q_{min} to q_{max} with time t_1 and then the heat flux drops to q_{min} for a time t_2 . This lead to the time period of the heating cycle (t_p) as the sum of t_1 and t_2 . Further for a periodic heating cycle, the instantaneous heat flux is given as

$$q(t) = \begin{cases} \frac{q_{avg}t_p}{\tau[\exp(\frac{t_1}{\tau})-1]+t_2} \exp(t/\tau) & t < t_1 \\ \frac{q_{avg}t_p}{\tau[\exp(\frac{t_1}{\tau})-1]+t_2} & t_1 \leq t \leq t_2 \end{cases} \quad (5.11)$$

To test the previous observation that if $q_{max} > q_{safe,vc}$ it will result in vertical coalescence, in this section two test cases are simulated with input heat parameter having q_{max} high enough for vertical coalescence. The heat flux pattern shown in Fig. 5.14 is utilized with

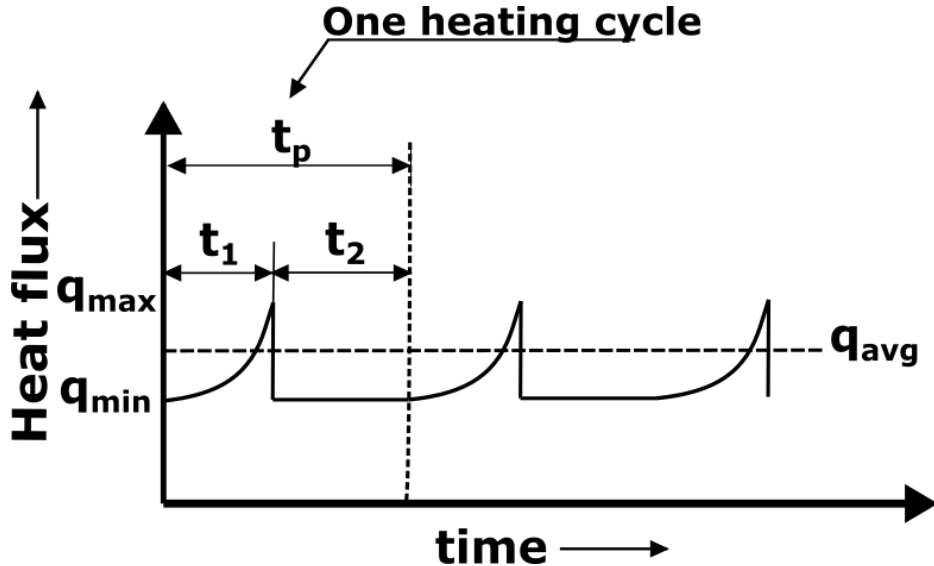


Figure 5.14: Schematic of transient heat flux supplied to the nucleate boiling system with one heating cycle consisting of an exponential rise and a delay period. During exponential rise the heat flux is varied from q_{min} to q_{max} within a time of t_1 , while during the delay period the heat flux is maintained at a constant value of q_{min} till a time of t_1 . The q_{avg} corresponds to the time averaged heat flux during one heating cycle.

heat input parameters provided in Table 5.4. An excursion time of 0.6 ms is selected which result in a q_{max} value much higher than $q_{safe,vc}$ for $q_{avg} = 5000\text{ W/m}^2$. The time period associated with exponential rise as well as delay period is varied resulting in shorter and longer delay time period in each case. It could be thus noticed from Table 5.4 for the case with $t_1 = 10\text{ ms}$ and $t_2 = 13\text{ ms}$, no vertical coalescence was observed while for $t_1 = 15\text{ ms}$ and $t_2 = 8\text{ ms}$ vertical coalescence was observed.

The hypothesis for the occurrence of vertical coalescence is that, within the time interval between bubble departure and seeding of the subsequent bubble, the departed bubble should not have risen beyond the seed diameter ($D_0 = 200\text{ }\mu\text{m}$). This requirement results in two timescales, one corresponding to the time taken by departed bubble to rise a distance equal to that of the initial seed diameter (t_{rise}) and the other being the time taken for heating the cavity to activation temperature (t_{activ}). Thus the timescale for t_{rise} is defined as

$$t_{rise} = \frac{\text{initial seed diameter}}{\text{departure velocity}} = \frac{D_0}{u_{dep}} \quad (5.12)$$

As shown in Fig. 5.15, good agreement is obtained between Mikic model (modified) (Mikic *et al.*, 1970) and present simulation for the bubble growth rate. Thus to evaluate the departure velocity Mikic model (modified) is utilized to calculate dD/dt at the instant of bubble departure (obtained from present simulation). The temporal variation in bubble

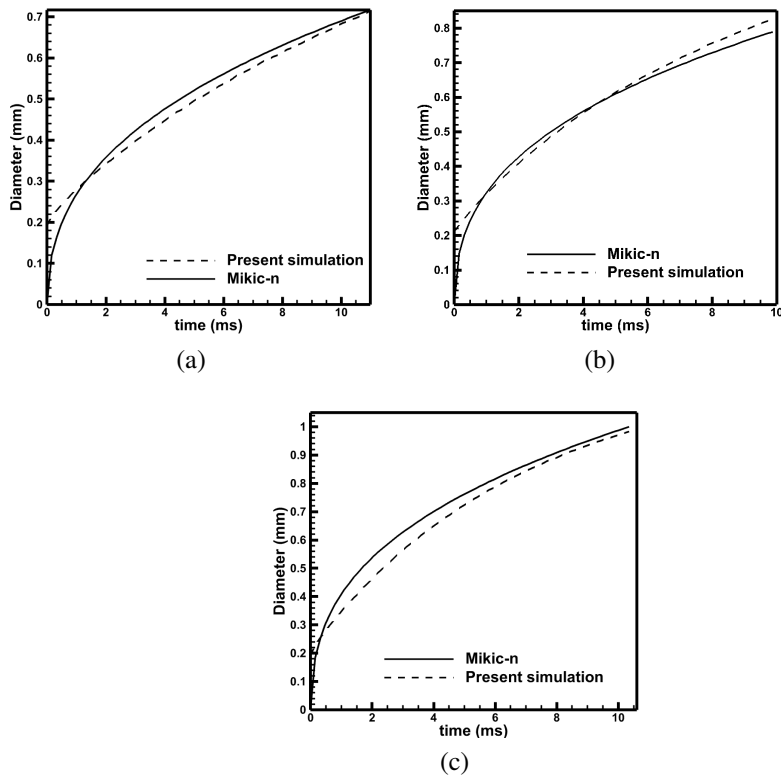


Figure 5.15: Comparison of timewise evolution in bubble diameter between present simulation and Mikic model with correction factor (n) at various q_{steady} values, a) 5000 W/m^2 and $n = 1.39$ b) 10000 W/m^2 and $n = 1.36$, and c) 15000 W/m^2 and $n = 1.35$

radius using Mikic model (modified) is given as

$$R^+ = \frac{2}{3}[(t^+ + 1)^n - (t^+)^n - 1] \quad (5.13)$$

where n is correction factor, R^+ and t^+ are non-dimensional radius and time, respectively, given as

$$R^+ = \frac{RA}{B^2} \text{ and } t^+ = \frac{tA^2}{B^2}$$

Further, the parameters A and B are defined as

$$A = \left(\frac{\pi h_{fg} \rho_v \Delta T}{7 \rho_l T_{\text{sat}}} \right)^{0.5} \text{ and } B = \left(\frac{12}{\pi} \alpha_l \right) Ja$$

Thus, evaluating the growth rate ($\frac{dD}{dt}$) at the instance of bubble departure and utilizing Eq. (5.12), t_{rise} is obtained as 7.67 ms , 6.6 ms , and 6.27 ms for q_{steady} values 5000 W/m^2 , 10000 W/m^2 , and 15000 W/m^2 , respectively. Further, from simulation during dynamic steady condition, the time taken by departed bubble to cover D_0 is obtained as 5.84 ms , 5.37 ms , and 5.31 ms for steady heat flux values 5000 W/m^2 , 10000 W/m^2 , and 15000 W/m^2 , respec-

tively. For various q_{steady} values, the simulated t_{rise} values are not significantly different. This is attributed to the thermo-physical properties of fluid and surface conditions utilized. Considering a percentage deviation between theoretical prediction and simulation of 23.9%, 18.6%, and 15.3% for q_{steady} values of 5000 W/m^2 , 10000 W/m^2 , and 15000 W/m^2 , respectively shows initial seed diameter and departure velocity as suitable scaling parameters for t_{rise} .

As discussed, another timescale of importance for vertical coalescence is t_{activ} . Once the bubble departs from the cavity (assumed to be at the center of vapor bubble), the cavity is quenched by low temperature fluid and seeding is done only when the cavity is reheated back upto the activation temperature. Since t_{activ} corresponds to bubble waiting period in the simulation, for various power transient conditions resulting in vertical coalescence the maximum waiting period between coalesced bubbles is lesser than t_{rise} (5.84 ms , 5.37 ms , and 5.31 ms), and as a consequence vertical coalescence occur due to the early seeding of bubble, which strengthens the aforementioned hypothesis proposed for vertical coalescence.

The bubble growth period and waiting period together controls the ebullition cycle. But for the various exponential power transients utilized, negligible variation in growth period is obtained. Thus, in bubble ebullition cycle, waiting period is influencing the vertical coalescence rather than the growth period. Hence, the nature of heat flux during this waiting time controls bubble seeding and consequently vertical coalescence. This could be observed in the present simulations, i.e., vertical coalescence occurs when excursion time is reduced thereby resulting in higher heat flux. Further, if solid substrate is considered a one-dimensional conduction model using energy conservation could be utilized to evaluate the time required for the temperature to rise from T_{sat} to T_{act} .

Hence, in terms of heat flux, during exponential rise of power transients, the heat flux should have reached a value higher than $q_{safe,vc}$ before the departed bubble risen more than the seed distance. These details are schematically represented in Fig. 5.16 which shows the necessary and sufficient condition for vertical coalescence. Fig. 5.16(a) shows the variation in exponential heat flux for a single heating cycle with q_{max} lesser than required heat flux for vertical coalescence. Such heating patterns does not lead to vertical coalescence. Whereas, in Fig. 5.16(b), the heating cycle with a specified t_p and τ are such that q_{max} is higher than $q_{safe,vc}$. Even though the condition $q_{max} > q_{safe,vc}$ is satisfied, it cannot always lead to vertical coalescence. For vertical coalescence to occur the required heat flux should be within a time-scale such that the previously departed bubble should be in close proximity i.e., $\sim 5\text{ms}$ for the present simulation set-up. Within this specified time-scale, if required heat flux is not attained by the heating pattern then such pattern

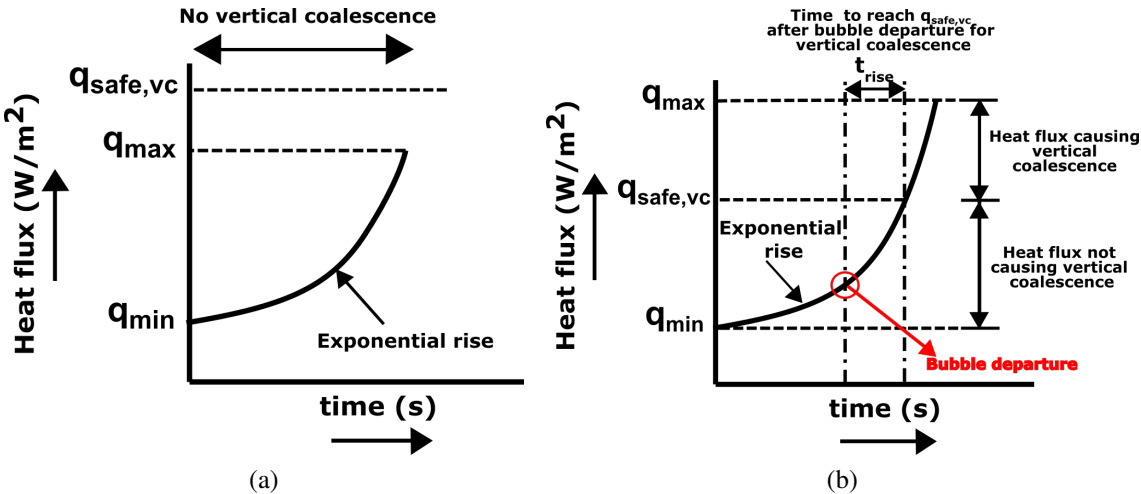


Figure 5.16: Schematic representation showing the various conditions resulting in the occurrence and non-occurrence of vertical coalescence if (a) $q_{max} < q_{safe,vc}$ and (b) $q_{max} > q_{safe,vc}$.

does not cause any vertical coalescence. This also shows that for the periodic heat flux shown in Fig. 5.14 as the delay time—time associated with q_{min} —increases there is delay in activating the cavity for nucleation which causes the departed bubble to be far from the vicinity of seed diameter thereby preventing coalescence as shown in Table 5.4. For the case with $\tau = 0.6 \text{ ms}$, $t_1 = 10 \text{ ms}$, $t_2 = 13 \text{ ms}$, and $q_{avg} = 5000 \text{ W/m}^2$, the average time taken to activate the cavity is 8.13 ms which is higher than aforementioned t_{rise} value for vertical coalescence. Whereas for the case with $\tau = 0.6 \text{ ms}$, $t_1 = 15 \text{ ms}$, $t_2 = 8 \text{ ms}$, and $q_{avg} = 5000 \text{ W/m}^2$ the t_{activ} is found to be 4.53 ms which is lesser than t_{rise} for vertical coalescence. This further signifies the role of t_{rise} and t_{activ} for vertical coalescence apart from $q_{max} > q_{safe,vc}$.

5.5.4 Effect of seed diameter (D_{seed}) and activation temperature

$$(\Delta T_{act})$$

The results discussed till the previous sections were carried out with a constant initial seed diameter ($D_{seed} = 200 \mu\text{m}$) and activation temperature ($\Delta T_{act} = 5 \text{ K}$). Since D_{seed} and ΔT_{act} are essential for single bubble nucleate boiling simulation (macroscopic nucleate boiling simulation), their influence on the bubble dynamics and vertical coalescence is evaluated in this section.

To study the effect of d_{seed} , an initial value of $200 \mu\text{m}$, $225 \mu\text{m}$ and $250 \mu\text{m}$ are selected with present grid size and the heat input parameters utilized are $q_{avg} = 10000 \text{ W/m}^2$, $t_p = 4 \text{ ms}$ and 16 ms . Table 5.5 shows a negligible variation in D_d , t_g and f for various D_{seed} . Similar trend is also observed for other combinations of input parameters of expo-

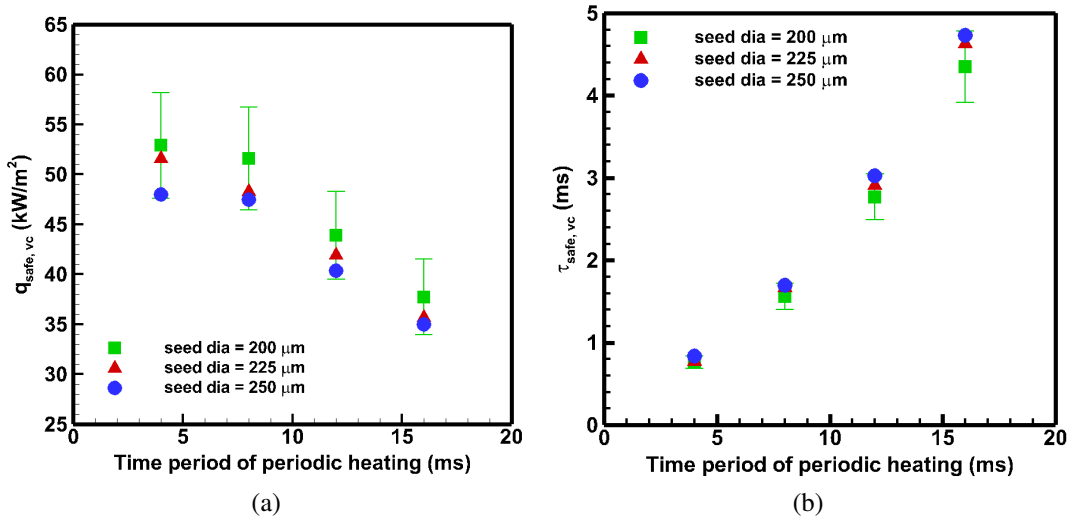


Figure 5.17: Effect of seed diameter (D_{seed}) on (a) $q_{safe,vc}$ and (b) $\tau_{safe,vc}$ for different heating times with constant $q_{avg} (= 10000 \text{ W/m}^2)$. The error bar shows a deviation of $\pm 10\%$.

nential heating cycle. Similarly, the effect of D_{seed} on $q_{safe,vc}$ is also investigated as shown in Fig. 5.17. When the seed diameter is increased there is a reduction in $q_{safe,vc}$ and an increase in $\tau_{safe,vc}$ as shown in Fig. 5.17(a) and Fig. 5.17(b), respectively. Further the figure also shows that the variation in $q_{safe,vc}$ and $\tau_{safe,vc}$ are within 10%.

As discussed previously, ΔT_{act} is another essential parameter required for initiating the single bubble nucleate boiling simulation. In a recent experimental study by Zakšek *et al.* (2020), the nucleate pool boiling of Ethanol and its water mixture is performed on smooth and textured surfaces. From the boiling curve, for $q_{steady} = 15000 \text{ W/m}^2$ as observed from that study, the ΔT_{act} can be obtained by linear interpolation as 9.4 K which is utilized here. Thus, by using $q_{avg} = 15000 \text{ W/m}^2$, $t_p = 4 - 16 \text{ ms}$, and the minimum τ from the parametric value shown in Table 5.2 with no vertical coalescence, the effect of ΔT_{act} is investigated. Even though D_d and t_g are similar by varying ΔT_{act} , increasing ΔT_{act} from 5 K to 9.4 K shows almost 55% reduction in f_{ebull} due to the increase in waiting time. Fig. 5.18 shows an increase in $q_{safe,vc}$ with ΔT_{act} since higher heat flux is required for

Table 5.5: Effect of seed diameter (D_{seed}) on D_d , t_g and f for two different heating conditions utilized.

t_p	τ	D_{seed}	D_d	t_g	f
4	1	200	0.828	10.28	50.02
		225	0.823	9.83	49.9
		250	0.816	9.612	49.98
16	6	200	0.842	9.89	42.68
		225	0.842	9.507	41.76
		250	0.839	9.107	41.73

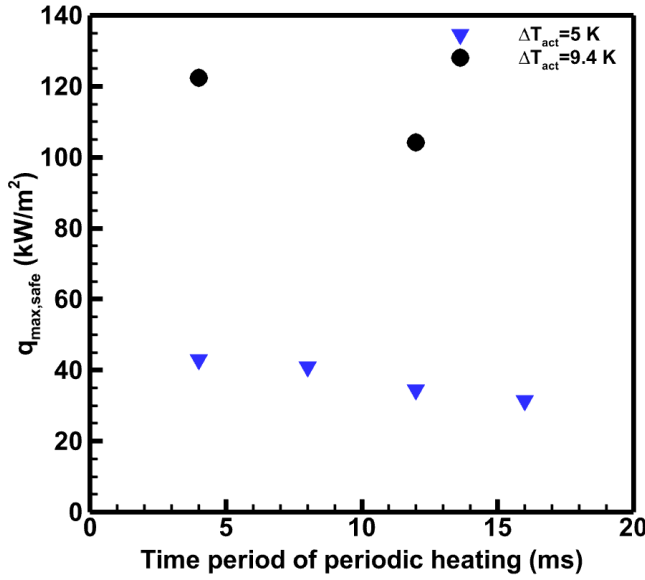


Figure 5.18: Variation of $q_{max,safe}$ with heating time for different ΔT_{act} . The plot corresponds to a constant q_{avg} ($= 15000 \text{ W/m}^2$) value.

vertical coalescence at higher ΔT_{act} . This signifies that as activation temperature increases the waiting time between subsequent nucleated bubbles increases thus demanding higher heat flux for vertical coalescence. Thus, for practical applications to handle higher heat flux without vertical coalescence during power transients, cavities with higher activation temperature is preferred due to higher $q_{safe,vc}$.

5.6 Time-wise evolution of vertical coalescence during nucleate boiling under the effect of periodic exponential heat flux

In the previous sections, only the onset of vertical coalescence is studied, which is extended here for its time-wise evolution for a constant $q_{avg} = 10000 \text{ W/m}^2$ and $t_p = 4 \text{ ms}$. From Fig. 5.12a, it could be seen that for aforementioned input parameters the $\tau_{safe,vc}$ value is 0.77 ms . Any τ value greater than or equal to 0.77 ms does not cause vertical coalescence and vice-versa. Since results are presented for $\tau \geq 0.77 \text{ ms}$, further simulations are performed for $\tau < 0.77 \text{ ms}$. Thus, overall three different behaviours of ebullition cycles are observed—periodic, quasi-periodic, and chaotic. Here, periodic ebullition cycle corresponds to cyclic growth, departure, and waiting period without any vertical coalescence, quasi-periodic cycle corresponds to a constant number of ebullition cycles between vertical coalescence, and chaotic represents irregular ebullition cycles between vertical coalescence. Thus, for the present input heat flux conditions, $\tau \geq 0.77$,

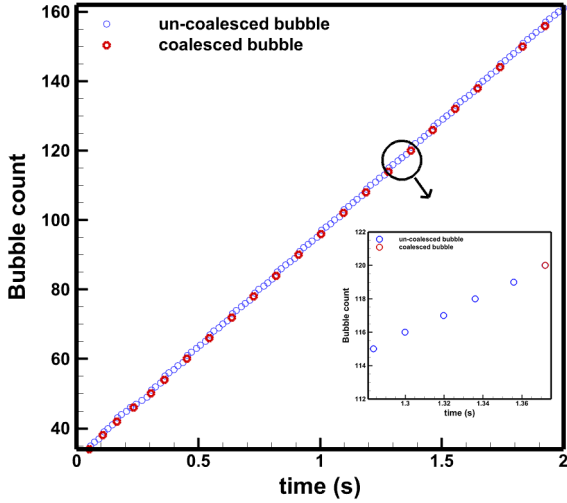


Figure 5.19: Time-wise evolution of bubble count representing periodic vertical coalescence phenomenon for $\tau = 0.74 \text{ ms}$, $t_p = 4 \text{ ms}$, and $q_{avg} = 10000 \text{ W/m}^2$. The blue and red colored unfilled circles represent seeded bubbles which are uncoalesced and coalesced with previously departed bubbles, respectively.

$0.74 \leq \tau > 0.77$, and $\tau < 0.74$ are found to be in periodic, quasi-periodic, and chaotic regimes; respectively. Since bubble dynamics is complex in chaotic regime, the present study is limited to quasi-periodic with an objective of comparing the ebullition cycle with and without vertical coalescence.

Figure 5.19 shows evolution of coalesced and uncoalesced bubbles with time for representing quasi-periodic regimes. This is established by showing the time-wise evolution of bubble count which corresponds to a counter for seeded bubble. Once seeded bubble grows and depart from solid wall, the time instance at which next seeding occur is recorded and utilized for plotting Fig. 5.19 which could be either a coalesced or uncoalesced seed. This distinction is also represented in the figure using different colored unfilled circles. Since periodic heat flux are initiated after dynamic steady condition is reached with steady heat flux, the initial bubble count is not starting from zero value. Further from Fig. 5.19 it could be noted that, for the initial 54 ebullition cycles, the vertical coalescence occur after three ebullition cycles and reaches a quasi-periodic state with coalescence occurring after every 5 ebullition cycles. In this quasi-periodic regime, a repeating bubble dynamic pattern from one coalescence to another (shown in the inset of Fig. 5.19) is utilized for studying the variation in T_{act} .

Figure 5.20(a) shows the time-wise evolution of cavity temperature and periodic exponential heat flux for the aforementioned bubble dynamics pattern (inset of Fig. 5.19). The activation temperature (83.5°C) utilized in the present study is also shown in this figure as horizontal line to indicate the occurrence of seeding once cavity temperature reaches T_{act} . The figure clearly shows that cavity temperature fluctuate with periodicity

of the heat flux BC. A sudden drop in heat flux results in an instantaneous reduction in cavity temperature and as the heat flux increases exponentially with time, the cavity temperature also rises. If thermal inertia of solid is incorporated in the simulation then a delay in this instantaneous drop in cavity temperature could be expected. The figure also shows the instances of seeding as vertical solid line. The variation in apparent diameter with time is plotted in Fig. 5.20(b) for the same ebullition cycle pattern (inset of Fig. 5.19). From the spike in apparent diameter, the instance at which vertical coalescence occur could be easily identified. This spike occur due to the merging of seeded bubble with previously departed bubble resulting in higher buoyant force causing the coalesced bubble to depart thereby preventing the further growth of seeded bubble. Figure 5.20(c) is plotted for comparing the cavity temperature with respect to bubble ebullition cycle. For various ebullition cycles, the time taken for bubble growth (seeding to departure) and waiting time are also shown in this figure. For coalesced bubble it could be noted that the bubble waiting period t_w or time period for the cavity to reach activation temperature is 5.23 ms which is lesser than t_{rise} (= 5.37 ms) obtained for $q_{avg} = 10000 \text{ W/m}^2$. This further strengthens our aforementioned hypothesis for vertical coalescence. A consolidated figure showing the time-wise evolution of apparent diameter, heat flux, and cavity temperature is shown in Fig. 5.20(d) for the repeating ebullition cycle pattern with vertical coalescence.

Additionally to investigate the effect of vertical coalescence on Nusselt number (Nu), variation in time averaged Nu (\overline{Nu}) for the aforementioned ebullition cycles need to be computed. For the present nucleate boiling simulation with periodic exponential heat flux BC, the wall averaged Nu (Nu_{wall}) is calculated as

$$Nu_{wall} = \frac{1}{A} \int_0^A Nu_L dA = \frac{1}{A} \int_0^A \frac{1}{\theta} dA \quad (5.14)$$

where A , Nu_L , and θ denotes surface area, local Nusselt number, and non-dimensional temperature. Once Nu_{wall} is computed, the time averaged Nusselt number (\overline{Nu}) for each ebullition cycle is calculated as

$$\overline{Nu} = \frac{1}{t_2 - t_1} \int_{t_1}^{t_2} Nu_{wall} dt \quad (5.15)$$

Figure 5.21 shows the variation in \overline{Nu} for various ebullition cycles in periodic vertical coalescence with almost constant \overline{Nu} for the ebullition cycles without vertical coalescence. An average Nu for these ebullition cycles without vertical coalescence is also shown in this figure as solid horizontal line. For an ebullition cycle with vertical coalescence, as

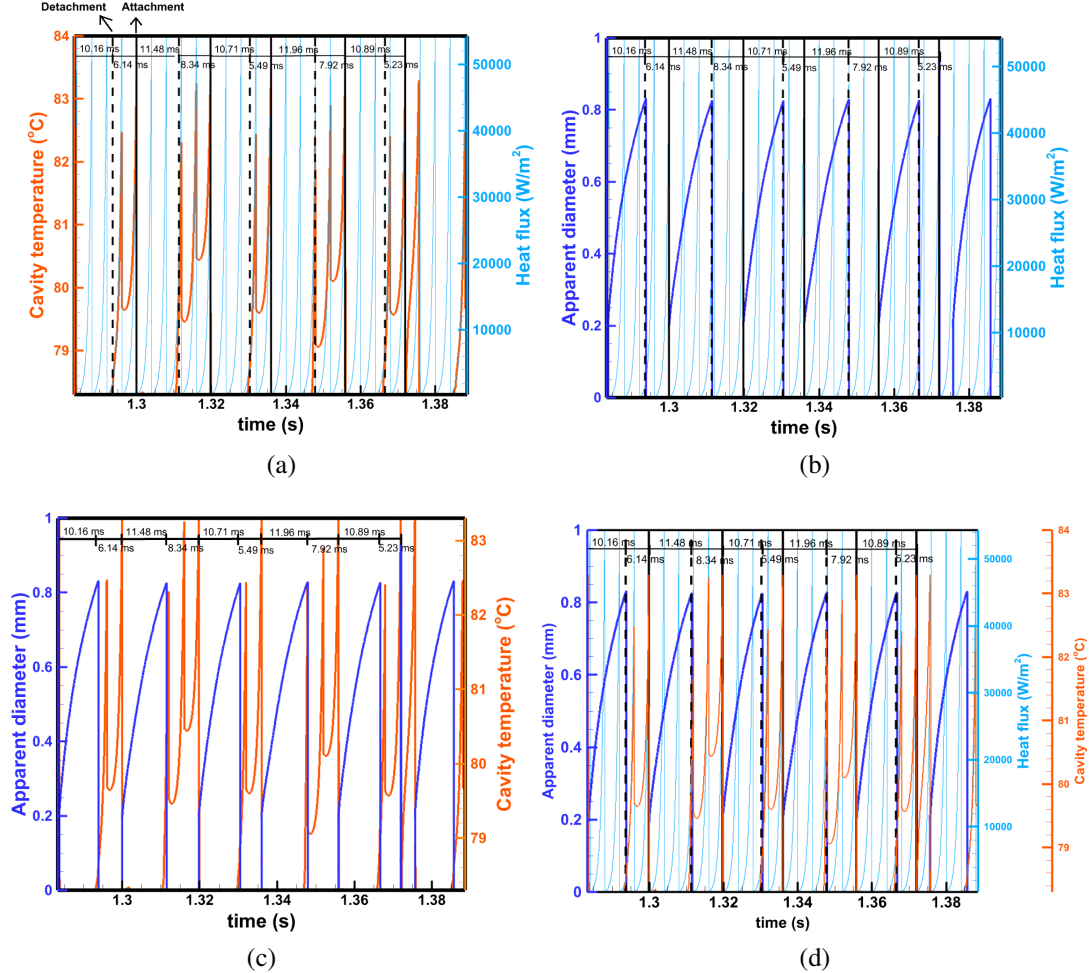


Figure 5.20: Time-wise evolution of cavity temperature with time for the ebullition cycles shown in the inset of Fig. 5.19. For better representation of the time-wise evolution of cavity temperature during this complex process only the instantaneous variation in a) cavity temperature with heat flux, b) apparent diameter with heat flux, c) apparent diameter with cavity temperature, and d) apparent diameter, cavity temperature, and heat flux consolidated together is shown.

indicated in Fig. 5.21, a slight reduction in \overline{Nu} is observable which corresponds to 2.5% from the averaged Nu over 5 ebullition cycles. This shows that for multiple bubble nucleation occurring over a solid surface undergoing vertical coalescence due to periodic exponential heating will result in significant drop in heat transfer performance.

5.7 Discussion

Effect of various heating parameters of exponential power transients on the ebullition cycle are investigated in the previous section. Based to the results observed, with the constraint $q_{avg} = q_{steady}$, time period of period heating t_p and excursion time τ are having significant affect on bubble departure frequency f but not on bubble departure diameter

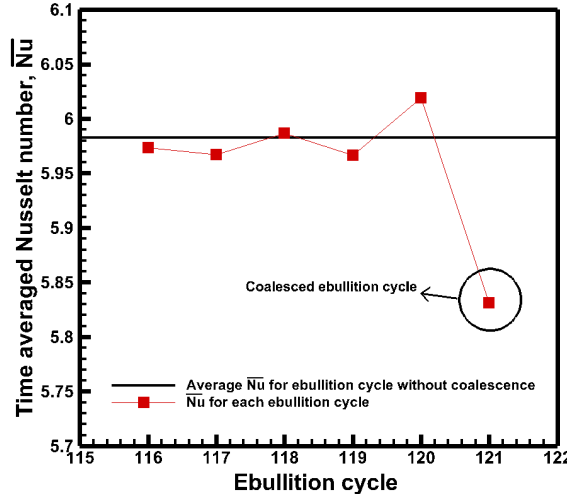


Figure 5.21: Variation in time averaged Nusselt number for various ebullition cycles shown in the inset of Fig. 5.19 with and without vertical coalescence.

D_d and bubble growth period t_g . This reveals the controllability of bubble using transient heat flux. For $q_{avg} = 5000 \text{ W/m}^2$, 10000 W/m^2 , and 15000 W/m^2 , a maximum increase of 50%, 25%, and 1.04% are obtained for bubble departure frequency f showing that lesser q_{avg} value is suitable for power transient-based bubble dynamics control. Further, there exists a limit for the maximum and minimum value possible for f . Vertical coalescence limits the increase in f whereas minimum value is limited by τ value which causes lesser deviation in q_{min} and q_{max} from q_{avg} . Apart from q_{avg} , t_p also influences f . The effect of t_p is evident for $q_{avg} = 5000 \text{ W/m}^2$ and 10000 W/m^2 , whereas for $q_{avg} = 15000 \text{ W/m}^2$ no variation in f was obtained with heating time. Even for $q_{avg} = 5000 \text{ W/m}^2$ and 10000 W/m^2 , the highest f was obtained with lowest heating time. Once the heating time increases, the maximum f reduces and finally a heating time is obtained with which no variation in f with τ . This is due to the increase in $\tau_{safe,vc}$, q_{min} and reduction in q_{max} . Overall, it could be realized that with power transients there exist a range for excursion time, q_{avg} and t_p in which controllability of bubble dynamics will be possible. Outside this range, either a steady behaviour or bubble coalescence will be obtained. These enhancements can be used for thermal management using nucleate boiling.

5.8 Closure

In part I of this study a numerical methodology was formulated on co-located grid robust enough to perform numerical investigation of NBPT. Whereas in this chapter of part II, proposing a simulation methodology the effect of periodic exponential heat flux on nucleate boiling is studied. The present formulation enable us to compare single bubble dynamics under steady and periodic exponential heating conditions. Moreover, the

periodic variation enable us to characterise the input heat flux and further lead to systematic investigation of various parameters associated with periodic exponential heat flux which could be easily extended to other transient heating conditions.

Chapter 6

Effect of Heating Patterns on Single Bubble Nucleate Boiling over a Base Plate

6.1 Introduction

Nucleate boiling under the effect of power transients is a widely observed phenomenon in various engineering applications like immersion cooling (El-Genk, 2012; Narumanchi *et al.*, 2008), nuclear reactors (Su *et al.*, 2016), inkjet printers (Asai, 1991), bubble actuated pumps (Geng *et al.*, 2001), bubble actuated micro-mixers (Tsai and Lin, 2002), micro array fabrication (Okamoto *et al.*, 2000), various MEMS applications (Li *et al.*, 2008) etc. Due to the complex interaction of nucleate boiling phenomenon and transient heating very less studies are reported in the field of *nucleate boiling with power transients* (NBPT) as compared to steady heating. Since various modes of power transients—exponential, step, and linear—has been reported in literature investigating mainly on ONB and CHF, it is essential to have an understanding on the effect of various power transients on nucleate boiling from the perspective of single bubble dynamics and its comparison, not available in literatures. With the aid of previously proposed numerical methodology for NBPT the present study aims to compare single bubble nucleate boiling phenomenon with various transient heat flux.

6.2 Numerical methodology

The discretization, solution methodology and solution algorithm of present SI-LSM_{col} is already discussed in the previous chapter for investigating periodic exponen-

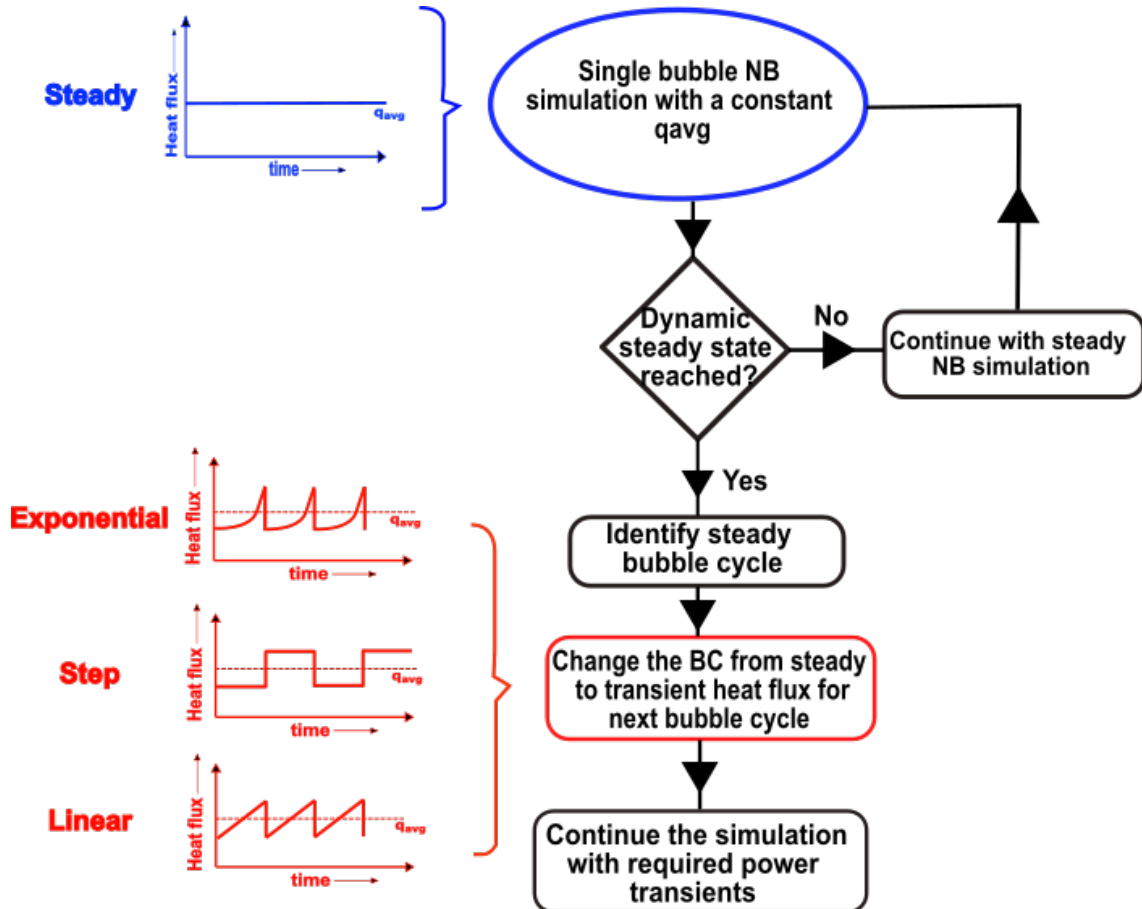


Figure 6.1: Simulation methodology utilized for investigating the effect of various modes of power transients.

tial heat flux. The difference involved in utilization of different heating patterns and the associated input parameters utilized are discussed in this section.

6.2.1 Heating patterns for power transients and associated input parameters

For performing the numerical simulation of single bubble nucleate boiling with power transients, various periodic heating patterns, considered in this study, the time-averaged heat flux q_{avg} during a cycle is kept constant. Thus, the present simulation is initiated with a steady heat flux boundary condition such that $q_{steady} = q_{avg}$. Once the ebullition cycle reaches a dynamic steady state, the steady heat flux boundary condition is changed to transient heat flux. Figure 6.1 shows this simulation methodology for power transient simulation with schematic representation of steady and transient heat flux during various stages of simulation. During power transients, the nature of variation in heat flux could be either exponential, step, or linear depending on the heating or

operating condition of the fluid subjected to nucleate boiling; discussed below.

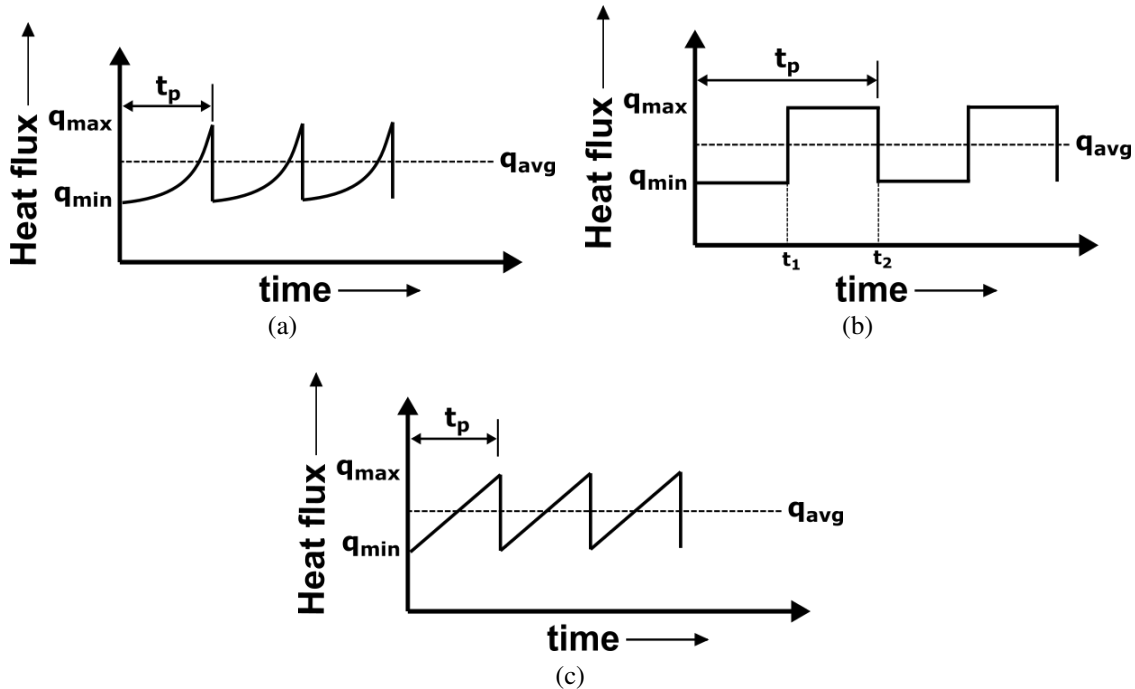


Figure 6.2: Periodic variation in heat flux with each cycle showing (a) exponential, (b) step, and (c) linear variations utilized to investigate the effect on single bubble nucleate boiling dynamics.

Power transients with periodic exponential heat flux

For exponential power transients, the periodic heat flux utilized is shown in Fig. 6.2(a); which is similar to the case described in previous chapter. In this heating pattern the periodic heat flux varies exponentially with time from q_{min} to q_{max} between $t = 0$ and $t = t_p$.

Power transients with periodic step heat flux

As shown in Fig. 6.1, once the dynamic steady state condition is reached with q_{steady} the steady heat flux BC is changed to periodic heat flux BC; given as

$$q(t) = \begin{cases} q_{min} & 0 \leq t < t_1 \\ q_{max} & t_1 \leq t < t_p \end{cases} \quad (6.1)$$

where q_{min} and q_{max} are the minimum and maximum heat flux of the periodic step heat flux, respectively. Whereas, t_1 denotes the time period in cyclic variation for heat flux q_{min} and t_p is the time period of step heat flux. Figure 6.2(b) shows the periodic step heat flux which consist of repeating cycles with variation in q_{min} and q_{max} within the cycle.

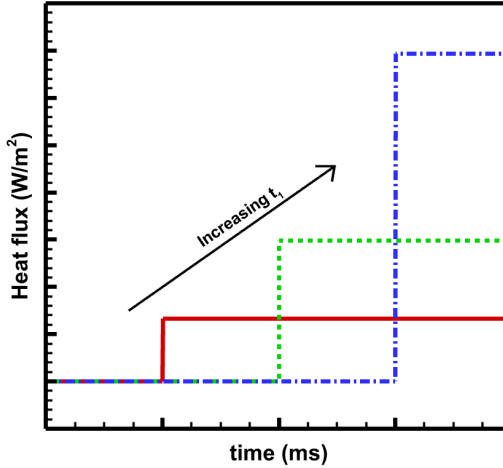


Figure 6.3: Schematic representation of a cycle in periodic step heat flux showing the variation in q_{max} with t_1 for constant q_{avg} and t_p

Since an objective of this study is to compare the effect of various heating patterns, the same is accomplished by the proposed simulation methodology utilized for periodic exponential heat flux. The criterion for this comparison is to keep q_{avg} and t_p value constant for any periodic heat flux. For periodic exponential heat flux, the parameters significantly influencing the input heat are q_{avg} , t_p , and τ . Whereas, for periodic step heat flux apart from q_{avg} and t_p , q_{min} and t_1 also influences the bubble dynamics. Thus, in the present study, q_{avg} , t_p , q_{min} , and t_1 are varied while investigating the effect of periodic step heat flux. For constant q_{avg} and t_p condition, only t_1 is varied by keeping q_{min} constant and repeated for different q_{min} value.

For periodic step heat flux, the time averaged heat flux is given as

$$q_{avg} = \frac{\int_0^{t_p} q(t)dt}{t_p} = \frac{\int_0^{t_1} q_{min}dt + \int_{t_1}^{t_p} q_{max}dt}{t_p} \quad (6.2)$$

From the above equation, for a known q_{min} , the maximum heat flux is obtained as

$$q_{max} = \frac{q_{avg}t_p - q_{min}t_1}{t_p - t_1} \quad (6.3)$$

Figure 6.3 shows a schematic representation of the variation between q_{max} and t_1 , q_{max} increases with increasing t_1 . This is similar to increase in q_{max} with decreasing excursion time τ in periodic exponential heat flux for a constant q_{avg} and t_p .

Power transients with periodic linear heat flux

Apart from the periodic exponential and step heat flux, another form of periodic heat flux studied is periodic linear heat flux. Figure 6.2(c) shows the periodic linear heat flux, with a linear time-wise variation in heat flux from q_{min} to q_{max} with time period t_p . The

Table 6.1: For a periodic step heating, with a constant $q_{avg} = 10000 \text{ W/m}^2$, $t_p = 8 \text{ ms}$, and $q_{min} = 100 \text{ W/m}^2$ variation in t_1 or t_2 and the resulting q_{max}

t_1 (ms)	t_2 (ms)	q_{max} (W/m ²)
2	6	13300
4	4	19900
6	2	39700

time averaged heat flux for the periodic linear heat flux is given as

$$q_{avg} = \frac{\int_0^{t_p} q(t)dt}{t_p} = \frac{\int_0^{t_p} (q_{min} + mt)dt}{t_p} \quad (6.4)$$

From the above equation, the minimum heat flux is obtained as

$$q_{min} = q_{avg} - \frac{mt_p}{2} \quad (6.5)$$

where m is the slope of linear curve which is a parameter that influences the input heat apart from q_{avg} and t_p .

6.2.2 Parametric values associated with input heat flux

For investigating the effect of periodic exponential heat flux in the previous chapter, q_{avg} was varied from 5000 W/m^2 - 15000 W/m^2 , t_p from 4 ms - 16 ms , and τ from 0.2 ms - 8 ms . It was observed that the frequency of ebullition cycle increases for various heat flux values except $q_{avg} = 15000 \text{ W/m}^2$. Hence, in this study, for comparing the dynamics of ebullition cycle, a constant value of $q_{avg} = 10000 \text{ W/m}^2$ is chosen, since similar trend is observed at other lower q_{avg} value of 5000 W/m^2 . Thus, the comparisons of the three types of periodic heating patterns are performed here for $q_{avg} = 10000 \text{ W/m}^2$.

For periodic step heat flux, the parameters that influences the heat input are q_{avg} , q_{min} , t_1 or t_2 , and t_p . The time period t_p of periodic step heat flux chosen is similar to the values utilized for periodic exponential heat flux—4ms, 8 ms, 12 ms, and 16ms. Apart from q_{avg} and t_p which are common parameters in both periodic exponential heat flux and periodic step heat flux, the periodic step heat flux also considers q_{min} and t_1 or t_2 as input parameter. For the present study a constant q_{min} value of 100 W/m^2 is utilized. For a constant t_p , t_1 is increased from a lower to higher value which leads to reduction in t_2 . Since q_{avg} is kept constant and q_{min} is associated with t_1 , increase in t_1 or reduction in t_2 results in increase in q_{max} . This is shown in Table 6.1 for a case of periodic step heating.

Table 6.2: For periodic linear heat flux, variation in q_{min} and q_{max} with the slope of the linear heating m .

m	q_{min} (W/m²)	q_{max} (W/m²)
0.2	9999.9992	10000.0008
0.4	9999.9988	10000.0012
0.6	9999.9976	10000.0024
0.8	9999.9968	10000.0032

For periodic linear heat flux, the slope m is the additional parameter along with q_{avg} and t_p . Similar to the above in periodic step heat flux, all the simulations for periodic linear heat flux are performed with q_{avg} of 10000 W/m² and t_p values of 4 ms, 8 ms, 12 ms, and 16 ms. Further, for the slope m is varied from 0.2 to 0.8 in steps of 0.2. Note that $m = 0$ and $m = 1$ are not considered since they are the limiting cases of periodic linear heat flux resulting in steady and periodic step heat flux, respectively. For the present periodic linear heat flux Table 6.2 shows an insignificant deviation in the values of q_{min} and q_{max} from q_{avg} due to the smaller time scale of time period. It could be thus inferred that linear heat flux will be having significant influence on nucleate boiling at larger time period t_p of the periodic heating.

6.3 Effect of Periodic-versus-Steady Heat Flux BC on the Bubble Dynamics during the Nucleate Boiling: A Comparative Study on Exponential, Step, and Linear Periodic Heating

In this section, a comparative study on the effect of various modes of periodic heat flux—exponential, step, and linear—on bubble dynamics parameter—bubble departure diameter (D_d), bubble growth period (t_g), and bubble departure frequency (f), are presented. Along with q_{avg} and t_p as the input parameters for exponential periodic heat flux, the effect of the additional parameters for the step and linear periodic heat fluxes are also investigated here.

6.3.1 Bubble departure diameter (D_d), and bubble growth period (t_g)

Along with common input parameters as— q_{avg} and t_p , the additional parameter varied in the present study is excursion time τ for exponential, ratio between time period

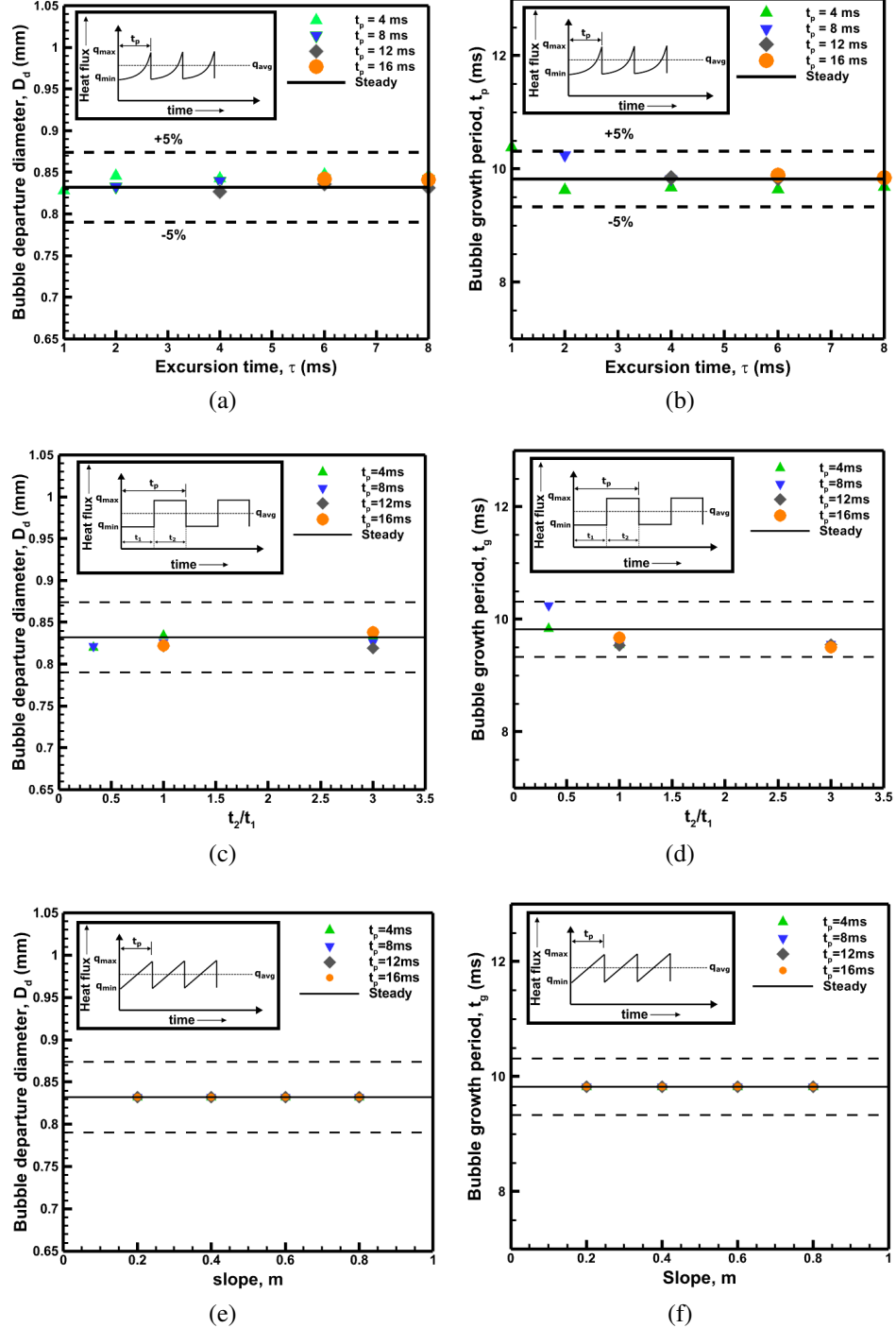


Figure 6.4: Variation in bubble departure diameter D_d and bubble growth period t_g with the input parameters —(a)-(b) τ for exponential, (c)-(d) t_2/t_1 for step, and (e)-(f) slope m for linear periodic heat fluxes for various time period t_p of periodic heating. All the simulations are performed with constant $q_{avg} = 10000 \text{ W/m}^2$ and $q_{min} = 100 \text{ W/m}^2$ for step heating. Further, the inset shows corresponding periodic heat flux utilized. For larger t_p note that the above results are not shown for smaller τ (t_2/t_1) value in the exponential (step) periodic heat flux since the cases correspond to vertical coalescence.

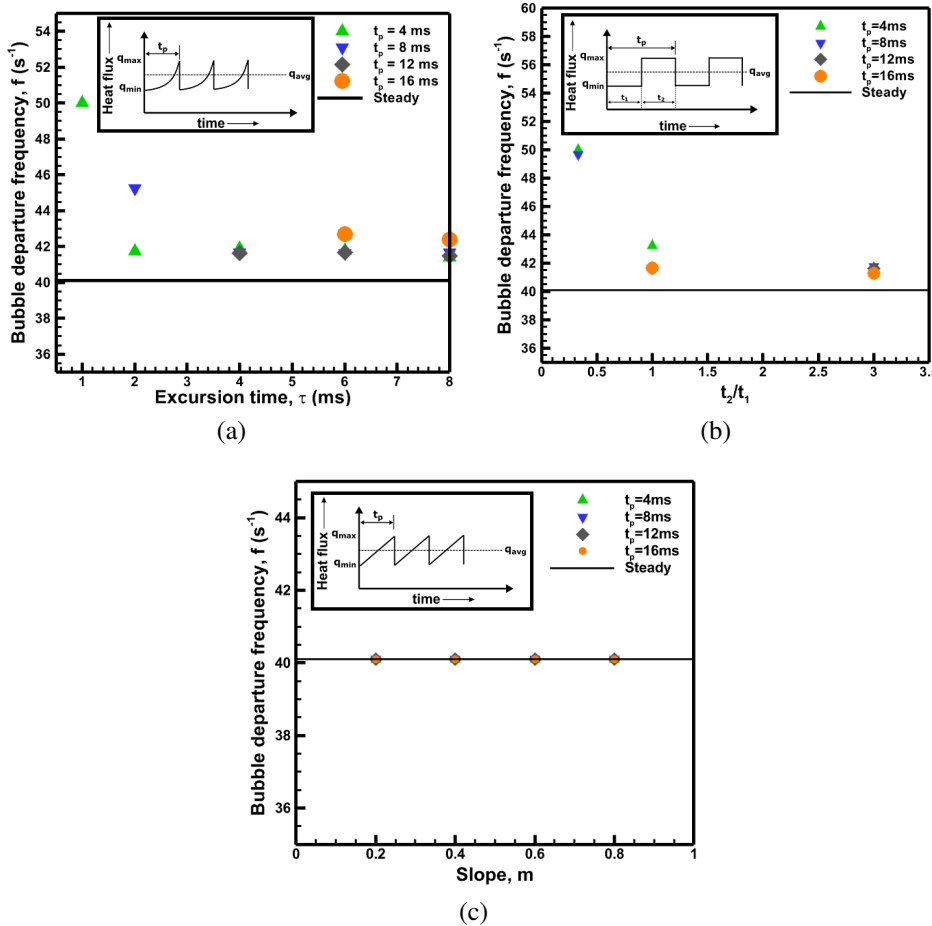


Figure 6.5: Variation in bubble departure frequency (f) with the input parameters —(a) τ for exponential, (b) t_2/t_1 for step, and (c) slope m for linear periodic heat fluxes for various time period t_p of periodic heating. All the simulations are performed with constant $q_{avg} = 10000 \text{ W/m}^2$ and $q_{min} = 100 \text{ W/m}^2$ for step heating. Further, the inset shows corresponding periodic heat flux utilized.

t_2 associated with q_{max} and t_1 associated with q_{min} for periodic exponential heat flux for a fixed q_{min} , and the slope m for periodic linear heat flux. The values utilized for each of these parameters are discussed in previous section. Further, all the simulations are compared at a constant q_{avg} value of 10000 W/m^2 . Here, as presented in previous chapter, bubble departure diameter D_d corresponds to the apparent diameter of vapor bubble at the instance of detachment from solid wall, and bubble growth period t_g is the interval between seeding of a vapor bubble and departure from solid wall.

Figure 6.4 shows the variation in bubble departure diameter and bubble growth period for exponential, step, and linear periodic heat flux. For plotting this figure initially single bubble nucleate boiling simulation is performed with $q_{steady} = 10000 \text{ W/m}^2$. For the periodic heat flux considered with constant q_{avg} , Fig. 6.4 shows no significant difference

in bubble departure diameter D_d and bubble growth period t_g since the data obtained under the transient heating condition is within $\pm 5\%$ of the data corresponding to q_{steady} .

6.3.2 Bubble departure frequency

Bubble departure frequency (f) calculated based on Eq. 5.10, is also compared in this study apart from the D_d and t_g . Figure 6.5 shows the variation in f obtained for various periodic heat flux for the input parameters discussed in previous section. Figure 6.5(a) shows an increase in f with reduction in τ . For constant q_{avg} and t_p , reduction in τ , increases q_{max} resulting in reduced waiting time. Since this phenomenon is discussed in detail in chapter 5 the same is not repeated. Figure 6.5(b) show similar phenomenon of increase in f for periodic step heating as the ratio t_2/t_1 decreases. In periodic step heating with constant q_{avg} , t_p , and q_{min} , as t_2 reduces to establish constant q_{avg} in the periodic cycle q_{max} also increases which is similar to reducing τ in periodic exponential heat flux. For both the case, this increase in q_{max} is resulting in increase of f . The upper limit in f is decided by vertical coalescence whereas the lower limit corresponds to f value of steady heating condition. As shown in Table 6.2 for periodic linear heat flux at the present time scale of t_p since there no significant variation in q_{min} and q_{max} from q_{avg} the D_d , t_g , and f is similar to the values of steady heating.

6.4 Vertical coalescence

Vertical coalescence is a phenomenon resulting due to coalescence of departed bubble with seeded bubble from same cavity, discussed in detail in chapter 5. As observed with periodic exponential heat flux, vertical coalescence is occurring in periodic step heat flux but not in periodic linear heat flux as expected.

Figure 6.6 shows a comparison of $q_{safe,vc}$ with t_p for various periodic heat flux boundary conditions. The maximum heat flux q_{max} associated with the periodic exponential and step heat fluxes, at which there is no vertical coalescence is referred here as $q_{safe,vc}$. Since q_{max} is a common input parameter for two types of periodic heat fluxes, as shown in Fig. 6.6, $q_{safe,vc}$ is utilized here for comparison. For periodic exponential heat flux, apart from $q_{safe,vc}$ the variation in $\tau_{safe,vc}$ with t_p was also shown in the previous chapter. It could be observed from Fig. 6.6 that $q_{safe,vc}$ increases substantially for both the heat fluxes. At lower values of t_p , it almost reach constant for the step heat flux, whereas, for the exponential heat flux, a significant reduction in increase of $q_{safe,vc}$ value could be seen showing it also reaching to a constant $q_{safe,vc}$ value towards smaller t_p . Additionally, for the step heat flux, to investigate the effect of q_{min} on $q_{safe,vc}$, the value of q_{min} is increased from

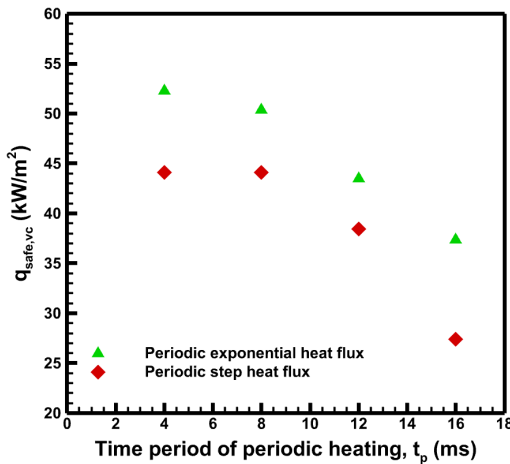


Figure 6.6: Variation of the $q_{safe,vc}$ (critical value of q_{max} above which there is an onset of vertical coalescence) with increasing time period (t_p) for periodic exponential and step heat fluxes. All simulations are performed with $q_{avg} = 10000 \text{ W/m}^2$ and $q_{min} = 100 \text{ W/m}^2$ for step heating.

100 W/m^2 to 1000 W/m^2 and similar simulations are performed for $t_p = 8 \text{ ms}$. This resulted in $q_{safe,vc}$ value of 43.35 kW/m^2 with $q_{min} = 1000 \text{ W/m}^2$ instead of $q_{safe,vc} = 44 \text{ kW/m}^2$ with $q_{min} = 100 \text{ W/m}^2$.

6.5 Effect of modified periodic heating patterns on the bubble dynamics

Apart from these conventional heating patterns some modified heating patterns, shown in Figure 6.7, is utilized to investigate their effect on bubble dynamic parameters and on vertical coalescence with an objective of understanding the nature of heat flux with which more control on bubble dynamics could be established, leading to boiling on demand. Further, the results obtained from periodic exponential heat flux—hereafter also referred as case-1 heating pattern—are utilized for comparing with the results of these modified periodic heat flux.

6.5.1 Power transients with exponential rise and delay (case-2 and case-3 heating pattern)

In the previous chapter, Fig.6.7(a) was utilized to show that $q_{max} > q_{safe,vc}$ is not the sufficient condition for vertical coalescence, and utilized here to investigate the effect of this pattern on bubble ebullition cycle. As discussed previously, this heating pattern consist of an exponential rise followed with delay period, referred hereafter as case-2 heating pattern. During exponential rise, the heat flux will vary from q_{min} to q_{max} with a particular

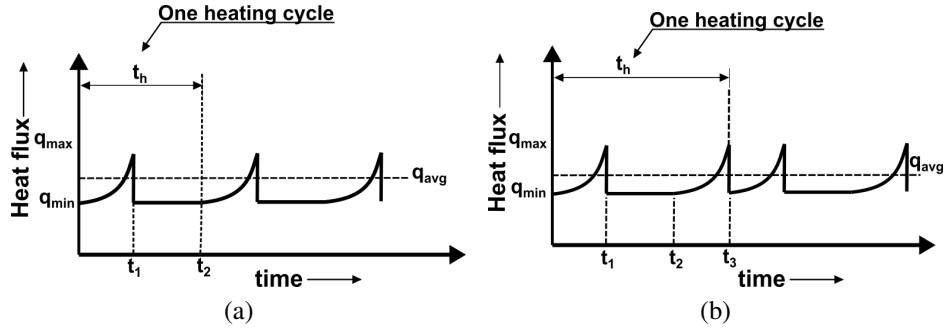


Figure 6.7: Various heating patterns investigated to study the effect on single bubble nucleate boiling dynamics, with each periodic heat flux cycle consisting of (a) exponential rise and delay, and (b) exponential rise, delay, and exponential rise.

exponential time period τ . Whereas during delay period, the heat flux will be constant with magnitude of q_{min} obtained during exponential rise. The figure also shows that heat flux undergoes exponential variation till t_1 , whereas delay between t_1 and t_2 , respectively. Figure 6.7(b) shows another heating pattern utilized consisting of exponential rise, delay, and exponential rise, referred hereafter as case-3 heating pattern. This pattern consist of two exponential rise in a heating cycle as compared to case-1 heating pattern. For the heating cycle of case-2, exponential rise occur till t_1 , delay between t_1 and t_2 , and exponential rise between t_2 , and t_3 . The major difference between case-2 and case-3 being the occurrence of one and two exponential rise in heat flux for a heating cycle, respectively.

Case-2 heating pattern:

The time-averaged heat flux is given as

$$q_{avg} = \frac{\int_0^{t_1} q_{min} \exp(t/\tau) dt + \int_{t_1}^{t_2} q_{min} dt}{t_h} \quad (6.6)$$

From the above equation, the minimum heat flux is obtained as

$$q_{min} = \frac{q_{avg} t_h}{\tau [\exp(t_1/\tau) - 1] + (t_2 - t_1)} \quad (6.7)$$

Case-3 heating pattern:

The time-averaged heat flux is given as

$$q_{avg} = \frac{\int_0^{t_1} q_{min} \exp(t/\tau) dt + \int_{t_1}^{t_2} q_{min} dt + \int_{t_2}^{t_3} q_{min} \exp(t/\tau) dt}{t_h} \quad (6.8)$$

From the above equation, the minimum heat flux is obtained as

$$q_{min} = \frac{q_{avg} t_h}{\tau [\exp(\frac{t_1}{\tau}) - 1] + (t_2 - t_1) + \tau [\exp(\frac{t_2}{\tau}) - \exp(\frac{t_3}{\tau})]} \quad (6.9)$$

For investigating the effect of case-1, heating pattern q_{avg} was varied from 5000 W/m^2 - 15000 W/m^2 , t_h from 4 ms - 16 ms , and τ from 0.2 ms - 8 ms ; as discussed earlier. It was observed that the frequency of ebullition cycle increases for various heat flux values except $q_{avg} = 15000 \text{ W/m}^2$. Hence, in this study, for comparing the dynamics of ebullition cycle q_{avg} value of 10000 W/m^2 is considered, since similar trend is obtained at lower q_{avg} , i.e., 5000 W/m^2 . Thus all the comparisons of heating patterns are performed at $q_{avg} = 10000 \text{ W/m}^2$.

For case-2 and case-3 heating patterns, since exponential rise is involved in the heating cycle, apart from q_{avg} other input parameters that characterise these heating cycles are exponential time period τ , cycle heating time t_h , and delay time (time period of delay in a heating cycle). Even though case-1 simulations were performed with various t_h — 4 ms , 8 ms , 12 ms , and 16 ms , t_h values of 4 ms and 16 ms are utilized for the present case-2 simulations, while for case-3 only $t_h = 4$ is utilized to evaluate any appreciable difference from case-2 simulations. Because, in case-1 simulations for a constant q_{avg} (5000 W/m^2 , and 10000 W/m^2) almost similar and an increase in f_{ebull} was observed at higher and lower t_h , respectively. Once the heating time is decided then the subsequent partitioning for delay and the exponential rise in heat flux need to be decided for both the heating patterns (case-2 and case-3). For case-2 since heating cycle consist of only an exponential rise and delay, the time associated with delay was increased from low value. Thus, for $t_h = 4 \text{ ms}$, the delay time utilized are 1 ms , 2 ms , and 3 ms causing heating time for exponential rise as 3 ms , 2 ms , and 1 ms , respectively. Whereas for $t_h = 16 \text{ ms}$, the delay time utilized are 2 ms , 8 ms , and 14 ms causing heating time for exponential rise as 14 ms , 8 ms , and 2 ms , respectively; since cycle heating time is the sum of time associated with exponential rise and delay. For case-3, since heating cycle consist of exponential rise, delay, and exponential rise, the time associated with delay was increased and suitably the time for remaining two exponential rise are evaluated. For delay time of 1 ms and 2 ms considered, the time for first exponential rise is 2 ms and second exponential rise is 1 ms for delay time of 1 ms , whereas time for both exponential rise is taken as 1 ms for delay time of 2 ms . Further, for excursion time period, the range of τ (0.2 ms – 8 ms) considered for case-1 is adopted.

6.5.2 Bubble departure diameter (D_d) and Bubble growth period (t_g)

Utilizing the heating pattern as shown in Figs. 6.7(a)s (case-2) and 6.7(b) (case-3), the effect of input parameters associated with heating pattern on bubble departure diameter D_d and bubble growth period t_g are investigated.

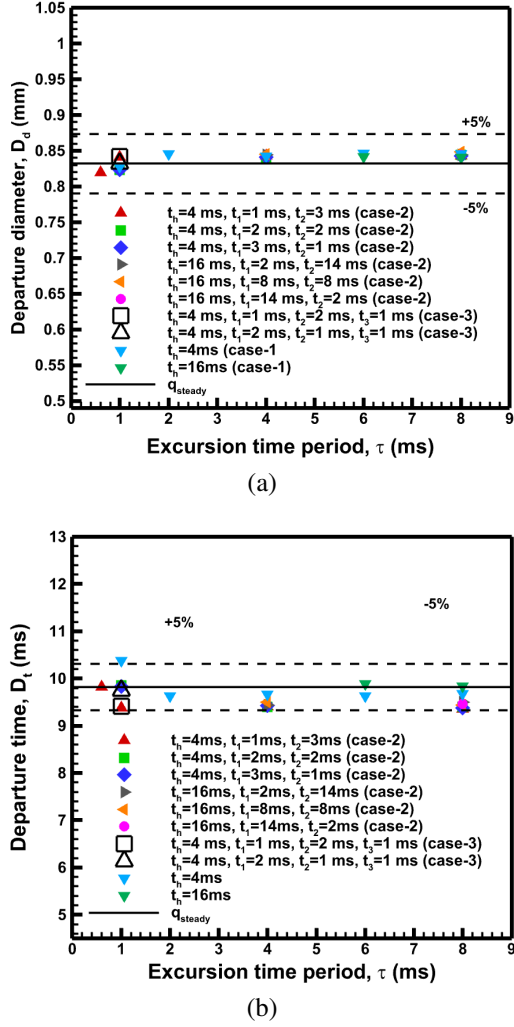


Figure 6.8: Effect of time period of periodic heating t_p and excursion time τ on (a)bubble departure diameter D_d and (b) bubble growth period t_g of the bubble for case-2 and case-3 heating patterns, compared with case-1 and steady heating condition for $q_{avg} = q_{steady} = 10000 \text{ W/m}^2$.

Figure 6.8 shows the variation in bubble departure diameter D_d and bubble growth period t_g of the bubble for various heating conditions—steady, case-1, case-2, and case-3. Figure shows six difference input parameters for case-2 with different combinations of t_1 and t_2 , such that delay time is shorter and larger delay time are involved. Whereas, for case-3, only two combinations are utilized with $t_h = 4 \text{ ms}$. Once the t_h and subsequent time for individual heating sections in heating cycle along with τ value is decided, then q_{min} is calculated using Eq. (6.7) and Eq. (6.9) for case-2 and case-3 heating patterns, respectively.

In previous chapter for case-1 heating pattern, as shown in Fig. 5.9, no appreciable difference was observed for departure diameter and departure time with various t_h , τ , and q_{avg} since the time averaged heat flux during the heating cycle was constant. Since this

q_{avg} was equal to q_{steady} , less than 5% variation was observed for D_d and t_g between steady and transient heat flux conditions. Similar to aforementioned observation, even for case-2 and case-3, no appreciable difference in D_d and t_g are observed as shown in Fig. (6.8(a)) and (6.8(b)), respectively, for different τ . Since $q_{steady} = q_{avg} = 10000 \text{ W/m}^2$, the obtained departure diameter and departure time are within $\pm 5\%$ from corresponding steady heating condition.

6.5.3 Bubble departure frequency f

Apart from D_d and t_g , another parameter which characterize the bubble dynamics is bubble release frequency, defined as the total number of ebullition cycles per unit time, given as

$$f_{ebull} = \frac{1}{t_g + t_w}$$

where t_w is the waiting time. Figure 6.9 shows the variation of f with τ , obtained for steady, case-1, case-2, and case-3 simulations keeping $q_{avg} = q_{steady} = 10000 \text{ W/m}^2$. For the case-1 heating pattern, it was observed that f increases with decreasing τ at a constant q_{avg} and t_p . But this increase was not observed at higher t_h due to the occurrence of vertical coalescence at higher values of $\tau_{safe,vc}$ as compared to lower value of $\tau_{safe,vc}$ at lower t_h . For case-2 heating pattern the Fig. 6.9 also shows the variation in f with τ for two different time period t_p for periodic heating, $t_p = 4 \text{ ms}$ and $t_p = 16 \text{ ms}$. Similar trend could be seen between case-1 and case-2 heating patterns, since f shows an increase at $t_p = 4 \text{ ms}$ whereas not for $t_p = 16 \text{ ms}$. Moreover, as shown in Fig. 6.9 maximum f obtained between case-1 and case-2 are almost similar. For case-3 heating pattern, two simulations were performed with $t_p = 4 \text{ ms}$ since an increase in f is obtained at lower t_p and the delay time was increased from 1 ms to 2 ms with subsequent calculation of time associated with exponential rise. As the delay time increases it could be noted that there is reduction in f . Whereas, the maximum f for case-3 heating pattern is not high as compared to case-1 and case-2 heating patterns, while the lower f is closer to f due to steady heating condition as observed for other heating cases. For case-3 with higher t_p , no increase in f is observed for the case-1 and case-2.

6.5.4 Vertical coalescence

For case-1 heating pattern, it was observed that if the condition $q_{max} > q_{safe,vc}$ is established within t_{rise} then the newly seeded bubble coalesce with previously departed bubble leading to vertical coalescence. For constant t_p and q_{avg} , it was also observed that no vertical coalescence occur if τ is higher than $\tau_{safe,vc}$. Similar investigation is carried

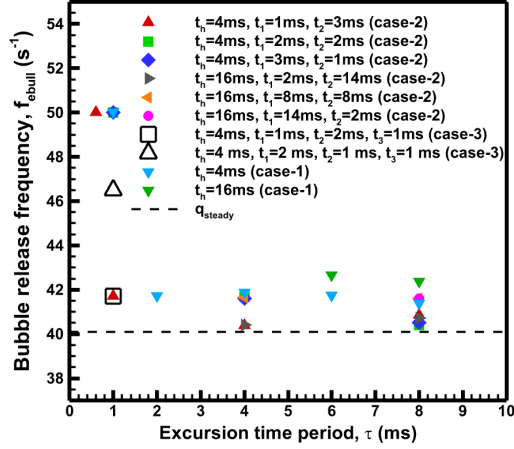


Figure 6.9: Effect of time period for periodic heating t_p and excursion time τ on bubble departure frequency f of the bubble for case-2 and case-3 heating patterns, compared with case-1 and steady heating condition for $q_{\text{avg}} = q_{\text{steady}} = 10000 \text{ W/m}^2$.

out here for case-2 and case-3 heating patterns. Figure 6.10 shows the $\tau_{\text{safe,vc}}$ obtained for case-2 and case-3 heating pattern. For these cases, to see any difference in $\tau_{\text{safe,vc}}$ from

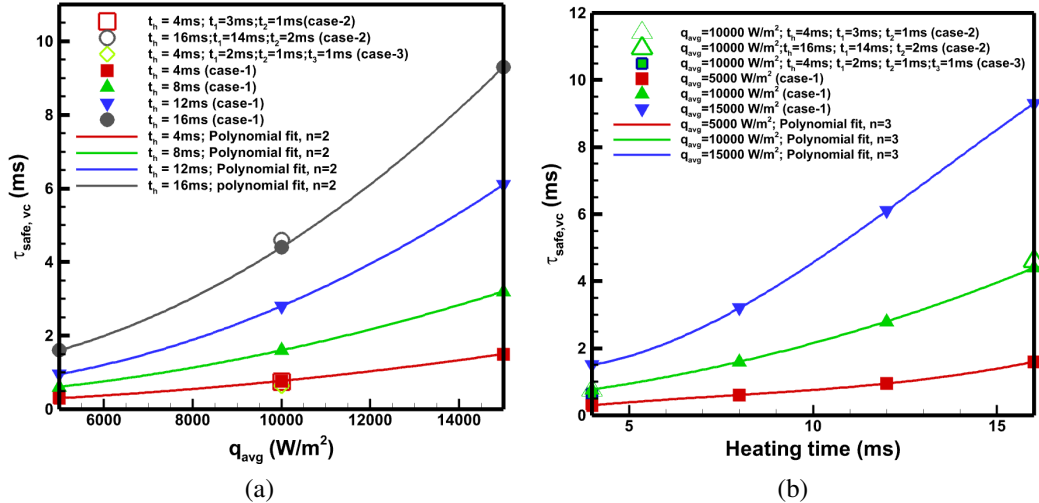


Figure 6.10: For case-1, case-2, and case-3 heating patterns variation in (a) $\tau_{\text{safe,vc}}$ with q_{avg} for various constant t_p and (b) $\tau_{\text{safe,vc}}$ with t_p for various q_{avg} constant values. The symbols correspond to numerical data and the solid line indicates curve fitted with a polynomial function with order n .

case-1 heating pattern, the case with least delay time is utilized due to their potential for early vertical coalescence. Thus, for case-2, the delay time utilized are 1 ms and 2 ms for t_p values of 4 ms and 16 ms, respectively. Similarly for case-3, the delay time utilized is 1 ms for $t_p = 4 \text{ ms}$. Figure 6.10(a) shows the variation in $\tau_{\text{safe,vc}}$ with q_{avg} , whereas Fig. 6.10(b) shows the variation in $\tau_{\text{safe,vc}}$ with t_p , with no appreciable difference in $\tau_{\text{safe,vc}}$ for case-2 and case-3 in comparison with case-1 heating pattern. The $q_{\text{safe,vc}}$ obtained based on this $\tau_{\text{safe,vc}}$ is shown in Fig. 6.11 which also shows no significant difference. To

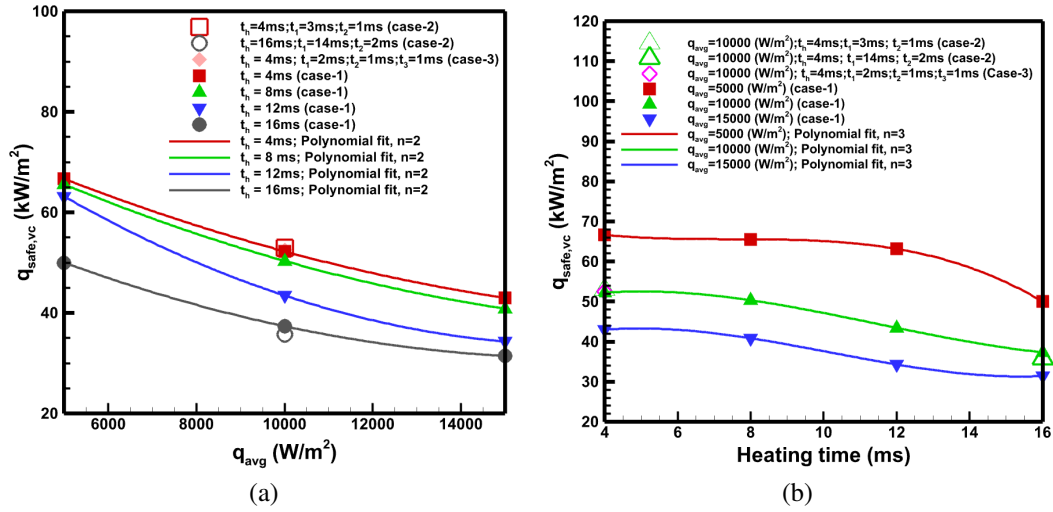


Figure 6.11: For case-1, case-2, and case-3 heating patterns variation in (a) $q_{safe,vc}$ with q_{avg} for various constant t_p and (b) $q_{safe,vc}$ with t_p for various q_{avg} constant values. The symbols correspond to numerical data and the solid line indicates curve fitted with a polynomial function with order n .

further validate, case-3 simulation with $t_p = 16 \text{ ms}$ and delay time of 2 ms was performed to obtain $q_{safe,vc}$ of 38.72 kW/m^2 in comparison to 35.75 kW/m^2 obtained with case-2 with $t_p = 16 \text{ ms}$ and delay time of 2 ms , showing a deviation of 8.3% between two cases.

6.6 Closure

This chapter is a continuation of chapter 5 for CmFD application and analysis. Various modes of power transients are investigated and compared based on the criterion of $q_{steady} = q_{avg}$. For all the heating patterns considered, almost similar departure diameter and departure time are observed for ethanol vapor if time averaged heat flux is equal. Moreover, the step heating is found to be detrimental as compared to exponential and linear heating due to the occurrence of early vertical coalescence under similar heating conditions. Whereas, linear heating is similar to steady heating due to the low time scale associated with time period of periodic heating. Various modified exponential heating patterns are also considered showing similar result to that of periodic exponential heat flux.

Chapter 7

Conclusions of the Present Work and Scope for Future Work

The conclusions drawn from the present work and the scope for future work are discussed in this chapter with separate subsections.

7.1 Conclusions of the present work

For the three chapters in Part I on CmFD development and two chapters in Part II on CmFD application and analysis, conclusion drawn from this study are presented in separate subsections below.

7.1.1 On Ghost Fluid Method-based Sharp Interface Level Set Method on a Co-located Grid and its comparison with Balanced Force-based Diffuse Interface Method

A ghost fluid method (GFM)-based SI-LSM is *proposed* for the co-located grid system, and its numerical methodology is compared with balanced force method (BFM)-based DI-LSM—using a unified numerical formulation for the *first* time in the literature. Relative performance of the present LSMs, as compared to the published VOF method, is comprehensively presented for a static droplet problem. Further, for the present LSMs, order of accuracy study is presented for a capillary wave problem while the relative performance is demonstrated for a dam break and droplet coalescence problems. The conclusions drawn from the present work are as follows:

- For SI-LSM, a Sharp Surface Force (SSF) model-based interfacial jump condition for pressure avoids pressure-interfacial force imbalance-based decoupling; thus,

eliminating the requirement of BFM (needed for the DI-LSM). Further, while implementing the BFM for the Continuum Surface Force (CSF) model-based DI-LSM, the volumetric surface tension term need to be excluded while defining the provisional velocity (Eq. 2.16) during the prediction of the velocity; in the present predictor-corrector approach-based Semi-Explicit pressure projection method.

- For testing the *coupling* of the surface tension force with the pressure gradient, needed for the pressure-interfacial force-balance, an exact curvature κ_{exact} is imposed on the static droplet. For the κ_{exact} case, the SSF model-based SI-LSM leads to much smaller error—for the pressure jump ($E(\Delta p)$ and $E(\Delta p_{max})$) and spurious velocity $E(U_{max})$ —as compared to the CSF model-based DI-LSM; in agreement with that reported, for the respective model-based VOF methods, by Francois *et al.* (2006). However, the error for the SSF model-based VOF method is smaller than the present SI-LSM.
- Whereas, for the computed curvature κ_{comp} case, the error for the present SI-LSM is close to that for the SSF-VOF with height function; their most accurate VOF solver (Francois *et al.*, 2006). Overall for the present LSMs, only the surface tension model affects the accuracy of the pressure-jump while the error in spurious velocity gets affected by both surface tension model and curvature estimation.
- Further, for the static droplet with the κ_{exact} , the increasing density ratio have almost no effect on $E(\Delta P)$ while $E(\vec{u}_{max})$ increases for present LSMs. Whereas, for the κ_{comp} case, variation in thermo-physical properties and time-step Δt have no affect on $E(\Delta P)$ whereas variation of surface tension coefficient σ , density ρ_1 , and Δt affects $E(\vec{u}_{max})$. For the VOF method (Francois *et al.*, 2006), similar results are reported for $E(\vec{u}_{max})$ while that for $E(\Delta P)$ is not available.
- For the other CmFD benchmark problems on dam break and Rayleigh-Taylor, the relative performance of present LSMs is demonstrated in the Cartesian and whereas for droplet coalescence on axisymmetric coordinate system. For these problems also, the accuracy of the results are more accurate for the SI-LSM as compared to DI-LSM. From an order of accuracy study, on a capillary wave problem, the present LSMs are in-between first and second order accurate.

The present work is significant as it presents *a novel* GFM-based SI-LSM on a co-located grid, a new *perspective* to the various types of numerical methodologies for the two-phase flow, and a relative *performance* study of the sharp-versus-diffuse approaches-based LSMs on the much simpler co-located grid.

7.1.2 On Comparison of Staggered and Co-located Grid-based Diffuse and Sharp Interface Level Set Method

For both sharp and diffuse interface level set methods a comparison of numerical methodologies on staggered and co-located are presented for the *first* time in literature. Further, for present LSMs, order of accuracy study is presented for a capillary wave problem while both validation and relative accuracy studies are presented for static droplet, dam break, and Rayleigh-Taylor instability. The conclusions drawn from present work are as follows:

- For CmFD, the mathematical formulation of GFM-based interfacial jump condition-based sharp surface force (SSF) in SI-LSM is shown to be similar on both staggered and co-located grid with difference in numerical implementation. Whereas, for continuum surface force (CSF) formulation in DI-LSM, mathematical formulation and numerical implementation are shown to be different on both grid systems.
- The pressure-interfacial force-decoupling is avoided by SSF method-based mathematical formulation while it is avoided later during the numerical formulation for the CSF method-based DI-LSM on a co-located grid whereas inherent on staggered grid.
- For a capillary wave problem, order of accuracy with present LSMs are in between first and second order accurate. For static droplet, dam break, and Rayleigh-Taylor instability, good agreement of the present LSMs is demonstrated as compared to the published analytical, numerical, and experimental results. Further, for these problems, SI-LSM on co-located grid results in better accuracy as compared to SI-LSM_{stag}, DI-LSM_{stag}, and DI-LSM_{col}; except for the leading edge distance in dam break simulation where SI-LSM_{stag} performs better.

The present work is significant as it presents and compares various numerical methodologies to clearly demonstrate the similarity and dissimilarity of various level set methods for the two-phase flow. The work also presents a detailed relative accuracy study of the sharp-versus-diffuse approaches-based LSMs on staggered-versus-co-located grid.

7.1.3 Sharp Interface Level Set Method on a Co-located Grid for CmFD with Heat Transfer-induced Phase Change

The present study establish robustness of interfacial jump condition-based formulation to avoid pressure-interfacial force imbalance for complex multiphase problems es-

pecially at high density ratio, $O(10^3)$; presented for *first* time in literature for LSM on co-located grid. Moreover, the present interfacial jump condition-based formulation is straightforward and robust to incorporate multi-physics effect on co-located grid. For CmFD with phase change, pressure jump at interface balance normal component of viscous stress, surface tension, and recoil pressure without violating the interfacial force balance criterion, essential on co-located grid.

Various benchmark CmFD with phase change problems—Solidification, one-dimensional moving interface, one-dimensional sucking interface, growth of suspended bubble in superheated liquid, film boiling, and single bubble nucleate boiling—are considered to test the present formulation on co-located grid. Further, this includes simulation on axisymmetric coordinate for growth of suspended bubble in superheated liquid and single bubble nucleate boiling simulations, whereas two dimensional Cartesian coordinate for other problems. All the problems shows good agreement with published results on literature. The agreement between present LSM on co-located grid and published experiment establish capability and robustness of co-located to handle high density ratio multi-physics problems.

To the authors knowledge, this study shows first successful application of LSM on co-located for CmFD with phase change, especially for high density ratio conditions. Thus showing its potential as a suitable substitute for staggered grid, for multi-disciplinary and multi-physics applications.

7.1.4 Single bubble nucleate boiling over a base plate, subjected to Power Transients

A numerical methodology to investigate the effect of power transients with exponential mode of heating on bubble dynamics and its comparison with steady heating condition is proposed and performed with in-house SI-LSM_{col} code. Major conclusions drawn from the present work are as follows:

- For power transients with exponential heating, the excursion time τ , time period of periodic heat flux t_p , and time-averaged heat flux in a periodic heat flux cycle q_{avg} characterises the heating cycle.
- Cyclic variation of exponential heat flux with time is utilized to investigate the effect of τ , t_p , and q_{avg} on bubble dynamics. The constraint imposed on heat flux ($q_{avg} = q_{steady}$) enables comparison between bubble dynamics under transient and steady heating conditions.

- If the q_{avg} is kept constant, then neither t_p and τ does not affect the bubble departure diameter D_d and bubble growth period t_g of the bubble.
- For constant q_{avg} and t_p , as excursion time τ decreases bubble departure frequency f increases except at higher heating time (16 ms in the present study). Whereas, for higher q_{avg} ($= 15000 \text{ W/m}^2$) with various t_p utilized, no increase in bubble release frequency f is observed due to the occurrence of vertical coalescence at higher $\tau_{safe,vc}$.
- Limiting condition for excursion time τ value causing maximum and minimum bubble departure frequency f is identified as the occurrence of vertical coalescence and steady condition, respectively. Because τ value cannot be increased indefinitely to increase f which results in vertical coalescence and beyond certain maximum value power transients and steady heat flux condition behaviour is similar.
- Necessary and sufficient condition for vertical coalescence is identified. Sufficient condition being the maximum heat flux in period heat flux (q_{max}) greater than minimum q_{max} value for vertical coalescence ($q_{safe,vc}$ at constant q_{avg} and t_p), whereas necessary condition being the occurrence of q_{max} within a time scale for the departed bubble to travel a distance of initial seed height.
- For constant t_p , $\tau_{safe,vc}$ increase with increase in q_{avg} . Similarly for constant q_{avg} , $\tau_{safe,vc}$ increases with t_p .
- For the various seed diameter no appreciable variation in $q_{safe,vc}$ is observed, whereas increasing ΔT_{act} shows a significant increase in $q_{safe,vc}$ because as T_{act} directly influences the waiting time of bubble and hence the vertical coalescence.
- Considering the application of nucleate boiling with power transients for bubble controllability and thermal management, there exist a region at which increased bubble departure frequency f can be obtained. Outside this region vertical coalescence or behaviour similar to steady heating condition is obtained. Thus lower q_{avg} with lesser time period of periodic heating t_p and excursion time τ (larger ramping) is favourable.

7.1.5 Effect of Heating Patterns on Single bubble nucleate boiling over a base plate

Utilizing the numerical methodology formulated in chapter 5 for exponential power transients, various other heating patterns are investigated and compared. Major conclusions drawn from the present work are:

- Among the various heating patterns considered—exponential, step, and linear—the effect on bubble dynamics was observed only with exponential and step. Whereas periodic linear heat flux resulted in bubble dynamics similar to steady heating. Because for the time-scale associated with t_p and constant q_{avg} , periodic linear heating resulted in q_{max} and q_{min} similar to q_{avg} , whereas significant difference is obtained for periodic exponential and step heat flux.
- Irrespective to the periodic heat flux considered, no significant difference in departure diameter and departure time are observed. Whereas for constant q_{avg} and t_p , as bubble release frequency increases with τ and $t_2/(t_p-t_2)$ for periodic exponential heat flux and periodic step heat flux, respectively. Even though the maximum increase in f_{ebul} obtained is similar for periodic exponential and step heat flux, at lower τ slightly increases f_{ebul} is obtained for periodic exponential heat flux as compared to periodic step heat flux at lower $t_2/(t_p-t_2)$.
- For vertical coalescence under similar heating conditions (constant q_{avg} and t_p), the minimum heat flux required for vertical coalescence ($q_{safe,vc}$) is lower for periodic step heat flux as compared to periodic exponential heat flux. This shows under similar heating conditions periodic step heat flux causes early occurrence of vertical coalescence as compared to periodic exponential heat flux. Whereas, for periodic linear heat flux, no vertical coalescence is observed.

7.2 Scope for Future Work

From CmFD development perspective, the present work demonstrated the capability of ghost fluid method-based SI-LSM on co-located grid to handle high density ratio CmFD problems with and without phase change. The variety of problems selected further establish its robustness. Whereas, from CmFD application and analysis perspective, a numerical methodology is formulated to investigate effect of power transients on nucleate boiling. Thus, the scope for future works in these research areas are:

CmFD development:

- The present method can be extended for complex geometries, adaptive mesh refinement etc., unlike the staggered-like implementation with BFM, the present SI- LSM_{col} will be straightforward to establish pressure-interfacial force balance.
- For CmFD, first derivative or gradient terms present in the source terms of Navier-Stokes equations are often troublesome. To avoid any future numerical instabilities, numerical methodology considering these first derivative or gradient terms in source term along with pressure need to be formulated. This avoids any decoupling between pressure and gradient source term, which is essential on co-located grid.
- Dual grid Level Set Method (DG-LSM) could be implemented on present DI- LSM_{col} and SI- LSM_{col} to avoid the interpolation of level set function from vertices to face-centers and for improved curvature estimation.
- The present DI- LSM_{col} could be extended to phase change problems, and comparison of sharp-versus-diffuse interface methods on staggered-versus-co-located grid could be performed to evaluate the solver performance with phase change.
- The computational time for present MPI-based parallelization performed on SI- LSM_{col} for investigating nucleate boiling simulation with high density ratio working fluids like water and its vapor are higher. Adaptive mesh refinement, GPU-based parallelization with openACC or CUDA should be tried to obtain results in feasible time. The present co-located based formulation significantly reduces the painstaking book-keeping procedure associated with staggered grid for these developments.

CmFD application and analysis:

- Similar to vertical coalescence another coalescence of importance in NBPT is horizontal coalescence leading to formation of vapor blanket above the substrate. Comparison of this horizontal coalescence between steady and transient heating condition is also essential.
- Conjugate heat transfer, showing the effect of solid substrate along with power transients is of much interest. The effect of solid material, substrate thickness etc. need to be investigated.
- Effect of sub-cooling is another major parameter that need to be considered for NBPT.

Appendix A

Numerical implementation details of SI-LSM_{col}

In Part I, an elaborate discussion on solution methodology was discussed for SI-LSM_{col}, whereas in this section a detailed numerical implementation of the same is shown. For the semi explicit pressure Projection method which involves prediction and correction of velocity since the numerical implementation of velocity prediction is straightforward only a detailed formulation is presented for velocity prediction and pressure Poisson equation.

A.1 A finite volume method-based pressure Poisson equation for SI-LSM on co-located grid

Figure 2.1(e) shows an interfacial cell “P” in fluid-1 with interface between “P” and “E” as well as between “P” and “N”-grid points, which results in discretized non-dimensional pressure Poisson as given below

$$-\beta_1 \left(\frac{P_{1,P}^{n+1} - P_{1,W}^{n+1}}{\delta X_w} \right) \Delta S_w + \beta_1 \left(\frac{P_{1,\Gamma_e}^{n+1} - P_{1,P}^{n+1}}{\psi_e \delta X_e} \right) \Delta S_e - \beta_1 \left(\frac{P_{1,P}^{n+1} - P_{1,S}^{n+1}}{\delta Y_s} \right) \Delta S_s + \beta_1 \left(\frac{P_{1,\Gamma_n}^{n+1} - P_{1,P}^{n+1}}{\psi_n \delta Y_n} \right) \Delta S_n = S_{m,P}^* \quad (\text{A.1})$$

To represent P_{1,Γ_e}^{n+1} in terms of $P_{1,P}^{n+1}$ and $P_{2,E}^{n+1}$, the interfacial boundary conditions are given as

$$P_{1,\Gamma_e}^{n+1} - P_{2,\Gamma_e}^{n+1} = B_e \quad (\text{A.2})$$

and,

$$\beta_1 \left(\frac{P_{1,\Gamma_e}^{n+1} - P_{1,P}^{n+1}}{\psi_e \delta X_e} \right) - \beta_2 \left(\frac{P_{2,E}^{n+1} - P_{2,\Gamma_e}^{n+1}}{(1 - \psi_e) \delta X_e} \right) = 0 \quad (\text{A.3})$$

Substituting P_{2,Γ_e}^{n+1} from Eq. (A.2) in Eq. (A.3) results in P_{1,Γ_e} , as given below

$$P_{1,\Gamma_e}^{n+1} = \frac{\beta_2 \psi_e P_{2,E}^{n+1} + (1 - \psi_e) \beta_1 P_{1,P}^{n+1} + \beta_2 \psi_e B_e}{(1 - \psi_e) \beta_1 + \psi_e \beta_2} \quad (\text{A.4})$$

Whereas, the interfacial boundary conditions to represent $P_{\Gamma_n^{n+1}}$ in terms of $P_{1,P}$ and $P_{1,P}$ and $P_{2,N}$ are given as

$$P_{1,\Gamma_n}^{n+1} - P_{2,\Gamma_n}^{n+1} = B_n \quad (\text{A.5})$$

and,

$$\beta_1 \left(\frac{P_{1,\Gamma_n}^{n+1} - P_{1,P}^{n+1}}{\psi_n \delta Y_n} \right) - \beta_2 \left(\frac{P_{2,N}^{n+1} - P_{2,\Gamma_n}^{n+1}}{(1 - \psi_n) \delta Y_n} \right) = 0 \quad (\text{A.6})$$

Substituting P_{2,Γ_n}^{n+1} from Eq. (A.5) in Eq. (A.6) results in P_{1,Γ_n}^{n+1} , as given below

$$P_{1,\Gamma_n}^{n+1} = \frac{\beta_2 \psi_n P_{2,N}^{n+1} + (1 - \psi_n) \beta_1 P_{1,P}^{n+1} + \beta_2 \psi_n B_n}{(1 - \psi_n) \beta_1 + \psi_n \beta_2} \quad (\text{A.7})$$

Similarly Fig. 2.1(f) shows an interfacial cell "P" in fluid-2 with interface between "P" and "W" as well as "S" grid points which results in discretized non-dimensional pressure Poisson equation as given below

$$\begin{aligned} & -\beta_2 \left(\frac{P_{2,P}^{n+1} - P_{2,\Gamma_w}^{n+1}}{\psi_w \delta X_w} \right) \Delta S_w + \beta_2 \left(\frac{P_{2,E} - P_{2,P}^{n+1}}{\delta X_e} \right) \Delta S_e - \beta_2 \left(\frac{P_{2,P}^{n+1} - P_{2,\Gamma_s}^{n+1}}{\psi_s \delta Y_s} \right) \Delta S_s + \\ & \qquad \qquad \qquad \beta_2 \left(\frac{P_{2,N}^{n+1} - P_{1,P}^{n+1}}{\delta Y_n} \right) \Delta S_n = S_{m,P}^* \end{aligned} \quad (\text{A.8})$$

To represent P_{2,Γ_w}^{n+1} in terms of $P_{1,W}^{n+1}$ and $P_{2,P}^{n+1}$, the interfacial boundary conditions are given as

$$P_{1,\Gamma_w}^{n+1} - P_{2,\Gamma_w}^{n+1} = B_w \quad (\text{A.9})$$

and,

$$\beta_1 \left(\frac{P_{1,\Gamma_w}^{n+1} - P_{1,W}^{n+1}}{(1 - \psi_w) \delta X_w} \right) - \beta_2 \left(\frac{P_{2,P}^{n+1} - P_{2,\Gamma_w}^{n+1}}{\psi_w \delta X_w} \right) = 0 \quad (\text{A.10})$$

Substituting P_{1,Γ_w}^{n+1} from Eq. (A.9) in Eq. (A.10) results in an equation for P_{2,Γ_w}^{n+1} , given as

$$P_{2,\Gamma_w}^{n+1} = \frac{\beta_1 \psi_w P_{1,W}^{n+1} + (1 - \psi_w) \beta_2 P_{2,P}^{n+1} - \beta_1 \psi_w B_w}{(1 - \psi_w) \beta_2 + \psi_w \beta_1} \quad (\text{A.11})$$

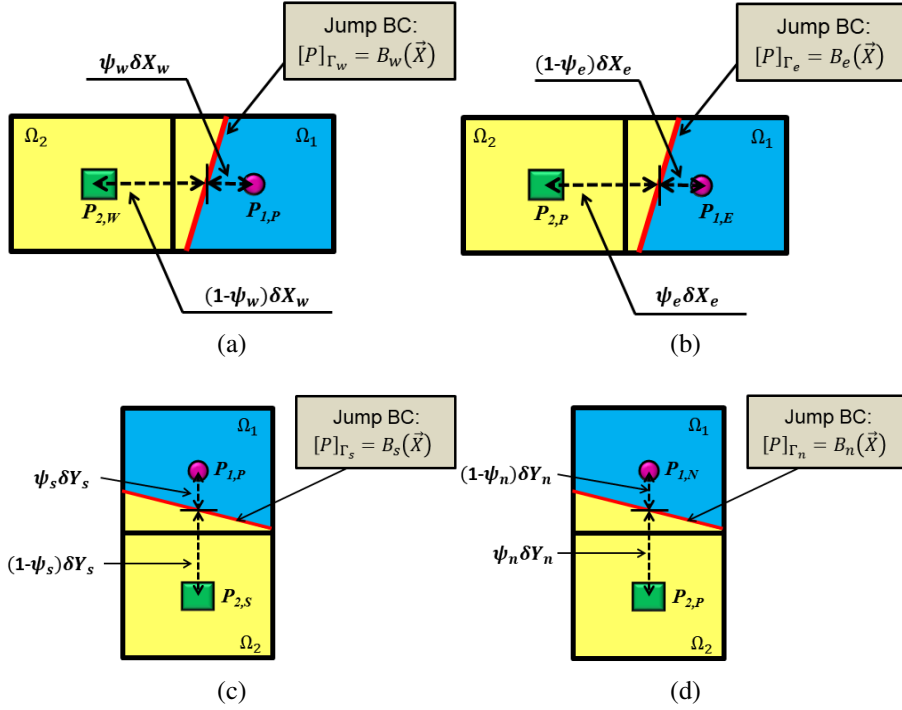


Figure A.1: Various interfacial control volumes depending on the position of interface with respect to “P” grid point, showing a) “P” grid in fluid-1 and interface between “P” and “W” grid points, b) “P” grid in fluid-2 and interface between “P” and “E” grid points, c) “P” grid in fluid-1 and interface between “P” and “S” grid points, and d) “P” grid in fluid-2 and interface between “P” and “N” grid points.

Similarly to represent P_{2,Γ_s}^{n+1} in terms of $P_{1,S}^{n+1}$ and $P_{2,P}^{n+1}$, the interfacial boundary condition is given as

$$P_{1,\Gamma_s}^{n+1} - P_{2,\Gamma_s}^{n+1} = B_s \quad (\text{A.12})$$

and,

$$\beta_1 \left(\frac{P_{1,\Gamma_s}^{n+1} - P_{1,S}^{n+1}}{(1 - \psi_s)\delta Y_s} \right) - \beta_2 \left(\frac{P_{2,P}^{n+1} - P_{2,\Gamma_s}^{n+1}}{\psi_s\delta Y_s} \right) = 0 \quad (\text{A.13})$$

Substituting P_{1,Γ_s}^{n+1} from Eq. (A.12) in Eq. (A.13), P_{2,Γ_s}^{n+1} is given as

$$P_{2,\Gamma_s}^{n+1} = \frac{\beta_1\psi_s P_{1,S}^{n+1} + (1 - \psi_s)\beta_2 P_{2,P}^{n+1} - \beta_1\psi_s B_s}{(1 - \psi_s)\beta_2 + \psi_s\beta_1} \quad (\text{A.14})$$

Apart from the configurations shown in Fig. 2.1 the interface can orient between “P” and “W” as well as “S” grid points with main interfacial cell in fluid-1. Similarly with main interfacial cell in fluid-2 the interface can orient between “P” and “E” as well as “N” grid point.

For the interfacial CV as shown in Fig. A.1(a),

$$P_{1,\Gamma_w}^{n+1} = \frac{\beta_2 \psi_w P_{2,W}^{n+1} + (1 - \psi_w) \beta_1 P_{1,P}^{n+1} + \beta_2 \psi_w B_w}{(1 - \psi_w) \beta_1 + \psi_w \beta_2} \quad (\text{A.15})$$

For the interfacial CV as shown in Fig. A.1(b),

$$P_{2,\Gamma_e}^{n+1} = \frac{\beta_1 \psi_e P_{1,E}^{n+1} + (1 - \psi_e) \beta_2 P_{2,P}^{n+1} - \beta_1 \psi_e B_e}{(1 - \psi_e) \beta_2 + \psi_e \beta_1} \quad (\text{A.16})$$

For the interfacial CV as shown in Fig. A.1(c),

$$P_{1,\Gamma_s}^{n+1} = \frac{\beta_2 \psi_s P_{2,S}^{n+1} + (1 - \psi_s) \beta_1 P_{1,P}^{n+1} + \beta_2 \psi_s B_s}{(1 - \psi_s) \beta_1 + \psi_s \beta_2} \quad (\text{A.17})$$

For the interfacial CV as shown in Fig. A.1(d),

$$P_{2,\Gamma_n}^{n+1} = \frac{\beta_1 \psi_n P_{1,N}^{n+1} + (1 - \psi_n) \beta_2 P_{2,P}^{n+1} - \beta_1 \psi_n B_n}{(1 - \psi_n) \beta_2 + \psi_n \beta_1} \quad (\text{A.18})$$

where P_{1,Γ_w}^{n+1} , and P_{1,Γ_s}^{n+1} corresponds to an interfacial cell “P” in fluid-1 with interface between “P” and “W” grid point, and between “P” and “S” grid point, respectively. Similarly, P_{2,Γ_e}^{n+1} and P_{2,Γ_n}^{n+1} corresponds to an interfacial cell “P” in fluid-2 with interface between “P” and “E” grid point, and between “P” and “N” grid point, respectively. Considering all possible orientations of an interface with main grid point (P) in fluid-1, the pressure Poisson equation is for an interfacial cell, modified form of Eq.(A.1)is given as

$$\begin{aligned} & -\beta_1 \left(\frac{P_{1,P}^{n+1} - P_{1,\Gamma_w}^{n+1}}{\psi_w \delta X_w} \right) \Delta S_w + \beta_1 \left(\frac{P_{1,\Gamma_e} - P_{1,P}^{n+1}}{\psi_e \delta X_e} \right) \Delta S_e - \beta_1 \left(\frac{P_{1,P}^{n+1} - P_{1,\Gamma_s}^{n+1}}{\psi_s \delta Y_s} \right) \Delta S_s + \\ & \qquad \qquad \qquad \beta_1 \left(\frac{P_{1,\Gamma_n}^{n+1} - P_{1,P}^{n+1}}{\psi_n \delta Y_n} \right) \Delta S_n = S_{m,P}^* \end{aligned} \quad (\text{A.19})$$

Substituting Eq. (A.4), (A.7), (A.15), and (A.17) in Eq. (A.19), the equation for pressure for an interfacial cell “P” within fluid-1 is given as

$$\begin{aligned} P_{1,P}^{n+1} = & \left[\hat{\beta}_w \left(\frac{\Delta S_w}{\delta X_w} \right) (P_{2,W}^{n+1} + B_w) + \hat{\beta}_e \left(\frac{\Delta S_e}{\delta X_e} \right) (P_{2,E}^{n+1} + B_e) + \hat{\beta}_s \left(\frac{\Delta S_s}{\delta Y_s} \right) (P_{2,S}^{n+1} + B_s) \right. \\ & \left. + \hat{\beta}_n \left(\frac{\Delta S_n}{\delta Y_n} \right) (P_{2,N}^{n+1} + B_n) - S_{m,P}^* \right] \frac{1}{(\hat{\beta}_w \frac{\Delta S_w}{\delta X_w} + \hat{\beta}_e \frac{\Delta S_e}{\delta X_e} + \hat{\beta}_s \frac{\Delta S_s}{\delta Y_s} + \hat{\beta}_n \frac{\Delta S_n}{\delta Y_n})} \end{aligned} \quad (\text{A.20})$$

Similarly, considering all possible orientations of an interface with main grid point (P) in fluid-1, the pressure Poisson equation is for an interfacial cell, modified form of Eq.(A.8)is

given as

$$\begin{aligned} -\beta_2 \left(\frac{P_{2,P}^{n+1} - P_{2,\Gamma_w}^{n+1}}{\psi_w \delta X_w} \right) \Delta S_w + \beta_2 \left(\frac{P_{2,\Gamma_e} - P_{2,P}^{n+1}}{\psi_e \delta X_e} \right) \Delta S_e - \beta_2 \left(\frac{P_{2,P}^{n+1} - P_{2,\Gamma_s}^{n+1}}{\psi_s \delta Y_s} \right) \Delta S_s + \\ \beta_2 \left(\frac{P_{2,\Gamma_n}^{n+1} - P_{2,P}^{n+1}}{\psi_n \delta Y_n} \right) \Delta S_n = S_{m,P}^* \end{aligned} \quad (\text{A.21})$$

Pressure for an interfacial cell “P” within fluid-2 is obtained by substituting Eq. (A.11), (A.14), (A.16), and (A.18) in Eq. (A.21), is given as

$$\begin{aligned} P_{2,P}^{n+1} = & \left[\hat{\beta}_w \left(\frac{\Delta S_w}{\delta X_w} \right) (P_{1,W}^{n+1} - B_w) + \hat{\beta}_e \left(\frac{\Delta S_e}{\delta X_e} \right) (P_{1,E}^{n+1} - B_e) + \hat{\beta}_s \left(\frac{\Delta S_s}{\delta Y_s} \right) (P_{1,S}^{n+1} - B_s) \right. \\ & \left. + \hat{\beta}_n \left(\frac{\Delta S_n}{\delta Y_n} \right) (P_{1,N}^{n+1} - B_n) - S_{m,P}^* \right] \frac{1}{\left(\hat{\beta}_w \frac{\Delta S_w}{\delta X_w} + \hat{\beta}_e \frac{\Delta S_e}{\delta X_e} + \hat{\beta}_s \frac{\Delta S_s}{\delta Y_s} + \hat{\beta}_n \frac{\Delta S_n}{\delta Y_n} \right)} \end{aligned} \quad (\text{A.22})$$

For an interior cell, since interfacial jump condition is absent ($B = 0$) and $\hat{\beta} = \beta$, the discretized form of pressure is given as

$$\begin{aligned} P_P^{n+1} = & \left[\beta_w \left(\frac{\Delta S_w}{\delta X_w} \right) P_W^{n+1} + \beta_e \left(\frac{\Delta S_e}{\delta X_e} \right) P_E^{n+1} + \beta_s \left(\frac{\Delta S_s}{\delta Y_s} \right) (P_S^{n+1}) + \beta_n \left(\frac{\Delta S_n}{\delta Y_n} \right) P_N^{n+1} - S_{m,P}^* \right] \\ & \times \frac{1}{\left(\hat{\beta}_w \frac{\Delta S_w}{\delta X_w} + \hat{\beta}_e \frac{\Delta S_e}{\delta X_e} + \hat{\beta}_s \frac{\Delta S_s}{\delta Y_s} + \hat{\beta}_n \frac{\Delta S_n}{\delta Y_n} \right)} \end{aligned} \quad (\text{A.23})$$

Suitably utilizing the thermo-physical properties the above equation will be applicable to interior cells within fluid-1 or fluid-2.

A.2 Velocity prediction equation for SI-LSM on co-located grid

For the interface configuration shown in Fig. 2.1(e), the discretized U-velocity prediction equation at cell-center with interfacial cell in fluid-1 is given as

$$U'_P = -\beta_1 \left(\frac{P_{1,\Gamma_e}^{n+1} - P_w^{n+1}}{0.5 \Delta X + \psi_e \Delta X} \right) \quad (\text{A.24})$$

For pressure at west face (P_w) and Γ_e (P_{Γ_e}) using linear interpolation and Eq. A.4, respectively, U'_P is given as

$$\begin{aligned} U'_P = & \frac{-1}{\Delta X (0.5 + \psi_e)} \left[\left(\frac{\beta_1}{\beta_2} \right) \hat{\beta}_e (1 - \psi_e) P_{1,P}^{n+1} + \hat{\beta}_e \psi_e P_{2,E}^{n+1} \right. \\ & \left. - \beta_1 \left(\frac{P_{1,W}^{n+1} + P_{1,P}^{n+1}}{2} \right) + \hat{\beta}_e \psi_e B_e \right] \end{aligned} \quad (\text{A.25})$$

For cell-centered V-Velocity, the prediction equation with interface between “P” and “N” grid point and interfacial cell “P” in fluid-1 as shown in Fig. 2.1(e) is given as

$$V'_P = \frac{-1}{\Delta y(0.5 + \psi_n)} \left[\left(\frac{\beta_1}{\beta_2} \right) \hat{\beta}_n (1 - \psi_n) P_{1,P}^{n+1} + \hat{\beta}_n \psi_n P_{2,N}^{n+1} - \beta_1 \left(\frac{P_{1,S}^{n+1} + P_{1,P}^{n+1}}{2} \right) + \hat{\beta}_n \psi_n B_n \right] \quad (\text{A.26})$$

Similarly for Fig. 2.1(f), the prediction of cell-centered U-velocity with interfacial cell “P” in fluid-2 is given as

$$U'_P = \frac{-1}{\Delta X(0.5 + \psi_w)} \left[- \left(\frac{\beta_2}{\beta_1} \right) \hat{\beta}_w (1 - \psi_w) P_{2,P}^{n+1} - \hat{\beta}_w \psi_w P_{1,W}^{n+1} + \beta_2 \left(\frac{P_{2,E}^{n+1} + P_{2,P}^{n+1}}{2} \right) + \hat{\beta}_w \psi_w B_w \right] \quad (\text{A.27})$$

For cell-center V-velocity, the prediction equation with interface between “P” and “S” grid point and interfacial cell “P” in fluid-2 as shown in Fig. 2.1(f) is given as

$$V'_P = \frac{-1}{\Delta y(0.5 + \psi_s)} \left[- \left(\frac{\beta_2}{\beta_1} \right) \hat{\beta}_s (1 - \psi_s) P_{2,P}^{n+1} - \hat{\beta}_s \psi_s P_{1,S}^{n+1} + \beta_2 \left(\frac{P_{2,N}^{n+1} + P_{2,P}^{n+1}}{2} \right) + \hat{\beta}_s \psi_s B_s \right] \quad (\text{A.28})$$

Apart from the above discussed configurations shown in Fig. 2.1(e) and Fig. 2.1(f), the U and V-velocity prediction equations for other interface configurations are shown below:

For cell-centered U-velocity prediction,

- Interface between “P” and “W” grid point with interfacial cell “P” in fluid-1 as shown in Fig. A.2(a), given as

$$U'_P = \frac{-1}{\Delta X(0.5 + \psi_w)} \left[- \left(\frac{\beta_1}{\beta_2} \right) \hat{\beta}_w (1 - \psi_w) P_{1,P}^{n+1} - \hat{\beta}_w \psi_w P_{2,W}^{n+1} + \beta_1 \left(\frac{P_{1,P}^{n+1} + P_{1,E}^{n+1}}{2} \right) - \hat{\beta}_w \psi_w B_w \right] \quad (\text{A.29})$$

- Interface between “P” and “E” grid point with interfacial cell “P” in fluid-2 as shown in Fig. A.2(b), given as

$$U'_P = \frac{-1}{\Delta X(0.5 + \psi_e)} \left[\left(\frac{\beta_2}{\beta_1} \right) \hat{\beta}_e (1 - \psi_e) P_{2,P}^{n+1} + \hat{\beta}_e \psi_e P_{1,E}^{n+1} - \beta_2 \left(\frac{P_{2,W}^{n+1} + P_{2,P}^{n+1}}{2} \right) - \hat{\beta}_e \psi_e B_e \right] \quad (\text{A.30})$$

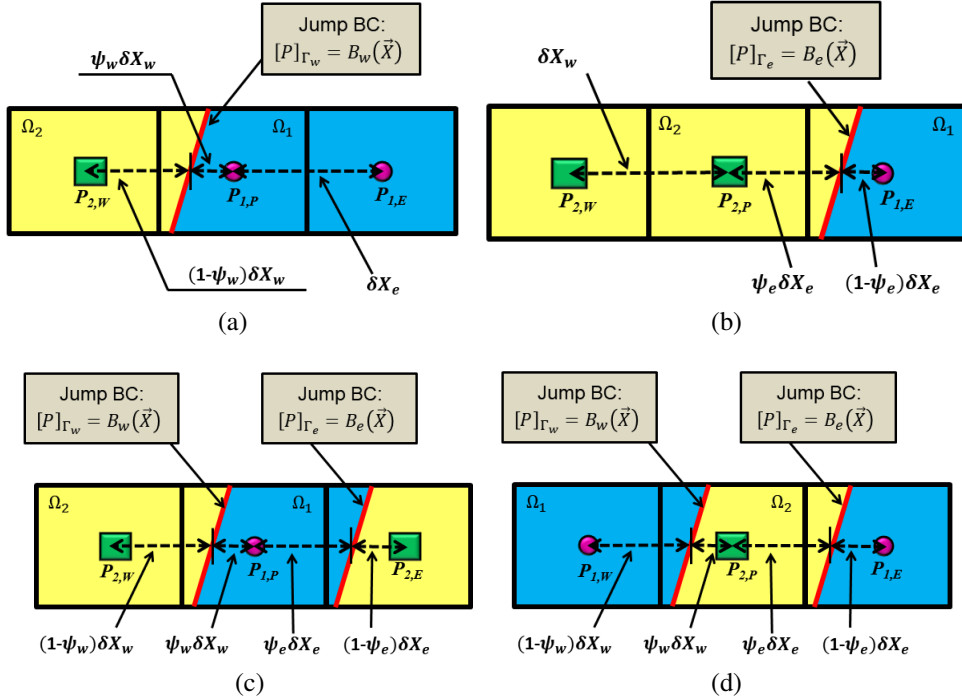


Figure A.2: Various interfacial control volumes for calculating U -velocity correction depending on the position of interface with respect to “ P ” grid point, showing a) “ P ” grid in fluid-1 and interface between “ P ” and “ W ” grid points, b) “ P ” grid in fluid-2 and interface between “ P ” and “ E ” grid points, c) “ P ” grid in fluid-1 and interface between “ P ” and “ W ” as well as “ P ” and “ E ” grid points, and d) “ P ” grid in fluid-2 and interface between “ P ” and “ W ” as well as “ P ” and “ E ” grid points.

- Interface between “ P ” and “ W ” as well as between “ P ” and “ E ” with interfacial cell “ P ” in fluid-1 as shown in Fig. A.2(c), given as

$$U'_P = -\beta_1 \left(\frac{P_{1,\Gamma e}^{n+1} - P_{1,\Gamma w}^{n+1}}{(\psi_w + \psi_e)\Delta X} \right) = \frac{-1}{\Delta X} \left[\frac{\hat{\beta}_e \hat{\beta}_w (\psi_w - \psi_e)}{\beta_2} P_{1,P}^{n+1} + \frac{\hat{\beta}_e \psi_e}{\psi_w + \psi_e} P_{2,E}^{n+1} - \frac{\hat{\beta}_w \psi_w}{\psi_w + \psi_e} P_{2,W}^{n+1} + \frac{\hat{\beta}_e \psi_e}{\psi_w + \psi_e} B_e - \frac{\hat{\beta}_w \psi_w}{\psi_w + \psi_e} B_w \right] \quad (A.31)$$

- Interface between “ P ” and “ W ” as well as between “ P ” and “ E ” with interfacial cell “ P ” in fluid-2 as shown in Fig. A.2(d), given as

$$U'_P = \frac{-1}{\Delta X} \left[\frac{\hat{\beta}_e \hat{\beta}_w (\psi_w - \psi_e)}{\beta_2} P_{1,P}^{n+1} + \frac{\hat{\beta}_e \psi_e}{\psi_w + \psi_e} P_{2,E}^{n+1} - \frac{\hat{\beta}_w \psi_w}{\psi_w + \psi_e} P_{2,W}^{n+1} + \frac{\hat{\beta}_e \psi_e}{\psi_w + \psi_e} B_e - \frac{\hat{\beta}_w \psi_w}{\psi_w + \psi_e} B_w \right] \quad (A.32)$$

For cell-centered V-velocity prediction,

- Interface between “ P ” and “ S ” grid point with interfacial cell “ P ” in fluid-1 as shown

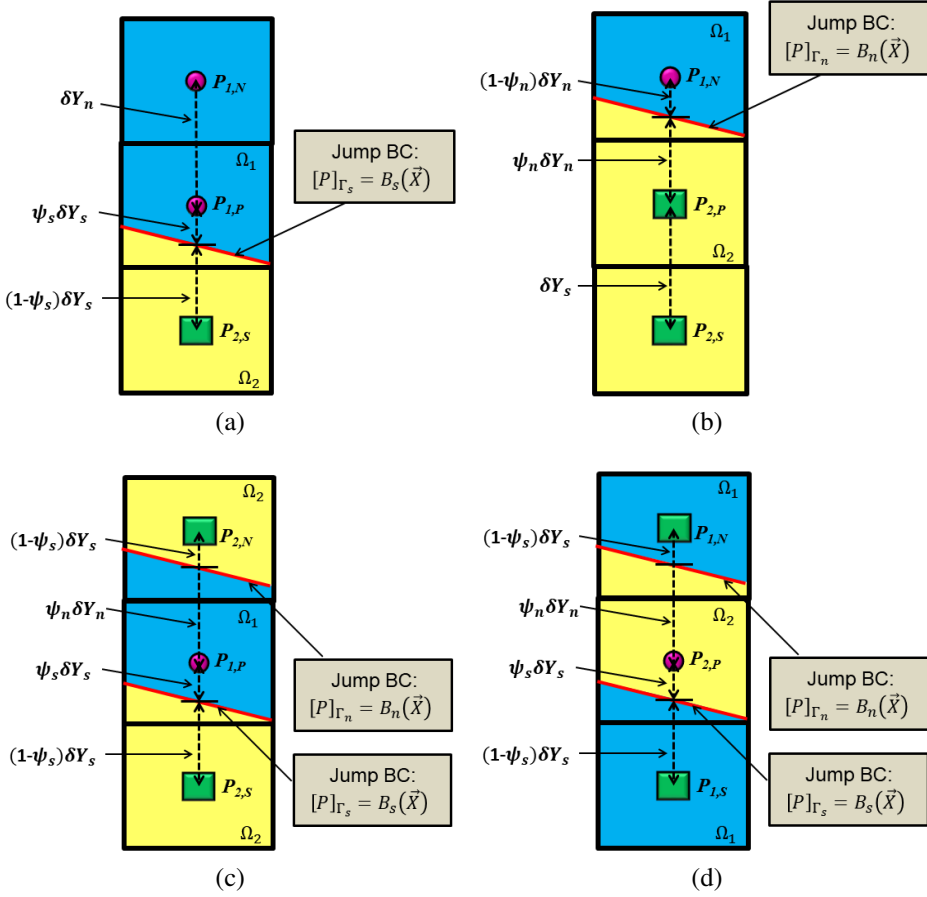


Figure A.3: Various interfacial control volumes for calculating V -velocity correction depending on the position of interface with respect to “ P ” grid point, showing a) “ P ” grid in fluid-1 and interface between “ P ” and “ S ” grid points, b) “ P ” grid in fluid-2 and interface between “ P ” and “ N ” grid points, c) “ P ” grid in fluid-1 and interface between “ P ” and “ S ” as well as “ P ” and “ N ” grid points, and d) “ P ” grid in fluid-2 and interface between “ P ” and “ S ” as well as “ P ” and “ N ” grid points.

in Fig. A.3(a), given as

$$V'_P = \frac{-1}{\Delta Y(0.5 + \psi_s)} \left[-\left(\frac{\beta_1}{\beta_2}\right) \hat{\beta}_s (1 - \psi_s) P_{1,P}^{n+1} - \hat{\beta}_s \psi_s P_{2,S}^{n+1} + \beta_1 \left(\frac{P_{1,N}^{n+1} + P_{1,P}^{n+1}}{2} \right) - \hat{\beta}_s \psi_s B_s \right] \quad (\text{A.33})$$

- Interface between “ P ” and “ N ” grid point with interfacial cell “ P ” in fluid-2 as shown in Fig. A.3(b), given as

$$V'_P = \frac{-1}{\Delta Y(0.5 + \psi_n)} \left[\left(\frac{\beta_2}{\beta_1}\right) \hat{\beta}_n (1 - \psi_n) P_{2,P}^{n+1} + \hat{\beta}_n \psi_n P_{1,N}^{n+1} - \beta_2 \left(\frac{P_{2,P}^{n+1} + P_{2,S}^{n+1}}{2} \right) - \hat{\beta}_n \psi_n B_n \right] \quad (\text{A.34})$$

- Interface between “P” and “S” as well as between “P” and “N” with interfacial cell “P” in fluid-1 as shown in Fig. A.3(c), given as

$$V'_P = -\beta_1 \left(\frac{P_{1,\Gamma n}^{n+1} - P_{1,\Gamma s}^{n+1}}{(\psi_s + \psi_n) \Delta Y} \right) = \frac{-1}{\Delta Y} \left[\frac{\hat{\beta}_n \hat{\beta}_s}{\beta_2} \left(\frac{\psi_s - \psi_n}{\psi_s + \psi_n} \right) P_{1,P}^{n+1} + \frac{\hat{\beta}_n \psi_n}{\psi_s + \psi_n} P_{2,N}^{n+1} - \frac{\hat{\beta}_s \psi_s}{\psi_s + \psi_n} P_{2,S}^{n+1} + \frac{\hat{\beta}_n \psi_n}{\psi_s + \psi_n} B_n - \frac{\hat{\beta}_s \psi_s}{\psi_s + \psi_n} B_s \right] \quad (\text{A.35})$$

- Interface between “P” and “S” as well as between “P” and “N” with interfacial cell “P” in fluid-2 as shown in Fig. A.3(d), given as

$$V'_P = \frac{-1}{\Delta Y} \left[\frac{\hat{\beta}_n \hat{\beta}_s}{\beta_1} \left(\frac{\psi_s - \psi_n}{\psi_s + \psi_n} \right) P_{2,P}^{n+1} + \frac{\hat{\beta}_n \psi_n}{\psi_s + \psi_n} P_{1,N}^{n+1} - \frac{\hat{\beta}_s \psi_s}{\psi_s + \psi_n} P_{1,S}^{n+1} - \frac{\hat{\beta}_n \psi_n}{\psi_s + \psi_n} B_n + \frac{\hat{\beta}_s \psi_s}{\psi_s + \psi_n} B_s \right] \quad (\text{A.36})$$

Bibliography

- Abadie, T., Aubin, J., and Legendre, D., 2015, “On the combined effects of surface tension force calculation and interface advection on spurious currents within volume of fluid and level set frameworks,” *Journal of Computational Physics* **297**, 611–636.
- Abarajith, H., and Dhir, V., 2002, “A numerical study of the effect of contact angle on the dynamics of a single bubble during pool boiling,” in *ASME International Mechanical Engineering Congress and Exposition*, Vol. 3638, pp. 467–475.
- Abu-Al-Saud, M. O., Popinet, S., and Tchelepi, H. A., 2018, “A conservative and well-balanced surface tension model,” *Journal of Computational Physics* **371**, 896–913.
- Aggarwal, V., Gada, V. H., and Sharma, A., 2013, “Parallelization methodology and performance study for level-set-method-based simulation of a 3-d transient two-phase flow,” *Numerical Heat Transfer, Part B: Fundamentals* **63**, 327–356.
- Aktinol, E., and Dhir, V. K., 2012, “Numerical simulation of nucleate boiling phenomenon coupled with thermal response of the solid,” *Microgravity Science and Technology* **24**, 255–265.
- Anderson, D. M., McFadden, G. B., and Wheeler, A. A., 1998, “Diffuse-interface methods in fluid mechanics,” *Annual review of fluid mechanics* **30**, 139–165.
- Aparajith, H., Dhir, D. V. K., and Son, G., 2006, “Numerical simulation of the dynamics of multiple bubble merger during pool boiling under reduced gravity,” *Multiphase Science and Technology* **18**
- Arienti, M., and Sussman, M., 2014, “An embedded level set method for sharp-interface multiphase simulations of diesel injectors,” *International Journal of Multiphase Flow* **59**, 1–14.
- Asai, A., 1991 11, “Bubble Dynamics in Boiling Under High Heat Flux Pulse Heating,” *Journal of Heat Transfer* **113**, 973–979.

- Aslam, T. D., 2004, “A partial differential equation approach to multidimensional extrapolation,” *Journal of Computational Physics* **193**, 349–355.
- Bahreini, M., Ramiar, A., and Ranjbar, A., 2017, “Numerical simulation of subcooled flow boiling under conjugate heat transfer and microgravity condition in a vertical mini channel,” *Applied Thermal Engineering* **113**, 170–185.
- Berenson, P. J., 1961 08, “Film-Boiling Heat Transfer From a Horizontal Surface,” *Journal of Heat Transfer* **83**, 351–356.
- Bi, J., Christopher, D. M., Zhao, D., Xu, J., and Huang, Y., 2019, “Numerical study of bubble growth and merger characteristics during nucleate boiling,” *Progress in Nuclear Energy* **112**, 7–19.
- Blanchette, F., and Bigioni, T. P., 2006, “Partial coalescence of drops at liquid interfaces,” *Nature Physics* **2**, 254–257.
- Bovard, S., Asadinia, H., Hosseini, G., and Alavi Fazel, S., 2017, “Investigation and experimental analysis of the bubble departure diameter in pure liquids on horizontal cylindrical heater,” *Heat and Mass Transfer* **53**, 1199–1210.
- Brackbill, J. U., Kothe, D. B., and Zemach, C., 1992, “A continuum method for modeling surface tension,” *Journal of computational physics* **100**, 335–354.
- Brown, E., Yan, Y., and Marcum, W. R., 2020, “A novel method for predicting power transient chf via the heterogeneous spontaneous nucleation trigger mechanism,” *Nuclear Technology* **206**, 1296–1307.
- Bureš, L., and Sato, Y., 2021, “Direct numerical simulation of evaporation and condensation with the geometric vof method and a sharp-interface phase-change model,” *International Journal of Heat and Mass Transfer* **173**, 121233.
- Butt, H.-J., Graf, K., and Kappl, M., 2013, *Physics and chemistry of interfaces* (John Wiley & Sons).
- Cao, Z., Zhou, J., Liu, A., Sun, D., Yu, B., and Wei, J., 2020, “A three dimensional coupled vof and level set (voset) method with and without phase change on general curvilinear grids,” *Chemical Engineering Science* **223**, 115705.
- Carlier, J., and Papalexandris, M. V., 2022, “An efficient tracking method for evaporative free surfaces on collocated grids,” *Available at SSRN 4095081*

- Carslaw, H., 1959, "J. c. jaeger," *Conduction of heat in solids* **2**
- Chang, Y.-C., Hou, T., Merriman, B., and Osher, S., 1996, "A level set formulation of eulerian interface capturing methods for incompressible fluid flows," *Journal of computational Physics* **124**, 449–464.
- Chen, H.-X., Li, L.-H., Wang, Y.-R., and Guo, Y.-X., 2022, "Heat transfer enhancement in nucleate boiling on micropillar-arrayed surfaces with time-varying wettability," *Applied Thermal Engineering* **200**, 117649.
- Chen, H.-X., Sun, Y., Xiao, H.-Y., and Wang, X.-D., 2020, "Bubble dynamics and heat transfer characteristics on a micropillar-structured surface with different nucleation site positions," *Journal of Thermal Analysis and Calorimetry* **141**, 447–464.
- Chen, Z., Wu, F., and Utaka, Y., 2018, "Numerical simulation of thermal property effect of heat transfer plate on bubble growth with microlayer evaporation during nucleate pool boiling," *International Journal of Heat and Mass Transfer* **118**, 989–996.
- Chirammel, S. S., Sharma, A., and Murallidharan, J. S., 2023a, "On ghost fluid method-based sharp interface level set method on a co-located grid and its comparison with balanced force-based diffuse interface method," *Journal of Computational Physics (Under review)*
- Chirammel, S. S., Sharma, A., and Murallidharan, J. S., 2023b, "Performance of sharp-versus-diffuse interface-based level set method on a staggered-versus-co-located grid for cmfd," *Computational Thermal Sciences: An International Journal* **15**, 21–35.
- Cole, R., 1956, *Investigation of transient pool boiling due to sudden large power surge*, Tech. Rep.
- Cornwell, K., and Kew, P. A., 1993, "Boiling in small parallel channels," in *Energy Efficiency in Process Technology* (Springer), pp. 624–638.
- Date, A. W., 2005, *Introduction to computational fluid dynamics* (Cambridge university press).
- Datta, D., Gada, V. H., and Sharma, A., 2011, "Analytical and level-set method-based numerical study for two-phase stratified flow in a plane channel and a square duct," *Numerical Heat Transfer, Part A: Applications* **60**, 347–380.

- Deev, V., Oo, H. L., Kharitonov, V., Kutsenko, K., and Lavrukhin, A., 2007, "Critical heat flux modeling in water pool boiling during power transients," *International journal of heat and mass transfer* **50**, 3780–3787.
- Desjardins, O., Moureau, V., and Pitsch, H., 2008, "An accurate conservative level set/ghost fluid method for simulating turbulent atomization," *Journal of computational physics* **227**, 8395–8416.
- Dhir, V. K., Abarajith, H. S., and Li, D., 2007, "Bubble dynamics and heat transfer during pool and flow boiling," *Heat Transfer Engineering* **28**, 608–624.
- Dixit, A. K., Kumar, R., and Das, A. K., 2022, "Investigation of film boiling at a liquid-liquid contact," *International Journal of Heat and Mass Transfer* **196**, 123234.
- Drach, V., Sack, N., and Fricke, J., 1996, "Transient heat transfer from surfaces of defined roughness into liquid nitrogen," *International journal of heat and mass transfer* **39**, 1953–1961.
- Duluc, M.-C., Stutz, B., and Lallemand, M., 2004, "Transient nucleate boiling under stepwise heat generation for highly wetting fluids," *International journal of heat and mass transfer* **47**, 5541–5553.
- El Achkar, G., Septet, C., Le Metayer, O., and Hugo, J.-M., 2022, "Experimental thermohydraulic characterisation of flow boiling and condensation in additive manufactured plate-fin heat exchanger," *International Journal of Heat and Mass Transfer* **199**, 123465.
- El-Genk, M. S., 2012, "Immersion cooling nucleate boiling of high power computer chips," *Energy conversion and management* **53**, 205–218.
- Fan, S., and Duan, F., 2020, "A review of two-phase submerged boiling in thermal management of electronic cooling," *International Journal of Heat and Mass Transfer* **150**, 119324.
- Fedkiw, R. P., Aslam, T., Merriman, B., and Osher, S., 1999a, "A non-oscillatory eularian approach to interfaces in multimaterial flows (the ghost fluid method)," *Journal of computational physics* **152**, 457–492.
- Fedkiw, R. P., Aslam, T., and Xu, S., 1999b, "The ghost fluid method for deflagration and detonation discontinuities," *Journal of Computational Physics* **154**, 393–427.

- Fitri, S. P., Fukuda, K., Liu, Q., and Park, J., 2007, "Transient pool boiling critical heat flux of fc-72 under saturated conditions," *Journal of Power and Energy Systems* **1**, 178–189.
- Francois, M. M., Cummins, S. J., Dendy, E. D., Kothe, D. B., Sicilian, J. M., and Williams, M. W., 2006, "A balanced-force algorithm for continuous and sharp interfacial surface tension models within a volume tracking framework," *Journal of Computational Physics* **213**, 141–173.
- Fukuda, K., Shiotsu, M., and Sakurai, A., 2000, "Effect of surface conditions on transient critical heat fluxes for a horizontal cylinder in a pool of water at pressures due to exponentially increasing heat inputs," *Nuclear Engineering and Design* **200**, 55–68.
- Fukuda, K., and Liu, Q., 2005, "Steady and transient critical heat fluxes on a horizontal cylinder in a pool of freon-113," *International Journal of Transport Phenomena* **7**, 71–83.
- Fuster, D., Bagué, A., Boeck, T., Le Moyne, L., Leboissetier, A., Popinet, S., Ray, P., Scardovelli, R., and Zaleski, S., 2009, "Simulation of primary atomization with an octree adaptive mesh refinement and vof method," *International Journal of Multiphase Flow* **35**, 550–565.
- Gada, V., 2012, "A novel level-set based cmfd methodology in 2d/3d cartesian and cylindrical coordinates and its application for analysis of stratified flow and film boiling," *IIT Bombay*
- Gada, V. H., Datta, D., and Sharma, A., 2013, "Analytical and numerical study for two-phase stratified-flow in a plane channel subjected to different thermal boundary conditions," *International journal of thermal sciences* **71**, 88–102.
- Gada, V. H., and Sharma, A., 2009a, "On derivation and physical interpretation of level set method-based equations for two-phase flow simulations," *Numerical Heat Transfer, Part B: Fundamentals* **56**, 307–322.
- Gada, V. H., and Sharma, A., 2009b, "Simulation of multi-mode film boiling using level set method," in *ASME International Mechanical Engineering Congress and Exposition*, Vol. 43826, pp. 1611–1620.
- Gada, V. H., and Sharma, A., 2011, "On a novel dual-grid level-set method for two-phase flow simulation," *Numerical Heat Transfer, Part B: Fundamentals* **59**, 26–57.

- Geng, X., Yuan, H., Oguz, H., and Prosperetti, A., 2001, "Bubble-based micropump for electrically conducting liquids," *Journal of Micromechanics and Microengineering* **11**, 270.
- Gerlach, D., Tomar, G., Biswas, G., and Durst, F., 2006, "Comparison of volume-of-fluid methods for surface tension-dominant two-phase flows," *International Journal of Heat and Mass Transfer* **49**, 740–754.
- Gibou, F., Chen, L., Nguyen, D., and Banerjee, S., 2007, "A level set based sharp interface method for the multiphase incompressible navier–stokes equations with phase change," *Journal of Computational Physics* **222**, 536–555.
- Giustini, G., Walker, S., Sato, Y., and Niceno, B., 2017, "Computational fluid dynamics analysis of the transient cooling of the boiling surface at bubble departure," *Journal of Heat Transfer* **139**
- Guion, A., Afkhami, S., Zaleski, S., and Buongiorno, J., 2018, "Simulations of microlayer formation in nucleate boiling," *International Journal of Heat and Mass Transfer* **127**, 1271–1284.
- Hardt, S., and Wondra, F., 2008, "Evaporation model for interfacial flows based on a continuum-field representation of the source terms," *Journal of Computational Physics* **227**, 5871–5895.
- Hazi, G., and Markus, A., 2009, "On the bubble departure diameter and release frequency based on numerical simulation results," *International Journal of Heat and Mass Transfer* **52**, 1472–1480.
- Héas, S., Robidou, H., Raynaud, M., and Lallemand, M., 2003, "Onset of transient nucleate boiling from a thick flat sample," *International journal of heat and mass transfer* **46**, 355–365.
- Herrmann, M., 2008, "A balanced force refined level set grid method for two-phase flows on unstructured flow solver grids," *Journal of computational physics* **227**, 2674–2706.
- Herrmann, M., 2010, "Detailed numerical simulations of the primary atomization of a turbulent liquid jet in crossflow," *Journal of Engineering for Gas Turbines and Power* **132**
- Hirt, C. W., and Nichols, B. D., 1981, "Volume of fluid (vof) method for the dynamics of free boundaries," *Journal of computational physics* **39**, 201–225.

- Hirt, C. W., Amsden, A. A., and Cook, J., 1974, “An arbitrary lagrangian-eulerian computing method for all flow speeds,” *Journal of computational physics* **14**, 227–253.
- Huang, Z., Lin, G., and Ardekani, A. M., 2020, “Consistent, essentially conservative and balanced-force phase-field method to model incompressible two-phase flows,” *Journal of Computational Physics* **406**, 109192.
- Huber, G., Tanguy, S., Sagan, M., and Colin, C., 2017, “Direct numerical simulation of nucleate pool boiling at large microscopic contact angle and moderate jakob number,” *International Journal of Heat and Mass Transfer* **113**, 662–682.
- Iida, Y., Okuyama, K., and Sakurai, K., 1994, “Boiling nucleation on a very small film heater subjected to extremely rapid heating,” *International Journal of Heat and Mass Transfer* **37**, 2771–2780.
- Irfan, M., and Muradoglu, M., 2017, “A front tracking method for direct numerical simulation of evaporation process in a multiphase system,” *Journal of Computational Physics* **337**, 132–153.
- Ito, K., Kunugi, T., Ohshima, H., and Kawamura, T., 2009, “Formulations and validations of a high-precision volume-of-fluid algorithm on nonorthogonal meshes for numerical simulations of gas entrainment phenomena,” *Journal of Nuclear Science and Technology* **46**, 366–373.
- Ivey, C. B., and Moin, P., 2017, “Conservative and bounded volume-of-fluid advection on unstructured grids,” *Journal of Computational Physics* **350**, 387–419.
- Jia, H., Zhang, P., Fu, X., and Jiang, S., 2015, “A numerical investigation of nucleate boiling at a constant surface temperature,” *Applied Thermal Engineering* **88**, 248–257.
- Jiang, G.-S., and Peng, D., 2000, “Weighted eno schemes for hamilton–jacobi equations,” *SIAM Journal on Scientific computing* **21**, 2126–2143.
- Johnson, H., 1971, “Transient boiling heat transfer to water,” *International Journal of Heat and Mass Transfer* **14**, 67–82.
- Juric, D., and Tryggvason, G., 1996, “A front-tracking method for dendritic solidification,” *Journal of computational physics* **123**, 127–148.
- Kalani, A., and Kandlikar, S. G., 2013, “Enhanced pool boiling with ethanol at subatmospheric pressures for electronics cooling,” *Journal of heat transfer* **135**

- Kampl, A., 2014, “Bitcoin 2-phase immersion cooling and the implications for high performance computing,” *Electronics Cooling Magazine* **1**
- Kang, M., Fedkiw, R. P., and Liu, X.-D., 2000, “A boundary condition capturing method for multiphase incompressible flow,” *Journal of Scientific Computing* **15**, 323–360.
- Karayannidis, T., and Mahmoud, M., 2017, “Flow boiling in microchannels: Fundamentals and applications,” *Applied Thermal Engineering* **115**, 1372–1397.
- Klimenko, V., 1981, “Film boiling on a horizontal plate-new correlation,” *International journal of heat and mass transfer* **24**, 69–79.
- Kunito, O., Yoshiyuki, K., Akira, I., and Shigebumi, A., 1988, “Transient boiling heat transfer characteristics of r113 at large stepwise power generation,” *International journal of heat and mass transfer* **31**, 2161–2174.
- Kunkelmann, C., Ibrahim, K., Schweizer, N., Herbert, S., Stephan, P., and Gambaryan-Roisman, T., 2012, “The effect of three-phase contact line speed on local evaporative heat transfer: Experimental and numerical investigations,” *International Journal of Heat and Mass Transfer* **55**, 1896–1904.
- Kunkelmann, C., and Stephan, P., 2009, “Cfd simulation of boiling flows using the volume-of-fluid method within openfoam,” *Numerical Heat Transfer, Part A: Applications* **56**, 631–646.
- Kunkelmann, C., and Stephan, P., 2010a, “Modification and extension of a standard volume-of-fluid solver for simulating boiling heat transfer,” in *Proc. 5th European Conference on Computational Fluid Dynamics ECCOMAS CFD2010, Lisbon, Portugal*
- Kunkelmann, C., and Stephan, P., 2010b, “Numerical simulation of the transient heat transfer during nucleate boiling of refrigerant hfe-7100,” *International Journal of Refrigeration* **33**, 1221–1228.
- Lakdawala, A. M., Gada, V. H., and Sharma, A., 2014, “A dual grid level set method based study of interface-dynamics for a liquid jet injected upwards into another liquid,” *International journal of multiphase flow* **59**, 206–220.
- Lakdawala, A. M., Thaokar, R., and Sharma, A., 2015, “Break-up of a non-newtonian jet injected downwards in a newtonian liquid,” *Sadhana* **40**, 819–833.

- Lee, J., and Son, G., 2017, "A sharp-interface level-set method for compressible bubble growth with phase change," *International Communications in Heat and Mass Transfer* **86**, 1–11.
- Lee, W., and Son, G., 2011, "Numerical simulation of boiling enhancement on a microstructured surface," *International communications in heat and mass transfer* **38**, 168–173.
- Lee, W., Son, G., and Jeong, J. J., 2010, "Numerical analysis of bubble growth and departure from a microcavity," *Numerical Heat Transfer, Part B: Fundamentals* **58**, 323–342.
- Lee, W., Son, G., and Yoon, H. Y., 2012, "Numerical study of bubble growth and boiling heat transfer on a microfinned surface," *International communications in heat and mass transfer* **39**, 52–57.
- Li, D., and Dhir, V. K., 2007, "Numerical study of single bubble dynamics during flow boiling,"
- Li, J., Peterson, G., and Cheng, P., 2008, "Dynamic characteristics of transient boiling on a square platinum microheater under millisecond pulsed heating," *International journal of heat and mass transfer* **51**, 273–282.
- Lin, S., Yan, J., Kats, D., and Wagner, G. J., 2019, "A volume-conserving balanced-force level set method on unstructured meshes using a control volume finite element formulation," *Journal of Computational Physics* **380**, 119–142.
- Ling, K., Li, Z.-Y., and Tao, W.-Q., 2014, "A direct numerical simulation for nucleate boiling by the vorset method," *Numerical Heat Transfer, Part A: Applications* **65**, 949–971.
- Ling, K., and Tao, W.-Q., 2018, "Numerical simulation of nucleate boiling in shallow liquid," *Computers & Fluids* **164**, 35–40.
- Liu, X.-D., Fedkiw, R. P., and Kang, M., 2000, "A boundary condition capturing method for poisson's equation on irregular domains," *Journal of computational Physics* **160**, 151–178.
- Luo, Y., Li, W., Zhang, J., and Minkowycz, W., 2020, "Analysis of thermal performance and pressure loss of subcooled flow boiling in manifold microchannel heat sink," *International Journal of Heat and Mass Transfer* **162**, 120362.

- Lurie, H., and Johnson, H., 1962, “Transient pool boiling of water on a vertical surface with a step in heat generation,”
- Lv, H., Ma, H., Mao, N., and He, T., 2022, “Boiling heat transfer mechanism of environmental-friendly refrigerants: A review,” *International Journal of Refrigeration* **133**, 214–225.
- Magnini, M., 2012, “Cfd modeling of two-phase boiling flows in the slug flow regime with an interface capturing technique,”
- Malan, L., Malan, A. G., Zaleski, S., and Rousseau, P., 2021, “A geometric vof method for interface resolved phase change and conservative thermal energy advection,” *Journal of Computational Physics* **426**, 109920.
- Malan, L., 2018, “Direct numerical simulation of free-surface and interfacial flow using the vof method: cavitating bubble clouds and phase change,”
- Manik, J., Dalal, A., and Natarajan, G., 2018, “A generic algorithm for three-dimensional multiphase flows on unstructured meshes,” *International Journal of Multiphase Flow* **106**, 228–242.
- Martin, J., and Moyce, W., 1952, “An experimental study of the collapse of fluid columns on a rigid horizontal plane, in a medium of lower, but comparable, density. 5..” *Philosophical Transactions of the Royal Society of London Series A-Mathematical and Physical Sciences* **244**, 325–334.
- Mathew, J., and Krishnan, S., 2022, “A review on transient thermal management of electronic devices,” *Journal of Electronic Packaging* **144**
- Mikic, B., Rohsenow, W., and Griffith, P., 1970, “On bubble growth rates,” *International Journal of Heat and Mass Transfer* **13**, 657–666.
- Mirjalili, S., Ivey, C. B., and Mani, A., 2020, “A conservative diffuse interface method for two-phase flows with provable boundedness properties,” *Journal of Computational Physics* **401**, 109006.
- Montazeri, H., Bussmann, M., and Mostaghimi, J., 2012, “Accurate implementation of forcing terms for two-phase flows into simple algorithm,” *International journal of multiphase flow* **45**, 40–52.

- Montazeri, H., Zandavi, S. H., and Bazylak, A., 2017, "Sharp interface models for two-phase flows: Insights towards new approaches," *Computer Methods in Applied Mechanics and Engineering* **322**, 238–261.
- Mukherjee, A., and Dhir, V., 2004, "Study of lateral merger of vapor bubbles during nucleate pool boiling," *J. Heat Transfer* **126**, 1023–1039.
- Mukherjee, A., and Kandlikar, S. G., 2005, "Numerical simulation of growth of a vapor bubble during flow boiling of water in a microchannel," *Microfluidics and Nanofluidics* **1**, 137–145.
- Municchi, F., El Mellas, I., Matar, O., and Magnini, M., 2022, "Conjugate heat transfer effects on flow boiling in microchannels," *International Journal of Heat and Mass Transfer* **195**, 123166.
- Muramatsu, H., Pillai, A. L., Kitada, K., and Kurose, R., 2022, "Numerical simulation of bi-component fuel droplet evaporation using level set method," *Fuel* **318**, 123331.
- Nam, Y., Aktinol, E., Dhir, V. K., and Ju, Y. S., 2011, "Single bubble dynamics on a superhydrophilic surface with artificial nucleation sites," *International Journal of Heat and Mass Transfer* **54**, 1572–1577.
- Narumanchi, S., Troshko, A., Bharathan, D., and Hassani, V., 2008, "Numerical simulations of nucleate boiling in impinging jets: Applications in power electronics cooling," *International Journal of Heat and Mass Transfer* **51**, 1–12.
- Nghiem, L., Merte, H., Winter, E., and Beer, H., 1981, "Prediction of transient inception of boiling in terms of a heterogeneous nucleation theory,"
- Nguyen, D. Q., Fedkiw, R. P., and Kang, M., 2001, "A boundary condition capturing method for incompressible flame discontinuities," *Journal of Computational Physics* **172**, 71–98.
- Nguyen-Thi, L.-Q., Nguyen, V.-D., Pierens, X., and Coorevits, P., 2021, "An experimental and numerical study of the influence of viscosity on the behavior of dam-break flow," *Theoretical and Computational Fluid Dynamics* **35**, 345–362.
- Ni, M.-J., Komori, S., and Morley, N. B., 2006, "Direct simulation of falling droplet in a closed channel," *International Journal of Heat and Mass Transfer* **49**, 366–376.
- Nichols, B., Hirt, C., and Hotchkiss, R., 1981, "Volume of fluid (vof) method for the dynamics of free boundaries," *J. Comput. Phys* **39**, 201–225.

- Ningegowda, B., and Premachandran, B., 2014, “A coupled level set and volume of fluid method with multi-directional advection algorithms for two-phase flows with and without phase change,” *International Journal of Heat and Mass Transfer* **79**, 532–550.
- Ningegowda, B., and Premachandran, B., 2017, “Numerical investigation of the pool film boiling of water and r134a over a horizontal surface at near-critical conditions,” *Numerical Heat Transfer, Part A: Applications* **71**, 44–71.
- Nomura, K., Koshizuka, S., Oka, Y., and Obata, H., 2001, “Numerical analysis of droplet breakup behavior using particle method,” *Journal of Nuclear Science and technology* **38**, 1057–1064.
- Nukiyama, S., 1966, “The maximum and minimum values of the heat q transmitted from metal to boiling water under atmospheric pressure,” *International Journal of Heat and Mass Transfer* **9**, 1419–1433.
- Okamoto, T., Suzuki, T., and Yamamoto, N., 2000, “Microarray fabrication with covalent attachment of dna using bubble jet technology,” *Nature biotechnology* **18**, 438–441.
- Okuyama, K., and Iida, Y., 1990, “Transient boiling heat transfer characteristics of nitrogen (bubble behavior and heat transfer rate at stepwise heat generation),” *International journal of heat and mass transfer* **33**, 2065–2071.
- Okuyama, K., Takehara, R., Iida, Y., and Kim, J.-H., 2005, “Pumping action by boiling propagation in a microchannel,” *Microscale Thermophysical Engineering* **9**, 119–135.
- Olsson, E., and Kreiss, G., 2005, “A conservative level set method for two phase flow,” *Journal of computational physics* **210**, 225–246.
- Osher, S., and Sethian, J. A., 1988, “Fronts propagating with curvature-dependent speed: Algorithms based on hamilton-jacobi formulations,” *Journal of computational physics* **79**, 12–49.
- Pan, Y., and Suga, K., 2003, “Capturing the pinch-off of liquid jets by the level set method,” *J. Fluids Eng.* **125**, 922–927.
- Pandey, V., Biswas, G., Dalal, A., and Welch, S. W., 2018, “Bubble lifecycle during heterogeneous nucleate boiling,” *Journal of Heat Transfer* **140**
- Park, J.-D., Fukuda, K., and Liu, Q., 2009, “Transient chf phenomena due to exponentially increasing heat inputs,” *Nuclear Engineering and Technology* **41**, 1205–1214.

- Patankar, S. V., 1980, "Numerical heat transfer and fluid flow, hemisphere publ," *Corp., New York* **58**, 288.
- Peng, D., Merriman, B., Osher, S., Zhao, H., and Kang, M., 1999, "A pde-based fast local level set method," *Journal of computational physics* **155**, 410–438.
- Perez-Raya, I., and Kandlikar, S., 2016, "Evaporation on a planar interface—numerical simulation and theoretical analysis of heat and mass transport processes," in *Advances in Heat Transfer*, Vol. 48 (Elsevier). pp. 125–190.
- Perez-Raya, I., and Kandlikar, S. G., 2018, "Numerical models to simulate heat and mass transfer at sharp interfaces in nucleate boiling," *Numerical Heat Transfer, Part A: Applications* **74**, 1583–1610.
- Popinet, S., 2009, "An accurate adaptive solver for surface-tension-driven interfacial flows," *Journal of Computational Physics* **228**, 5838–5866.
- Popinet, S., 2018, "Numerical models of surface tension," *Annual Review of Fluid Mechanics* **50**, 49–75.
- Popinet, S., and Zaleski, S., 1999, "A front-tracking algorithm for accurate representation of surface tension," *International Journal for Numerical Methods in Fluids* **30**, 775–793.
- Prosperetti, A., 1981, "Motion of two superposed viscous fluids," *The Physics of Fluids* **24**, 1217–1223.
- Raeini, A. Q., Blunt, M. J., and Bijeljic, B., 2012, "Modelling two-phase flow in porous media at the pore scale using the volume-of-fluid method," *Journal of Computational Physics* **231**, 5653–5668.
- Raut, H. S., Bhattacharya, A., and Sharma, A., 2021, "Dual grid level set method based direct numerical simulations of nucleate boiling with oscillating base plate," *International Journal of Thermal Sciences* **162**, 106785.
- Raut, H. S., Bhattacharya, A., and Sharma, A., 2022, "Sustaining nucleate boiling in zero gravity using asymmetric sinusoidal base-plate oscillation," *International Journal of Heat and Mass Transfer* **184**, 122262.
- Renardy, Y., and Renardy, M., 2002, "Prost: a parabolic reconstruction of surface tension for the volume-of-fluid method," *Journal of computational physics* **183**, 400–421.

- Rhie, C. M., and Chow, W.-L., 1983, "Numerical study of the turbulent flow past an airfoil with trailing edge separation," *AIAA journal* **21**, 1525–1532.
- Rosenthal, M. W., 1957, "An experimental study of transient boiling," *Nuclear Science and Engineering* **2**, 640–656.
- Ruan, C., Xing, F., Huang, Y., Xu, L., and Lu, X., 2017, "A parametrical study of the breakup and atomization process of two impinging liquid jets," *Atomization and sprays* **27**
- Ruhlamath, 2022, "Thermal inkjet - inkjet printing with the effect of heat [online: last accessed august 2022]," <https://www.ruhlamat.com/en/wiki/thermal-inkjet-inkjet-printing-effect-heat>
- Sakurai, A., and Shiotsu, M., 1977a, "Transient pool boiling heat transfer-part 1: Incipient boiling superheat,"
- Sakurai, A., and Shiotsu, M., 1977b, "Transient pool boiling heat transfer-part 2: Boiling heat transfer and burnout,"
- Sakurai, A., Shiotsu, M., and Hata, K., 1992, "Boiling heat transfer characteristics for heat inputs with various increasing rates in liquid nitrogen," *Cryogenics* **32**, 421–429.
- Sakurai, A., Shiotsu, M., and Hata, K., 1996, "Boiling phenomenon due to quasi-steadily and rapidly increasing heat inputs in ln2 and lhe i," *Cryogenics* **36**, 189–196.
- Sakurai, A., Shiotsu, M., Hata, K., and Fukuda, K., 2000, "Photographic study on transitions from non-boiling and nucleate boiling regime to film boiling due to increasing heat inputs in liquid nitrogen and water," *Nuclear Engineering and Design* **200**, 39–54.
- Sakurai, A., Shiotsu, M., Hata, K., and Takeuchi, Y., 1989, "Quasi-steady nucleate boiling and its life caused by large stepwise heat input in saturated pool liquid he i," *Cryogenics* **29**, 597–601.
- Salih, A., and Ghosh Moulic, S., 2009, "Some numerical studies of interface advection properties of level set method," *Sadhana* **34**, 271–298.
- Sanjid, C., Murallidharan, J. S., and Sharma, A., 2021a, "Performance of sharp-versus-diffuse interface-based level set method on a staggered-versus-co-located grid," in *Proceedings of the 26th National and 4th International ISHMT-ASTFE Heat and Mass Transfer Conference December 17-20, 2021, IIT Madras, Chennai-600036, Tamil Nadu, India* (Begel House Inc.).

- Sanjid, C., Murallidharan, J. S., and Sharma, A., 2021b, "Sharp interface level set method on a co-located grid for high density ratio two-fluid flow," in *Fluid Mechanics and Fluid Power* (Springer). pp. 91–98.
- Sato, Y., and Ničeno, B., 2012, "A conservative local interface sharpening scheme for the constrained interpolation profile method," *International Journal for Numerical Methods in Fluids* **70**, 441–467.
- Sato, Y., and Ničeno, B., 2013, "A sharp-interface phase change model for a mass-conservative interface tracking method," *Journal of Computational Physics* **249**, 127–161.
- Sato, Y., and Niceno, B., 2015, "A depletable micro-layer model for nucleate pool boiling," *Journal of Computational physics* **300**, 20–52.
- Sato, Y., and Niceno, B., 2017, "Nucleate pool boiling simulations using the interface tracking method: Boiling regime from discrete bubble to vapor mushroom region," *International Journal of Heat and Mass Transfer* **105**, 505–524.
- Schrage, R. W., 1953, "A theoretical study of interphase mass transfer," in *A Theoretical Study of Interphase Mass Transfer* (Columbia University Press).
- Scriven, L., 1962, "On the dynamics of phase growth," *Chemical Engineering Science* **17**, 55.
- Shaikh, J., Sharma, A., and Bhardwaj, R., 2016, "On sharp-interface level-set method for heat and/or mass transfer induced stefan problem," *International Journal of Heat and Mass Transfer* **96**, 458–473.
- Shaikh, J., Sharma, A., and Bhardwaj, R., 2018, "On comparison of the sharp-interface and diffuse-interface level set methods for 2d capillary or/and gravity induced flows," *Chemical Engineering Science* **176**, 77–95.
- Shaikh, J., Sharma, A., and Bhardwaj, R., 2019, "On sharp-interface dual-grid level-set method for two-phase flow simulation," *Numerical Heat Transfer, Part B: Fundamentals* **75**, 67–91.
- Sharma, A., 2015, "Level set method for computational multi-fluid dynamics: A review on developments, applications and analysis," *Sadhana* **40**, 627–652.
- Sharma, A., 2016, *Introduction to computational fluid dynamics: development, application and analysis* (John Wiley & Sons).

- Shibahara, M., Fukuda, K., and Liu, Q., 2018, "Transient nucleate boiling on a horizontal heated cylinder in liquid d-mannitol," *Applied Thermal Engineering* **144**, 342–348.
- Shin, S., Abdel-Khalik, S., Daru, V., and Juric, D., 2005, "Accurate representation of surface tension using the level contour reconstruction method," *Journal of Computational Physics* **203**, 493–516.
- Shin, S., and Juric, D., 2002, "Modeling three-dimensional multiphase flow using a level contour reconstruction method for front tracking without connectivity," *Journal of Computational Physics* **180**, 427–470.
- Shiotsu, M., Hata, K., and Sakurai, A., 1992, "Comparison of transient heat transfer characteristics for large stepwise heat input in he i and he ii," *Cryogenics* **32**, 455–460.
- Siegel, R., and Keshock, E., 1964, "Effects of reduced gravity on nucleate boiling bubble dynamics in saturated water," *AICHE Journal* **10**, 509–517.
- Singh, N. K., and Premachandran, B., 2018, "A coupled level set and volume of fluid method on unstructured grids for the direct numerical simulations of two-phase flows including phase change," *International journal of heat and mass transfer* **122**, 182–203.
- Singh, N. K., and Premachandran, B., 2020, "Numerical investigation of film boiling on a horizontal wavy wall," *International Journal of Heat and Mass Transfer* **150**, 119371.
- Son, G., and Dhir, V. K., 1997 08, "Numerical Simulation of Saturated Film Boiling on a Horizontal Surface," *Journal of Heat Transfer* **119**, 525–533.
- Son, G., and Dhir, V. K., 1998 02, "Numerical Simulation of Film Boiling Near Critical Pressures With a Level Set Method," *Journal of Heat Transfer* **120**, 183–192.
- Son, G., and Dhir, V. K., 2007, "A level set method for analysis of film boiling on an immersed solid surface," *Numerical Heat Transfer, Part B: Fundamentals* **52**, 153–177.
- Son, G., and Dhir, V. K., 2008, "Numerical simulation of nucleate boiling on a horizontal surface at high heat fluxes," *International Journal of heat and Mass transfer* **51**, 2566–2582.
- Son, G., Dhir, V. K., and Ramanujapu, N., 1999, "Dynamics and heat transfer associated with a single bubble during nucleate boiling on a horizontal surface,"
- Son, G., Ramanujapu, N., and Dhir, V. K., 2002, "Numerical simulation of bubble merger process on a single nucleation site during pool nucleate boiling," *J. Heat Transfer* **124**, 51–62.

- Spencer, S., Andrews, G., and Deacon, C., 2013, "Contact angle of ethanol–water solutions on crystalline and mesoporous silicon," *Semiconductor science and technology* **28**, 055011.
- Su, G.-Y., Bucci, M., McKrell, T., and Buongiorno, J., 2016, "Transient boiling of water under exponentially escalating heat inputs. part i: Pool boiling," *International Journal of Heat and Mass Transfer* **96**, 667–684.
- Su, G., et al., 2015, *Experimental study of transient pool boiling heat transfer under exponential power excursion on plate-type heater*, Ph.D. thesis (Massachusetts Institute of Technology).
- Sun, D., and Tao, W., 2010, "A coupled volume-of-fluid and level set (voset) method for computing incompressible two-phase flows," *International Journal of Heat and Mass Transfer* **53**, 645–655.
- Sussman, M., Almgren, A. S., Bell, J. B., Colella, P., Howell, L. H., and Welcome, M. L., 1999, "An adaptive level set approach for incompressible two-phase flows," *Journal of Computational Physics* **148**, 81–124.
- Sussman, M., Fatemi, E., Smereka, P., and Osher, S., 1998, "An improved level set method for incompressible two-phase flows," *Computers & Fluids* **27**, 663–680.
- Sussman, M., Smereka, P., and Osher, S., 1994, "A level set approach for computing solutions to incompressible two-phase flow," *Journal of Computational physics* **114**, 146–159.
- Tachibana, F., Akiyama, M., and Kawamura, H., 1968, "Heat transfer and critical heat flux in transient boiling,(i) an experimental study in saturated pool boiling," *Journal of Nuclear Science and Technology* **5**, 117–126.
- Tanasawa, I., 1991, "Advances in condensation heat transfer," in *Advances in heat transfer*, Vol. 21 (Elsevier). pp. 55–139.
- Tanguy, S., Ménard, T., and Berlemont, A., 2007, "A level set method for vaporizing two-phase flows," *Journal of Computational Physics* **221**, 837–853.
- Tanguy, S., Sagan, M., Lalanne, B., Couderc, F., and Colin, C., 2014, "Benchmarks and numerical methods for the simulation of boiling flows," *Journal of Computational Physics* **264**, 1–22.

- Tomar, G., Biswas, G., Sharma, A., and Agrawal, A., 2005, "Numerical simulation of bubble growth in film boiling using a coupled level-set and volume-of-fluid method," *Physics of Fluids* **17**, 112103.
- Tomar, G., Fuster, D., Zaleski, S., and Popinet, S., 2010, "Multiscale simulations of primary atomization," *Computers & Fluids* **39**, 1864–1874.
- Tsai, J.-H., and Lin, L., 2002, "Active microfluidic mixer and gas bubble filter driven by thermal bubble micropump," *Sensors and Actuators A: Physical* **97**, 665–671.
- Unverdi, S. O., and Tryggvason, G., 1992, "A front-tracking method for viscous, incompressible, multi-fluid flows," *Journal of computational physics* **100**, 25–37.
- Utaka, Y., Kashiwabara, Y., and Ozaki, M., 2013, "Microlayer structure in nucleate boiling of water and ethanol at atmospheric pressure," *International Journal of Heat and Mass Transfer* **57**, 222–230.
- Utaka, Y., Kashiwabara, Y., Ozaki, M., and Chen, Z., 2014, "Heat transfer characteristics based on microlayer structure in nucleate pool boiling for water and ethanol," *International Journal of Heat and Mass Transfer* **68**, 479–488.
- Vachaparambil, K. J., and Einarsrud, K. E., 2019, "Comparison of surface tension models for the volume of fluid method," *Processes* **7**, 542.
- Villegas, L. R., Alis, R., Lepilliez, M., and Tanguy, S., 2016, "A ghost fluid/level set method for boiling flows and liquid evaporation: application to the leidenfrost effect," *Journal of Computational Physics* **316**, 789–813.
- Visentini, R., Colin, C., and Ruyer, P., 2014, "Experimental investigation of heat transfer in transient boiling," *Experimental thermal and fluid science* **55**, 95–105.
- Walunj, A., and Sathyabhama, A., 2016, "Dynamic pool boiling heat transfer due to exponentially increasing heat input-a review," *Procedia Technology* **25**, 1137–1145.
- Walunj, A., and Sathyabhama, A., 2018, "Transient chf enhancement in high pressure pool boiling on rough surface," *Chemical Engineering and Processing-Process Intensification* **127**, 145–158.
- Wang, S.-L., and Sekerka, R. F., 1996, "Algorithms for phase field computation of the dendritic operating state at large supercoolings," *Journal of Computational Physics* **127**, 110–117.

- Welch, J. E., Harlow, F. H., Shannon, J. P., and Daly, B. J., 1965, *The MAC method-a computing technique for solving viscous, incompressible, transient fluid-flow problems involving free surfaces*, Tech. Rep. (Los Alamos National Lab.(LANL), Los Alamos, NM (United States)).
- Welch, S. W., 1995, "Local simulation of two-phase flows including interface tracking with mass transfer," *Journal of Computational Physics* **121**, 142–154.
- Welch, S. W., and Wilson, J., 2000, "A volume of fluid based method for fluid flows with phase change," *Journal of computational physics* **160**, 662–682.
- Wu, J., and Dhir, V. K., 2010, "Numerical simulations of the dynamics and heat transfer associated with a single bubble in subcooled pool boiling," *Journal of heat transfer* **132**
- Wu, J., Dhir, V. K., and Qian, J., 2007, "Numerical simulation of subcooled nucleate boiling by coupling level-set method with moving-mesh method," *Numerical Heat Transfer, Part B: Fundamentals* **51**, 535–563.
- Yap, Y., Chai, J., Toh, K., and Wong, T., 2006, "Modeling the flows of two immiscible fluids in a three-dimensional square channel using the level-set method," *Numerical Heat Transfer, Part A: Applications* **49**, 893–904.
- Yap, Y., Chai, J., Toh, K., Wong, T., and Lam, Y., 2005, "Numerical modeling of unidirectional stratified flow with and without phase change," *International journal of heat and mass transfer* **48**, 477–486.
- Yoon, H. Y., Koshizuka, S., and Oka, Y., 2001, "Direct calculation of bubble growth, departure, and rise in nucleate pool boiling," *International Journal of Multiphase Flow* **27**, 277–298.
- Zakšek, P., Zupančič, M., Gregorčič, P., and Golobič, I., 2020, "Investigation of nucleate pool boiling of saturated pure liquids and ethanol-water mixtures on smooth and laser-textured surfaces," *Nanoscale and Microscale Thermophysical Engineering* **24**, 29–42.
- Zhang, S., Ni, M., and Ma, H., 2011, "Vof method for simulation of multiphase incompressible flows with phase change," in *AIP Conference Proceedings*, Vol. 1376 (American Institute of Physics). pp. 579–581.

List of Publications

International Journals:

1. Chirammel, S. S., Sharma, A., & Murallidharan, J. S. . Performance of Sharp-versus-Diffuse Interface-based Level Set Method on a Staggered-versus-Co-located Grid for CmFD. *Computational Thermal Sciences: An International Journal*, 15(2) (2023).
2. Sanjid S. Chirammel, Atul Sharma, and Janani S. Murallidharan, On Ghost Fluid Method-based Sharp Interface Level Set Method on a Co-located Grid and its comparison with Balanced Force-based Diffuse Interface Method, *Journal of Computational Physics* (under review - Received first review with minor corrections).
3. Sanjid S. Chirammel, Atul Sharma, and Janani S. Murallidharan, CmFD development Sharp-versus-Diffuse Interface-Based Level Set Method on a Staggered-versus-Co-located Grid, *International Journal of Multiphase Flow* (under review).
4. Sanjid S. Chirammel, Atul Sharma, and Janani S. Murallidharan, Sharp Interface Level Set Method on a Co-located Grid for CmFD with Heat Transfer-induced Phase Change (under preparation).
5. Sanjid S. Chirammel, Janani S. Murallidharan, and Atul Sharma, Single bubble nucleate boiling over a base plate, subjected to Power Transients (under preparation).

Edited Book:

1. J. Pinto, C.S. Sanjid, J.S. Murallidharan, & A. Sharma Advances in Computational and Experimental Methodologies for Single-Bubble Nucleate Boiling, Advances in Multiphase Flow, Edited by A. De, A. K. Gupta, A. Kushari, S. K. Aggarwal, A. K. Runchal, Begell House Inc., New York, 2022.

International Conference:

1. Sanjid, C. S., Janani Srree Murallidharan, and Atul Sharma. "Sharp interface level set method on a co-located grid for phase change heat transfer". Proceedings of the 25th National and 3rd International ISHMT-ASTFE Heat and Mass Transfer Conference (IHMT-2019). Begel House Inc., 2019
2. Sanjid, C. S., Janani Srree Murallidharan, and Atul Sharma. "Performance of Sharp- versus-Diffuse Interface-based Level Set Method on a Staggered-versus-Colocated grid." Proceedings of the 26th National and 4th International ISHMT-ASTFE Heat and Mass Transfer Conference, IIT Madras. Begel House Inc, 2021

National Conference:

1. Sanjid, C.S., Sharma, Atul, & Murallidharan, Janani Srree Ghosh, PradyumnaShrivastava, Atul, Shrivastava, Atul, & Nayak, Arun K. (Eds.). (2018). Collocated grid based interface capturing method for two-phase flows. India: Excel India Publishers.
2. C. S. Sanjid, Janani Srree Murallidharan, and Atul Sharma, Sharp Interface Level Set Method on a Co-located Grid for High Density Ratio Two-Fluid Flow, Fluid Mechanics and Fluid Power, Lecture Notes in Mechanical Engineering, Springer, Singapore, pp. 91-98, 2021 (https://link.springer.com/chapter/10.1007/978-981-16-0698-4_10)

Acknowledgements

Firstly, I would like to express my sincere gratitude to my supervisor Prof. Janani Srree Murallidharan for the continuous support of my Ph.D. study and related research, for her patience, motivation, and immense knowledge. Her guidance helped me in all the time of research and writing of this thesis. Her insightful comments and constructive criticisms at different stages of my research which were thought-provoking and helped me to focus my work with positive energy.

I sincerely thank my Ph.D. co-supervisor Prof. Atul Sharma for introducing me to this exciting and challenging domain of CFD development. His insight, focus, and critical thinking was thought-provoking and inspiring. His comments and suggestions to improve the quality of this work is invaluable. I am grateful to god for blessing me with such supportive supervisors who cares about professional as well as personal well-being.

Besides my supervisors, I would like to thank the rest of my thesis committee: Prof. Sandip Kumar Saha, Prof. Shyamprasad Karagadde, and Prof. Abhilash J. Chandy for their questions and critical analysis to broaden various aspects of this work.

I am extremely thankful to senior labmates Dr. Namshad and Nitin for their companionship and guidance during my initial struggles of solver development. I would also thank other labmates Dr. Charu, Dr. Vinay, Dr. Siddharth, Dr. Harshal, Sourabh, and Sumant for cooperation and friendship. I express my sincere thanks to all my friends at the institute Sarvesh, Sachin, Yogi, Uddipta, Nazim, Mohnish and many more for their support. Healthy discussions with John is also gratefully acknowledged.

Last but not least, the emotional support and blessings from my parents as well as my brother and sister during this Ph.D. and life in general could not be thanked in words. Their efforts will be always acknowledged throughout my life silently. I find myself lucky to have a companion in form of my wife, whose support, and motivation throughout this journey is indebted.

SANJID C S
IIT Bombay